VNIVERSITAT DE VALÈNCIA

Departamento de Física Teórica

Testing neutrino physics and dark radiation properties with cosmological measurements

Ph.D. Thesis

Elena Giusarma

Supervisor

Dr. Olga Mena Requejo

Instituto de Física Corpuscular, IFIC/CSIC-UV

Valencia, October 2013.

OLGA MENA REQUEJO, Científica Titular del Consejo Superior de Investigaciones Científicas (CSIC), perteneciente al Instituto de Física Corpuscular (IFIC), centro mixto del CSIC y de la Universitat de València,

CERTIFICA:
Que la presente memoria " TESTING NEUTRINO PHYSICS AND DARK RADIATION PROPERTIES WITH COSMOLOGICAL MEASUREMENTS " ha sido realizada bajo su dirección en el IFIC y en el Departamento de Física Teórica de la Universitat de València, por ELENA GIUSARMA y constituye su Tesis para optar al grado de Doctor en Física.

Y para que así conste, en cumplimiento de la legislación vigente, presenta en el Departamento de Física Teórica de la Universitat de València la referida Tesis Doctoral, y firma el presente certificado.

Valencia, a 31 de Julio de 2013.

Olga Mena Requejo

Visto bueno de la tutora: Pilar Hernández.

In loving memory of my aunt Lina

Neutrinos, they are very small.
They have no charge and have no mas
And do not interact at all.
The earth is just a silly ball

To them, through which they simply pass,
Like dustmaids through a drafty hall
Or photons through a sheet of glass.
They snub the most exquisite gas,

Ignore the most substantial wall,
Cold-shoulder steel and sounding brass,
Insult the stallion in his stall,
And scorning barriers of class,

Infiltrate you and me! Like tall
And painless guillotines, they fall
Down through our heads into the grass.
At night, they enter at Nepal

And pierce the lover and his lass
From underneath the bed-you call
It wonderful; I call it crass.

John Updike, Cosmic Gall

Acknowledgments-Ringraziamenti-Agradecimientos

It is now time to thank all those people who have contributed to this thesis and all those who have been by my side during these years.

First of all I would like to express my gratitude to my supervisor, Dr. Olga Mena for the continuous support of my Ph.D study, for her patience, enthusiasm and knowledge. Without her help probably this work would not exist. In addition to being a good teacher she is also a great person. She helped me a lot when I moved to Valencia, she has been able to understand my difficult moments and on top of that she always pushed me to do my best. With her confidence she has managed to make me believe more in myself. For this reason, I thank her very much and I hope to collaborate again with her in the future.

I am enormously grateful to Alessandro Melchiorri to be always present in my professional life. It was under his tutelage that I developed an interest in cosmology and thanks to his encouragement I applied for a PhD in Valencia. I am grateful for allowing me to collaborate again with him and and his research group of the University “La Sapienza" of Rome and for the availability that he showed me during these years.

I would like to thank Roland De Putter for his help with programming, for his advice on this thesis and on top of that for the time spent explaining me many things in cosmology. I thank him for the opportunity to learn from his teachings and for his patience with me and with my english.

I would also like to express my gratitude to my two collaborators, and also friends, Maria Archidiacono e Stefania Pandolfi. I thank them for all discussions about cosmology, for suggestions, and our conversations via chat.

Un ringraziamento speciale va ai miei genitori, a mio fratello Sesto e a mia sorella Daniela per aver sempre appoggiato le mie scelte e per essere sempre al mio fianco in tutti i momenti della mia vita. Se sono arrivata fin qui è anche merito loro.

Un sincero agradecimiento a mis amigos Alberto, Paola F., Elisa, Paola S., Gioia, Nuria y Moritz. Son las primeras personas que conocí en Valencia y son ellos los que me ayudaron a superar los primeros momentos de dificultad en un ambiente nuevo. En ellos he descubierto verdaderos amigos, en los que siempre puedes contar.

También quisera agradecer mi compañero de doctorado y amigo Manuel por haber alegrado estos años de doctorado, entre conferencias y seminarios, con su simpatía y sobre todo gracias por haberme ayudado a practicar mi español.

No puedo no agradecer la “colonia" de italianos que encontré en el IFIC (algunos fuera) y que considero como mi segunda familia. Gracias a: Francesca A., Andrea, Eleonora, Roberta, Miguel, Francesca M., Michele y Fabio por todos los buenos momentos vividos dentro y fuera del IFIC. Sin ellos mi estancia en Valencia no hubiera sido lo mismo.

Un especial agradecimiento va a Mauricio por haber estado a mi lado durante estos meses y por haber soportado mis continuos cambios de humor. Aunque venimos de dos realidades completamente diferentes creo que hay algo muy fuerte que nos une.

Cuando decidí aceptar el doctorado en Valencia no estaba muy segura de mi elección, sobre todo por el tener que empezar una nueva vida en otro país. Por suerte durante mi camino he conocido a muchas personas, cada una de las cuales ha dejado en mí una señal que permanecerá para siempre. Por tanto, a todas las personas que, aunque no aparecen aquí con nombres, han estado presentes de alguna forma en mi vida durante estos años de doctorado, dirijo mi más sincera gratidud.

Un ultimo, ma non per ordine di importanza, ringraziamento va ai miei amici Italiani. Grazie per avermi sempre supportato e sopportato, per aver sempre creduto in me e soprattuto per il grande affetto dimostratomi. Non potrei desiderare amici migliori. Grazie a: Francesca C., Francesca T., Enrico, Gennaro, Danilo, Giuseppe, Lella, Crispino, Grazia, Tiziano e Claudio.

Resumen de la tesis

Los neutrinos son una de las partículas más misteriosas del universo. Actualmente sabemos, por los resultados experimentales de oscilaciones de neutrinos, que los neutrinos son masivos. Desafortunadamente, los experimentos de oscilaciones no son sensibles a la escala absoluta de las masas de los neutrinos.

La cosmología constituye uno de los medios para probar la escala absoluta de masas y juega un papel importante a la hora de determinar las propriedades de los neutrinos. Estas partículas afectan tanto a la física del fondo de radiación cósmico (CMB, del inglés *Cosmic Microwave Background*), así como al agrupamiento de las galaxias, dejando una huella significativa tanto en la forma completa (full shape) de la señal del agrupamiento (*clustering*) (explotado por las medidas del espectro de potencias de la materia) como en la señal geométrica (explotado a través de las medidas de la oscilación acústica de los bariones (BAO)).

En esta tesis hemos derivado los límites en las masas y en las abundancias de los neutrinos utilizando los datos cosmológicos recientes y considerando un escenario ΛCDM así como otros posibles escenarios cosmológicos.

El Capítulo I contiene una breve descriptión del modelo cosmológico actual y de las mediciones que lo apoyan. Una descripción detallada del impacto en cosmología de las propiedades de los neutrinos, como su masa y su abundancia, se puede encontrar en el Capítulo II.

En el Capítulo III hemos estudiado un escenario ΛCDM con $N_{\rm eff}$ especies totales, inluyendo tanto tres neutrinos activos como neutrinos masivos estériles, con el fin de comprobar los modelos (3+2) con los datos cosmológicos. Hemos encontrado que este modelo está permitido a un nivel de confianza del 95 % por los datos cosmolgícos actuales (que incluyen CMB, agrupamiento de las galaxias y Supernovas Ia). También hemos considerado las abundancias del Helio-4 y del Deuterio de *Big Bang Nucleosynthesis* y hemos encontrado que estas últimas medidas puede comprometer la viabilidad de los modelos (3+2). Además, hemos presentado una predicción para estimar los errores en los parámetros de los neutrinos activos y estériles de datos futuros. Los datos cosmológicos futuros podrían determinar la masas, en sub-eV, de los neutrinos activos y estériles y de las abundancias de los neutrinos estériles con una precisión del 10−30%, para masas de neutrinos estériles en el rango 0.5 eV$> m_{\nu_s} >$ 0.1 eV. Hemos también mostrado que la presencia de neutrinos estériles masivos en el universo podría deducirse a partir de las inconsistencias entre los valores de la

constante de Hubble H_0 obtenidos a partir de los datos del CMB y de la agrupación de las galaxias y de los derivados a partir de medidas independientes de la constante de Hubble en la próxima década.

En el Capítulo IV hemos derivado los límites a las masas de los neutrinos a partir del espectro de potencia angular del catálogo de galaxias BOSS, parte del experimento Sloan Digital Sky Survey III, Data Release Eight (BOSS DR8), usando la muestra fotométrica de las galaxias CMASS que hemos dividido en cuatro *redshift bins* fotométricos, con redshifts de $z = 0.45$ hasta $z = 0.65$, y considerando un libre parámetro de *bias* constante para cada uno de estas muestras. Hemos calculado los espectros de potencia en dos rangos de multipolos, $30 < \ell < 150$ y $30 < \ell < 200$, con el fin de minimizar los efectos no lineares y hemos considerado un modelo ΛCDM plano junto con tres neutrinos masivos activos. Combinando los datos de BOSS DR8 con los datos de CMB de WMAP7, hemos encontrado un límite superior a la suma de las masas de los tres neutrinos activos de $\sum m_\nu < 0.56$ eV al 95% CL para $\ell_{max} = 200$ y un límite superior de $\sum m_\nu < 0.26$ eV al 95% CL si se incluye también la medida de la costante de Hubble procedente de los datos del Telescopio Hubble (HST, del inglés *Hubble Space Telescope*). También hemos mostrado que considerando los datos de Supernova y/o BAO los límites de la masa de los neutrinos no mejoran, una vez que se incluye la medida prodecente de HST.

Las nuevas medidas a altos multipolos del CMB realizada a finales de 2012 y principios de 2013 por el *South Pole Telescope*, SPT, y por el *Atacama Cosmology Telescope*, ACT, parecen dar resultados diferentes en lo referente a las masas de los neutrinos y sus abundancias. Motivados por las discrepancias existentes entre los resultados de SPT y de ACT, hemos explorado en el Capítulo V los límites cosmológicos en varios escenarios de neutrinos y de radiación oscura, utilizando los datos de CMB (WMAP9), las nuevas medidas a altos multipolos ℓ de SPT y de ACT , los datos de BAO, las medidas de la constante de Hubble (HST) y los datos de Supernovas. En el escenario usual (ΛCDM), ya sea con tres especies de neutrinos masivos o con un número $N_{\rm eff}$ de neutrinos sin masa, los dos experimentos de CMB a altos multipolos, esto es, SPT y ACT, dan resultados similares si los datos de BAO se eliminan de los análisis y si se considera también la medida de H_0 procedente de HST. En el caso de $N_{\rm eff}$ especies de neutrinos masivos, el análisis de los datos de SPT y de ACT muestran resultados muy diferentes en lo que se refiere a $\sum m_\nu$: mientras que la evidencia ($\sum m_\nu \sim 0.5$ eV) encontrada por los datos de SPT persiste independientemente del conjunto de datos combinados en el análisis, los datos de ACT proveen un límite superior a $\sum m_\nu$ de ~ 0.4 eV a un nivel de confianza del 95%. A continuación, hemos explorado dos escenarios cosmológicos extendidos con una ecuación de estado de la energía oscura y con una variación del índice espectral y hemos mostrado que la evidencia de la existencia de masas de los neutrinos detectada por el experimento SPT desaparece para las combinaciones de todos los datos. Una vez más, el acuerdo entre las dos medidas del CMB a altos multipolos mejora notoriamente al añadir los datos de HST.

En el capítulo VI hemos estudiado un modelo de radiación oscura que interacciona con la materia oscura, derivando los límites procedentes de los datos cosmológicos recientes a la abundancia de la radiación oscura así como a su velocidad efectiva y a su parámetro de viscosidad. Suponiendo la existencia de especies de radiación oscura adicionales que interactúan con el sector de la materia oscura, las propiedades de agrupación de estas partículas adicionales de radiación oscuras podrían ser diferentes a las de los neutrinos del Modelo Estándar (para los cuales $c^2_{\rm eff} = c^2_{\rm vis} = 1/3$), ya que las partículas adicionales de radiación oscura están acopladas al fluido de la materia oscura. Hemos encontrado que los límites cosmológicos en el número de especies adicionales de radiación oscura no cambian cuando se consideran modelos de interacción, mientras los errores en las propiedades de agrupamiento de la radiación oscura incrementan notoriamente (alrededor de un orden de magnitud), sobre todo debido a las correlaciones existentes entre la intensidad de la interacción entre la radiación oscura y la materia oscura y $c^2_{\rm eff}$, $c^2_{\rm vis}$. En el caso del parámetro de viscosidad $c^2_{\rm vis}$, los errores sobre este parámetro se duplican al considerar escenarios con interacciones entre la materia y radición oscuras. Asimismo, hemos analizado las perspectivas con datos del CMB futuros. Si la radiación y materia oscuras interaccionan en la naturaleza, pero los datos se analizan asumiendo el modelo sin interacción, los valores reconstruidos para la velocidad efectiva y para el parámetro de viscosidad se desplazarán con respecto a su valor estándar de 1/3 ($c^2_{\rm eff} = 0.34^{+0.006}_{-0.003}$ y $c^2_{\rm vis} = 0.29^{+0.002}_{-0.001}$, ambos a un nivel de confianza del 95%) para datos procedentes de la futura misión COrE de CMB.

Las últimas medidas de las anisotropías de temperatura del CMB estrenados del satélite Planck, proporcionan las más estricta restricción a los parámetros cosmológicos hasta la fecha. Sin embargo, estas medidas no proporcionan un límite fuerte a la suma de las masas de los neutrinos si no se combinan con otras medidas externas. El límite superior de los datos de Planck, considerando *lensing*, combinados con las medidas de polarización a bajos multipolos ℓ (WMAP9) es $\sum m_\nu < 1.1$ eV a un nivel de confianza del 95%. Si se a?ande la madida de constante de Hubble (HST) dicho límite mejora las restricciones a $\sum m_\nu < 0.21$ eV a un nivel de confianza del 95%. Las medidas de Planck no encuentran evidencia de la existencia de partículas relativistas adicionales más allá de las tres familias de neutrinos en el Modelo Estándar. El límite obtenido combinando los datos del CMB de Planck con la medida de la costante de Hubble (HST) es $N_{\rm eff} = 3.62 \pm 0.25$.

El catálo de galaxias futuro Euclid, podría proporcionar la herramienta ideal para probar las propiedades del neutrino con la cosmología. Combinando varias medidas de Euclid con datos del CMB, la suma de las masas de los neutrinos podría medirse con una precisión a un nivel de 1σ (desviación estándar) de 0,01 eV asumiendo para las predicciones un modelo con $\sum m_\nu = 0.056$ eV. La misma combinación de datos puede llegar a un 1σ de sensibilidad a $N_{\rm eff}$ de 0.02, con lo cual, la pequeña desviación de 0.046 de la expectativa estándar de 3 (que resulta mayoritariamente debido al desacoplamiento no instantáneo del neutrino) podría ser probado a un nivel de 2σ.

Introduction

Cosmology is a science whose main purpose is to understand the origin and the evolution of the structures we observe today in our universe.

The discovery of the recession of galaxies, of the Cosmic Microwave Background (CMB) radiation, of the abundances and the synthesis of light elements and of the large scale structure formation, have shown that the Standard Cosmological Model provides an accurate description of the current universe. The recent measurements of the luminosity distance of Type Ia supernovae at high redshift have further confirmed the Cosmological Model, implying an accelerated expansion of the universe. Current cosmological data indicate that the universe has an almost flat geometry and only a 5% of the total energy density is composed of ordinary matter (baryonic). The rest is in the form of non visible matter, called *dark matter*, whose total amount represents about the 22% of the total energy, and the remaining 73% is attributed to a fluid with a negative pressure, responsible of the current acceleration of the expansion of the universe and known as *dark energy*. The nature of the dark matter and the dark energy components are among the most important problems in physics nowadays.

In particular, dark matter has important consequences in the evolution of the Universe and in the structure formation processes. While the major contribution to the dark matter component should arise from *cold dark matter* (CDM), a small component of *hot dark matter* (HDM) can also be present. CDM consists of particles which were non-relativistic at the epoch when the universe became matter-dominated; HDM, by contrast, consists of particles with large thermal velocities (i.e. they are hot relics) which were relativistic at time at which they decoupled from the thermal bath. HDM affects the evolution of cosmological perturbations erasing the density contrasts on wavelenghts smaller than the free-streaming scale (scale at which the particles move freely in random directions with a speed close to that of light). An obvious candidate for the HDM component is the neutrino.

In the Standard Model of elementary particles neutrinos have no mass. In this model, there are three massless neutrino species that only interact through the weak force. Over the last decades, experiments involving solar, atmospheric, reactor and accelerator neutrinos have adduced robust evidence for the existence of neutrino oscillations, implying that neutrinos have masses. However, oscillation experiments only provide bounds on the neutrino squared mass differences, and therefore the absolute scale of neutrino masses must come from different observations. Direct information on the absolute neutrino mass scale can be

extracted from kinematical studies of tritium beta decay or from searches for neutrino-less double beta decay. The former (yet unobserved) rare decay sets a limit on the neutrino mass scale if neutrinos have a Majorana characater.

Cosmological data provide an independent tool to tackle the absolute scale of neutrino and to study its properties. Neutrinos can leave key signatures in several cosmological data sets. In the early universe, the standard model neutrinos are in thermal equilibrium at temperatures larger than about a MeV, after which they decouple when they are still relativistic, leaving a distribution of relic neutrinos that contribute to the mass-energy density of the universe. These neutrinos affect the expansion rate of the universe and change the epoch of matter-radiation equality, leaving an imprint on the CMB anisotropies (through the so-called Integrated Sachs-Wolfe effect) and on structure formation. After becoming non-relativistic, the neutrino hot dark matter relics suppress the growth of matter density fluctuations and, consequently, galaxy clustering. Measurements of all of these observations have been used to place new constraints on neutrino physics providing an upper limit on the sum of neutrino masses below ~ 0.5 eV.

The simplest explanation of neutrino masses requires the existence of right handed, singlet neutrino states. However, there is no fundamental symmetry in the Standard Model that fixes the number of such sterile neutrino states. This means that there could be sterile neutrinos in nature. Cosmological data allow us also to measure the amount of relativistic energy density in the universe in terms of the effective number of neutrinos, $N_{\rm eff}$. The Standard Model prediction for $N_{\rm eff}$ is 3.046. A larger number of neutrino species, or in general, of any other hot thermal relic contributing to $N_{\rm eff}$, will leave an imprint in several cosmological observables. As an example, a value of $N_{\rm eff}$ larger than its canonical expectation at the Big Bang Nucleosynthesis (BBN) era will affect the Hubble expansion rate, causing weak interactions to become uneffective earlier. This will lead to a larger neutron-to-proton ratio and will change the standard BBN predictions for light element abundances. Concerning CMB physics, a larger value of $N_{\rm eff}$ will change the epoch of the matter-radiation equality, that will occur later in time, and will lead to an enhancement of the height of the first peak and to a shift of the position of acoustic peaks.

In this Thesis we will focuse on the study of the neutrino properties using the most recent and available cosmological data. In particular we will explore the bounds on the active and sterile neutrino masses as well as on the number of dark radiation species within the ΛCDM cosmological scenario as well as in other extended scenarios.

The thesis is organized in three parts: a Theoretical Introduction, the Scientific Research and a final Summary.

In the Theoretical Introductory Chapter we describe the Standard Cosmological Model and the observations that support its validity. The second introductory Chapter deals with the basic properties of the CMB, showing the impact of neutrinos and dark radiation on the

CMB and on large scale structure formation.

In the Scientific research we present the scientific work carried out in this thesis where each chapter contains a scientific referred publication.

In Chapter III we perform an analysis of current cosmological data and derive bounds on the masses of the active and sterile neutrino states as well as on the number of sterile states. We also present a forecast to compute the errors on the active and sterile neutrino parameters from the ongoing Planck CMB mission together with BOSS and Euclid galaxy survey data.

In Chapter IV we derive neutrino mass bounds from the angular power spectra of the clustering of galaxies density at different redshifts, in combination with priors from the CMB and other cosmological data sets. For our analysis we consider the CMASS sample of 900,000 luminous galaxies with photometric redshifts measured from Sloan Digital Sky Survey III Data Release Eight (SDSS DR8).

In Chapter V we present new bounds on the dark radiation and neutrino properties in different cosmological scenarios combining the Atacama Cosmology Telescope (ACT) and the South Pole Telescope (SPT) data with the nine-year data release of the Wilkinson Microwave Anisotropy Probe (WMAP-9), BAO data, Hubble Telescope measurements of the Hubble constant and Supernovae Ia luminosity distance data. We start with the standard three massive neutrino case within a ΛCDM scenario, then we move to the case in which there are $N_{\rm eff}$ massive species with a total mass given by $\sum m_\nu$ and at last we enlarge the minimal ΛCDM scenario allowing for more general models with a constant dark energy equation of state or with a running of the scalar spectral index of primordial perturbations.

In Chapter VI we study the cosmological signatures of a dark radiation component which interacts with the cold dark matter and we derive the cosmological constraints on the dark radiation abundance, on its effective velocity and on its viscosity parameter. We than explore the perspectives from future CMB data in dark radiation-dark matter coupled models.

In the Summary and conclusions, we summarize the objectives and achievements of the work presented in this thesis.

Publications

This thesis is based on the following publications:

Chapter 3
Constraints on massive sterile neutrino species from current and future cosmological data
By E. Giusarma, M. Corsi, M. Archidiacono, R. de Putter, A. Melchiorri, O. Mena and S. Pandolfi.
Feb 2011. 9 pp. [e-Print Archive: astro-ph/1102.4774]
Published in Phys. Rev. D83: 115023, (2011).

Chapter 4
New Neutrino Mass Bounds from Sloan Digital Sky Survey III Data Release 8 Photometric Luminous Galaxies
By R. de Putter, O. Mena, E. Giusarma, S. Ho, A. Cuesta, H. -J. Seo, A. Ross, M. White, D. Bizyaev, H. Brewington, D. Kirkby, E. Malanushenko, V. Malanushenko, D. Oravetz, K. Pan, W. J. Percival, N. P. Ross, D. P. Schneider, A. Shelden, A. Simmons, S. Snedden.
Jan 2012. 14 pp. [e-Print Archive: astro-ph/ 1201.1909].
Published in Astrophys. J. 761, 12 (2012).

Chapter 5
Neutrino and Dark Radiation properties in light of latest CMB observations
By M. Archidiacono, E. Giusarma, A. Melchiorri and O. Mena.
Mar 2013. 11 pp. [e-Print Archive:astro-ph/1303.0143]
Published in Phys. Rev. D 87, 103519 (2013).

Chapter 6:
Dark Radiation and interacting scenarios
By R. Diamanti, E. Giusarma, O. Mena, M. Archidiacono and A. Melchiorri.
Dec 2012. 8 pp. [e-Print Archive: astro-ph/1212.6007]
Published in in Phys. Rev. D 87, 063509 (2013).

Papers not discussed in the thesis:

Cosmic dark radiation and neutrinos
By M. Archidiacono, E. Giusarma, S. Hannestad and O. Mena.

Jul 2013. 22 pp. [e-Print Archive: astro-ph/1307.0637]
Submitted to the Advances in High Energy Physics Journal.

Constraints on neutrino masses from Planck and Galaxy Clustering data
By E. Giusarma, R. de Putter and O. Mena.
Jun 2013. 9 pp. [e-Print Archive: astro-ph/1306.5544]
Submitted to the Physical Review D Journal.

Testing standard and non-standard neutrino physics with cosmological data
By E. Giusarma, R. de Putter and O. Mena.
Dec 2012. 8 pp. [e-Print Archive: astro-ph/1211.2154]
Published in Phys. Rev. D87: 043515, (2013).

Dark Radiation in extended cosmological scenarios
By M. Archidiacono, E. Giusarma, A. Melchiorri and O. Mena.
Jun 2012. 7 pp. [e-Print Archive:astro-ph/1206.0109]
Published in Phys. Rev. D86: 043509, (2012).

Sterile neutrino models and nonminimal cosmologies
By E. Giusarma, M. Archidiacono, R. de Putter, A. Melchiorri and O. Mena.
Dec 2011. 8 pp. [e-Print Archive:astro-ph/1112.4661
Published in Phys. Rev. D85: 083522, (2012).

Impact of general reionization scenarios on extraction of inflationary parameters
By S. Pandolfi, E. Giusarma, E. W. Kolb, M. Lattanzi, A. Melchiorri, O. Mena, M. Pena and A. Cooray.
Sep 2010. 10 pp. [e-Print Archive: astro-ph/1009.5433]
Published in Phys. Rev. D82: 123527, (2010).

Harrison-Z'eldovich primordial spectrum is consistent with observations
By S. Pandolfi, A. Cooray, E. Giusarma, E. W. Kolb, A. Melchiorri, O. Mena and P. Serra.
Mar 2010. 4 pp. [e-Print Archive: astro-ph/1003.4763]
Published in Phys. Rev. D81: 123509, (20010).

Contents

Part I

Cosmology Overview

Chapter 1

The standard cosmological model

The current theory of the evolution of the universe is described by the Standard Cosmological Model, also known as the Hot Big Bang Model. This model, which provides the expansion of the universe, is based on two fundamental elements: the *Cosmological Principle*, which assumes the isotropy and homogeneity of the universe, and the *Einstein Field Equations*, which describe the behavior and the evolution of a physical system under the action of gravity. In this first chapter we will illustrate the standard cosmological model, deriving the equations that govern the evolution of the universe as well as describing the main methods used to measure the parameters which characterize such a universe.

1.1 Friedmann-Robertson-Walker metric

One of the most important assumptions of modern cosmology is the *Cosmological Principle*, according to which, on scales larger than 100 Mpc, the universe is homogeneous and isotropic. The homogeneity implies that the universe has no privileged positions, in other words, the universe is invariant under translations, while the isotropy implies that there are no privileged directions, and thus the universe is invariant under rotations. On smaller scales, the universe is highly inhomogeneous.

The homogeneity and the isotropy implied by the Cosmological Principle seem to agree with observations of the distribution of galaxies clusters and with observations of the Cosmic Microwave Background (CMB).

The geometrical properties of a homogeneous and isotropic universe are defined in a frame of reference in which each point in the space-time is associated with a vector in the four-dimensional space, having three space components $x^\mu\,(\mu = 1, 2, 3)$ and one time component t. In this coordinate system, the interval between two points is defined as:

$$ds^2 = g_{\mu\nu} dx^\mu dx^\nu \ , \tag{1.1}$$

where repeated suffixes imply summations and indices μ and ν range from 0 to 3; the first one refers to the time coordinate ($dx^0 = dt$) and the last three are space coordinates.

The tensor $g_{\mu\nu}$ is a symmetric tensor known as the *metric* and describes the space-time geometry [1].

In special relativity, the separation between two events in the space-time and in polar coordinates, can be written as:

$$ds^2 = -c^2dt^2 + dr^2 + r^2d\Omega^2 \ , \tag{1.2}$$

where $d\Omega^2 = d\theta^2 + \sin^2\theta d\phi^2$.

This equation defines the *Minkowski metric* that describes a space-time flat and static; therefore not curved by the presence of mass and energy.

In a homogeneous and isotropic universe, in an expanding or contracting phase, in which is present matter and energy, the Minkowski metric is not suitable to describe the properties of space-time.

The most general metric for such a universe, in which the Cosmological Principle holds, is the *Friedmann-Robertson-Walker (FRW) metric*:

$$ds^2 = c^2dt^2 - a^2(t)\left[\frac{dr^2}{1-kr^2} + r^2(d\theta^2 + \sin^2\theta d\phi^2)\right] \ , \tag{1.3}$$

where r, θ and ϕ are the comoving coordinates, t is the time measured by an observer who sees the universe expanding uniformly around her/him, and k is the curvature parameter which may have three different values: $k = 0$ if the universe is flat, $k = +1$ if the universe is closed and $k = -1$ if the universe is open. The function $a(t)$ is called *cosmic scale factor*; it describes the time evolution of the universe.

1.2 Hubble Law and Redshift

It is useful to introduce two new variables related to scale factor a: the *Hubble parameter* and the *redshift*.

The Hubble parameter is defined as:

$$H(t) = \frac{1}{a}\frac{da}{dt} = \frac{\dot{a}}{a} \ , \tag{1.4}$$

and measures how rapidly the scale factor changes. The value of this parameter evaluated at the present time (*Hubble constant*) is known to great accuracy. Recent results from the Hubble Space Telescope [2], provide a value of $H(t_0) = H_0 = 73.8 \pm 2.4$ km s^{-1}Mpc^{-1}.

At low-redshift, this constant relates the recessional velocity of galaxies and their distance from the observer by the **Hubble Law**:

$$v = H_0 d \ . \tag{1.5}$$

It is conventional to parametrize H_0 as:

$$H_0 = 100\ h\frac{\text{km}}{\text{s Mpc}} \ , \tag{1.6}$$

with $h \sim 0.7$.

The **redshift** of a luminous source is defined by the quantity:

$$z = \frac{\lambda_0 - \lambda_e}{\lambda_e} \ , \tag{1.7}$$

where λ_0 is the wavelength of the radiation from the source observed at 0, that we assume to be the origin of our coordinate system, at a time t_0; λ_e is the wavelength emitted at a time t_e by the source which is at a comoving coordinate r. It is possible to derive the link between the redshift and the scale factor.

During its travel from the source to the observer, the radiation propagates along the null geodesic $ds^2 = 0$ and, therefore,

$$cdt = -a(t)\frac{dr}{\sqrt{1-kr^2}} \ . \tag{1.8}$$

The light ray emitted from the source at a time t_e reaches the observer at a time t_0, therefore we can write:

$$c\int_{t_e}^{t_0}\frac{dt}{a(t)} = -\int_{r_1}^{0}\frac{dr}{\sqrt{1-kr^2}} \ . \tag{1.9}$$

The subsequent light ray emitted at a time $t_e + dt_e$ will be observed at a time $t_0 + dt_0$ satisfying:

$$c\int_{t_e+dt_e}^{t_0+dt_0}\frac{dt}{a(t)} = -\int_{r_1}^{0}\frac{dr}{\sqrt{1-kr^2}} \ . \tag{1.10}$$

Given that equation (1.9) does not change because r is a comoving coordinate and both the source and the observer are moving with the cosmological expansion, we can combine the previous equations, (1.9) and (1.10), and we obtain:

$$\int_{t_e+dt_e}^{t_0+dt_0}\frac{dt}{a(t)} = \int_{t_e}^{t_0}\frac{dt}{a(t)} \ , \tag{1.11}$$

from wich we derive:

$$\frac{dt_e}{a(t_e)} = \frac{dt_0}{a(t_0)} \ . \tag{1.12}$$

In particular, if we consider the frequencies of the emitted and observed light, $\nu_e = 1/dt_e$ and $\nu_0 = 1/dt_0$, we have:

$$\nu_e a(t_e) = \nu_0 a(t_0) \tag{1.13}$$

or, equivalently,

$$\frac{a(t_e)}{\lambda_e} = \frac{a(t_0)}{\lambda_0} \ . \tag{1.14}$$

Using the definition of redshift, eq. (1.7), we finally find the relation between redshift and the expansion factor:

$$1 + z = \frac{a(t_0)}{a(t_e)} \ . \tag{1.15}$$

We use the usual convention that $a(t_0) = a_0 = 1$.

Thus the redshift we observe for a distant object depends only on the relative scale factor at the time of emission.

1.3 Cosmological distances

The *proper distance* $d_p(t)$ between two points, which we take to be in the origin of a set of polar coordinates r, θ and ϕ, is the length of the spatial geodesic at a fixed time, $dt = 0$. Along the geodesic the angle (θ, ϕ) is a constant, thus the equation (1.3) reduces to:

$$ds = a(t)\frac{dr}{\sqrt{1 - kr^2}} \ . \tag{1.16}$$

Integrating the previous equation over the radial comoving coordinate r [1] we obtain the proper distance:

$$d_p(t) = a(t) \int_0^r \frac{dr}{\sqrt{1 - kr^2}} = a(t) f(r) \ , \tag{1.17}$$

where the function $f(r)$ is:

$$f(r) = \begin{cases} \sin^{-1}(r) & \text{if} \quad k = 1 \\ r & \text{if} \quad k = 0 \\ \sinh^{-1}(r) & \text{if} \quad k = -1 \end{cases} \tag{1.18}$$

The proper distance at a time t is related to the proper distance at the present time t_0 by the relation:

$$d_p(t_0) = a_0 f(r) = \frac{a_0}{a} d_p(t), \tag{1.19}$$

where $a_0 = 1$.

One can define other kinds of distances which are measurable. One of these is the *luminosity distance* d_L.

If we know the power L emitted by a source at a point P, it is possible to define d_L using its measured flux f:

$$d_L = \left(\frac{L}{4\pi f}\right)^{1/2} \ . \tag{1.20}$$

[1] r is in units of curvature radius

The area of a spherical surface centred on P and passing through the observation point P_0 at a time t_0 is $4\pi a_0^2 r^2$. The expansion of the universe causes the photons emitted by the source arrive at this surface redshifted by a factor a_0/a. Therefore we find that [3]:

$$f = \frac{L}{4\pi a_0^2 r^2}\left(\frac{a}{a_0}\right)^2 , \tag{1.21}$$

from which we derive:

$$d_L = a_0^2 \frac{r}{a} . \tag{1.22}$$

Using this equation and the definition of the proper distance, eq. (1.19), for a spatially flat universe, we can derive the relation between the luminosity distance and the proper distance:

$$d_L = d_p \frac{a_0}{a} = (1+z) d_p . \tag{1.23}$$

Astronomers usually employ in place of L and f two quantities empirically defined: the *apparent magnitude* m and the *absolute magnitude* M. The first one is a measure of the flux of a source as seen by an observer on Earth, while the second one is a measure of the flux emitted by the source. This is defined as the apparent magnitude that the source would have if it were placed at a distance of 10 pc ($1\ pc = 3.086 \times 10^{16}\ m = 3.261\ ly$).

If we know the apparent magnitude m and the absolute magnitude M of a source, we can derive the luminosity distance of this:

$$d_L = 10^{(m-M-25)/5} , \tag{1.24}$$

where the quantity $m - M$ is called the *distance module*.

Another useful distance measurement is the *angular diameter distance* d_A.

Let us suppose we know a proper length ℓ of an object aligned perpendicular to our line of sight. Measuring the angular size of the object, $\delta\theta$, it is possible to compute the angular distance from the relation:

$$d_A = \frac{\ell}{\delta\theta} . \tag{1.25}$$

If the universe is static and Euclidean, this distance is equal to the proper distance.

In a spatially flat universe, the relation between the angular diameter distance and the luminosity distance is:

$$d_A = \frac{d_L}{(1+z)^2} . \tag{1.26}$$

1.4 Einstein equations

The expansion of the universe is governed by the Einstein field equations [4]:

$$G_{\mu\nu} = R_{\mu\nu} - \frac{1}{2} g_{\mu\nu} R = 8\pi G T_{\mu\nu} , \tag{1.27}$$

in which $G_{\mu\nu}$ is the Einstein tensor, $R_{\mu\nu}$ is the *Ricci tensor*, R is the *Ricci scalar*, G is the Newton's constant and and $T_{\mu\nu}$ is the *stress-energy tensor*. The Ricci tensor is defined as:

$$R_{\mu\nu} = \Gamma^{\alpha}_{\mu\nu,\alpha} - \Gamma^{\alpha}_{\mu\alpha,\nu} + \Gamma^{\alpha}_{\beta\alpha}\Gamma^{\beta}_{\mu\nu} - \Gamma^{\alpha}_{\beta\nu}\Gamma^{\beta}_{\mu\alpha} \ , \tag{1.28}$$

where $\Gamma^{\delta}_{\mu\nu}$ are the Christoffel symbols:

$$\Gamma^{\delta}_{\mu\nu} = \frac{1}{2} g^{\delta\alpha}\left(\frac{\partial g_{\mu\alpha}}{\partial x^{\nu}} + \frac{\partial g_{\alpha\nu}}{\partial x^{\mu}} - \frac{\partial g_{\mu\nu}}{\partial x^{\alpha}}\right) , \tag{1.29}$$

and commas denote derivatives with respect to x (for example, $\Gamma^{\alpha}_{\mu\nu,\alpha} = \frac{\partial \Gamma^{\alpha}_{\mu\nu}}{\partial x^{\alpha}}$).

When Einstein proposed these equations, he supposed that the universe was finite and static and that the primary contribution to the energy density of the universe was from non relativistic matter. But soon after, he realized that a static universe containing only matter would tend to collapse, therefore he modified his equations adding a new term, called the *cosmological constant* Λ, in order to allow for a static universe:

$$R_{\mu\nu} - \frac{1}{2} g_{\mu\nu} R + g_{\mu\nu}\Lambda = 8\pi G T_{\mu\nu} \ . \tag{1.30}$$

This constant represents a vacuum energy and works as a repulsive force opposed to the collapse of the universe. In 1929 Hubble discovered the recession of galaxies and, consequently, the expansion of the universe. Einstein abandoned the cosmological constant referring to it as the greatest blunder of his career. In addition, in 1930, Eddington [5] showed that the Einstein's static universe was unstable under spatillay homogeneous and isotropic perturbations.

Today this constant is considered as mandatory to describe the current universe.

1.5 Friedmann equations

In cosmology, the stress-energy tensor is that of a perfect fluid:

$$T_{\mu\nu} = (\rho + p) U_{\mu} U_{\nu} + p g_{\mu\nu} \ , \tag{1.31}$$

where ρ is the energy density, p is the pressure and U_{μ} is the fluid four-velocity which satisfies the normalization condition: $U_{\mu}U^{\mu} = 1$.

In a homogeneous and isotropic universe $T_{\mu\nu}$ can be written as:

$$T_{\mu\nu} = \begin{pmatrix} -\rho & 0 & 0 & 0 \\ 0 & p & 0 & 0 \\ 0 & 0 & p & 0 \\ 0 & 0 & 0 & p \end{pmatrix} \ .$$

Combining this tensor with the FRW metric, eq. (1.3), and the Einstein equations, eq. (1.27), we obtain the *Friedmann equations* [6, 7]:

$$
\begin{aligned}
H^2 = \left(\frac{\dot{a}}{a}\right)^2 &= \frac{8\pi G}{3}\rho - \frac{k}{a^2} + \frac{\Lambda}{3} \,, \\
\dot{H} + H^2 = \frac{\ddot{a}}{a} &= -\frac{4\pi G}{3}\left(\rho + 3p\right) + \frac{\Lambda}{3} \,.
\end{aligned}
\tag{1.32}
$$

If we consider the cosmological constant as a fluid with a constant energy density during the expansion of the universe:

$$
\rho_\Lambda = \frac{\Lambda}{8\pi G} \,, \tag{1.33}
$$

the Friedman equations can be rewritten as:

$$
\left(\frac{\dot{a}}{a}\right)^2 = \frac{8\pi G}{3}\rho - \frac{k}{a^2} \,, \tag{1.34}
$$

$$
\frac{\ddot{a}}{a} = -\frac{4\pi G}{3}\left(\rho + 3p\right) \,, \tag{1.35}
$$

where ρ and p are the total energy density and pressure of the universe, including the cosmological constant contribution.

From these equations, it is possible to define the *critical energy density*:

$$
\rho_{\rm c} = \frac{3H^2}{8\pi G} \,, \tag{1.36}
$$

that represents the density with which we would have a spatially flat universe ($k = 0$). If the energy density is larger than this value, the universe is positively curved ($k = +1$); if it is smaller than this value, the universe is negatively curved ($k = -1$).

Typically, it is more convenient to use the ratio of the absolute density of the universe to the critical energy density. This ratio is known as the *density parameter* [2]:

$$
\Omega = \frac{\rho}{\rho_{\rm c}} . \tag{1.37}
$$

In terms of this parameter, the first Friedmann equation (1.34) takes the form:

$$
1 - \Omega = -\frac{k}{a^2 H^2} . \tag{1.38}
$$

Therefore, the density parameter is related to the spatial geometry of the universe as:

$$
\begin{array}{rrcl}
\text{for an open universe:} & \Omega < 1 & \Rightarrow & k = -1 \\
\text{for a flat universe:} & \Omega = 1 & \Rightarrow & k = 0 \\
\text{for a closed universe:} & \Omega > 1 & \Rightarrow & k = +1
\end{array}
$$

[2] All of density parameters are characterized by a zero in the subscript if they refer to the present time.

The right hand side of the eq. (1.38) is known as the *curvature parameter*:

$$\Omega_{\rm k} = -\frac{k}{a^2 H^2} \ , \tag{1.39}$$

and its energy density is the so-called *curvature density*, $\rho_{\rm k} = -3k/8\pi a^2 G$.

The Friedmann equations are not independent and, in order to solve them, we need a third equation which relates the density and the pressure. This equation is the *equation of state* of a perfect fluid:

$$p = w\rho. \tag{1.40}$$

where w is a dimensionless number that depends on each component of the universe. In order to solve this, we can combine the equations (1.34) and (1.35), obtaining the continuity equation that it directly follows from conservation of stress-energy tensor:

$$\dot{\rho} = -3\frac{\dot{a}}{a}(\rho + p) = -3\frac{\dot{a}}{a}\rho(1 + w) \ . \tag{1.41}$$

A general solution of this equation, for w constant, is:

$$\rho \propto a^{-3(1+w)} \ . \tag{1.42}$$

The evolution of the universe is complicated by the fact that it contains different components (non relativistic matter, radiation and a cosmological constant, or even more exotic components) with different equations of state. Fortunately the energy density and the pressure for these components of the universe are additive, therefore we can solve the continuity equation and the Friedmann equations for each of them separately, as long as the different components do not interact.

- *Non relativistic matter*

  In this case $w = 0$ and the fluid has zero pressure, consequently the matter density evolves as $\rho_m \propto a^{-3}$. We therefore conclude that the energy density associated to non relativistic matter decreases as the universe expands.

  In addition, if we consider a spatially flat universe, it is also possible to solve the Friedmann equation obtaining the temporal evolution of the scale factor:

  $$a(t) \propto t^{2/3} \ . \tag{1.43}$$

- *Relativistic matter*

  For a universe dominated by radiation, $w = 1/3$, the energy density evolves as $\rho_{\rm r} \propto a^{-4}$. In this case, for $k = 0$, the temporal evolution of the scale factor is:

  $$a(t) \propto t^{1/2} \ . \tag{1.44}$$

- *Vacuum energy*

  If the universe was dominated by a cosmological constant, $w = -1$ and therefore $p_\Lambda = -\rho_\Lambda$. For a spatially flat universe, the scale factor grows as:

$$a(t) \propto exp(Ht) \ . \tag{1.45}$$

More generally, for a universe with arbitrary k and having three components, matter, radiation and a cosmological constant, the total density is:

$$\rho(a) = \rho_{\rm c}^0 \left[\Omega_{\rm m}^0 a^{-3} + \Omega_{\rm r}^0 a^{-4} + \Omega_\Lambda^0\right] \ , \tag{1.46}$$

where:

$$\Omega_{\rm m}^0 = \frac{8\pi G\rho_{\rm m}^0}{3H_0^2c^2} \ , \qquad \Omega_{\rm r}^0 = \frac{8\pi G\rho_{\rm r}^0}{3H_0^2c^2} \ , \qquad \Omega_\Lambda^0 = \frac{\Lambda c^2}{3H_0^2} \ . \tag{1.47}$$

Therefore from the Friedmann equation we can derive the time dependence of the Hubble function:

$$H^2 = H_0^2[\Omega_{\rm k}^0 a^{-2} + \Omega_{\rm m}^0 a^{-3} + \Omega_{\rm r}^0 a^{-4} + \Omega_\Lambda^0] \ , \tag{1.48}$$

and we can obtain the following relation:

$$\Omega_{\rm m} + \Omega_{\rm r} + \Omega_\Lambda + \Omega_{\rm k} = 1 \ . \tag{1.49}$$

Also the neutrino component contributes to the expansion rate of the universe via its energy density Ω_ν, but this aspect it will be discussed in detail in the next chapter.

1.6 Cosmological perturbation theory

The homogeneity and isotropy of the universe are true only at first approximation; today the universe has developed nonlinear structures that take the form, for example, of galaxies, clusters and superclusters of galaxies. These structures are formed from small initial perturbations due to gravitational instability.

In the case of a non relativistic fluid, the perturbations on scales not exceeding the Hubble horizon [3] are described by the Newtonian theory of gravity. In the case of a relativistic fluid we have to use General Relativity for short and long wavelength perturbations.

In this thesis we consider the gravitational instability with the relativistic treatment.

[3] The growth of perturbations is governed by the distance $R_H = H^{-1}$ known as Hubble horizon. Its current value is $R_0 = H_0^{-1} = 3000h^{-1}Mpc$. Therefore we can say that a perturbation with a wavelength λ is inside the horizon if, at the time t, $a\lambda < H^{-1}$ and it is outside the horizon if $a\lambda > H^{-1}$. Introducing the wave vector $k = 2\pi/\lambda$, the equivalent conditions:

$$\lambda = 1/aH, \quad k = aH$$

correspond to the horizon crossing of a perturbation.

1.6.1 Gauge transformations

To perturb the equations we must first of all perturb the metric, writing at first order:

$$g_{\mu\nu} = g^{(0)}_{\mu\nu} + g^{(1)}_{\mu\nu} \ ,$$

where the homogenoeus background part $g^{(0)}_{\mu\nu}$ depends only on cosmic time and the perturbed metric $g^{(1)}_{\mu\nu}$ contains spatially dependent perturbations which are small with respect to the zero-th order part. The General Relativity equations are invariant with respect to a general coordinate change. This means that, since the metric $ds^2 = g_{\mu\nu}dx^\mu dx^\nu$ has to remain constant, changing dx^μ induces changes in the metric coefficients. Therefore we select a class of transformations that leaves $g^{(0)}_{\mu\nu}$ as it is, and only changes the coefficient of $g^{(1)}_{\mu\nu}$. These transformations are called gauge transformations.

In the following, we consider only two particular gauge choices: the *synchronous* and the *conformal Newtonian gauge*. The first one is commonly used in numerical publicly available codes because the equations are easier to integrate. In this case the observers are attached to the free falling particles, so they do not see any velocity field and do not measure a gravitational potential. Instead, in the Newtonian gauge the observers are attached to the unperturbed particles so that they can detect their velocity fields and measure a gravitational potential.

In the synchronous gauge the line element is given by [8]:

$$ds^2 = a^2(\tau)\left[-d\tau^2 + (\delta_{ij} + h_{ij})dx^i dx^j\right] \ , \tag{1.50}$$

where τ is the conformal time defined as $d\tau = dt/a(t)$, and h_{ij} is the metric perturbation. From now on, dots will denote derivatives with respect to τ, for example $\dot{a} = da/d\tau$. Moreover we can rewrite the Hubble parameter as $\mathcal{H} = (1/a)(da/d\tau) = aH(t)$.

The Newtonian gauge is used for the scalar modes of the metric perturbations. In this case the line element is:

$$ds^2 = a^2(\tau)\left[-(1+2\psi)d\tau^2 + (1-2\phi)dx^i dx_i\right] \ , \tag{1.51}$$

in which ψ and ϕ are the gravitational potential and the spatial curvature perturbation, respectively.

It is convenient to write the Einstein equations in linear perturbation theory:

Synchronous gauge [8]:

$$k^2\eta - \frac{1}{2}\frac{\dot{a}}{a}\dot{h} = 4\pi G a^2 \delta T^0_0 \ , \tag{1.52a}$$

$$k^2\dot{\eta} = 4\pi G a^2 \left(\rho + p\right)\theta \ , \tag{1.52b}$$

$$\ddot{h} + 2\frac{\dot{a}}{a}\dot{h} - 2k^2\eta = -8\pi G a^2 \delta T^i_i \ , \tag{1.52c}$$

$$\ddot{h} + 6\ddot{\eta} + 2\frac{\dot{a}}{a}(\dot{h} + 6\dot{\eta}) - 2k^2\eta = -24\pi G a^2(\rho + p)\sigma \ , \tag{1.52d}$$

where $h(\mathbf{k},\tau)$ and $\eta(\mathbf{k},\tau)$ are the scalar perturbations in the synchronous gauge.

The variables θ and σ are defined as:

$$(\rho+p)\theta = ik^j\delta T^0_j, \quad (\rho+p)\sigma = -\left(\hat{\mathbf{k}}_i\cdot\hat{\mathbf{k}}_j - \tfrac{1}{3}\delta_{ij}\right)\Sigma^i_j \ ,$$

in wich Σ^i_j is the traceless component of T^i_j. The σ variable is also related to the anisotropic stress perturbation Π by $\sigma = 2\Pi p/3(\rho+p)$.

Newtonian gauge [8]:

$$k^2\phi + 3\frac{\dot{a}}{a}\left(\dot{\phi}+\frac{\dot{a}}{a}\psi\right) = 4\pi G a^2\delta T^0_0, \tag{1.53a}$$

$$k^2\left(\dot{\phi}+\frac{\dot{a}}{a}\psi\right) = 4\pi G a^2\left(\rho+p\right)\theta \ , \tag{1.53b}$$

$$\ddot{\phi}+\frac{\dot{a}}{a}(\dot{\psi}+2\dot{\phi})+\left(2\frac{\ddot{a}}{a}-\frac{\dot{a}^2}{a}\right)\psi+\frac{k^2}{3}(\phi-\psi) = \frac{4}{3}\pi G a^2\delta T^i_i \ , \tag{1.53c}$$

$$k^2(\phi-\psi) = 12\pi G a^2(\rho+p)\sigma \ . \tag{1.53d}$$

The perturbed stress-energy tensor is:

$$T^0_0 = -(\rho+\delta\rho) \ , \tag{1.54}$$

$$T^0_i = -(\rho+p)v_i = -T^i_0 \ , \tag{1.55}$$

$$T^i_j = -(p+\delta p)\delta^i_j + \Sigma^i_j \ , \tag{1.56}$$

where for a fluid moving with a small coordinate velocity $v_i = dx_i/d\tau$ is a perturbation similat to $\delta\rho$ and δp, which are the density and pressure perturbations, respectively.

Using the stress energy tensor conservation:

$$T^{\mu\nu}_{;\mu} = \partial_\mu T^{\mu\nu} + \Gamma^\nu_{\alpha\beta}T^{\alpha\beta} + \Gamma^\alpha_{\alpha\beta}T^{\nu\beta} = 0 \ , \tag{1.57}$$

we obtain:

Synchronous gauge [8]:

$$\dot{\delta} = -(1+w)\left(\theta+\frac{\dot{h}}{2}\right) - 3\frac{\dot{a}}{a}\left(\frac{\delta p}{\delta\rho}-w\right)\delta \ , \tag{1.58a}$$

$$\dot{\theta} = -\frac{\dot{a}}{a}(1-3w)\theta - \frac{\dot{w}}{1+w}\theta + \frac{\delta p/\delta\rho}{1+w}k^2\delta - k^2\sigma \ . \tag{1.58b}$$

Newtonian gauge [8]:

$$\dot{\delta} = -(1+w)(\theta-3\dot{\phi}) - 3\frac{\dot{a}}{a}\left(\frac{\delta p}{\delta\rho}-w\right)\delta \ , \tag{1.59a}$$

$$\dot{\theta} = -\frac{\dot{a}}{a}(1-3w)\theta - \frac{\dot{w}}{1+w}\theta + \frac{\delta p/\delta\rho}{1+w}k^2\delta - k^2\sigma + k^2\psi \ . \tag{1.59b}$$

in which θ is the divergence of the fluid velocity and $\delta = \delta\rho/\rho$ is the density perturbation.

These equations are valid for a single uncoupled fluid. They need to be modified for individual components if the components interact with each other.

1.6.2 Growth factor

The Newtonian gauge is used in particular when we are interested to study the sub-horizon modes ($k \gg \mathcal{H}$) and the quasi static limit. In this case equation (1.53b) tells us that $\dot{\phi} + \mathcal{H}\psi = 0$, so the equation (1.53a) gives the Poisson equation:

$$k^2\phi = -4\pi G a^2 \delta\rho = -\frac{3}{2}\mathcal{H}^2\delta\rho \tag{1.60}$$

in which we used the unperturbed Friedmann equation. If we consider only a single Cold Dark Matter (i.e., pressureless, non relativistic and uncoupled) component, the equations (1.59a) and (1.59b) can be rewritten as:

$$\dot{\delta} = -\theta + 3\dot{\phi} \simeq -\theta \ , \tag{1.61}$$

$$\dot{\theta} = -\mathcal{H}\theta + k^2\phi \ , \tag{1.62}$$

where δ is the cold dark matter overdensity and θ is the comoving dark matter peculiar velocity divergence. Deriving equation (1.61) and using equation (1.62), we obtain:

$$\ddot{\delta} = \mathcal{H}\theta - k^2\psi \ . \tag{1.63}$$

Finally translating the derivatives with respect to the conformal time to the derivatives with respect to the scale factor we get the growth equation:

$$\delta'' + \delta'\left(\frac{3}{a} + \frac{H'}{H}\right) - \frac{k^2\psi}{a^4H^2} = 0 \ , \tag{1.64}$$

in which $' = d/da$, and, using and neglecting the dark energy component, reads

$$\delta'' + \delta'\left(\frac{3}{a} + \frac{H'}{H}\right) - \frac{3}{2}\frac{\Omega_{\rm m}(a)}{(H/H_0)^2}\frac{\delta}{a^2} = 0 \ . \tag{1.65}$$

The modes we are interested in are the growing modes. The solution to equation (1.65) is [1]:

$$\delta(a) \equiv D(a) \propto H(a)\int^a \frac{da'}{(a'H(a'))^3} \ , \tag{1.66}$$

that takes the name of *growth factor*. It describes the amplitude of the growing mode and for a spatially flat universe dominated by matter is equal to a. For practical purposes, it is also convenient to define a function that expresses the growth rate of the fluctuations:

$$f(a) = \frac{d\ln D(a)}{d\ln a} \ , \tag{1.67}$$

known as growth function.

1.7 Cosmological measurements

Current cosmological measurements point to a spatially flat universe ($\Omega_{\rm k} = -0.0005^{+0.0065}_{-0.0066}$ [9]), composed by baryonic matter and cold dark matter ($\Omega_b h^2 = 0.02217 \pm 0.00033$ and $\Omega_c h^2 = 0.1186 \pm 0.0031$ [9]), in which the principal element is the dark energy component, ($\Omega_\Lambda = 0.693 \pm 0.019$ [9]). This dark energy component is responsible for the current accelerated expansion of the universe. If it is made of a cosmological constant (representing the vacuum energy), the equation of state is $w = -1$. This minimal scenario is the so-called ΛCDM cosmology, which is described by six parameters: the baryon and cold dark matter densities ($\omega_{\rm b} = \Omega_{\rm b} h^2$ and $\omega_{\rm c} = \Omega_{\rm c} h^2$), the ratio between the sound horizon and the angular diameter distance at the decoupling of photons $\Theta_{\rm s}$, the optical depth τ, the scalar spectral index $n_{\rm s}$, and the amplitude of the primordial spectrum $A_{\rm s}$. Extensions to this ΛCDM model include a dark energy fluid, a quintessence field, in which, in general, w is not constant in time and differs from -1, or modified gravity theories.

In the following, we review the observations that support the cosmological model briefly described above. In particular we will see how the cosmological parameters (as $\Omega_{\rm k}$, $\Omega_{\rm m}$, H_0 and others) can be constrained by measurements of Supernovae luminosity distances, Cosmic Microwave Background (CMB), Big Bang Nucleosynthesis (BBN), Baryon Acoustic Oscillations (BAO) and Large Scale Structure (LSS).

1.7.1 Supernovae

We have seen that the Hubble parameter measures the expansion rate of the universe at a particular time t. In order to understand the effect of the acceleration of the universe, we can define the *deceleration parameter*:

$$q_0 = -\frac{\ddot{a}a}{\dot{a}^2} = -\left(\frac{\ddot{a}}{aH^2}\right)_{t_0} . \tag{1.68}$$

A positive value of q_0 corresponds to $\ddot{a} < 0$, meaning that the universe's expansion is decelerating; a negative value of q_0 corresponds to $\ddot{a} > 0$, so the universe's expansion is accelerating. For a universe containing radiation, matter and a cosmological constant:

$$q_0 = \frac{\Omega_{\rm m}}{2} + \Omega_{\rm r} - \Omega_\Lambda , \tag{1.69}$$

from which we can see that if observations agree with an accelerated expansion, a cosmological model with only matter and radiation can not explain it.

Using q_0 and a Taylor series expansion for the scale factor around the present time, we can rewrite the luminosity distance for $z \ll 1$ as:

$$d_L(z) \approx \frac{cz}{H_0}\left[1 + \frac{1}{2}(1 + q_0)z\right] . \tag{1.70}$$

When $z \ll 1$ we have $d_L = czH_0^{-1}$, the Hubble law; at larger redshifts we will have deviations from this law that are connected with the deceleration parameter.

Therefore the parameters H_0 and q_0 provide a general description of the expansion of the universe and in order to reconstruct them we need to measure the luminosity distance.

As shown in eq. (1.24), this distance can be obtained measuring the difference between the apparent and absolute magnitude of a given source. Therefore in order to obtain d_L we need to find astrophysical sources whose the absolute magnitude M is theoretically known. These kind of sources are known as *Standard Candles*.

In recent years, because of a relationship between their peak brightness and light-curve width, Supernovae are considered as standardizable candles. They are defined as explosive variables and are divided into two classes based on their spectra: type I supernovae (SNI) that contain no hydrogen absorption lines in their spectra and type II supernovae (SNII) that contain strong hydrogen absorption lines. All SNII are massive stars whose cores collapse to form a black hole or a neutron star when their nuclear fuel is exhausted. SNI are separated into three subclasses Ia, Ib and Ic according to the differences in their emission spectra and in their light curves (curves that describe the behaviour of luminosity with time). Type Ib and Ic supernovae are massive stars which lost their outer layers in a stellar wind before core collapse. They are essentially the same as SNII because in all these, the iron core of a massive star collapses and rebounds; the only differences in the spectra of these supernovae are due to superficial differences in the exploding stars. Type Ia supernovae are completely different and they are considered standard candles because they are extraordinarily luminous and hence can be seen from a large distance.

The former type of supernova occurs in a binary system in which one of the two stars is a white dwarf. The companion star, usually a red giant, transfers mass to the white dwarf that eventually reaches its Chandrasekhar limit, $M_C = 1.4 M_\odot$.[4] When this limit is exceeded, the white dwarf starts to collapse until its increased density triggers a runaway nuclear fusion reaction. Since all SNIa explode starting from the same initial condition, we can assume that the produced luminosity is always the same. When a SNIa is observed, we need to study the dependency of its luminosity on time to obtain the light curve; from this curve we can calculate the apparent and the absolute magnitudes (m and M), thus, through eq. (1.24), we can obtain the luminosity distance d_L.

In addition, the SNIa can also constrain the cosmological parameters as Ω_m, Ω_b and Ω_Λ. Using equations (1.17) and (1.23) and defining the comoving coordinate r in a spatially flat universe as:

$$r(a) = \frac{1}{H_0} \int_{1/(1+z)}^{1} \frac{da'}{a'^2 \sqrt{\Omega_\Lambda + \Omega_\mathrm{m} a'^{-3} + \Omega_\mathrm{r} a'^{-4}}} \,, \tag{1.71}$$

we can rewrite the luminosity distance in terms of the components of the energy density of the universe in the following way:

$$d_L(a) = \frac{1+z}{H_0} \int_{1/(1+z)}^{1} \frac{da'}{a'^2 \sqrt{\Omega_\Lambda + \Omega_\mathrm{m} a'^{-3} + \Omega_\mathrm{r} a'^{-4}}} \,. \tag{1.72}$$

[4] $M_\odot$ is the mass of the sun: $M_\odot \sim 2 \times 10^{30}$ kg.

Two research teams, The Supernova Cosmology Project [10] and the High-z Supernova Search Team [11] conducted searches for supernovae in distant galaxies. They used light curves and redshifts of SNIa to measure the cosmological parameters and the acceleration of the universe. In particular these observations led to discovery of cosmic acceleration.

After these, the combined work of several different teams during the past decade has provided an impressive increase in the total number of SNIa and in the quality of the individual measurements.

Currently the most recent SNIa luminosity distance data are provided by the 3 year Supernova Legancy Survey (SNLS3) [12, 13, 14]. In Fig. 1.1 is plotted the $m-M$ magnitude versus the redshift for different type Ia supernovae measured from the Supernova Cosmology Project Union2 [15].

The data are compared to four different models, assuming a spatilally flat universe. From the plots we can see that a high redshift it is straightforward to rule out the hypothesis that the universe contains only matter ($\Omega_{\rm m} = 1$, $\Omega_\Lambda = 0$).

The ongoing Dark Energy Survey (DES) [5], will discover and make detailed measurements of several thousand supernovae with the aims of improving both the statistical precision of supernova cosmology and the control of systematic errors in using supernovae to measure distances. DES is designed to probe the origin of the accelerating universe and help in discovering the nature of dark energy by measuring the 14-billion-year history of cosmic expansion with high precision.

1.7.2 Cosmic Microwave Background

The Cosmic Microwave Background (CMB) contains a wealth of information about the cosmological parameters of the universe and on specific features of the theoretical models, as, for instance, dark energy or modified gravity models.

In the primordial universe the photons were tightly coupled to the baryons forming a plasma, the photon-baryon fluid. At a temperature of roughly 3000 K, protons combined with electrons to form neutral hydrogen atoms (*recombination*) and photons decoupled from baryons to travel freely through space. At this point the universe becomes transparent. The time at which a CMB photon underwent its last scattering from an electron is known as epoch of *last scattering* and the surface that surround every observer of the universe and from which the CMB photons have been streaming freely is called *last scattering surface* ($z \approx 1100$). Therefore when we observe these photons today, we are looking at the universe when it was 300,000 years old.

Before recombination the photons were in thermal equilibrium with electrons and thus they present a black body spectrum:

$$I(\nu, T) = \frac{4\pi\hbar\nu^3}{c^2} \frac{1}{e^{2\pi\hbar\nu/k_B T} - 1} \ , \tag{1.73}$$

[5] http://www.darkenergysurvey.org/

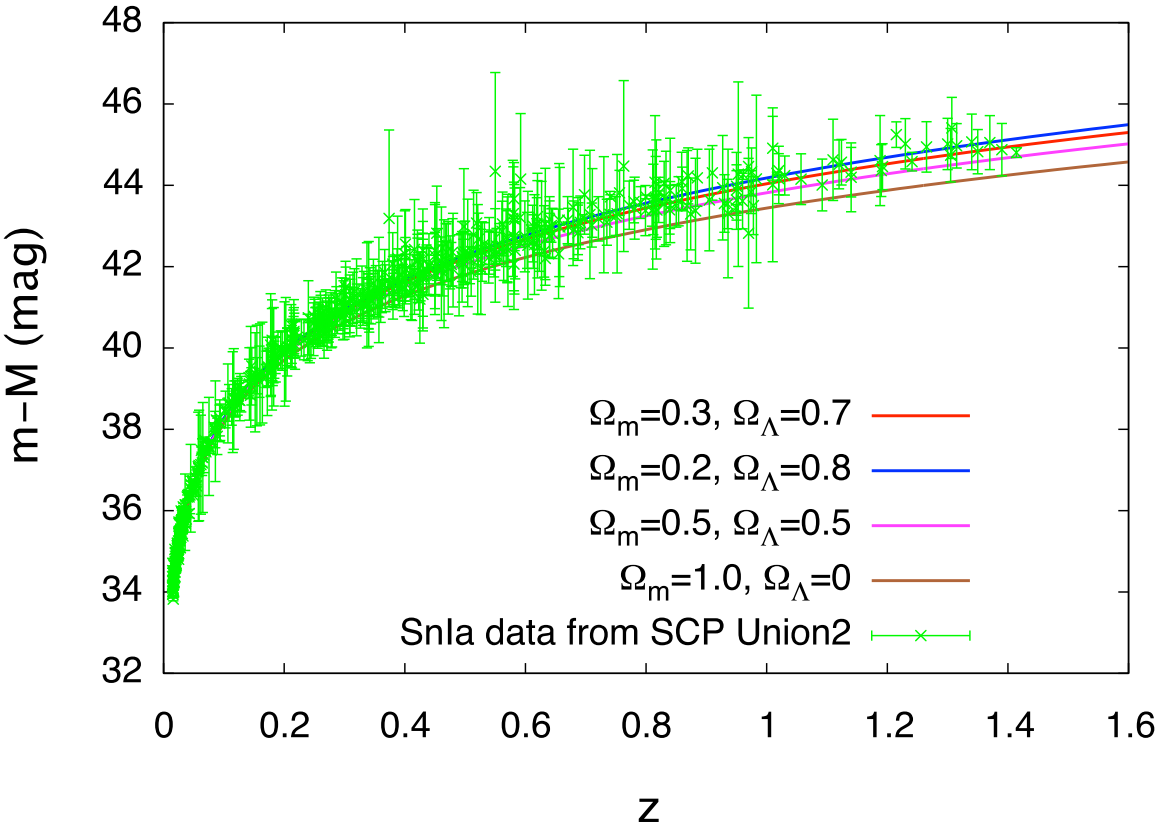

Figure 1.1: Distance modulus versus redshift for SNIa measured from the Supernova Cosmology Project Union2 [15]. The plot shows as well predictions from a number of theoretical models (assuming flatness).

where $I(\nu, T)$ is the energy per unit of time, per unit of area of the emitting surface, per unit of solid angle and per unit of frequency, with an average temperature $T = 2.725$ K.

The CMB spectrum was first measured accurately over a wide range of wavelengths by the COsmic Background Explorer (COBE) satellite [16], launched in 1989, into an orbit 900 km above the Earth's surface. The COBE observations were crucial for cosmology. From the point of view of the structures of the universe on the largest angular scales, they show that the cosmic radiation is homogeneously and isotropically distributed in all directions (in agreement with the Cosmological Principle), with fluctuations (anisotropies) of the order of 10^{-5}. Defining the dimensionless temperature fluctuation around the mean value $T_0 = \langle T \rangle$ and at a given point on the sky as:

$$\frac{\delta T}{T}(\theta, \phi) = \frac{T(\theta, \phi) - \langle T \rangle}{\langle T \rangle} \ , \tag{1.74}$$

COBE found that the root mean square of the temperature fluctuations is:

$$\left\langle \left(\frac{\delta T}{T} \right)^2 \right\rangle^{1/2} = 1.1 \times 10^{-5}. \tag{1.75}$$

It is possible to calculate [1, 17] the evolution of the photon-baryon fluid before the recombination epoch and therefore to calculate the temperature anisotropies $\Theta \equiv (T - T_0)/T_0$ at the last scattering surface.

Since temperature fluctuations are defined on a spherical surface, it is useful to expand them in spherical harmonics:

$$\Theta(\vec{x}, \hat{p}, \tau) = \sum_{\ell=1}^{\infty} \sum_{m=-\ell}^{\ell} a_{\ell m}(\vec{x}, \tau) Y_{\ell m}(\hat{p}) \ , \tag{1.76}$$

where $\hat{p}$ is a normalized vector that defines the direction of the sky $(\theta_{sky}, \phi_{sky})$, $\vec{x}$ is the position of the observer and $a_{\ell m}(\vec{x}, \tau)$ are the coefficients of the expansion that contain all the information about the temperature perturbations.

Using the orthogonality property of the spherical harmonics:

$$\int d\Omega Y_{\ell m}(\hat{p}) Y^*_{\ell' m'}(\hat{p}) = \delta_{\ell \ell'} \delta_{m m'} \ , \tag{1.77}$$

where Y^* is the complex conjugate of Y and Ω is the solid angle spanned by $\hat{p}$, we can obtain the equations for the amplitudes $a_{\ell m}$:

$$a_{\ell m}(\vec{x}, \tau) = \int \frac{d^3k}{(2\pi)^3} e^{i\vec{k}\cdot\vec{x}} \int d\Omega Y^*_{\ell m}(\hat{p}) \Theta(\vec{k}, \hat{p}, \tau) \ . \tag{1.78}$$

Given that there is a linear relation between multipoles $a_{\ell m}$ and Fourier modes $\Theta(\vec{k}, \hat{p}, \tau)$, it is clear that if we assume that the perturbations arise from a gaussian distribution, also the

$a_{\ell m}$ are gaussian distributed, and their statistics is fully described by two-point correlation functions:

$$\langle a_{\ell m} a^*_{\ell' m'} \rangle = \delta_{\ell \ell'} \delta_{m m'} C_\ell \ , \tag{1.79}$$

where diagonality follows from rotational symmetry.

The mean value of all the $a_{\ell m}$'s is zero but not the variance, that is called angular power spectrum, C_ℓ. This spectrum is precisely the quantity that we want to compute for a given cosmological model and to compare with observations. The true harmonic power spectrum in our universe cannot be extracted from observations, since we only observe one realization of the universe. However, using the ergotic principle, we can build an estimator of the true power spectrum, $\hat{C}_\ell$, taking advantage of the fact that all multipoles with a given ℓ should have the same variance C_ℓ:

$$\hat{C}_\ell = \frac{1}{2\ell + 1} \sum_{m=-\ell}^{+\ell} a^*_{\ell m} a_{\ell m} \ . \tag{1.80}$$

This estimator has a variance, called *cosmic variance* ($\Delta C_\ell / C_\ell = [2/(2\ell+1)]^{1/2}$), intrinsic in the definition of the estimator itself and it changes with ℓ; in fact this variance decreases with increasing ℓ, since for high multipoles we can average over more independent realizations of the same stochastic process. Moreover there are two general caveats to consider during the CMB measurements. The first one is that can exist any source of noise, instrumental or astrophysical, which increases the errors. If the noise is also Gaussian and has a known power spectrum, the variance is given by the sum of the signal and noise power spectra:

$$\Delta C_\ell = \sqrt{\frac{2}{2\ell + 1}} \left(C_\ell + C_{\ell,N} \right) \ . \tag{1.81}$$

Because astrophysical foregrounds are typically non-Gaussian it is usually also necessary to remove heavily contaminated regions, e.g. the galaxy. In this case the variance is:

$$\Delta C_\ell = \sqrt{\frac{2}{(2\ell + 1) f_s}} \left(C_\ell + C_{\ell,N} \right) \ , \tag{1.82}$$

in which f_s is the fraction of the sky covered.

During the last decade, the value of C_ℓ as a function of the multipole moment ℓ has been measured from a large amount of experiments detecting a series of acoustic peaks in the anisotropy power spectrum. The most important and recent are: WMAP, SPT, ACT and Planck.

The Wilkinson Microwave Anisotropy Probe (WMAP) [18] is a satellite, proposed to NASA in 1995, launched in 2001. On December 20, 2012, the final nine-year WMAP data and related images were released. The positioning of WMAP satellite made use of the lagrangian point L, at $\sim 1.5 \times 10^6$ km from the Earth, in order to observe over the full sky. WMAP satellite has produced spectacular all sky maps of the temperature anisotropy

yielding a highly precise measurement of the angular power spectrum up to multipoles of $\ell \sim 600$, corresponding to an angular scale of $\sim 20'$.

The South Pole Telescope (SPT) is a 10 meter diameter telescope operating at the South Pole research station since 2007. SPT lies on the Antarctic Plateau, at an altitude of 2800 m. The low temperature at the South Pole reduces the water vapor content of the atmosphere, lowering both atmospheric emission and fluctuations in brightness. The SPT collaboration has recently presented their observations of 2540 deg^2 of sky, providing the CMB temperature anisotropy power over the multipole range $650 < \ell < 3000$ [19, 20, 21], corresponding to the region from the third to the ninth acoustic peak.

The Atacama Cosmology Telescope (ACT) [22, 23] is a six-metre telescope operating in the Atacama Desert of Chile at an altitude of 5200 meters. ACT complements measurements from WMAP by observing from $\ell \sim 300$ to $\ell = 10000$. This widens the range of data available to constrain both cosmological parameters through the Silk damping tail of the primary CMB [24] and the residual power from secondary sources (galaxy clusters) between us and the surface of last scattering.

Planck [9, 25] is a space telescope of the European Space Agency launched in May 2009. Its aim is to measure the temperature and polarization anisotropies with micro-Kelvin sensitivity per resolution element over the entire sky. The wide frequency coverage of Planck (30-857 GHz) was chosen to provide accurate discrimination of the Galactic emission from the primordial anisotropies.

In Fig. 1.2 we show the CMB power spectra for the best fit parameters for the ΛCDM model from Planck together with WMAP, SPT, ACT and Planck data. In the plot we can see several peaks which indicate the presence of correlations between temperature anisotropies at different angular separations ($\theta \approx \pi/\ell$). In particular these peaks represent the acoustic waves in the photon-baryon plasma of the primordial universe. Those waves were originated from the primordial inhomogeneities in the distribution of dark matter as the result of the competition between two forces: on one hand radiation pressure acts as a repulsive force, on the other hand gravity tries to compress matter. The first peak corresponds to the mode that was compressed once inside potential wells before recombination, the second the mode that was compressed and then rarefied, the third the mode that was compressed then rarefied then compressed, etc. Depending on the content of baryons, dark matter and dark energy in the universe, the shape, position and height of those peaks varies [26] . Therefore, the study of them reveals information about the cosmological parameters.

The first acoustic peak determines the size of the horizon at the time of decoupling, providing therefore, information about the geometry of the universe. The position in ℓ-space is related to the parameters n_s, $\Omega_c h^2$ and $\Omega_b h^2$. The amplitude of the first peak is positively correlated with $\Omega_m = \Omega_b + \Omega_c + \Omega_\nu$ [6] and the amplitude of the second peak is negatively correlated to $\Omega_b h^2$. An increase in the baryon density reduces the sound velocity in the photon-baryon plasma leading to a shift of the acoustic oscillations and and increasing the height of the peaks of compression (odd peaks). A larger value of n_s increases the slope of the angular power spectrum; increasing the cosmological constant leads a shift of the

[6] Ω_ν refers to the neutrino contribution, as we shall see in the following chapter.

spectrum towards lower multipoles.

Therefore, by measuring the CMB temperature power spectrum it is possible to obtain information on the primordial universe and on how it evolved after recombination.

Moreover CMB photons are also polarized and observing their polarization pattern it is possible to extract more information on the evolution of the universe [27]. CMB photons are in fact polarized by the temperature quadrupole that can be sourced both by scalar perturbations as well as by tensor perturbations from gravity waves produced by primordial inflation [1]. Therefore it is possible to describe CMB polarization through E *modes* and B *modes*, distinguished by the polarization pattern around a considered point in the sky. As for the temperature, cosmological information can be obtained from the polarization power spectra and also from their cross correlations; we can in fact define the following angular power spectra:

$$\begin{aligned} C_\ell^{TT} &= \langle a_{\ell m}^{*T} a_{\ell m}^{T} \rangle \,, \\ C_\ell^{EE} &= \langle a_{\ell m}^{*E} a_{\ell m}^{E} \rangle \,, \\ C_\ell^{BB} &= \langle a_{\ell m}^{*B} a_{\ell m}^{B} \rangle \,, \\ C_\ell^{TE} &= \langle a_{\ell m}^{*T} a_{\ell m}^{E} \rangle \,, \\ C_\ell^{TB} &= \langle a_{\ell m}^{*T} a_{\ell m}^{B} \rangle \,, \\ C_\ell^{EB} &= \langle a_{\ell m}^{*E} a_{\ell m}^{B} \rangle \,, \end{aligned} \tag{1.83}$$

where the cross correlations TB and EB are expected to vanish due to the fact that B has opposite parity to both T and E.

CMB photons are also affected by gravitational lensing due to the matter that is placed between us and the last scattering surface. In particulae large scale structure between the last scattering surface and the observer gravitationally lenses the temperature and polarization anisotropy of the CMB. The effect is that the photons of the CMB are deflected from their original positions. Gravitational CMB lensing can improve the CMB constraints on several cosmological parameters, since it is strongly connected with the growth of perturbations and gravitational potentials at redshifts $z < 1$ and, therefore, it can break important degeneracies. Therefore, studying CMB lensing it is possible to reconstruct the evolution of matter perturbations after the last scattering surface.

1.7.3 Big Bang Nucleosynthesis

When the universe was much hotter and denser and the temperature was of order of $\sim$ MeV, there were no neutral atoms or bound nuclei because the vast amount of radiation ensured that any atom or nucleus produced would be destroyed by a photon with a high energy. The primordial cosmic plasma consisted of: relativistic particles in equilibrium (photons, electrons and positrons), decoupled relativistic (neutrinos) and non-relativistic

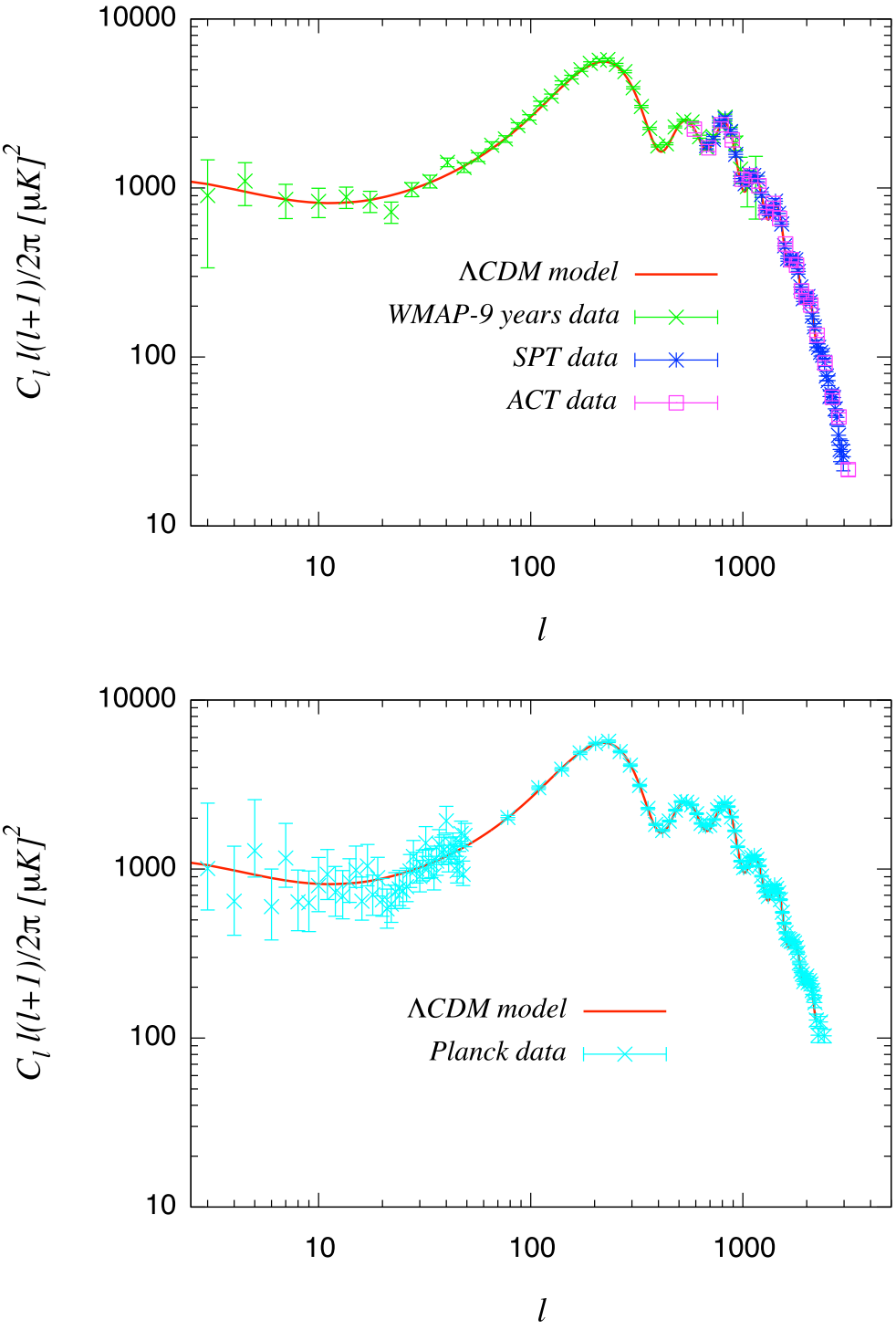

Figure 1.2: Temperature power spectrum versus the multipole moment ℓ for the best fit parameters for the ΛCDM scenario from Planck data. We depict the data from the WMAP, SPT, ACT (upper panel) and Planck (lower panel) experiments. CMB data have been taken from http://lambda.gsfc.nasa.gov/ and from http://pla.esac.esa.int/pla/aio/planckProducts.html.

particles (baryons). These particles were in equilibrium through these reactions:

$$\begin{aligned} \gamma + \gamma &\rightleftharpoons e^+ + e^- \\ n + \nu_e &\rightleftharpoons p + e^- \\ n + e^+ &\rightleftharpoons p + \bar{\nu}_e \end{aligned}$$

When the temperature of the universe fell below the binding energy of a typical nucleus, light elements, like ^{2}H and ^{3}He, began to form. This epoch of nuclear fusion is commonly called epoch of *Big Bang Nucleosynthesis* (BBN).

In order to analyze the early universe, it is necessary to know the species which contribute to the energy of the universe at a given time, as well as their distribution functions. If the reaction rate Γ for an interacting particle is much higher than the expansion rate H, the interaction can maintain those particles in a thermodynamic equilibrium at a temperature T. Therefore they can be treated as Fermi-Dirac (+) or Bose-Einstein (-) gases with a distribution function:

$$f(E,T) = \left[\exp\left(\frac{E-\mu}{k_B T}\right) \pm 1\right]^{-1} , \tag{1.84}$$

where μ is the chemical potential, k_B is the Boltzamnn constant and $E^2 = p^2 + m^2$. From this function we can compute the number density n, the energy density ρ and the pressure p of the different species:

$$n = \frac{g}{(2\pi\hbar)^3}\int_0^\infty \frac{4\pi p^2}{e^{(E-\mu)/k_B T} \pm 1} dp , \tag{1.85}$$

$$\rho = \frac{g}{(2\pi\hbar)^3}\int_0^\infty E\frac{4\pi p^2}{e^{(E-\mu)/k_B T} \pm 1} dp , \tag{1.86}$$

$$p = \frac{g}{(2\pi\hbar)^3}\int_0^\infty \frac{p^2}{E}\frac{4\pi p^2}{e^{(E-\mu)/k_B T} \pm 1} dp , \tag{1.87}$$

where g is the number of degrees of freedom of the species. The numerical density of a nucleus with mass number A in the non-relativistic limit is given by:

$$n_A = g_A \left(\frac{m_A T}{2\pi}\right)^{3/2} e^{-\frac{m_A - \mu_A}{T}} , \tag{1.88}$$

As long as the reaction rates are higher than the expansion rate, the chemical equilibrium imposes the chemical potential to be:

$$\mu_a = Z\mu_p + (A-Z)\mu_n , \tag{1.89}$$

with μ_p, μ_n the chemical potential of protons and neutrons and Z the atomic number. Using this formula and expressing μ_p and μ_n as n_p and n_n, the eq. (1.88) becomes:

$$n_A = g_A 2^{-A}\left(\frac{m_A}{m_p^Z m_n (A-Z)}\right)^{3/2}\left(\frac{2\pi\hbar}{k_B T}\right)^{3(A-1)/2} n_p^Z n_n^{A-Z} e^{\frac{B_A}{k_B T}} , \tag{1.90}$$

in which $B_A = Zm_p + (A - Z)m_n - m_A$ is the binding energy of the nucleus.

Introducing a new parameter η, defining as the baryon-to-photon ratio:

$$\eta = \frac{n_b}{n_\gamma} \, , \tag{1.91}$$

and the mass fraction of the element A:

$$X_A = A\frac{n_A}{n_b} = A\frac{n_A}{n_\gamma}\eta^{-1} \, , \tag{1.92}$$

we obtain the abundances of atomic nuclei in thermodynamical equilibrium:

$$X_A \propto \eta^{A-1} X_p^Z X_n^{A-Z} e^{\frac{B_A}{k_B T}}. \tag{1.93}$$

Since the basic building blocks for nucleosynthesis are neutrons and protons, it is also important to calculate the ratio between the number of these particles. Defining the difference in rest energy of the neutron and the proton as $Q = m_n - m_p \approx 1.29$ MeV, the neutron-to-proton ratio is:

$$\frac{n_n}{n_p} = \exp\left(-\frac{Q}{k_B T}\right). \tag{1.94}$$

At temperature $k_B T \gg Q$, the number of neutrons is nearly equal to the number of protons. When $k_B T \gg Q$ protons begin to be strongly favored and the neutron-to-proton ratio decreases exponentially. When the temperature of the universe decreases reaching an equilibrium point of about 0.72 MeV, the abundance ratio of the neutron-to-proton is aproximately 1/6. However, this fraction does not remain constant, because neutrons are still converting into protons via β -decay. When the temperature reaches 0.1 MeV, the neutron-to-proton abundance ratio reduces to 1/7.

The Helium abundance is an example that depends on this ratio. This element is composed by two neutrons and two protons ($n_{He} \approx n_n/2$) and its abundance is:

$$Y = A\frac{n_{He}}{n_b} = \frac{4(n_n/2n_p)}{1 + (n_n/n_p)} \approx 0.25 \, , \tag{1.95}$$

assuming a neutron-to-proton ratio of about 1/7. In the Big Bang Nucleosynthesis only the light elements with nuclei no more massive than ^{7}Li (^{2}H, ^{3}He, ^{4}He, ^{7}Li) are produced. Heavier nuclei are only synthesized in stars or as a consequence of stellar explosions. The BBN theory yields precise quantitative predictions for the mixture of these elements, that is, the primordial abundances at the end of the Big Bang period. Therefore, BBN light element abundances can be used as another probe to extract the cosmological parameters describing our universe.

1.7.4 Large Scale Structure

We have seen that, on large scales, the universe can be approximated as being homogeneous and isotropic. On small scales, the universe contains density fluctuations ranging from

subatomic quantum fluctuations up to the large supercluster and voids which characterize the distribution of galaxies in space. Cosmologists use the term *Large Scale Structure* (LSS) to refer to all structures bigger than individual galaxies. From the study of these structures, in particular from the distribution of matter on large scales, we can extract information to constrain the cosmological parameters.

To understand how to characterize this distribution it is often useful to work in Fourier space. We consider a catalog of galaxies in a volume V with a mass density $\rho(\mathbf{r})$ and a density contrast $\delta(\mathbf{r}) = (\rho - \rho_0)/\rho_0$ (ρ_0 is the mean value of the matter density). From the Fourier transform of $\delta(\mathbf{r})$:

$$\delta_{\mathbf{k}} = \frac{1}{V}\int \delta(\mathbf{r}) e^{i\mathbf{k}\cdot\mathbf{r}} d^3r \ , \tag{1.96}$$

we can define the *power spectrum* $P(k)$ as:

$$P(\mathbf{k}) = V\langle|\delta_{\mathbf{k}}|^2\rangle. \tag{1.97}$$

Introducing the *correlation function* for the density contrast:

$$\xi(\mathbf{r}) = \langle\delta(\mathbf{r}_1)\delta(\mathbf{r}_1+\mathbf{r})\rangle = \frac{2\pi^3}{V}\sum\langle|\delta_{\mathbf{k}}|^2\rangle e^{i\mathbf{k}\cdot\mathbf{r}} = \int P(\mathbf{k}) e^{-i\mathbf{k}\cdot\mathbf{r}} \frac{d^3k}{(2\pi)^3} \ , \tag{1.98}$$

where the average is taken over the entire statistical ensemble of points with a comoving distance $\mathbf{r}$ from the point $\mathbf{r}_1$, the $P(\mathbf{k})$ can be rewritten as:

$$P(\mathbf{k}) = \int \xi(\mathbf{r}) e^{i\mathbf{k}\cdot\mathbf{r}} d^3r. \tag{1.99}$$

Therefore we can see that the power spectrum is the Fourier transform of the correlation function.

The shape of the power spectrum depends on the cosmological parameters. By using galaxy catalogs, the power spectrum can be reconstructed, at least in a range of k's (see for example [28, 29, 30]). There are several observables to probe large scale structure, as for example Lyman-*alpha* systems, weak lensing, quasar clustering, galaxy cluster mass function (see for example Ref. [31]), but in this thesis we will only focus on galaxy clustering.

In the last decades, a number of galaxy surveys have been designed to measure the large scale structure in the universe. The most important large survey is the *Sloan Digital Sky Survey* (SDSS) [32]. Over eight years of operations (SDSS-I, 2000-2005; SDSS-II, 2005-2008), it obtained deep, multi-color images covering more than a quarter of the sky and created 3-dimensional maps containing more than 930,000 galaxies and more than 120,000 quasars. During its first phase of operations, 2000-2005, the SDSS experiment [33] imaged more than 8,000 square degrees of the sky in five optical band-passes, and it obtained spectra of galaxies and quasars selected from 5,700 square degrees of that imaging. SDSS-III [34], a program of four new surveys using SDSS facilities, began observations in July 2008 and released Data Release 8 in January 2011 and Data Release 9 in August 2012. SDSS-III

will continue operating and releasing data through 2014.

The Baryon Oscillation Spectroscopic Survey (BOSS) is one of the four surveys of SDSS-III. It aims to measure the cosmic distance scales and to determine the expansion history of the universe with high precision by using Baryon Acoustic Oscillations, that are an example of a LSS measurement and that we shall describe in the next section. BOSS is performing a redshift survey of 1.5 million massive luminous galaxies ($0.3 < z < 0.7$) and 150,000 quasars at $z > 2.5$ and it covers an area of 10,000 deg^2. The observations began in 2009, and the last data will be acquired in 2014. BOSS galaxy selection is based on a series of color-magnitude cuts. These cuts are intended to select a sample of luminous and massive galaxies with an approximately uniform distribution of stellar masses from $z \sim 0.2$ to $z \sim 0.6$ [35, 36]. In particular, the selection is the union of two cuts: cut I (Low Redshift sample, LOZ), aimed at selecting luminous and massive galaxies at $0.2 < z < 0.4$ and cut II (CMASS sample, for ¡Èconstant mass¡É [37]), designed to select galaxies at $z > 0.4$ and with the stellar mass of the system approximately constant.

From the imaging data in the SDSS it is possible to measure the two-dimensional (2D) angular power spectrum C_ℓ that is closely related to the 3D power spectrum $P(k)$. The relation between the 2D angular power spectrum of galaxies and the 3D galaxy power spectrum is [38, 39]:

$$C_\ell = 4\pi \int_0^\infty P_g(k,z) f_\ell(k)^2 \frac{dk}{k} \ , \tag{1.100}$$

where $f_\ell(k)$ is the Bessel transform of the radial selection function $f(r)$, given by the equation:

$$f_\ell(k) = \int_0^\infty f(r) j_\ell(kr) dr \ , \tag{1.101}$$

with $j_\ell(kr)$ the spherical Bessel function. Specifically, $f(r) = g(r)h(r)$, in which $g(r)$ is the probability distribution for the comoving distance from us to a random galaxy in the survey and $h(r)$ is a bias and clustering evolution term of the order of unity. Considering the number of galaxies within a sphere of radius r:

$$g(r) \propto \frac{dN}{dr} = \frac{dN/dz}{dr/dz} = \frac{H(z)}{c} \frac{dN}{dz} \ , \tag{1.102}$$

the eq. (1.100) becomes:

$$C_\ell = 4\pi \int P_g(k,z) \frac{dk}{k} \left[\int \frac{dN}{dz} j_\ell(kr) dz \right]^2 . \tag{1.103}$$

The evolution of the galaxy power spectrum in linear theory reads:

$$P_g(k,z) = \frac{k^3 P_g(k,0)}{2\pi^2} \left(\frac{D(z)}{D(0)} \right)^2 \frac{1}{(1+z)^2} \ , \tag{1.104}$$

were $D(z)$ is the growth factor, eq. (1.66). The final expression of the 2D power spectrum is:

$$C_\ell = \frac{2}{\pi}\int P_g(k,0)k^2dk\left[\int \frac{dN}{dz}j_\ell(kr)\left(\frac{D_(z)}{D(0)}\right)\frac{1}{(1+z)}dz\right]^2 . \tag{1.105}$$

In the limit of small angles we can use the *Limber approximation*, $kr = \ell$. In this limit the integral of the Bessel function can be approximated as:

$$\int_0^\infty j_\ell(kr)dr = \frac{\sqrt{\pi}}{2}\frac{\Gamma\left(\frac{\ell+1}{2}\right)}{\Gamma\left(\frac{\ell+2}{2}\right)} \approx \sqrt{\frac{\pi}{2}} , \tag{1.106}$$

and the C_ℓ's are defined by the following relation:

$$C_\ell = \int P_g(k,0)\left(\frac{dN}{dz}\right)^2\frac{dz}{dr}\left(\frac{D(z)}{D(0)}\right)^2\frac{1}{(1+z)^2}\frac{1}{r(z)^2}dz . \tag{1.107}$$

In Fig 1.3, upper panel, we show the matter power spectrum for three different models including the possibility of a dark energy equation of state parameter w different from -1. We illustrate the case of the best fit parameters from the Planck data set for a ΛCDM cosmology and we also include the data from the SDSS II. The lower panel of Fig 1.3 depicts the 2D power spectrum for the same models illustrated in the upper panel. The data correspond to the observed power spectrum obtained from BOSS DR8 in the redshift bin $0.45< z <0.5$ [40].

It is important to note that the density perturbation in observed galaxies, $\delta_g(k,z)$, is not necessarily equal to the total matter density perturbation $\delta(k,z)$. So, in the Fourier space, we can define a function, called *bias*, that parametrizes the relation between galaxy clustering and matter clustering:

$$b(z) = \frac{\delta_g(k,z)}{\delta(k,z)} , \tag{1.108}$$

and we can relate the power spectrum of galaxies to that of total matter power spectrum via a linear bias model:

$$P_g(k,z) = b^2(z)P(k,z) . \tag{1.109}$$

The bias model should be accounted for when galaxy clustering measurements are used to extract cosmological parameters, in order to relate the observed galaxy power spectra to the underlying matter power spectrum, and, in principle, it can dependend on the scale. Moreover galaxies have peculiar velocities $\mathbf{v}$ relative to the general Hubble expansion. Thus it is necessary, in general, to distinguish between a galaxy's *redshift distance* s and the *true distance* r, normalized to velocity units [41]:

$$s = cz , \tag{1.110}$$
$$r = H_0 d , \tag{1.111}$$

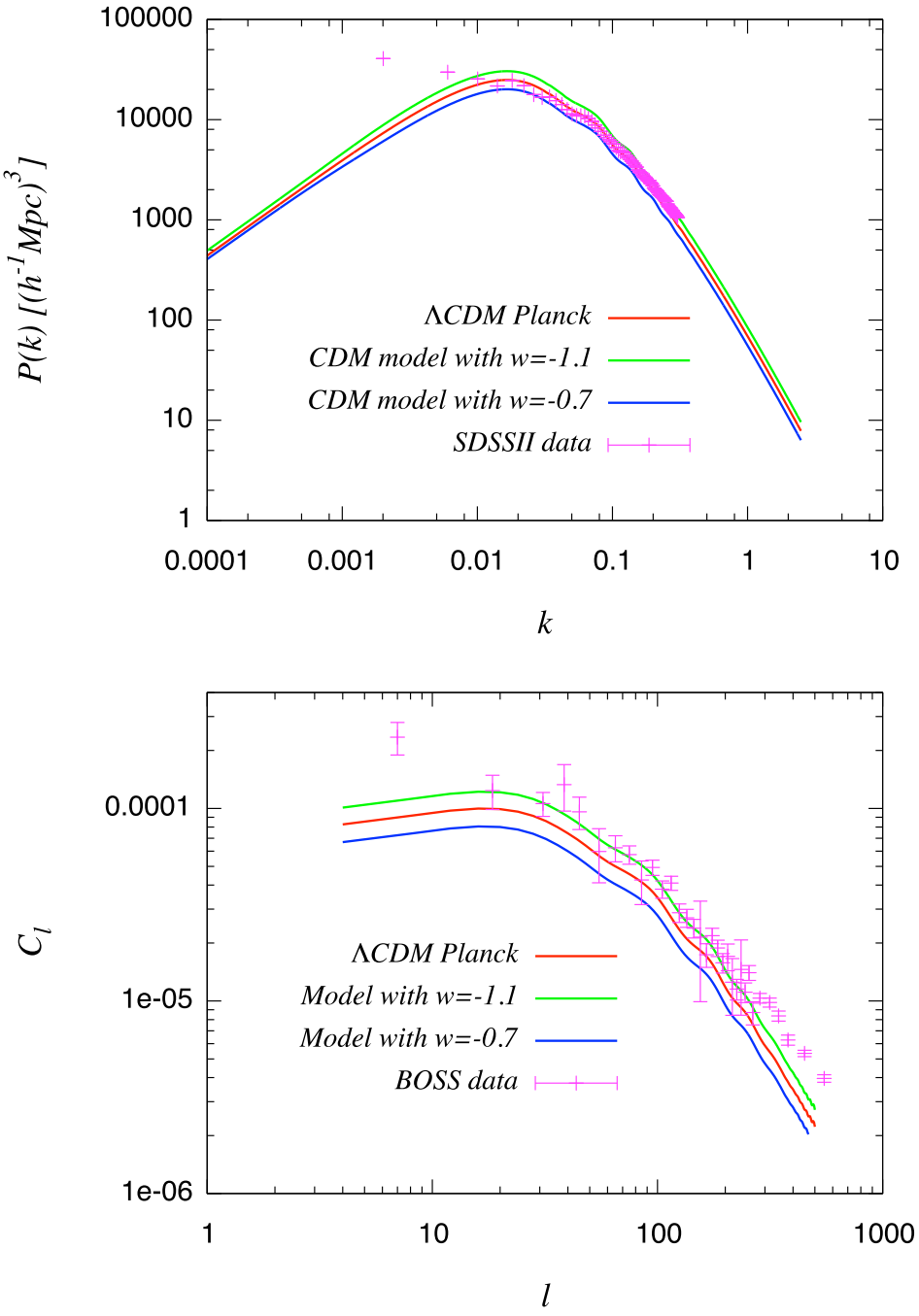

Figure 1.3: Upper (lower) panel: The red lines depict the matter power spectra $P(k)$ (2D power spectra, C_ℓ) for the best fit parameters for a ΛCDM model from the Planck data set. The others curves show the two scenarios with a dark energy equation of state parameter w different from -1. The data correspond to the clustering measurements of luminous red galaxies from SDSS II Data Release 9 [34] in which we have added a bias of 3, and from the CMASS sample in Data Release 8 [40] of the Baryon Oscillation Spectroscopic Survey.

where the first relation holds at relatively low redshifts. The redshift distance s of a galaxy differs from the true distance r by its peculiar velocity $v = (\hat{\mathbf{r}}) \cdot \mathbf{v}$ along the line of sight:

$$s = r + v \ . \tag{1.112}$$

The peculiar velocity of galaxies, thus, causes them to appear displaced along the line-of-sight in redshift space and these displacements are known as *redshift space distortions*.

Although such distortions complicate the interpretation of redshift maps, they have the advantage of bearing information about the dynamics of galaxies. In particular, the amplitude of distortions on large scales yields a measure of the *linear redshift distortion parameter* β, which, assuming a ΛCDM universe, is related to the cosmological density $\Omega_{\rm m}$ by:

$$\beta = \frac{f}{b} \simeq \Omega_{\rm m}^{0.6} \ , \tag{1.113}$$

where f is the linear growth rate, defined in eq. (1.67), and b is the bias. Measurements of the β parameter can be used as a test to distinguish between dark energy models and models in which the gravitational sector of the theory is modified to explain the current accelerated expansion of the universe, since, in this case, the growth factor is scale dependent.

1.7.5 Baryon Acoustic Oscillations

As previously stated, in the photon-baryon fluid at $z > 1100$, the competition between gravity and radiation pressure brings to oscillations in the plasma which propagate as acoustic waves, known as Baryon Acoustic Oscillations (BAO), with a velocity c_s given by:

$$c_s = \frac{\delta p}{\delta \rho} \approx \frac{c^2 \delta \rho_\gamma / 3}{\delta \rho_\gamma \delta \rho_b} = \frac{c^2}{3(1+R)} \ , \tag{1.114}$$

where $R \equiv 3\rho_b / 4\rho_\gamma$ and ρ_γ and ρ_b are the energy density of photons and baryons, respectively.

At recombination ($z \sim 1100$), the photons decouple from the baryons and start to free stream, whereas the pressure waves get frozen. As a result, baryons accumulate at a fixed distance from the original over-density and this distance is equal to the sound horizon length at the decoupling time. The result is a peak in the mass correlation function ξ, see eq. (1.98) at the comoving scale. The BAO provides a standard rule to measure the distance to various redshifts using the clustering distribution of galaxies measured from large galaxy surveys. This distance-redshift relation depends, for example, on the values of the cosmological parameters so it can be used to infer the cosmic expansion history of the universe.

We have already explained that in a galaxy survey, we measure distances in term of angles and redshift. These observed quantities can be related to known distances using the FRW metric. The differential radial distance is inversely proportional to the expansion rate $H(z)$ [42]:

$$dr(z) = \frac{c}{H(z)} dz \ , \tag{1.115}$$

while the angular diameter distance is proportional to the integral of $dr(z)$:

$$d_A(z) = \frac{c}{1+z}\int_0^z \frac{dz'}{H(z')} \ , \tag{1.116}$$

for a spatially flat universe [7].

To use the BAO method, we must measure the acoustic scale from the clustering of galaxies. This is typically done statistically using the 2-point correlation function of galaxy separations, eq. (1.98), or its Fourier transform, the power spectrum, eq. (1.99). From these functions, it is possible to measure two different quantities corresponding to the oscillations parallel and perpendicular to the line of sight:

$$\delta z_s = r_s(z_d)\frac{H(z)}{c} \ , \tag{1.117}$$

$$\delta\theta_s = \frac{r_s(z_d)}{d_A(z)(1+z)} \ , \tag{1.118}$$

in which $r_s(z_d)$ is the sound horizon dimension at the drag epoch (when baryons became dynamically decoupled form the photons):

$$r_s(z_d) = c\int_0^{t_d}\frac{c_s(t)dt}{a} = c\int_0^{a_d}\frac{c_s da}{a^2 H(a)} \ . \tag{1.119}$$

The imprint of the baryon acoustic oscillations has been detected in a variety of low-redshift data sets. Significant detections of BAOs have now been reported by independent galaxy surveys, spanning a range of redshifts $0.1 < z < 0.8$: the SDSS [43], the WiggleZ Dark Energy Survey [44], the 6-degree Field Galaxy Survey [45] and the SDSS-III Baryon Oscillation Spectroscopic Survey [46].

The WiggleZ Dark Energy Survey is a large-scale galaxy redshift survey of bright emissionline galaxies which was carried out at the Anglo-Australian Telescope between August 2006 and January 2011. The survey is now complete, comprising of order 200,000 redshifts and covering of order 800 deg^2 of equatorial sky. The galaxy sample includes a total of 158,741 galaxies in the redshift range $0.2 < z < 1.0$ [44].

The 6-degree Field Galaxy Survey is a combined redshift and peculiar velocity survey covering nearly the entire southern sky. The 6dFGS sample contains 75,117 galaxies distributed over $\sim$ 17,000 deg^2 with a mean redshift of $z = 0.106$.

[7] An other important technique used to determine the cosmological parameters is the study of the *Lyman-α forest*. The spectrum of quasi-stellar objects (QSO) that reach the earth contain lots of information about the distribution of the intergalactic medium. When the radiation emitted by a QSO penetrates a cloud of gas containing neutral hydrogen, this will absorb a part of the radiation and the spectrum of quasars will present absorption lines arising from the Lyman-alpha transition. The use of the Lyman-α forest allow the study of the distribution of the intergalactic medium at redshifts $z \sim 2\frac{3}{4}4$, and can be used to constrain the cosmological parameters.

Most of these detection of the BAO have used spherically averaged clustering statistics, measuring an effective distance:

$$D_V \equiv \left[(1+z)^2 d_A^2(z)\frac{cz}{H(z)}\right]^{1/3} . \tag{1.120}$$

Usually BAO measurements are given in terms of the relative distance:

$$r_{BAO} = \frac{r_s(z_d)}{D_V(z)}. \tag{1.121}$$

Figure 1.4 shows estimates of r_{BAO}, as quoted by each of the experimental groups, divided by the best-fit Planck prediction for a ΛCDM universe. Here we show the results from four redshift surveys: the SDSS DR7 measurements at $z = 0.35$ [43], the WiggleZ measurements at $z = 0.44$, 0.60 and 0.73 [44], the 6dF Galaxy Survey measurement at $z = 0.1$ [45] and the BOSS DR9 measurement at $z = 0.57$ [46, 47]. We can see that all the BAO measurements are compatible with the base ΛCDM parameters from Planck. We also show in Fig.1.4 the theoretical predictions for different dark energy models. Here we present the cases of $w = -1.1$ and $w = -0.9$.

A next generation of BAO surveys, eBOSS, BigBOSS and Subaru Prime Focus Spectrograph (PFS), plans to map the high redshift Universe in the range $0.6 < z < 3.5$. The Extended Baryon Oscillation Spectroscopic Survey (eBOSS) is a 4-year cosmology project that pushes the reach of the Sloan Telescope to map large scale structure beyond $z = 0.6$. It will measure with high accuracy the expansion history of the Universe throughout eighty percent of cosmic history and improve constraints on the nature of dark energy and dark matter. Furthermore, the distribution of eBOSS targets on very large scales will be able to constrain the mass of the neutrino and the nature of the ¡Èinflationary epoch¡É in the very early Universe, which produced the primordial fluctuations leading to the formation of galaxies and larger structures. BigBOSS is a ground-based experiment designed to probe the nature of dark energy through the measurement of baryon acoustic oscillations (BAO) and redshift space distortions. Building on the SDSS-III BOSS survey, BigBOSS will measure redshifts of luminous red galaxies (LRGs), quasars (QSOs), and emission line galaxies (ELGs) between $0.2 < z < 3.5$. The measurements from BigBOSS will lead to new levels of precision in the dark energy equation of state and the growth of structures in the universe. The main goals for the PFS cosmology survey are: to constrain the angular diameter distance and the Hubble expansion rate via the BAO experiment, use the shape and amplitude of galaxy correlation function in order to constrain cosmological parameters as well as the growth rate of structure formation, use the distance measurements for determining the dark energy density parameter, derive the BAO constraints in a redshift range that is complementary to those probed by the existing planned BAO surveys.

The future Euclid mission (http://sci.esa.int/), planned by the European Space Agency (ESA), in collaboration with NASA, is scheduled to be launched in 2019. The mission will investigate the distance-redshift relationship and the evolution of cosmic structures

by measuring shapes and redshifts of galaxies and clusters of galaxies out to redshifts ~ 2. In this way, Euclid will cover the entire period over which dark energy played a significant role in accelerating the expansion. To do these measurements, Euclid will use the weak gravitational lensing and Baryonic Acoustic Oscillations.

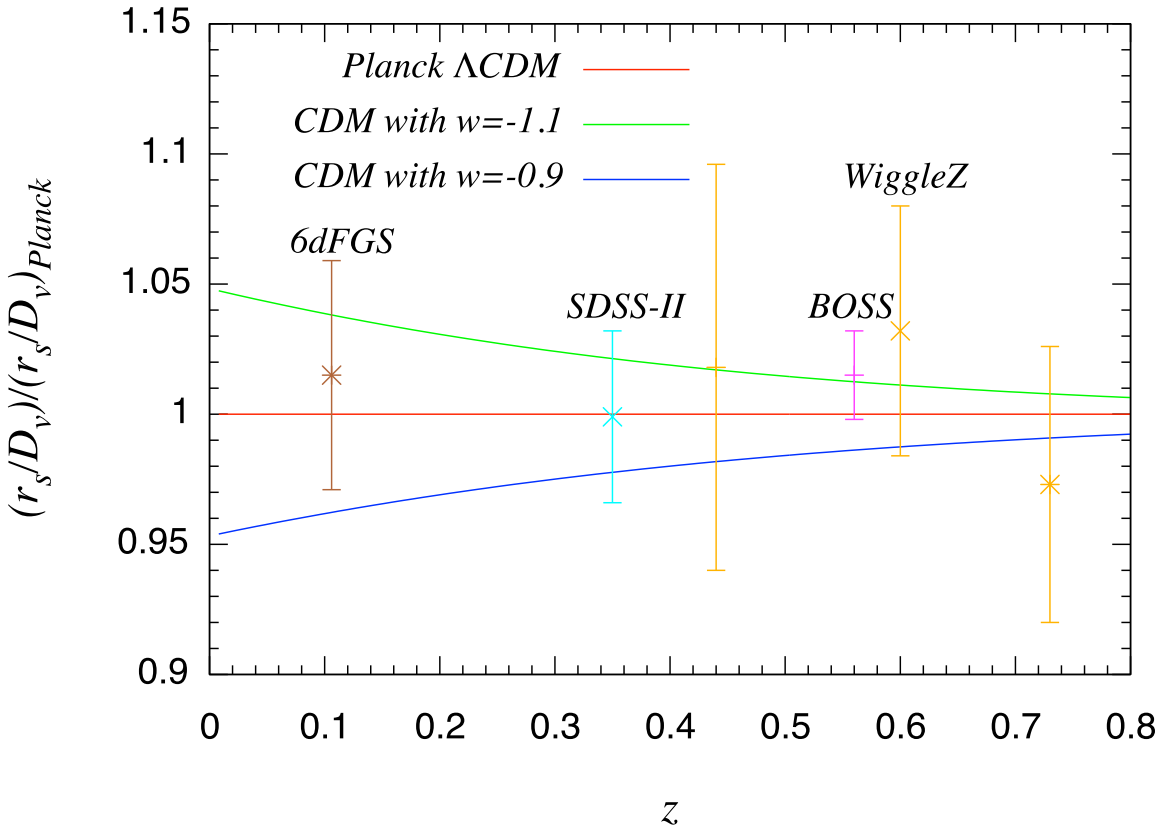

Figure 1.4: The BAO distance-redshift relation divided by the best-fit model for the spatially flat, ΛCDM prediction from Planck measurements. We show the results form SDSS-II LRG [43], WiggleZ [44], 6dF Galaxy Redshift Survey [45] and BOSS DR9 [47] data. We also show the theoretical predictions from varying the dark energy equation of state, $w = -1.1$ (green line) and $w = -0.9$ (blue line).

Chapter 2

Massive neutrinos and Dark Radiation in Cosmology

In this chapter we introduce neutrinos and their properties. We discuss the neutrino oscillations and the role of neutrinos in cosmology, describing the impact of massless and massive neutrinos on cosmological perturbations. We also present some basic properties of the Cosmic Neutrino Background, introducing the dark radiation scenario, and we end the chapter illustrating the main effects that neutrinos and dark radiation induce in cosmology, in particular on the CMB and on Large Scale Structure formation.

2.1 Relic neutrinos

The standard hot big bang model predicts the existence of a relic sea of neutrinos that is in number slightly below to that of relic photons of the CMB. Cosmic neutrinos were produced at large temperature in the early universe by frequent weak interactions and they were maintained in equilibrium with other particles of the primordial plasma. Once the temperature of the universe reached a few MeV they decoupled from the electromagnetic plasma and could travel as free particles, keeping the perfect Fermi-Dirac distribution, eq. (1.84). It is important to note that while a massive Fermi-Dirac distribution is not conserved under free-streaming, this can be ignored because $\sum m_\nu \ll 1$ MeV.

After neutrino decoupling, the photon temperature dropped below the electron mass favouring $e^\pm$ annihilation, $e^+e^- \rightleftharpoons \gamma\gamma$, that heated the photons. Neutrinos are basically left undisturbed by pair annihilation, because the analogous weak process $e^+e^- \rightleftharpoons \nu\bar{\nu}$ have a low rate compared to the Hubble parameter, and only a tiny fraction of $e^\pm$ goes into neutrinos. Therefore applying entropy conservation and counting interacting degrees of freedom, we can calculate the ratio of neutrino and photon temperatures (for more details see [17]):

$$\frac{T_\nu}{T_\gamma} = \left(\frac{4}{11}\right)^{1/3} . \tag{2.1}$$

Given that the CMB temperature is $T_{\gamma,0} = 2.725$ K, the present relic neutrino temperature is $T_{\nu,0} = 1.945$ K (1.676×10^{-4} eV). The number density of relic neutrinos per species

today is given by:

$$n_{\nu,0} = \frac{g}{(2\pi\hbar)^3}\int_0^\infty \frac{4\pi p^2}{e^{(p)/k_B T_{\nu 0}} \pm 1} dp = \frac{3}{11} n_\gamma \ , \tag{2.2}$$

that leads to a value of 113 neutrinos plus anti-neutrinos of each flavour per cm^3. The energy density can be calculated numerically, with two analytical limits (relativistic and non-relativistic):

$$\rho_\nu(m_\nu \ll T_\nu) = \frac{7\pi^2}{120}\left(\frac{4}{11}\right)^{4/3} T_\gamma^4 \ , \tag{2.3}$$

$$\rho_\nu(m_\nu \gg T_\nu) = m_\nu n_\nu \ . \tag{2.4}$$

Thus, when neutrinos become non-relativistic (at a redshift of $\sim 2000(m_\nu/1\text{eV})$), they behave as matter; while in the relativistic regime they behave as radiation.

Using the present value of the critical density, $\rho_{c,0} = 1.054 \times 10^4 h^2$ eV/cm, and eq. (2.2), we obtain the neutrino density parameter:

$$\Omega_\nu h^2 = \frac{\sum_i m_{\nu i} n_{\nu,0}}{\rho_{c,0}} = \frac{\sum_i m_{\nu i}}{93.3\ eV} \ , \tag{2.5}$$

in which we sum only over neutrinos which are non-relativistic today. If they were relativistic today $\Omega_\nu h^2 = 6 \times 10^{-6}$.

Neutrinos fix the expansion rate during the cosmological era when the universe is dominated by radiation. After $e^\pm$ annihilation, the universe was populated only by photons and neutrinos, therefore the corresponding energy density can be written as:

$$\rho_r = \left[1 + \frac{7}{8}\left(\frac{4}{11}\right)^{4/3} \times 3\right] \rho_\gamma \ , \tag{2.6}$$

in which it is assumed that there are only three light neutrino species and no other relativistic species. However, the three neutrino scenario is a minimal scheme, and there is no fundamental symmetry in nature forcing a definite number of right-handed (sterile) neutrino species, as those are allowed in the Standard Model fermion content. For this reason, it is convenient to parametrize the total radiation energy density in terms of the *effective number of relativistic species* $N_{\rm eff}$:

$$\rho_r = \left[1 + \frac{7}{8}\left(\frac{4}{11}\right)^{4/3} N_{\rm eff}\right] \rho_\gamma \ . \tag{2.7}$$

The Standard Model predicts a value of $N_{\rm eff} = 3.046$, corresponding to the three active neutrino contribution. The departure of $N_{\rm eff}$ from its standard value, three, is explained in the following.

In particular, in a more accurate analysis, the assumption of instantaneous neutrino decoupling can be modified. The main physical reason is that the neutrino plasma receives

a contribution from the $e^{\pm}$ annihilation and, thus, some relic interactions between $e^{\pm}$ and neutrinos occur. These processes are more efficient for neutrinos with larger energies that are more heated, leading to a distortion in the neutrino spectra. A proper calculation of the process of non-instantaneous neutrino decoupling requires the numerical solution of the Boltzmann equations (see Refs. [48, 49]). Quantum Electrodynamics (QED) finite temperature corrections and neutrino oscillations need also to be addressed in the Boltzmann equations, see Refs. [50, 51]. The final result, after considering non instantaneous neutrino decoupling, QED corrections and neutrino oscillations is $N_{\rm eff} = 3.046$.

Measuring $N_{\rm eff}$ is of great interest today and in this thesis we will consider cosmological scenarios where this parameter is not fixed to three, and testing, therefore, sterile neutrino schemes.

2.2 Massive neutrinos

The existence of neutrino was postulated in 1930 by Wolfgang Pauli, as an attempt to explain the continuous energy spectrum observed in beta-decay experiments. It was postulated as a neutral particle that scatters only through the weak interaction, and consequently rarely interacts with matter. In elementary particle physics, neutrinos are fermions with spin 1/2 and they are members of the family of elementary particles called leptons. They differ from the quarks of the Standard Model (particles with spin 1/2 which participate in strong and electromagnetic interactions) and from the other leptons, which are charged and thus interact electromagnetically. Due to their very small cross section, the detection of neutrino is particularly challenging. The neutrino was first detected in 1956 in an experiment carried out by Frederick Reines and Clyde Cowan [52], a quarter of a century after the existence of that particle was predicted.

In the Standard Model of elementary particles, neutrinos are massless particles. However, during the last several years, oscillation experiments involving solar, atmospheric, reactor and accelerator neutrinos have adduced robust evidence for the existence of neutrino oscillations, implying that neutrinos have masses.

2.2.1 Neutrino oscillations

In 1957 Bruno Pontecorvo realized that if neutrinos were massive there could exist processes, named *neutrino oscillations*, where the neutrino flavour is not conserved. The existence of flavour neutrino oscillations implies that if a neutrino of a given flavour, for example ν_μ, is produced in some weak interaction process at a sufficiently large distance from the detector location, the probability to find a neutrino of a different flavour, say ν_τ, is different from zero.

Neutrinos are produced and detected, via the weak interaction, as flavour eigenstates ν_e, ν_μ or ν_τ and they propagate as mass eigenstates ν_1, ν_2 or ν_3. In a three-neutrino scenario, the flavour states, $\alpha = (e,\ \mu,\ \tau)$, are related to the mass eigenstates, i=(1, 2, 3), by a mixing

matrix called the Pontecorvo-Maki-Nakahawa-Sakata matrix (PMNS) [53, 54]:

$$|\nu_\alpha\rangle = U_{\alpha,i}\ |\nu_i\rangle\ , \tag{2.8}$$

which is parametrized as:

$$U_{\alpha,i} = \begin{pmatrix} 1 & 0 & 0 \\ 0 & c_{23} & s_{23} \\ 0 & -s_{23} & c_{23} \end{pmatrix} \begin{pmatrix} c_{13} & 0 & s_{13}e^{-i\delta} \\ 0 & 1 & 0 \\ -s_{13}e^{i\delta} & 0 & c_{13} \end{pmatrix} \begin{pmatrix} c_{12} & s_{12} & 0 \\ -s_{12} & c_{12} & 0 \\ 0 & 0 & 1 \end{pmatrix}\ , \tag{2.9}$$

where $c_{ij} = \cos\theta_{ij}$ and $s_{ij} = \sin\theta_{ij}$ for $ij = 12, 23$ or 13, and δ is a CP-violating phase.

We can order the neutrino masses m_i such that m_3 is the most splitted state and $m_2 > m_1$, and we can define $\triangle m = m_{ij}^2 = m_j^2 - m_i^2$. With this choice, $|\triangle m_{31}^2|$ and θ_{13} are the atmospheric parameters and $\triangle m_{21}^2 > 0$ and θ_{12} are the solar parameters. Oscillation experiments can only measure squared mass differences and the mixing angles, and their current 1σ allowed regions are (see for example [55, 56, 57]):

$$\triangle m_{21}^2 = \left(7.5^{+0.18}_{-0.19}\right) \times 10^{-5}\ \text{eV}^2\ , \tag{2.10}$$

$$\triangle m_{31}^2 = \left(+2.473^{+0.070}_{-0.067}\right) \times 10^{-3}\ \text{eV}^2\ , \tag{2.11}$$

$$\theta_{12} = 33.36^{+0.81}_{-0.78}\ , \tag{2.12}$$

$$\theta_{23} = 40.0^{+2.1}_{-1.5}\ , \tag{2.13}$$

$$\theta_{13} = 8.66^{+0.44}_{-0.46}\ . \tag{2.14}$$

Unfortunately these experiments are not sensitive to the absolute scale of neutrino masses. Also, current oscillation experiments are unable to extract the sign of $|\triangle m_{31}^2|$, leading to two possible schemes, see Fig. 2.1, known as normal and inverted hierarchies and characterized by the sign of $\triangle m_{31}^2$, positive and negative, respectively.

In Fig. 2.2 we show the sum of the three neutrino masses, $\sum m_\nu$, as a function of the mass of the lightest neutrino mass for the normal and inverted hierarchies. The width of the curves is related to the current 3σ error on the mass splittings. We can note that in the normal hierarchy scheme, the minimum value for the sum of neutrino masses is $\sum m_\nu \simeq 0.06$ eV while in the inverted hierarchy scheme, this value becomes $\sum m_\nu \simeq 0.1$ eV.

Information on the absolute scale of neutrino masses can be extracted from kinematical studies of weak decays producing neutrinos. The upper bound on the electron-neutrino mass from tritium beta decay experiments is $m < 2.05 - 2.3$ eV [58, 59]. This bound is expected to be improved by the KATRIN [60] project to measure neutrino masses in the range $0.3 - 0.35$ eV. The neutrinoless double beta decay experiments also put constraints on neutrino masses, providing constraints on the so called effective Majorana mass, $m_{ee} < 0.36$ eV [61]

However the three neutrino oscillation picture is a minimal approach. Additional light sterile neutrinos (particles that do not interact via any of the fundamental interactions of the Standard Model except gravity) may exist in nature, since they are not forbidden by

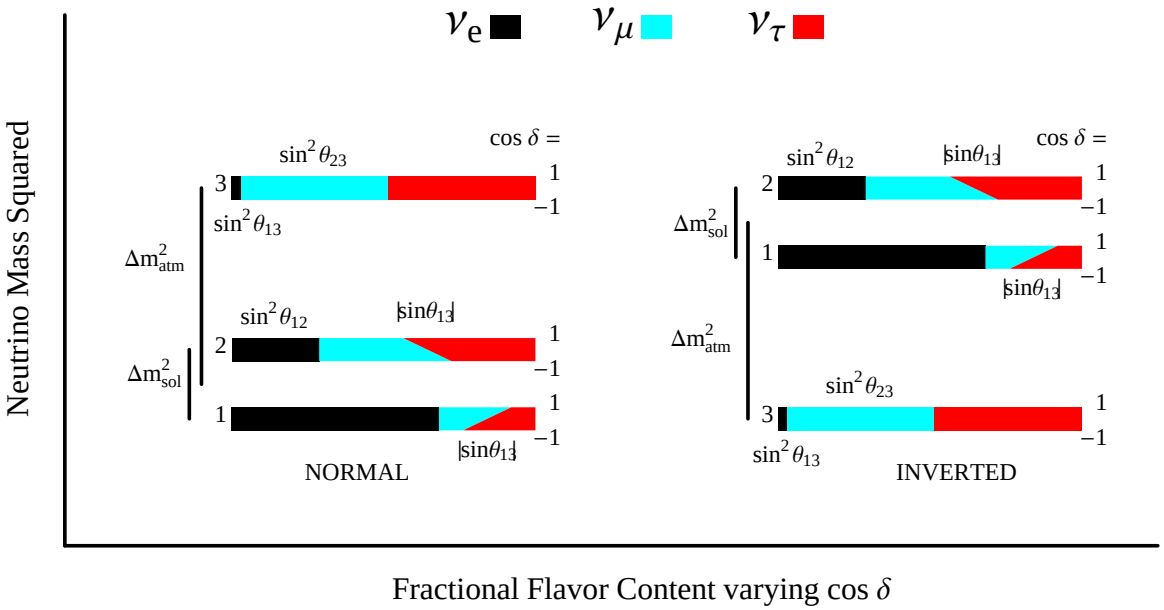

Figure 2.1: The two neutrino schemes allowed if $\triangle m^2_{31}$ has a positive or negative sign: normal hierarchy and inverted hierarchy. The colored bars represent the flavour content of the mass eigenstates [62].

any symmetry in the standard model, see the review of Ref. [63]. Indeed, there a number of experiments that investigate neutrino oscillations involving eV-scale sterile neutrino mass states.

In general, there are two possible types of neutrino oscillations measurements: appearance and disappearance measurements. In the first one, a neutrino of some weak flavour is produced, and a different neutrino type is observed at some distance from the neutrino source. In the second one, a known amount of neutrinos of some weak flavour type is produced, and a smaller amount of that same weak flavour type is observed after some distance. In 1996 the Liquid Scintillator Neutrino Detector (LSND) [64] experiment reported evidence for the appearance of $\bar{\nu}_e$ in a $\bar{\nu}_\mu$ beam produced via muon decay at rest. The short baseline of the LSND experiment, coupled with the relatively low neutrino energies ($\simeq$ 10-50 MeV) suggests that these oscillations are associated with a mass-splitting on the order of 1 eV^2 (corresponding to the ratio between the neutrino energy and the distance between the source and the detector). This mass splitting is difficult to reconcile with the atmospheric and solar neutrino oscillations which indicate a mass splitting more that two orders of magnitude smaller. Attempts to explain the solar and atmospheric neutrino oscillations and including as well the results from LSND typically rely on extensions to the standard model including models with additional sterile neutrino species. The LSND result has been tested by the MiniBooNE [65] experiment at Fermilab. Recent MiniBooNE an-

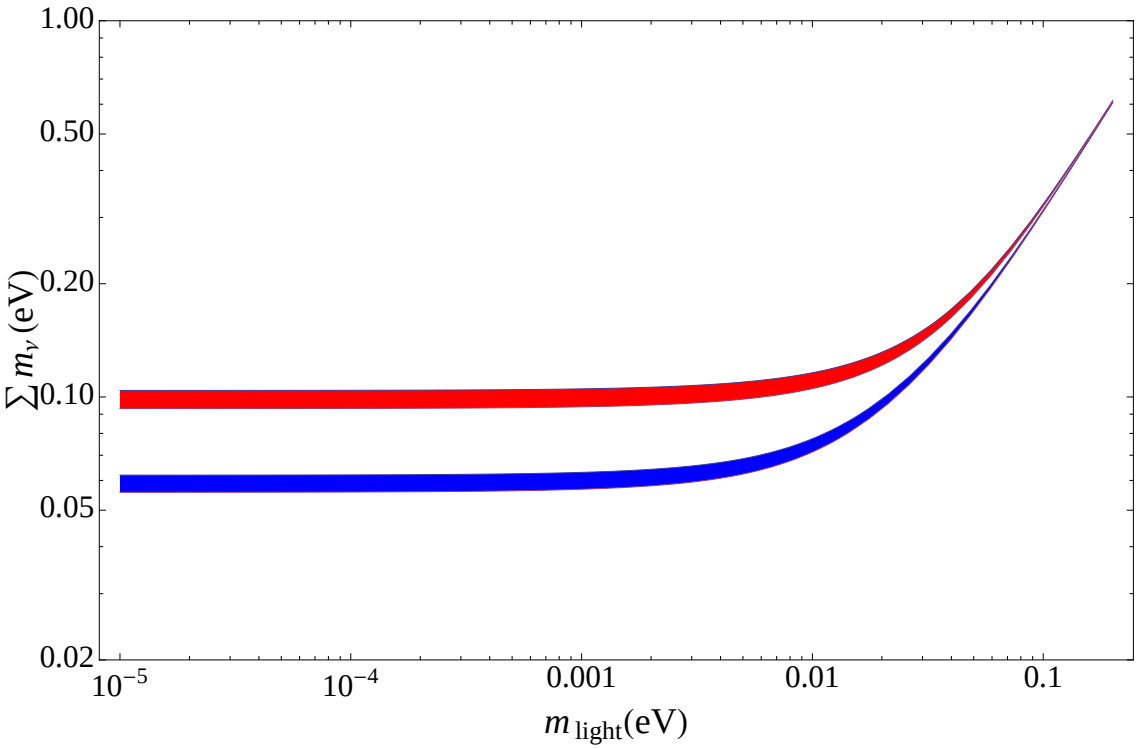

Figure 2.2: $\sum m_{\nu_i}$ as a function of the mass of the lightest neutrino for both hierarchies. The blue (red) curve shows the normal (inverted) hierarchy case.

tineutrino data has some overlap with the evidence for antineutrino oscillations from LSND. The neutrino mode running also shows an excess at low energy, but the energy distribution of the excess is marginally compatible with a simple two neutrino oscillation formalism [66]. Models with one additional ~ 1 eV massive sterile neutrino, i.e. the so called (3+1) models, were introduced to explain LSND short baseline (SBL) antineutrino data [64] by means of neutrino oscillations. A much better fit to SBL appearance data and, to a lesser extent, to disappearance data, is provided by models with two sterile neutrinos (3+2) [67, 68] or with three sterile neutrinos (3+3) [69]. While (3+1) and (3+2) models show some tension with BBN bounds on $N_\nu^{\rm eff}$, the extra sterile neutrinos do not necessarily have to feature thermal abundances at decoupling, and therefore, these models can be perfectly compatible with current cosmological data. In Chapters III and V we will explore the cosmological constraints on massive sterile neutrino scenarios.

2.3 Neutrino cosmological perturbations

Here we present the formalism describing the cosmological perturbations of neutrinos in the massless limit, as well as in the more realistic massive case.

2.3.1 The Boltzmann equation

The evolution of cosmological perturbations associated to relativistic particles, as neutrinos, is governed by the *Boltzmann equation*, which takes the form:

$$\frac{df}{dt} = C[f] \ , \tag{2.15}$$

where C denotes the eventual collision terms. In the absence of collisions, the distribution function obeys $df/dt = 0$.

The momentum of each individual neutrino can be labeled by P_i, which is the canonical conjugate of the comoving coordinate x^i. It differs from the proper momentum p_i measured by an observer at a fixed spacial coordinate by:

$$\begin{aligned} P_i &= a(\delta_{ij} + \tfrac{1}{2}h_{ij})p^j \ , \quad \text{in synchronous gauge,} \\ P_i &= a(1-\phi)p_i \ , \quad \text{in conformal Newtonian gauge.} \end{aligned} \tag{2.16}$$

The phase space distribution of the particles gives their number in a differential volume $dx^1dx^2dx^3dP_1dP_2dP_3$ in phase space:

$$f(x^i, P_j, \tau)dx^1dx^2dx^3dP_1dP_2dP_3 = dN \ . \tag{2.17}$$

The zero-th order phase space distribution is [8]:

$$f_0 = f_0(q) = \frac{g_s}{h^3}\frac{1}{e^{q/k_BT_0} \pm 1} \ , \tag{2.18}$$

in which + sign refers to the Fermi-Dirac distribution for fermions and − sign is the Bose-Einstein distribution for bosons. The factor g_s is the number of spin states and $T_0 = aT$ denotes the temperature of the particles today.

Usually, it is convenient to replace P_j with the comoving 3-momentum, $q_j = ap_j$, in order to eliminate the metric perturbation from the definition of the momenta and it is also possible to express q_j in terms of its magnitude and direction: $q_j = qn_j$, where $n^i n_i = \delta_{ij} n^i n^j = 1$. This allows us to replace $f(x^i, P_j, \tau)$ by $f(x^i, q, n_j, \tau)$ and write the perturbed phase space distribution as:

$$f(x^i, q, n_j, \tau) = f_0(q)[1 + \Psi(x^i, q, n_j, \tau)] \ , \tag{2.19}$$

where the function $\Psi \ll 1$ describe the perturbation to f_0.

The general expression for the stress-energy tensor computed in terms of the distribution function and the 4-momentum component is given by:

$$T_{\mu\nu} = \int dP_1 dP_2 dP_3 (-g)^{-1/2} \frac{P_\mu P_\nu}{P^0} f(x^i, P_j, \tau) \ , \tag{2.20}$$

in which g denotes the determinant of $g_{\mu\nu}$. In the synchronous gauge, we have $(-g)^{-1/2} = a^{-4}(1 - 1/2h)$ and $dP_1 dP_2 dP_3 = (1 - 1/2h)q^2 dq d\Omega$ up to linear order, where $h \equiv h_{ij}$ and $d\Omega$ is the solid angle associated with the direction n_i. In the conformal Newtonian gauge, $(-g)^{-1/2} = a^{-4}(1 - \psi + 3\phi)$ and $dP_1 dP_2 dP_3 = (1 - 3\phi)q^2 dq d\Omega$. Using the relations $\int d\Omega n_i n_j = 4\pi\delta_{ij}/3$ and $\int d\Omega n_i = \int d\Omega n_i n_j n_k = 0$, from eq. (2.20) it follows that, in both gauges, the form of energy-momentum tensor is [8]:

$$T_0^0 = -a^{-4} \int q^2 dq d\Omega \sqrt{q^2 + m^2 a^2} f_0(q)(1 + \Psi) \ , \tag{2.21}$$

$$T_i^0 = a^{-4} \int q^2 dq d\Omega q n_i f_0(q) \Psi \ , \tag{2.22}$$

$$T_j^i = a^{-4} \int q^2 dq d\Omega \frac{q^2 n_i n_j}{\sqrt{q^2 + m^2 a^2}} f_0(q)(1 + \Psi) \ , \tag{2.23}$$

to linear order in perturbation theory.

We can now write the Boltzmann equation, which describes the evolution of the phase space distribution, in terms of our variables (x^i, q, n_j, τ):

$$\frac{df}{dt} = \frac{\partial f}{\partial \tau} + \frac{dx^i}{d\tau}\frac{\partial f}{\partial x^i} + \frac{dq}{d\tau}\frac{\partial f}{\partial q} + \frac{dn_i}{d\tau}\frac{\partial f}{\partial n_i} = \left(\frac{\partial f}{\partial \tau}\right)_C \ . \tag{2.24}$$

The terms $\frac{dn_i}{d\tau}$ and $\frac{\partial f}{\partial n_i}$ are first-order quantities, thus the term $\frac{dn_i}{d\tau}\frac{\partial f}{\partial n_i}$ in the Boltzmann equation can be neglected to first order. Therefore the Boltzmann equation, in k space and in the two gauges, can be written as [8]:

Synchronous gauge:

$$\frac{d\Psi}{d\tau} + i\frac{q}{\epsilon}(\vec{k} \cdot \hat{n})\Psi + \frac{d\ln f_0}{d\ln q}\left[\dot{\eta} - \frac{\dot{h} + 6\dot{\eta}}{2}(\hat{k} \cdot \hat{n})^2\right] = \frac{1}{f_0}\left(\frac{\partial f}{\partial \tau}\right)_C \ , \tag{2.25}$$

Newtonian gauge:

$$\frac{d\Psi}{d\tau} + i\frac{q}{\epsilon}(\vec{k}\cdot\hat{n})\Psi + \frac{d\ln f_0}{d\ln q}\left[\dot{\phi} - i\frac{\epsilon}{q}(\vec{k}\cdot\hat{n})\psi\right] = \frac{1}{f_0}\left(\frac{\partial f}{\partial\tau}\right)_C \ . \tag{2.26}$$

2.3.2 Massless Neutrinos

The energy density and pressure for massless neutrinos are $\rho_\nu = 3p_\nu = -T^0_0 = T^i_i$. From eq. (2.23), the unperturbed energy density $\bar{\rho}_\nu$ and pressure $\bar{p}_\nu$ are given by:

$$\bar{\rho}_\nu = 3\bar{p}_\nu = a^{-4}\int q^2 dq d\Omega q f_0(q) \ , \tag{2.27}$$

and the perturbation in the energy density $\delta\rho_\nu$, in the pressure δp_ν, in the energy flux $\delta T^0_{\nu i}$ and in the shear stress $\Sigma^i_{\nu j} = T^i_{\nu j} - p_\nu\delta_{ij}$ are[8] :

$$\delta\rho_\nu = 3\delta p_\nu = a^{-4}\int q^2 dq d\Omega q f_0(q)\Psi \ , \tag{2.28}$$

$$\delta T^0_{\nu i} = a^{-4}\int q^2 dq d\Omega q n_i f_0(q)\Psi \ , \tag{2.29}$$

$$\Sigma^i_{\nu j} = a^{-4}\int q^2 dq d\Omega q (n_i n_j - \frac{1}{3}\delta_{ij}) f_0(q)\Psi \ . \tag{2.30}$$

For a massless neutrino $\epsilon = q$, simplifying the Boltzmann equation. To reduce the number of variables we can integrate out the q dependence in the neutrino distribution function and expand the angular dependence of the perturbation in a series of Legendre polynomials $P_l(\hat{k}\cdot\hat{n})$:

$$F_\nu(\vec{k},\hat{n},\tau) \equiv \frac{\int q^2 dq q f_0(q)\Psi}{q^2 dq q f_0(q)} \equiv \sum_{l=0}^{\infty}(-i)^l(2l+1)F_\nu(\vec{k},\tau)P_l(\hat{k}\cdot\hat{n}) \ . \tag{2.31}$$

In terms of $F_\nu(\vec{k},\hat{n},\tau)$, the perturbations δ_ν, θ_ν and Σ_ν can be written as:

$$\delta_\nu = \frac{1}{4\pi}\int d\Omega F_\nu(\vec{k},\hat{n},\tau) = F_{\nu 0} \ , \tag{2.32}$$

$$\theta_\nu = \frac{3i}{16\pi}\int d\Omega(\vec{k}\cdot\hat{n})F_\nu(\vec{k},\hat{n},\tau) = \frac{3}{4}kF_{\nu 1} \ , \tag{2.33}$$

$$\Sigma_\nu = -\frac{3}{16\pi}\int d\Omega\left[(\vec{k}\cdot\hat{n})^2 - \frac{1}{3}\right]F_\nu(\vec{k},\hat{n},\tau) = \frac{1}{2}F_{\nu 2} \ . \tag{2.34}$$

Integrating the equations (2.25) and (2.26) over $q^2 dq q f_0(q)$ and dividing them by $\int q^2 dq q f_0(q)$, the Boltzmann equations for massless neutrino in the two gauges becomes [8]:

Synchronous gauge

$$\frac{\partial F_\nu}{\partial \tau} + ik\mu F_\nu = -\frac{2}{3}\dot{h} - \frac{4}{3}(\dot{h} + 6\dot{\eta})P_2(\mu) \ , \tag{2.35}$$

Newtonian gauge

$$\frac{\partial F_\nu}{\partial \tau} + ik\mu F_\nu = 4(\dot{\phi} - ik\mu\psi) \ , \tag{2.36}$$

where $\mu \equiv \hat{k} \cdot \hat{n}$ and $P_{\mu 2} = 1/2(3\mu^2 - 1)$ is the Legendre polynomial of degree 2. Using the Legendre expansion for F, together with the orthonormality property of the Legendre polynomials and the recursion relation $(l+1)P_{l+1}(\mu) = (2l+1)\mu P_l(\mu) - lP_{l-1}(\mu)$, we obtain:

Synchronous gauge:

$$\dot{\delta}_\nu = -\frac{4}{3}\theta_\nu - \frac{2}{3}\dot{h} \ , \tag{2.37a}$$

$$\dot{\theta}_\nu = k^2\left(\frac{1}{4}\delta_\nu - \sigma_\nu\right) \ , \tag{2.37b}$$

$$\dot{F}_{\nu 2} = 2\dot{\sigma}_\nu = \frac{8}{15}\theta_\nu - \frac{3}{5}kF_{\nu 3} + \frac{4}{5}\dot{h} + \frac{8}{5}\dot{\eta} \ , \tag{2.37c}$$

$$\dot{F}_{\nu l} = \frac{k}{2l+1}[lF_{\nu(l-1)} - (l+1)F_{\nu(l+1)}] \ , l \geq 3 \ . \tag{2.37d}$$

Newtonian gauge:

$$\dot{\delta}_\nu = -\frac{4}{3}\theta_\nu + 4\dot{\phi} \ , \tag{2.38a}$$

$$\dot{\theta}_\nu = k^2\left(\frac{1}{4}\delta_\nu - \sigma_\nu\right) + k^2\psi \ , \tag{2.38b}$$

$$\dot{F}_{\nu l} = \frac{k}{2l+1}[lF_{\nu(l-1)} - (l+1)F_{\nu(l+1)}] \ , l \geq 3 \ . \tag{2.38c}$$

These equations govern the evolution of the phase space distribution of massless neutrinos. Later in this Chapter we shall see how these equations change in the case of a general dark radiation fluid.

2.3.3 Massive Neutrinos

Massive neutrinos also obey the collisionless Bolztmann equations. However, their distribution function is complicated by the fact that they have a non zero mass. From eq. (2.23),

the unperturbed energy density and pressure for massive neutrinos are given by [8]:

$$\bar{\rho}_\nu = a^{-4}\int q^2 dq d\Omega \epsilon f_0(q) \ , \tag{2.39}$$

$$\bar{p}_\nu = \frac{1}{3}a^{-4}\int q^2 dq d\Omega \frac{q^2}{\epsilon} f_0(q) \ , \tag{2.40}$$

where $\epsilon = \sqrt{q^2 + m_\nu^2 a^2}$.

The perturbations are:

$$\delta\rho_\nu = a^{-4}\int q^2 dq d\Omega \epsilon f_0(q)\Psi \ , \tag{2.41}$$

$$\delta p_\nu = \frac{1}{3}a^{-4}\int q^2 dq d\Omega \frac{q^2}{\epsilon} f_0(q)\Psi \ , \tag{2.42}$$

$$\delta T^0_{\nu i} = a^{-4}\int q^2 dq d\Omega q n_i f_0(q)\Psi \ , \tag{2.43}$$

$$\Sigma^i_{\nu j} = a^{-4}\int q^2 dq d\Omega \frac{q^2}{\epsilon}(n_i n_j - \frac{1}{3}\delta_{ij}) f_0(q)\Psi \ . \tag{2.44}$$

In this case we cannot integrate out the q dependence in the distribution function, as we did for the massless neutrinos, because $\epsilon(q,\tau)$ depends on the momentum and time. However, it is possible to expand the perturbation Ψ in multipoles space:

$$\Psi(\vec{k},\hat{n},q,\tau) = \sum_{l=0}^{\infty}(-i)^l(2l+1)\Psi_l((\vec{k},q,\tau)P_l(\hat{k}\cdot\hat{n}) \ . \tag{2.45}$$

Therefore the perturbed energy density, pressure, energy flux and shear stress in k-space become:

$$\delta\rho_\nu = 4\pi a^{-4}\int q^2 dq \epsilon f_0(q)\Psi_0 \ , \tag{2.46}$$

$$\delta p_\nu = \frac{4\pi}{3}a^{-4}\int q^2 dq \frac{q^2}{\epsilon} f_0(q)\Psi_0 \ , \tag{2.47}$$

$$(\bar{\rho}_\nu + \bar{p}_\nu)\theta_\nu = 4\pi k a^{-4}\int q^2 dq q f_0(q)\Psi_1 \ , \tag{2.48}$$

$$(\bar{\rho}_\nu + \bar{p}_\nu)\sigma_\nu = \frac{8\pi}{3}a^{-4}\int q^2 dq \frac{q^2}{\epsilon} f_0(q)\Psi_2 \ . \tag{2.49}$$

Following the same strategy used for massless neutrinos, we can obtain the Boltzmann equations for massive neutrinos in the two gauges:

Synchronous gauge:

$$\dot{\Psi}_0 = -\frac{qk}{\epsilon}\Psi_1 - \frac{1}{6}\dot{h}\frac{d\ln f_0}{d\ln q} \ , \tag{2.50a}$$

$$\dot{\Psi}_1 = \frac{qk}{3\epsilon}(\Psi_0 - 2\Psi 2) \ , \tag{2.50b}$$

$$\dot{\Psi}_2 = \frac{qk}{5\epsilon}(2\Psi_1 - 3\Psi_3) - \left(\frac{1}{15}\dot{h} + \frac{2}{5}\dot{\eta}\right)\frac{d\ln f_0}{d\ln q}, \tag{2.50c}$$

$$\dot{\Psi}_l = \frac{qk}{(2l+1)\epsilon}[l\Psi_{(l-1)} - (l+1)\Psi_{(l+1)}] \ , l \geq 3 \ . \tag{2.50d}$$

Newtonian gauge:

$$\dot{\Psi}_0 = -\frac{qk}{\epsilon}\Psi_1 - \dot{\phi}\frac{d\ln f_0}{d\ln q} \ , \tag{2.51a}$$

$$\dot{\Psi}_1 = \frac{qk}{3\epsilon}(\Psi_0 - 2\Psi 2) - \frac{\epsilon k}{3q}\Psi\frac{d\ln f_0}{d\ln q} \ , \tag{2.51b}$$

$$\dot{\Psi}_l = \frac{qk}{(2l+1)\epsilon}[l\Psi_{(l-1)} - (l+1)\Psi_{(l+1)}] \ , l \geq 2 \ . \tag{2.51c}$$

Because of the q dependence, the integration of these equations is computationally expensive.

2.4 Dark radiation models

One of the major theoretical predictions of standard cosmology is the existence of a relativisitc energy component (Cosmic Neutrino Background, CNB), besides CMB photons, whose energy density is given by eq. (2.7). The cosmological abundance of relativistic particles as active or steriles neutrinos or any other light particle is parametrized in terms of the effective number of relativistic degrees of freedom $N_{\rm eff}$. As we have seen in section 2.1, the expected value of $N_{\rm eff}$ is 3.046, which corresponds to the standard case of the three active neutrino species.

In recent years, cosmological data seem to suggest values for $N_{\rm eff}$ higher than the standard one. Measurements of CMB anisotropies from WMAP combined with ACT, SPT, BAO and HST data sets have provided the constraint $N_{\rm eff} = 3.84 \pm 0.40$ [18]; more recently, Planck data combined with WMAP polarization, high-ℓ CMB data and BAO have reported the bound $N_{\rm eff} = 3.30^{+0.54}_{-0.51}$ at 95% CL [9].

A larger value for $N_{\rm eff}$ could arise from new physics, not only related to sterile neutrinos, as is the case of axions [70, 71], decaying of non-relativistic matter models [72], gravity waves [73], extra dimension [74, 75, 76], dark energy [77] or asymmetric dark matter models [78]. Information on the dark relativistic background can be obtained not only from its effects on the expansion rate of the universe but also from its clustering properties. For example,

if dark radiation is made of massless neutrinos it should behave as relativistic particles also from the point of view of perturbation theory. Therefore, following [79] and considering the set of equations that describes perturbations in the massless neutrino case (2.37), one can derive:

$$\dot{\delta}_{dr} = \frac{\dot{a}}{a}(1-3c^2_{\rm eff})\left(\delta_{dr}+4\frac{\dot{a}}{a}\frac{\theta_{dr}}{k^2}\right)-\frac{4}{3}\theta_{dr}-\frac{2}{3}\dot{h}\ , \tag{2.52}$$

$$\dot{\theta}_{dr} = 3k^2c^2_{\rm eff}\left(\frac{\delta_{dr}}{4}+\frac{\dot{a}}{a}\frac{\theta_{dr}}{k^2}\right)-\frac{\dot{a}}{a}\theta_{dr}-\frac{1}{2}k^2\pi_{dr}\ , \tag{2.53}$$

$$\dot{\pi}_{dr} = \frac{8}{5}c^2_{\rm vis}\left(\frac{\theta_{dr}}{k}+\sigma\right)-\frac{3}{5}kF_{dr,3}\ , \tag{2.54}$$

$$\dot{F}_{dr,l} = \frac{k}{2l+1}[lF_{dr,(l-1)}-(l+1)F_{dr,(l+1)}]\ , l\geq 3\ . \tag{2.55}$$

in which $c^2_{\rm eff}$ is the effective sound of speed that describes pressure fluctuations, $c^2_{\rm vis}$ is the viscosity parameter, π_{dr} is the anisotropic stress perturbation, and σ is the metric shear defined as $\sigma=(\dot{h}+6\dot{\eta})/(2k)$, with h and η the scalar metric perturbations in the synchronous gauge. The relationship between metric shear and anisotropic stress is parametrized through the viscosity parameter, $c^2_{\rm vis}$:

$$\dot{\pi}_{dr}=-3\frac{\dot{a}}{a}\pi_{dr}+4c^2_{\rm vis}(\theta_{dr}+\sigma). \tag{2.56}$$

The physical interpretation of this equation is that the anisotropic stress will act to damp out velocity fluctuations on shear-free frames if $c^2_{\rm vis}>0$. In other words the viscosity parameter controls the relationship between velocity/metric shear and anisotropic stresses in the neutrino background.

For standard neutrinos, we have $c^2_{\rm eff}=c^2_{\rm vis}=1/3$. This value for $c^2_{\rm vis}$ means that free streaming of relativistic neutrinos produces anisotropies in the neutrino background; if $c^2_{\rm vis}=0$, we have the case of a perfect fluid without anisotropic stress, with only density and pressure perturbations.

2.4.1 Interacting dark matter dark radiation scenarios

Interacting dark radiation arises naturally in the so-called asymmetric dark matter models (see Ref. [80]) , in which the dark matter production mechanism is similar and related to the one in the baryonic sector. In these models, there exists a particle-antiparticle asymmetry at high temperatures in the dark matter sector. The thermally symmetric dark matter component will annihilate and decay into dark radiation degrees of freedom. Since the dark radiation and the dark matter fluids are interacting, there was an epoch in the early universe in which these two dark fluids were strongly coupled. This results in a tightly coupled fluid with a pressure producing oscillations in the matter power spectrum analogous to the acoustic oscillations in the photon-baryon fluid before the recombination era. Due to the presence of a dark radiation-dark matter interaction, the clustering properties of the

dark radiation component can be modified. In other words, if dark radiation is made of interacting particles, the values of the clustering parameters $c^2_{\rm eff}$ and $c^2_{\rm vis}$ may differ from the canonical $c^2_{\rm eff} = c^2_{\rm vis} = 1/3$.

The dark matter component behaves as a non-relativistic fluid described, in the uncoupled case, by the equations (1.53) with $\delta p/\delta\rho = w = 0$ and metric shear $\sigma = 0$. The dark radiation component is described by the equations (2.52) and (2.53). In the presence of a dark radiation-dark matter interaction, the modified Euler equations for these two fluids read:

$$\dot{\theta}_{dm} = -\frac{\dot{a}}{a}\theta_{dm} + \frac{4\rho_{dr}}{3\rho_{dm}} a n_{dm}\sigma_{dm-dr}(\theta_{dr} - \theta_{dm}) \ , \tag{2.57}$$

$$\dot{\theta}_{dr} = \frac{1}{4}k^2(\delta_{dr} - 2\pi_{dr}) + a n_{dm}\sigma_{dm-dr}(\theta_{dm} - \theta_{dr}) \ , \tag{2.58}$$

in which we have considered the standard value of $c^2_{\rm eff}$ for brevity. The term $a n_{dm}\sigma_{dm-dr}(\theta_{dm} - \theta_{dr})$ in eq. (2.58) represents the momentum transferred to the dark radiation component and the quantity $a n_{dm}\sigma_{dm-dr}$ is the differential opacity which gives the scattering rate of dark radiation by dark matter.

The complete Euler equation for dark radiation, including the interaction term with dark matter, reads:

$$\dot{\theta}_{dr} = 3k^2 c^2_{\rm eff}\left(\frac{1}{4}\delta_{dr} - \frac{\dot{a}}{a}\frac{\theta_{dr}}{k^2}\right) - \frac{\dot{a}}{a}\theta_{dr} - \frac{1}{2}k^2\pi_{dr} + a n_{dm}\sigma_{dm-dr}(\theta_{dm} - \theta_{dr}) \ . \tag{2.59}$$

It is convenient [81] to parametrize the coupling between dark radiation and dark matter through a cross section given by:

$$\langle\sigma_{dm-dr}|v|\rangle \sim Q_0\, m_{dm} \ , \tag{2.60}$$

if it is constant, or

$$\langle\sigma_{dm-dr}|v|\rangle \sim \frac{Q_2}{a^2}\, m_{dm} \ , \tag{2.61}$$

if it is proportional to T^2, where the parameters Q_0 and Q_2 are constants in cm^2 MeV^{-1} units. It has been shown in Ref. [78] that the cosmological implications of both constant and T-dependent interacting cross sections are very similar. In Chapter VI we will present the cosmological constraints on interacting dark radiation schemes assuming a constant interaction rate.

In the next section we will explain the impact of dark radiation species on the CMB and on Large Scale Structure measurements.

2.5 Neutrino properties and cosmological observations

2.5.1 Standard cosmology plus three massive neutrinos

Cosmology can provide strong bounds for the sum of the neutrino masses. This is because neutrinos play a relevant role in large-scale structure formation and leave key signatures in

several cosmological data sets.

If a fraction of the dark matter is made up of neutrinos ($\Omega_{\rm m} = \Omega_{\rm b} + \Omega_{\rm DM} = \Omega_{\rm b} + \Omega_{\rm CDM} + \Omega_\nu$), they modify the evolution of matter perturbations. In particular, once the CDM perturbations enter into the matter dominated era, neutrinos will slow down the rate at which these perturbations grow. In order to understand this effect, we use eq. (1.63) to compute the linear growth of CDM perturbations in a universe containing massive neutrinos. The difference with the equation governing the evolution of CDM perturbations in a neutrinoless universe is that neutrinos affect the expansion rate:

$$H^2 = \frac{8\pi G}{3}(\bar{\rho}_{CDM} + \bar{\rho}_\nu + \bar{\rho}_b) \ . \tag{2.62}$$

Let us assume that neutrinos are non-relativistic at some epoch of the matter dominated era and we introduce the parameter:

$$f_\nu = \frac{\bar{\rho}_\nu}{(\bar{\rho}_{CDM} + \bar{\rho}_b + \bar{\rho}_\nu)} = \frac{\Omega_\nu}{\Omega_{\rm m}} \ , \tag{2.63}$$

whose value remains approximately constant because the neutrino energy density will scale as $\bar{\rho}_\nu \propto a^{-3}$. Then, the scale factor still evolves like τ^2 and the equation of evolution reads as[1]:

$$\ddot{\delta}_{CDM} + \frac{2}{\tau}\dot{\delta}_{CDM} - \frac{6}{\tau^2}(1 - f_\nu)\delta_{\rm CDM} = 0 \ , \tag{2.64}$$

whose solutions are $\delta_{\rm CDM} = A\tau^{\alpha_+} + B\tau^{\alpha_-}$, with:

$$\alpha_\pm = \frac{-1 \pm \sqrt{1 + 24(1 - f_\nu)}}{4} \ . \tag{2.65}$$

Therefore, in the matter dominated era, the growth of CDM perturbations is suppressed by the presence of massive neutrinos as:

$$D_1(a) \simeq a^{1-(3/5)f_\nu} \ . \tag{2.66}$$

The growth of CDM perturbations is reduced due the fact that one of the component in the universe contributes to the homogeneous expansion rate but not to the gravitational clustering.

In Fig. 2.3 we plot the linear power spectrum, computed with CAMB [82], for a massless neutrino universe using the best fit parameters from Planck measurements, [9], (red line). We also plot the linear power spectrum of different cosmological models with three degenerate massive neutrinos.

Notice that neutrinos suppress the power on spatial scales below the free streaming scale when they become non relativistic (we will carefully explain this effect in Chapter IV). The redshift at which neutrinos become non relativistic reads

$$1 + z_{\rm nr} \simeq 1890 \left(\frac{m_\nu}{1\ {\rm eV}}\right) \ , \tag{2.67}$$

[1]This equation refers to spatial scales smaller than the neutrino free streaming scale.

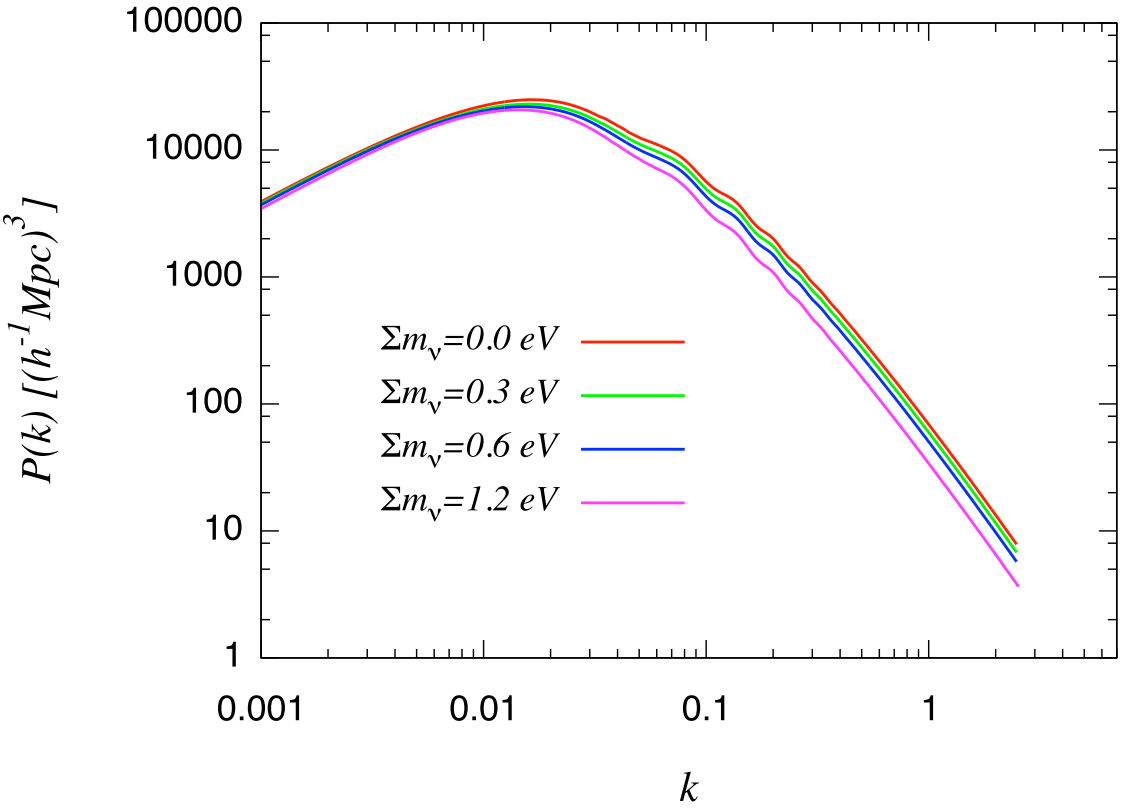

Figure 2.3: Linear power spectrum for three cosmological models with three degenerate massive neutrinos and for one with massless neutrinos. The red line depicts the matter power spectrum $P(k)$ for the best fit parameters for a ΛCDM model with massless neutrinos from the Planck data set. Neutrino free-streaming produces a decrease in the amplitude of the power spectrum on small scales.

while the wavenumber associated to the free streaming scale is given by

$$k_{\rm fs} \simeq \frac{0.677}{(1+z)^{1/2}} \left(\frac{m_\nu}{1\ {\rm eV}}\right) \Omega_m^{1/2} h{\rm Mpc}^{-1} \ , \tag{2.68}$$

being m_ν the neutrino mass, and Ω_m the total matter component, see the Appendix of [83] for more details.

This suppression comes from the two effects. The first one is that neutrinos modify the matter radiation equality. This time represents the epoch when the contribution of radiation to the total energy content of the universe equals the contribution from matter and is given by:

$$a_{\rm eq} = \frac{\Omega_{\rm r}}{\Omega_{\rm b} + \Omega_{\rm CDM}} \tag{2.69}$$

with $\Omega_{\rm r}$ taking contributions from both photons and neutrinos. Since both cosmological models, with massive or massless neutrinos, make the same contribution to $\Omega_{\rm r}$ at this epoch (at the time of matter-radiation equality, neutrinos of masses $\sum m_\nu \lesssim 1$ eV are relativistic, so they contribute to the energy density as radiation instead of as matter), the decrease in $\Omega_{\rm CDM}$, which is due to massive neutrinos, modifies the matter radiation equality time by a factor $(1-f_\nu)^{-1}$:

$$a_{\rm eq}^{f_\nu} = a_{\rm eq}^{f_\nu=0}(1-f_\nu)^{-1} \ . \tag{2.70}$$

Given that perturbations do not grow as fast in the radiation dominated era as in the matter dominated era, we expect that structures would be less evolved in the case with massive neutrinos, i.e. the power spectrum on small scales should be suppressed. As we have explained above, the second one effect is due to the fact that neutrinos slow down the rate at which CDM perturbations grow, eq. (2.66). This effect produces a suppression in the matter power spectrum on small scales. On very small scales, the suppression caused by neutrinos can be estimated to be (see Ref. [84])

$$\frac{P(k)^{f_\nu}}{P(k)^{f_\nu=0}} = (1-f_\nu)^3 [1.9\times 10^5 g(a_0)\Omega_m h^2 f_\nu/N_\nu]^{-(6/5)f_\nu} \ , \tag{2.71}$$

with $g(a_0)$ a function, evaluated today, that accounts for the change in the growth factor due to the presence of a cosmological constant. For values of $f_\nu < 0.07$ the above expression can be approximated by the well known formula [85]:

$$\frac{P(k)^{f_\nu} - P(k)^{f_\nu=0}}{P(k)^{f_\nu=0}} = \frac{\triangle P}{P} \cong -8 f_\nu \ . \tag{2.72}$$

For a model with three degenerate massive neutrinos, we have that for $f_\nu \leq 0.1$, neutrino species are still relativistic at the time of decoupling, and the direct effect of free-streaming neutrinos on the evolution of photon-baryon acoustic oscillations is the same for both cases with massive and massless neutrinos. The main effect in the CMB anisotropy spectrum is due the *Early Integrated Sachs Wolfe effect*. In a matter-dominated universe with zero

mean curvature, gravitational potentials remain constant to first order in linear perturbation theory. Adding components that do not cluster, while keeping the curvature fixed to zero, increases the expansion rate which causes the gravitational potentials to decay. As photons traverse these decaying potentials, new anisotropies are created by the so-called Integrated Sachs-Wolfe (ISW). The ISW anisotropy is generated in the CDM model both at early times, as photons free stream after decoupling (the early ISW) and at late times after the cosmological constant becomes important (the late ISW) [19]. The transition from the relativistic to the non relativistic neutrino regime will affect the decays of the gravitational potentials at the decoupling period. This produces an enhancement of small-scale perturbations, especially near the first acoustic peak. Since neutrinos are still relativistic at decoupling they sould be counted as radiation instead of matter around the time of equality. Therefore, when f_ν increases, $a_{\rm eq}$ increases proportionally to $(1-f_\nu)^{-1}$ and the equality is postponed. When this occurs the time of equality increases slightly the size of the sound horizon at recombination (that is, the integral of $c_s dt a(t)$ between 0 and $\tau_{\rm rec}$) and the acoustic peaks are shifted to the left, towards smaller multipoles. At last, massive neutrinos suppress the lensing power. We can see these effects in Fig. 2.4 in which we plot the CMB temperature anisotropy spectrum for three different models.

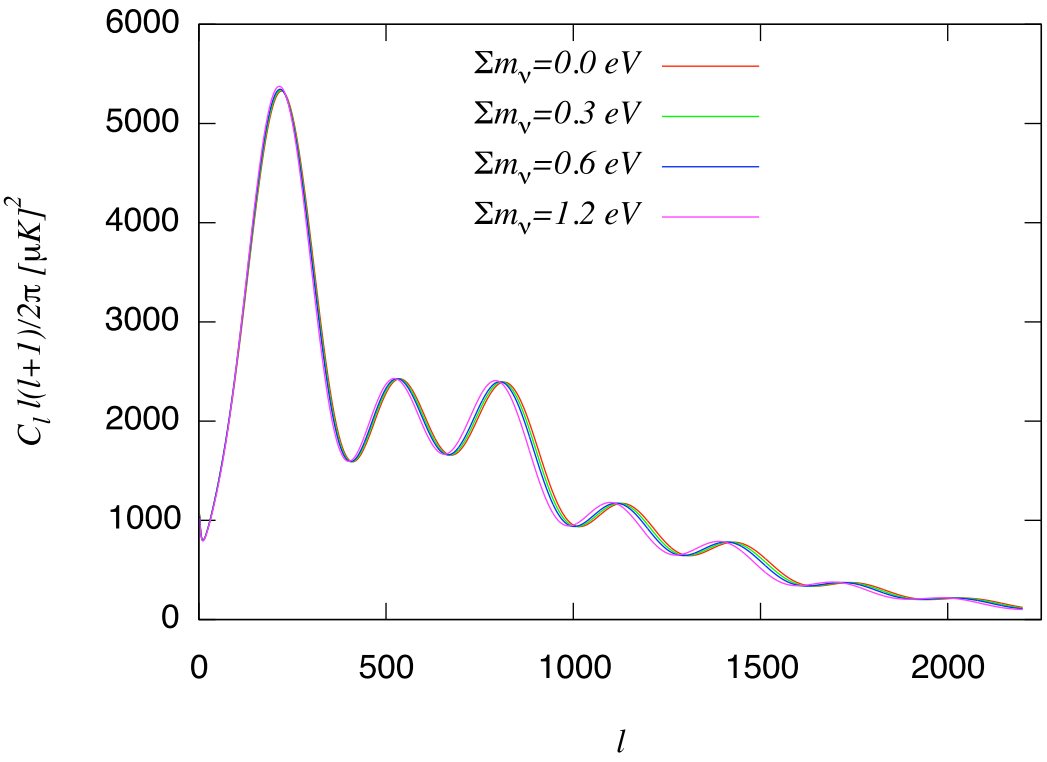

Figure 2.4: CMB temperature anisotropy spectrum C_ℓ for four models: the massless neutrino ΛCDM model (red line), and three models with three massive degenerate neutrinos. We consider the best fit parameters for a ΛCDM model from Planck measurements.

If neutrinos were heavier than a few eV, they would be already non-relativistic at decoupling. This case would require a more complicated description that would affect the photon-baryon fluid. However, we will see in this thesis that this situation is highly disfavoured by current cosmological data.

Since the two-dimensional (2D) power spectrum of galaxies is related to 3D matter power spectrum $P(k)$, eq. (1.105), in the presence of massive neutrinos, also the angular power spectrum is suppressed at any redshift and this suppression could be partially compensated by increasing the cold dark matter energy density. In Fig. 2.5 we illustrate this effect for four models with different values of $\sum m_\nu$.

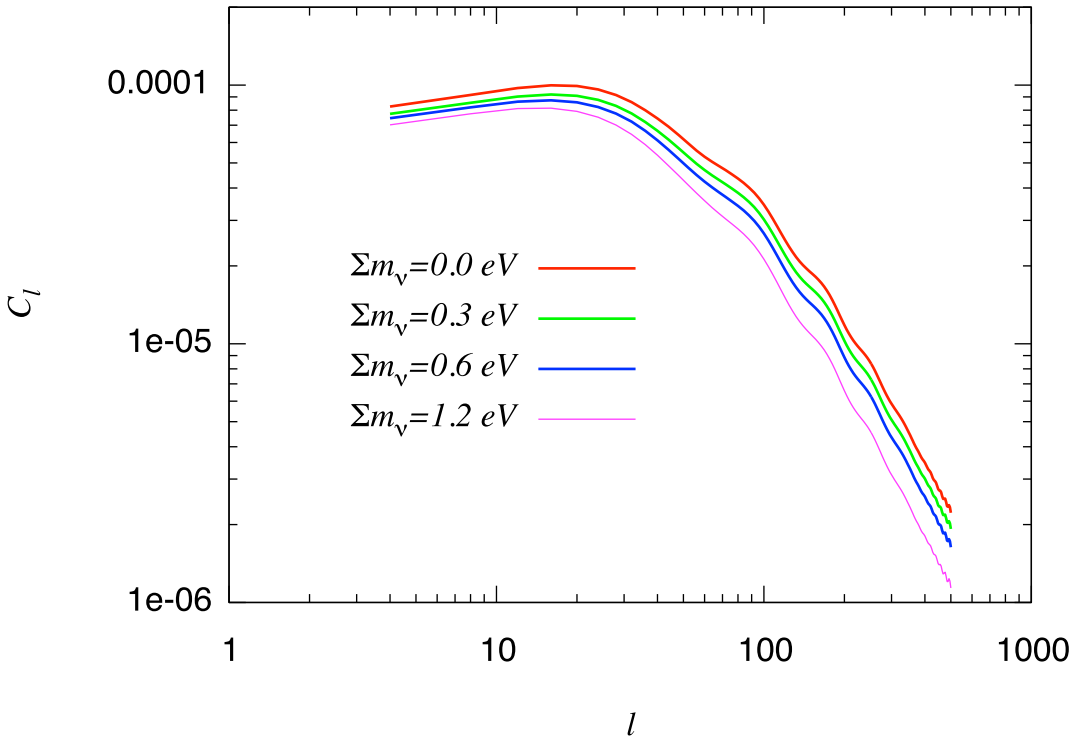

Figure 2.5: Effect of neutrinos on the matter angular power spectra, C_ℓ, for the best fit parameters for a ΛCDM model from the Planck data. We consider four cases with different values of $\sum m_\nu$. The data correspond to the observed power spectrum obtained from BOSS DR8 in the redshift bin $0.45< z <0.5$ [40]. The red line depicts 2D spectra for a ΛCDM model assuming no massive neutrino species.

The impact of massive neutrinos on the C_ℓ power spectra will be carefully analysed in Sec. IV.

Measurements of all of these observables have been used to place new bounds on neutrino physics from cosmology, setting an upper limit on the neutrino mass below ~ 0.5 eV. Recent

results from the Planck experiment combined with WMAP polarization, high-ℓ CMB data and BAO measurements provide an upper limit on the sum of the masses of neutrinos of $\sum m_\nu < 0.23$ eV [9].

Additional sterile neutrino species will have the same impact in the cosmological observables with the difference that, in this case, $N_{\rm eff}$ is also modified. We will explain the impact of $N_{\rm eff}$ on the different cosmological observables in the next section. Models with additional sterile neutrino species will be fully examined in Chapters III and V.

2.5.2 Dark radiation

As previously stated, the effective number of neutrinos is $N_{\rm eff} = 3.046$ in which we take into account some corrections due to non instantaneous neutrino decoupling. A larger value of $N_{\rm eff}$ would imply the existence of an extra relativistic component.

To illustrate the effects of $N_{\rm eff}$ on the CMB, we plot the CMB power spectra for several values of $N_{\rm eff}$ in Fig. 2.6, considering the best fit parameters from the Planck data set [9] . From Fig. 2.6 we can see that increasing the value of $N_{\rm eff}$, the height of the first peak is enhanced and the positions of acoustic peaks are shifted to higher multipoles. Also, the amplitude on small scales (higher multipoles) is suppressed.

This occurs because one of the main effects of $N_{\rm eff}$ on the CMB temperature anisotropies arises from the change of the epoch of the radiation-matter equality. By increasing (decreasing) the value of $N_{\rm eff}$, the radiation-matter equality occurs later (earlier). Thus the increase (decrease) of $N_{\rm eff}$ gives an almost the same effect of the decrease (increase) of energy density of matter. This leads to an enhancement of the height of the first peak due to the early integrated Sachs-Wolfe (ISW) effect in which fluctuations of the corresponding scale, having crossed the sound horizon in the radiation-dominated epoch, are boosted by the decay of the gravitational potential [86] . Thus a larger amount of relativistic species drives the first peak higher. Another effect is the shift of the position of acoustic peaks due to the change of the radiation-matter equality through the changes of $N_{\rm eff}$. This position is given by the acoustic scale θ_A, which reads:

$$\theta_A = \frac{r_s(z_{rec})}{r_\theta(z_{rec})} \ , \tag{2.73}$$

where $r_\theta(z_{rec})$ and $r_s(z_{rec})$ are the comoving angular diameter distance to the last scattering surface and the sound horizon at the recombination epoch z_{rec}, respectively. Although $r_\theta(z_{rec})$ almost remains the same for different values of $N_{\rm eff}$, $r_s(z_{rec})$ becomes smaller when $N_{\rm eff}$ is increased. Therefore, the positions of acoustic peaks are shifted to higher multipoles (smaller angular scales) if the value of $N_{\rm eff}$ is increased. Furthermore, since the position of the n-th peak can be written as $\ell_n \sim n\pi/\theta_A$, separations of the peaks become also greater for larger $N_{\rm eff}$. However, this effect can be compensated by changing the cold dark matter density, in such a way that z_{rec} remains fixed, see ref [87]. Therefore, due to the degeneracy with the cold dark matter component, the change induced at low ℓ is negligible and the largest impact of $N_{\rm eff}$ on the CMB temperature anisotropies comes from its effect on high

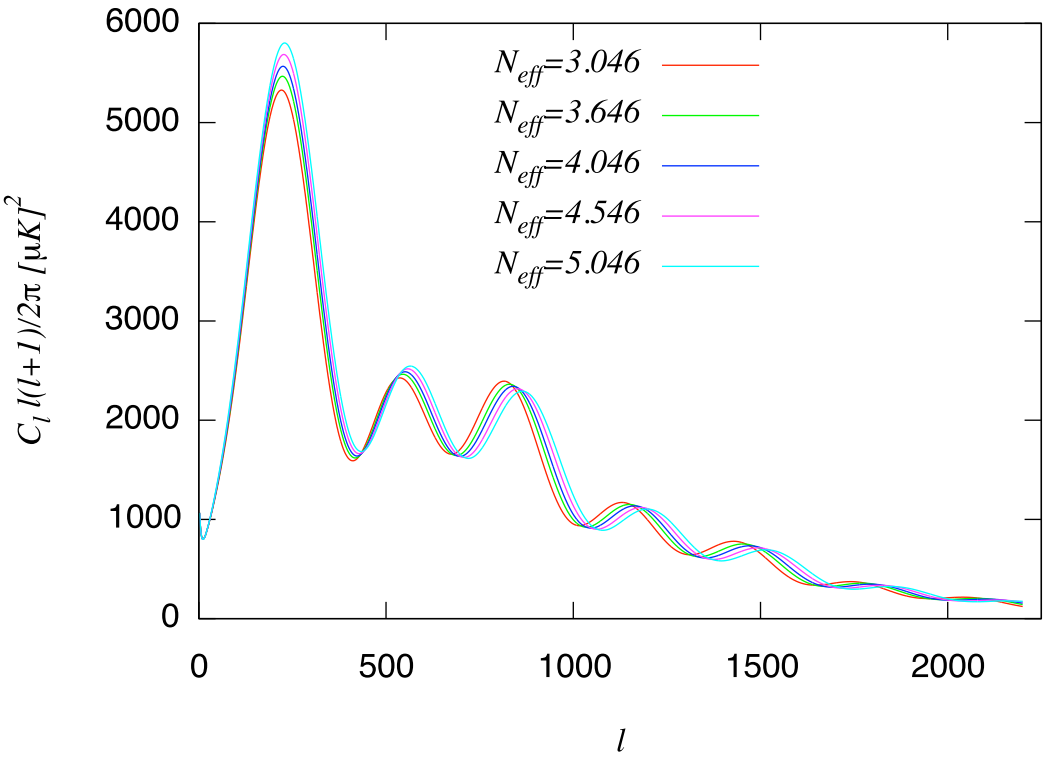

Figure 2.6: CMB temperature power spectrum C_ℓ for five models with a different value of $N_{\rm eff}$ considering the best fit parameters for a ΛCDM model from the Planck data. The red line depicts the standard case with $N_{\rm eff} = 3.046$. An increase of $N_{\rm eff}$ leads to an enhancement of the first peak and a shift of the acoustic peaks towards higher multipoles.

multipoles ℓ, since a higher value of $N_{\rm eff}$ will induce a drop in power at small scales due to an increased Silk damping. Silk damping refers to the suppression in power of the CMB temperature anisotropies on scales smaller than the photon diffusion length.

An increase of the effective number of neutrino $N_{\rm eff}$ also produces a suppression in the matter power spectrum due to the change in the epoch of matter-radiation equality.

A change in the effective sound speed $c^2_{\rm eff}$ and in the viscosity parameter $c^2_{\rm vis}$ affects both the CMB spectrum and the matter power spectrum.

Varying $c^2_{\rm vis}$ modifies the ability of the dark radiation to free-stream out of the potential wells. In particular, lowering $c^2_{\rm vis}$ to the value $c^2_{\rm vis} = 0$, the TT power spectrum is enhanced with respect to the standard case. This situation can be explained, roughly, as the dark radiation component becoming a perfect fluid. That is, we are dealing with a single fluid characterized by an effective viscosity. Disregarding the fluid nature and the physical origin of the viscosity, the general consideration holds: for a given perturbation induced in the fluid, the amplitude of the oscillations that the viscosity produces increases as the viscosity

is reduced. Therefore, lowering $c^2_{\rm vis}$ diminishes the amount of damping induced by the dark radiation viscosity, and, consequently, the amplitude of the CMB oscillations will increase, increasing in turn the amplitude of the angular power spectrum.

On the other hand, a change of $c^2_{\rm eff}$ implies a decrease of pressure perturbations for the dark radiation components in its rest frame. In particular, a decrease in $c^2_{\rm eff}$ from its canonical $1/3$ to the value $c^2_{\rm eff} = 0$ leads to a damping of the CMB peaks, since dark radiation is behaving as a pressureless fluid from the perturbation perspective. Thus as $c^2_{\rm eff}$ decreases, the height of the acoustic peaks decreases.

While varying the viscosity parameter $c^2_{\rm vis}$, the matter power barely change, a change in $c^2_{\rm eff}$ changes dramatically. For instance, if $c^2_{\rm eff} = 0$, dark radiation is a pressureless fluid which behaves as dark matter, inducing an enhancement of the matter fluctuations.

These perturbation parameters can be constrained through measurements of the CMB anisotropies since dark radiation is coupled through gravity with all the remaining components. This opens a new window for testing the dark radiation component, since, for example, a smaller value for $c^2_{\rm vis}$ could indicate possible non standard interactions. Constraints on these parameters have been obtained by several authors, since the observation of deviations from the standard values could hint for non-standard physics. The most recent constraints for $c^2_{\rm eff}$ and $c^2_{\rm vis}$ have been obtained combining current Planck data with WMAP low-ℓ measurements for polarization plus BAO and HST data sets: $c^2_{\rm eff} = 0.306 \pm 0.013$ and $c^2_{\rm vis} = 0.53 \pm 0.16$ [88].

In Chapter V, we will present bounds from recent cosmological data on the dark radiation parameters $N_{\rm eff}$, $c^2_{\rm eff}$ and $c^2_{\rm vis}$ extending the ΛCDM cosmological model and analyzing the correlations among the dark radiation parameters and the remaining cosmological parameters, as the dark energy equation of state or the scalar spectral index. In Chapter VI, we will explore the bounds on $N_{\rm eff}$,$c^2_{\rm eff}$ and $c^2_{\rm vis}$ considering a ΛCDM cosmology plus a dark radiation-dark matter interaction.

Part II

Scientific Research

Chapter 3

Constraints on massive sterile neutrino species from current and future cosmological data

In this Chapter we study a flat ΛCDM scenario with $N_{\rm eff}$ active plus sterile massive neutrino species, in order to test the so-called (3+2) model with cosmological data. This Chapter is a copy of the paper:

Constraints on massive sterile neutrino species from current and future cosmological data, Elena Giusarma, Martina Corsi, Maria Archidiacono, Roland De Putter, Alessandro Melchiorri, Olga Mena & Stefania Pandolfi, 2011, Physical Review D83, 115023.

3.1 Introduction

Solar, atmospheric, reactor, and accelerator neutrinos have provided compelling evidence for the existence of neutrino oscillations, implying non-zero neutrino masses (see Ref. [89] and references therein). The present data require the number of massive neutrinos to be equal or larger than two, since there are at least two mass squared differences ($\Delta m^2_{\rm atmos}$ and $\Delta m^2_{\rm solar}$) driving the atmospheric and solar neutrino oscillations respectively. Unfortunately, oscillation experiments only provide bounds on the neutrino mass squared differences, i.e. they are not sensitive to the overall neutrino mass scale.

Cosmology provides one of the means to tackle the absolute scale of neutrino masses. Neutrinos can leave key signatures in several cosmological data sets. The amount of primordial relativistic neutrinos changes the epoch of the matter- radiation equality, leaving an imprint on both Cosmic Microwave Background (CMB) anisotropies (through the so-called Integrated Sachs-Wolfe effect) and on structure formation, while non relativistic neutrinos in the recent Universe suppress the growth of matter density fluctuations and galaxy clustering, see Ref. [84]. Cosmology can therefore weigh neutrinos, providing an upper bound on the sum of the three active neutrino masses, $\sum m_\nu \sim 0.58$ eV at the 95% CL [90]. The former bound is found when CMB measurements from the Wilkinson Microwave Anisotropy

Probe (WMAP) are combined with measurements of the distribution of galaxies (SDSSII-BAO) and of the Hubble constant H_0 (HST) [1] in the assumption of a flat universe with a cosmological constant, i.e. a ΛCDM cosmology.

However, the three neutrino scenario is a minimal scheme, and there is no fundamental symmetry in nature forcing a definite number of right-handed (sterile) neutrino species, as those are allowed in the Standard Model fermion content. Indeed, cosmological probes have been extensively used to set bounds on the relativistic energy density of the universe in terms of the effective number of neutrinos $N_\nu^{\rm eff}$ (see, for instance, Refs. [91, 92, 93, 94, 95]). Currently, WMAP, SDSSII-BAO and HST data provide a 68% CL range on $N_\nu^{\rm eff} = 4.34^{+0.86}_{-0.88}$ [90] in the assumption of a ΛCDM universe. If the effective number of neutrinos $N_\nu^{\rm eff}$ is larger than the Standard Model prediction of $N_\nu^{\rm eff} = 3.046$ at the Big Bang Nucleosynthesis (BBN) era, the relativistic degrees of freedom, and, consequently, the Hubble expansion rate will also be larger causing weak interactions to become uneffective earlier. This will lead to a larger neutron-to-proton ratio and will change the standard BBN predictions for light element abundances. Combining Deuterium and ^{4}He data, the authors of Ref. [93] found $N_\nu^{\rm eff} = 3.1^{+1.4}_{-1.2}$ at the 95% CL.

Models with one additional $\sim$ 1 eV massive sterile neutrino, i.e. the so called (3+1) models, were introduced to explain LSND short baseline (SBL) antineutrino data [64] by means of neutrino oscillations. A much better fit to SBL appearance data and, to a lesser extent, to disappearance data, is provided by models with two sterile neutrinos (3+2) [67, 68] which can also explain both the MiniBooNE neutrino [65] and antineutrino data [96] if CP violation is allowed [97]. CP violation can even occur in (3+1) scenarios with only one relevant mass squared difference in the presence of non standard neutrino interactions (NSI). Therefore, the (3+1) NSI model can also nicely explain current data [98]. While (3+1) and (3+2) models show some tension with BBN bounds on $N_\nu^{\rm eff}$, the extra sterile neutrinos do not necessarily have to feature thermal abundances at decoupling. The first analysis of both SBL oscillation data and cosmological data was performed by the authors of Ref. [99], where the usual full thermalization scenario for the sterile neutrino species was not assumed. Instead, the sterile abundances were computed taking into account the multi flavour mixing processes operating at the neutrino decoupling period. Robust bounds on sterile neutrino masses, mixings and abundances were derived. However, the masses of the three active neutrinos were fixed to $m_1 \sim 0$, $m_2 \sim \sqrt{\Delta m^2_{\rm solar}}$ and $m_3 \sim \sqrt{\Delta m^2_{\rm atmos}}$. In Ref. [100] the authors derived the bounds on a light sterile neutrino scenario enlarging the usual thermal scenario. More recently, the authors of Ref. [101] have used current cosmological data to analyze two possible active plus sterile neutrino scenarios, one with massless active neutrinos (and massive steriles) and the other one with massless steriles states of unknown number (and massive active species). However, there are no cosmological bounds on the more natural and oscillation-data motivated scenario in which both the sterile and the active neutrinos have masses. Active neutrinos are *massive*; this is what oscillation data are telling us. In the same way, the LSND and MiniBooNE antineutrino data, if explained in terms of neutrino oscillations, point to the existence of *massive* sterile neutrino species. What oscillation data

[1] For other recent analyses, see also Refs. [91, 92].

can not tell us is the absolute scale of neutrino masses and this is precisely what we address in this study, in the spirit of Ref. [102], via present and future cosmological measurements.

The paper is organized as follows. In Sec. 3.2 we present the constraints on the active and sterile neutrino masses and on the number of sterile species from current cosmological data as well as from BBN measurements of light element abundances. Section 3.3 is devoted to future errors on these parameters. We describe the Fisher matrix method used here for forecasting errors and discuss the potential results from the ongoing Planck CMB mission combined with future BOSS and Euclid galaxy survey data. We also describe the induced biases on some parameters (such as H_0 and m_ν) when the cosmological model does not account for the presence of sterile states to describe the data. We conclude in Sec. 3.4.

3.2 Current constraints

Here we summarize the constraints from current data on the active neutrino masses and on the sterile neutrino thermal abundance and masses. We have modified the Boltzmann CAMB code [82] incorporating the extra massive sterile neutrino parameters and extracted cosmological parameters from current data using a Monte Carlo Markov Chain (MCMC) analysis based on the publicly available MCMC package `cosmomc`[103]. We consider here a flat ΛCDM scenario plus three (N_{ν_s}) active (sterile) massive neutrino species, described by a set of cosmological parameters

$$\{\omega_b, \omega_c, \Theta_s, \tau, n_s, \log[10^{10} A_s], m_\nu, m_{\nu_s}, N_{\nu_s}\} \ , \tag{3.1}$$

where $\omega_b \equiv \Omega_b h^2$ and $\omega_c \equiv \Omega_c h^2$ are the physical baryon and cold dark matter densities, Θ_s is the ratio between the sound horizon and the angular diameter distance at decoupling, τ is the optical depth, n_s is the scalar spectral index, A_s is the amplitude of the primordial spectrum [2], m_ν is the active neutrino mass, m_{ν_s} is the sterile neutrino mass and N_{ν_s} is the number of thermalized sterile neutrino species. We assume that both active and sterile neutrinos have degenerate mass spectra (m_ν and m_{ν_s} are the individual masses, not the sum of the masses). The flat priors assumed on these cosmological parameters are shown in Tab. 6.1.

Our basic data set is the seven–year WMAP data [90, 104] (temperature and polarization) with the routine for computing the likelihood supplied by the WMAP team. We consider two cases: we first analyze the WMAP data together with the luminous red galaxy clustering results from SDSSII (Sloan Digital Sky Survey) [105] and with a prior on the Hubble constant from HST (Hubble Space Telescope) [106], referring to it as the "run1" case. We then include to these data sets Supernova Ia Union Compilation 2 data [15], and we will refer to this case as "run2". In addition, we also add to the previous data sets the BBN measurements of the ^{4}He abundance, considering separately helium fractions of $Y_p^1 = 0.2561 \pm 0.0108$ (see Ref. [107]) and of $Y_p^2 = 0.2565 \pm 0.0010$ (stat.) ± 0.0050 (syst.) from Ref. [108]. Finally, we also consider the Deuterium abundance measurements $\log(D/H) = 4.56 \pm 0.04$ from Ref. [109].

[2] The pivot scale assumed in this study corresponds to $k_0 = 0.05$ Mpc^{-1}.

Parameter	Prior
$\Omega_b h^2$	0.005-0.1
$\Omega_c h^2$	0.01-0.99
Θ_s	0.5-10
τ	0.01-0.8
n_s	0.5-1.5
$\ln(10^{10} A_s)$	2.7-4
m_{ν_s} [eV]	0-3
m_ν [eV]	0-3
N_{ν_s}	0-6

Table 3.1: Flat priors for the cosmological parameters considered here.

It is important to clarify that CMB anisotropies also depend on the value of Y_p but since Y_p is constrained loosely by current CMB/LSS data, it is consistent to fix it to value $Y_p = 0.24$ in the CMB runs and to consider it as an independent parameter constrained by BBN observations.

Given a cosmological model, we predict the theoretical primordial abundance of Y_p and $\log(D/H)$ by making use of the public available PArthENoPE BBN code (see [110]).

Since running cosmomc and getting at the same time the theoretical predictions from Parthenope for BBN would be be exceedingly time-consuming we perform importance sampling obtaining the predicted values for Y_p and $\log(D/H)$ with an interpolation routine using a grid of Parthenope predictions for each (ω_b, N_{ν_s}), as in [111].

Parameter	68% CL(r1)	95% CL(r1)	68% CL (r2)	95% CL (r2)
N_{ν_s}	< 2.5	< 4.1	< 2.0	< 3.2
m_ν [eV]	< 0.13	< 0.30	< 0.10	< 0.20
m_{ν_s} [eV]	< 0.22	< 0.46	< 0.20	< 0.50

Table 3.2: 1D marginalized bounds on the active and sterile neutrino parameters using the two combinations of data sets described in the text (r1 refers to "run 1" and r2 refers to "run 2", respectively).

Table 3.2 shows the 1D marginalized bounds on N_{ν_s}, m_{ν_s} and m_ν arising from the two different analyses performed here on cosmological data sets. The marginalized limits have been computed setting a lower limit of 0 in all the three neutrino parameters here explored. The bounds obtained on the parameters associated to the dark matter candidates considered here are consistent with those obtained in Ref. [71] after taking into account the differences in the thermal abundances of sterile neutrinos and QCD thermal axions. When we marginalize over all the cosmological parameters, see Tab. 3.2, the 95% CL upper bound for N_{ν_s} is 4.1 (3.2) using "run1" ("run2") data sets. Therefore, current cosmological data does not exclude

	Y_p^1 [107]	Y_p^2 [108]	$Y_p^1 + D$ [109]	$Y_p^2 + D$ [109]
N_{ν_s}	< 2.3	< 1.7	< 1.7	< 1.4
m_ν [eV]	< 0.17	< 0.15	< 0.15	< 0.15
m_{ν_s} [eV]	< 0.62	< 0.67	< 0.69	< 0.68

Table 3.3: 1D marginalized 95% CL bounds on N_{ν_s}, m_{ν_s} and m_ν after combining the results of "run 2" with those coming from different measurements of BBN light element abundances.

at the 95% CL the existence of ~ 2 sterile neutrino species with sub-eV masses plus three sub-eV active massive neutrinos. It would be interesting to further explore if a model with sterile neutrinos is preferred over the model with only three active neutrinos. The results here are also in very good agreement with those of Ref. [101] even if in the former analysis the two species, i.e. the active and sterile neutrino states, were not considered to be massive at the same time.

Table 3.3 shows the 95% 1D marginalized bounds on N_{ν_s}, m_{ν_s} and m_ν arising when different combinations of BBN light element abundances measurements are combined with "run 2" results. Note that when measurements of the ^{4}He abundance are added to CMB, galaxy clustering and SNIa data, the 95% CL upper limit on N_{ν_s} is 2.3 (1.7) if $Y_p^1 = 0.2561 \pm 0.0108$ ($Y_p^2 = 0.2565 \pm 0.0010 \pm 0.0050$) is assumed. Since the number of sterile species after adding BBN constraints is smaller than before, the sterile (active) neutrino masses can get slightly larger (smaller) values, since BBN data is insensitive to the dark matter density in the form of massive neutrinos at late times. The combination of Helium and Deuterium abundance measurements compromises the viability of (3+2) models, leading to $N_{\nu_s} < 1.7 - 1.4$ at the 95% CL. However, the two sterile states might not have thermal properties at decoupling and evade BBN constraints. A complete analysis [112] including sterile neutrino mixing parameters and recent reactor neutrino oscillation results [113] is mandatory.

Figure 3.1, top panel to the left, depicts the 68% and 95% CL allowed contours in the m_ν–N_{ν_s} plane. The blue (red) contours denote the allowed regions by "run1" ("run2") data sets. Notice that there exists a degeneracy between these two quantities. This degeneracy is similar to the one found by the authors of Ref. [101]. When the mass energy density in the form of massive neutrinos is increased, the number of extra relativistic species must also be increased to compensate the effect. This will be the case for massless sterile species. In our analysis, the degeneracy is milder since sterile neutrinos are massive and therefore they behave as an additional dark matter component at late times. The degeneracy will show up when the active neutrinos have relatively large masses, since, in that case, a tiny amount of sterile neutrino masses will be allowed. The sterile states will then behave as relativistic particles at the decoupling era and will compensate the effect of a large active neutrino mass.

Figure 3.1, bottom panel, depicts the 68% and 95% CL allowed contours in the m_ν–m_{ν_s} plane. There exists a very strong anticorrelation between these two quantities, since both contribute to the dark matter energy density at late times and therefore if the mass of the

sterile neutrino states grows, the mass of the active ones must decrease. The situation is analogous to that of QCD thermal axions and massive (active) neutrinos, see Ref. [71].

The top panel to the right of Fig. 3.1 depicts the 68% and 95% CL allowed contours in the N_{ν_s}–m_{ν_s} plane. In this case, the larger the sterile neutrino mass is, the lower its thermal abundance must be, as expected.

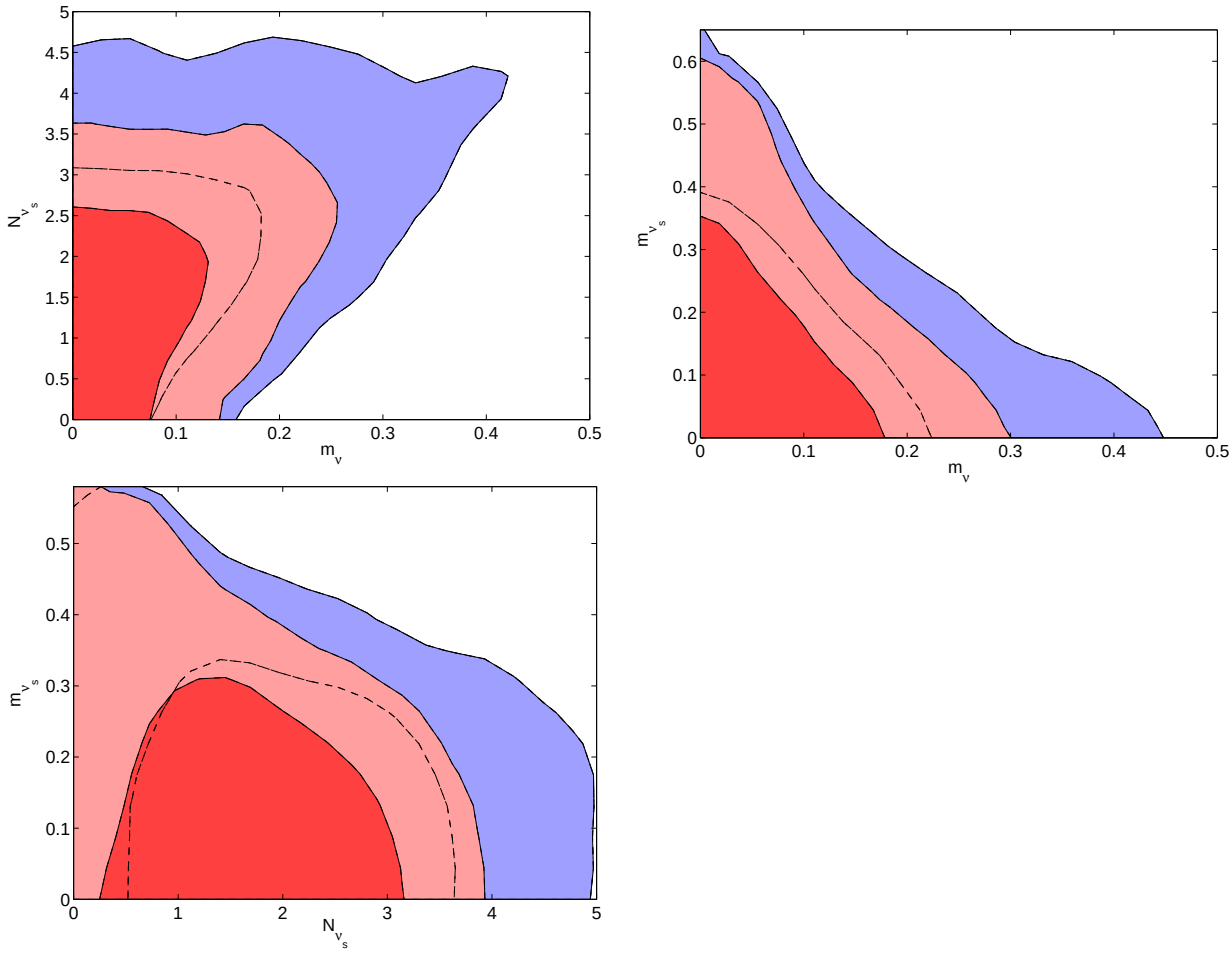

Figure 3.1: The top and bottom panels show the 68% and 95% CL constraints on the plane m_ν-N_{ν_s}, m_ν-m_{ν_s} and m_{ν_s}-N_{ν_s}, respectively. The blue (red) contours denote the allowed regions by "run1" ("run2") data sets, see text for details. The masses of the sterile and active neutrinos are both in eV units.

3.3 Future constraints

We present here the constraints on the neutrino sector parameters explored in this work from future CMB and galaxy survey measurements, making use of the Fisher matrix formalism,

see also Ref. [114] for a recent analysis. We also compute the potential shifts in the different cosmological parameters when the sterile neutrino parameters are neglected in the analysis.

3.3.1 Methodology

The Fisher matrix is defined as the expectation value of the second derivative of the likelihood surface about the maximum. As long as the posterior distribution for the parameters is well approximated by a multivariate Gaussian function, its elements are given by [115, 116, 117]

$$F_{\alpha\beta} = \frac{1}{2}\mathrm{Tr}\left[C^{-1}C_{,\alpha}C^{-1}C_{,\beta}\right] \ , \tag{3.2}$$

where $C = S + N$ is the total covariance which consists of signal S and noise N terms. The commas in Eq. (3.2) denote derivatives with respect to the cosmological parameters within the assumed fiducial cosmology. Our fiducial model is a ΛCDM cosmology with five parameters: the physical baryon and CDM densities, $\omega_b = \Omega_b h^2$ and $\omega_c = \Omega_c h^2$, the scalar spectral index, n_s, h (being the Hubble constant $H_0 = 100\ h$ km Mpc^{-1}s^{-1}) and the dimensionless amplitude of the primordial curvature perturbations, A_s (see Tab. 3.4 for their values). Furthermore, we add to the ΛCDM fiducial cosmology three additional parameters for the neutrino sector: the mass of active neutrinos m_ν, the mass of sterile neutrinos m_{ν_s} and the number of sterile neutrino species N_{ν_s}. Notice that, for simplicity, we have kept fixed the reionization optical depth τ since it has no impact on large scale structure data and we do not expect a strong degeneracy between τ and the neutrino parameters, see Ref. [118]. We assume that both active and sterile neutrinos have a degenerate spectrum and that the sterile species are fully thermalized. The fiducial values of the neutrino parameters are listed as well in Tab. 3.4, and they are based on the constraints from current data presented in the previous section, from which we conclude that $m_\nu = 0.1$ eV, $m_{\nu_s} \leq 0.5$ and $N_{\nu_s} = 1, 2$ are within the allowed regions for these parameters.

$\Omega_b h^2$	$\Omega_c h^2$	n_s	h	A_s	m_ν [eV]	m_{ν_s} [eV]	N_{ν_s}
0.02267	0.1131	0.96	0.705	$2.64 \cdot 10^{-9}$	0.1	0.1-0.5	1-2

Table 3.4: Values of the parameters in the fiducial models explored in this study.

We compute the CMB Fisher matrix to obtain forecasts for the Planck satellite [119]. We follow here the method of Ref. [120], considering the likelihood function for a realistic experiment with partial sky coverage, and noisy data

$$\begin{aligned} -2\ln\mathcal{L} = \sum_\ell (2\ell+1)\Bigg\{ & f_{sky}^{BB}\ln\left(\frac{\mathbf{C}_\ell^{BB}}{\hat{\mathbf{C}}_\ell^{BB}}\right) + \sqrt{f_{sky}^{TT}f_{sky}^{EE}}\ln\left(\frac{\mathbf{C}_\ell^{TT}\mathbf{C}_\ell^{EE}-(\mathbf{C}_\ell^{TE})^2}{\hat{\mathbf{C}}_\ell^{TT}\hat{\mathbf{C}}_\ell^{EE}-(\hat{\mathbf{C}}_\ell^{TE})^2}\right) \\ & + \sqrt{f_{sky}^{TT}f_{sky}^{EE}}\frac{\hat{\mathbf{C}}_\ell^{TT}\mathbf{C}_\ell^{EE}+\mathbf{C}_\ell^{TT}\hat{\mathbf{C}}_\ell^{EE}-2\hat{\mathbf{C}}_\ell^{TE}\mathbf{C}_\ell^{TE}}{\mathbf{C}_\ell^{TT}\mathbf{C}_\ell^{EE}-(\mathbf{C}_\ell^{TE})^2} + f_{sky}^{BB}\frac{\hat{\mathbf{C}}_\ell^{BB}}{\mathbf{C}_\ell^{BB}} - 2\sqrt{f_{sky}^{TT}f_{sky}^{EE}} \\ & - f_{sky}^{BB}\Bigg\} \ , \end{aligned} \tag{3.3}$$

and compute its second derivatives to obtain the corresponding Fisher matrix

$$F^{\rm CMB}_{\alpha\beta} = \left\langle -\frac{\partial^2 \mathcal{L}}{\partial p_\alpha \partial p_\beta} \right\rangle |_{\mathbf{p}=\bar{\mathbf{p}}}\,. \tag{3.4}$$

In Eq. (3.3) $\mathbf{C}_\ell^{XY} = \mathcal{C}_\ell^{XY} + \mathcal{N}_\ell^{XY}$ with $\mathcal{C}_\ell^{XY}$ the temperature and polarization power spectra ($X, Y \equiv \{T, E, B\}$) and $\mathcal{N}_\ell$ the noise bias. Finally, f_{sky}^{XY} is the fraction of observed sky which can be different for the T-, E-, and B-modes.

For the galaxy redshift survey Fisher matrix, we follow the prescription of Ref. [121]. Assuming the likelihood function for the band powers of a galaxy redshift survey to be Gaussian, the Fisher matrix can be approximated as:

$$\begin{aligned} F^{\rm LSS}_{\alpha\beta} &= \int_{\vec{k}_{\rm min}}^{\vec{k}_{\rm max}} \frac{\partial \ln P_{\rm gg}(\vec{k})}{\partial p_\alpha} \frac{\partial \ln P_{\rm gg}(\vec{k})}{\partial p_\beta} V_{\rm eff}(\vec{k}) \frac{d\vec{k}}{2(2\pi)^3} \\ &= \int_{-1}^{1} \int_{k_{\rm min}}^{k_{\rm max}} \frac{\partial \ln P_{\rm gg}(k,\mu)}{\partial p_\alpha} \frac{\partial \ln P_{\rm gg}(k,\mu)}{\partial p_\beta} V_{\rm eff}(k,\mu) \\ &\quad \frac{2\pi k^2 dk d\mu}{2(2\pi)^3}\,, \end{aligned} \tag{3.5}$$

where $V_{\rm eff}$ is the effective volume of the survey:

$$V_{\rm eff}(k,\mu) = \left[\frac{nP(k,\mu)}{nP(k,\mu)+1}\right]^2 V_{\rm survey}, \tag{3.6}$$

μ being the cosine of the angle between the vector along the line of sight and $\vec{k}$ and n being the galaxy number density, which is assumed to be constant throughout the survey. The linear redshift-space galaxy power spectrum $P_{\rm gg}$ is related to the real-space linear power dark matter spectrum $P_{\rm dm}$ as

$$P_{\rm gg}(k) = P_{\rm dm}(k)(b + f\mu^2)^2 \tag{3.7}$$

where b is the bias relating galaxy to dark matter overdensities in real space and f is the linear growth factor. Both the bias and the growth factor are assumed to vary in each redshift bin and are considered as additional parameters in the Fisher analysis of galaxy survey data.

We consider here two redshift surveys: the BOSS (Baryon Oscillation Spectroscopic Survey) [35] and the Euclid [122, 123] experiments. For the BOSS survey we assume a sky area of 10000 deg^2, a redshift range of $0.15 < z < 0.65$ and a mean galaxy density of 2.66×10^{-4}. For Euclid we consider an area of 20000 deg^2, a redshift range of $0.15 < z < 1.95$ and a mean galaxy density of 1.56×10^{-3}. We divide the surveys in redshift bins of width $\Delta z = 0.1$ (a value that is much larger than standard redshift spectroscopic errors), set $k_{\rm max}$ to be $0.1h$/Mpc and $k_{\rm min}$ to be greater than $2\pi/\Delta V^{1/3}$, where ΔV is the volume of the redshift shell.

Combining the Planck and redshift survey Fisher matrices ($F_{\alpha\beta} = F^{\rm LSS}_{\alpha\beta} + F^{\rm CMB}_{\alpha\beta}$) we get the joint constraints for $\Omega_b h^2$, $\Omega_c h^2$, n_s, H_0, A_s, m_ν, m_{ν_s} and N_{ν_s}, after marginalizing over the bias b and the growth factor f. The 1–σ error on parameter p_α marginalized over the other parameters is $\sigma(p_\alpha) = \sqrt{(F^{-1})_{\alpha\alpha}}$, F^{-1} being the inverse of the Fisher matrix.

3.3.2 Results

Tables 3.5 and 3.6 contain the 1–σ marginalized forecasted errors on the cosmological parameters for a fiducial cosmology with $m_\nu = 0.1$ eV, $m_{\nu_s} = 0.3$ eV and $N_{\nu_s} = 1$ and 2, respectively. We illustrate the results of our Fisher analysis for both BOSS and Euclid galaxy redshift survey data combined with Planck CMB measurements. Note that the errors on the pure ΛCDM model parameters, i.e $\Omega_b h^2$, $\Omega_c h^2$, n_s, h and A_s are always around or below the 1% level. The error on the active neutrino mass is around 60% for BOSS and half for Euclid. The error on the number of sterile neutrino species is always smaller than 25%. Regarding the error on the sterile neutrino mass, it can reach 100% relative errors for BOSS plus Planck data. Naively, one would expect that the BOSS and Euclid errors are related by a factor of $\sqrt{V_{\rm BOSS}/V_{\rm Euclid}}$ (being V the volume of the survey) when the shot noise is subdominant. However, in practice, the forecasted errors on the pure ΛCDM parameters are sometimes similar for the BOSS and Euclid cases, which implies that those parameters are mainly determined by CMB measurements. Of course this is not the case for the active and sterile neutrino masses, whose errors are mainly driven by galaxy clustering data and differ by a factor of $\sim 2-3$ for BOSS and Euclid cases, as naively expected. A word of caution is needed here: while computing the errors on the active and sterile neutrino masses and on the sterile neutrino abundances, a ΛCDM scenario has been chosen as fiducial cosmology. These errors can change if the equation of state of the dark energy component is allowed to vary [124] and/or interactions between the dark matter and dark energy sectors are stwiched on [125, 126].

We also present here the joint constraints in a two-parameter subspace (marginalized over all other cosmological parameters) to study the covariance between the sterile neutrino masses and/or abundances and the other cosmological parameters considered in this work. We have explored several possible scenarios with different sterile neutrino masses and thermal abundances (see Tab. 3.4). However, for the sake of simplicity, we illustrate here only the case $N_{\nu_s} = 1$, $m_{\nu_s} = 0.3$ eV and $m_\nu = 0.1$ eV.

Figure 3.2, left panel, shows the correlation between the number of sterile species N_{ν_s} and the active neutrino mass m_ν. The expected error on the number of sterile species is very similar for BOSS and Euclid data, which indicates that the constraints on N_{ν_s} arise mostly from Planck CMB measurements. Since the total energy density in the form of massive neutrinos is the sum of the active plus sterile contributions, a higher neutrino mass is compensated with a lower abundance of massive sterile species. The 1–σ marginalized error on N_{ν_s} from Planck plus BOSS (Euclid) data is 0.26 (0.1), see Tab. 3.5. The right panel of Fig. 3.2 shows the correlation between the masses of sterile and active neutrinos. As expected from the results presented in Fig. 3.1 (middle panel) and as previously explained, higher active neutrino masses are allowed for very low values of the sterile neutrino masses. The 1–σ marginalized errors on the massive species m_{ν_s} and m_ν from Planck plus BOSS (Euclid) data are 0.25 (0.08) eV and 0.06 (0.03) eV respectively. If nature has chosen an active neutrino with mass ~ 0.1 eV, BOSS (Euclid) data, combined with CMB Planck measurements, could provide a 1.5–σ (3–σ) detection, even in the presence of massive sterile species.

Parameter	BOSS+PLANCK	EUCLID+PLANCK
$\Omega_b h^2$	0.7%	0.3%
$\Omega_c h^2$	2.9%	1.3%
$\ln(10^{10} A_s)$	0.7%	0.4%
h [km/s/Mpc]	1.4%	0.7%
n_s	0.6%	0.3%
m_ν [eV]	63.1%	28.0%
m_{ν_s} [eV]	83.2%	26.2%
N_{ν_s}	25.9%	10.6%

Table 3.5: 1σ marginalized relative errors for a fiducial cosmology with N_{ν_s}=1, m_ν=0.1 eV and m_{ν_s}=0.3 eV.

Parameter	BOSS+PLANCK	EUCLID+PLANCK
$\Omega_b h^2$	0.7%	0.3%
$\Omega_c h^2$	1.5%	1.7%
$\ln(10^{10} A_s)$	0.4%	0.4%
h [km/s/Mpc]	1.4%	0.8%
n_s	0.5%	0.4%
m_ν [eV]	64.9%	35.9%
m_{ν_s} [eV]	41.9%	16.4%
N_{ν_s}	10.2%	7.5%

Table 3.6: 1–σ marginalized relative errors for all parameters for a N_{ν_s}=2, m_ν=0.1 eV and m_{ν_s}=0.3 eV fiducial cosmology.

Figure 3.3, left panel, shows the correlation between the active neutrino mass m_ν and the cold dark matter energy density $\Omega_c h^2$. Notice that the extraction of the cold dark matter component arise mostly from Planck CMB measurements. At late times, neutrinos contribute as an additional ingredient to the dark matter fluid and therefore a higher neutrino mass is compensated by a lower cold dark matter energy density. The right panel of Fig. 3.3 shows the correlation between cold dark matter and the sterile neutrino abundance. These two parameters are mostly extracted from CMB Planck data [3]. The sterile neutrinos considered here with 0.3 eV masses are relativistic at decoupling. A higher number of relativistic species will shift to a later period the matter radiation equality era and also enhance the first CMB acoustic peak. These effects can be compensated with a higher cold dark matter energy density, as shown by the positive correlation among the two parameters.

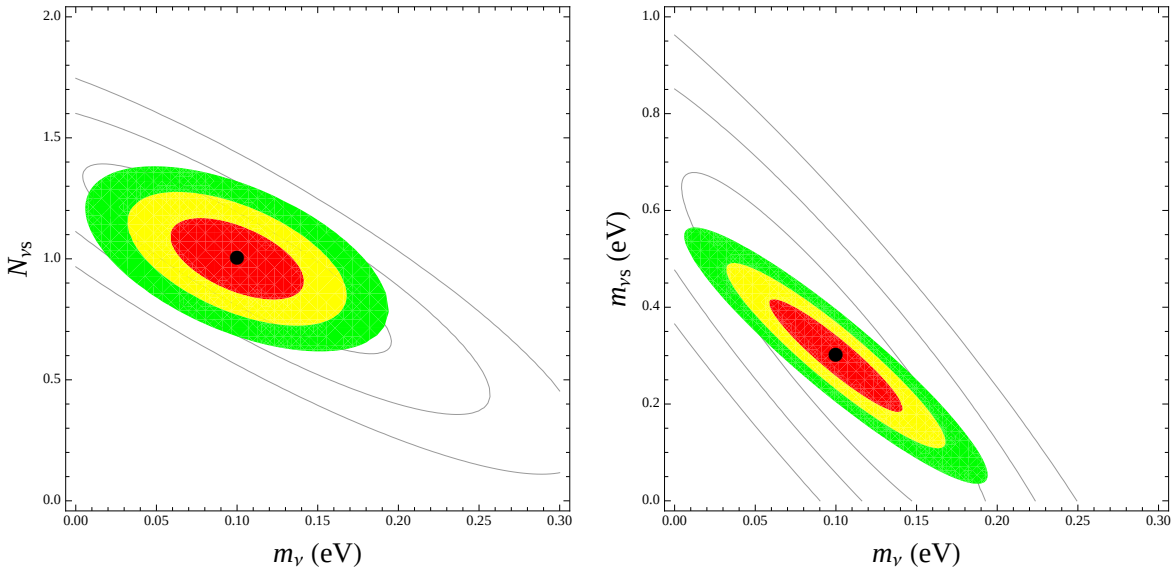

Figure 3.2: The empty (filled) contours denote the 68%, 95% and 99.73% CL regions for Planck plus BOSS (Euclid) data. The neutrino parameters in the fiducial model are $N_{\nu_s} = 1$, $m_{\nu_s} = 0.3$ eV and $m_\nu = 0.1$ eV.

3.3.3 Cosmological parameter shifts

In order to test the capabilities of future experiments to discriminate between different theoretical models, regardless of their parameters, we follow here the method of Ref. [127].

The idea is the following: if the data is fitted assuming a model M' with n' parameters, but the true underlying cosmology is a model M characterized by n parameters (with $n > n'$ and the parameter space of M including the model M' as a subset), the inferred values of the n' parameters will be shifted from their true values to compensate for the fact that the model used to fit the data is wrong. In the case illustrated here, M will be the model *with*

[3] However, the addition of galaxy clustering measurements help in breaking degeneracies

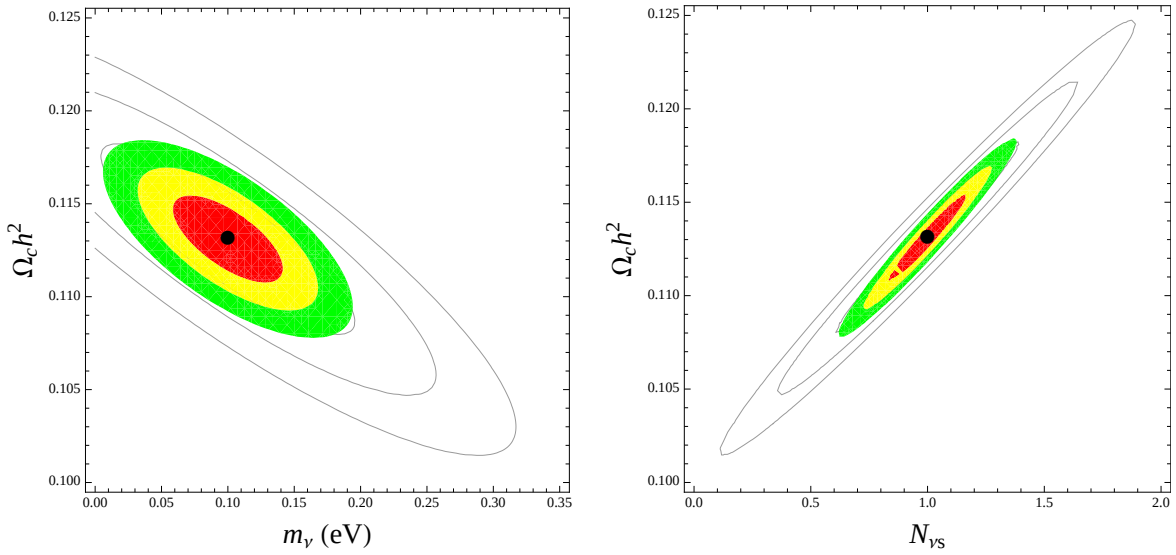

Figure 3.3: The empty (filled) contours denote the 68%, 95% and and 99.73% CL regions for Planck plus BOSS (Euclid) data. The neutrino parameters in the fiducial model are $N_{\nu_s} = 1$, $m_{\nu_s} = 0.3$ eV and $m_\nu = 0.1$ eV.

massive sterile neutrinos and M' the one *without* massive sterile neutrinos. While the first n' parameters are the same for both models, the remaining $n - n' = p$ parameters in the enlarged model M are accounting for the presence of massive sterile neutrinos, i.e. m_{ν_s} and N_{ν_s}. Assuming a gaussian likelihood, the shifts of the remaining n' parameters is given by [127]:

$$\delta\theta'_\alpha = -(F'^{-1})_{\alpha\beta} G_{\beta\zeta} \delta\psi_\zeta \qquad \alpha, \beta = 1 \ldots n', \zeta = n' + 1 \ldots n \ , \tag{3.8}$$

where F' represents the Fisher sub-matrix for the model M' without massive steriles and G denotes the Fisher matrix for the model M with $m_{\nu_s}, N_{\nu_s} > 0$.

We have computed the shifts induced in the cosmological parameters in several *true* cosmologies with a number of sterile neutrinos $N_{\nu_s} = 1, 2$ of masses $m_{\nu_s} = 0.1, 0.3$ and 0.5 eV. The mass of the active neutrino has been kept to 0.1 eV. These cosmologies are then wrongly fitted to a cosmology without sterile massive neutrino species. While certain parameters are exclusively measured by CMB probes or by the combination of CMB and other cosmological data sets (like $\Omega_c h^2$, $\Omega_b h^2$, n_s and A_s), there are other parameters such as the Hubble constant H_0 or the active neutrino mass m_ν which can be determined by other experiments. Then it is possible to verify the cosmological model assumptions by comparing the values of H_0 and m_ν extracted from CMB and LSS cosmological data to the values of these parameters obtained by other experiments, as missions devoted to measure the Hubble constant and tritium beta decay experiments [4]. The former experiments measure

[4]Neutrinoless double beta decay provides also a bound on the so-called effective neutrino mass $\langle m \rangle \equiv |\sum_i U_{ei}^2 m_i|$. However, these bounds apply only in the case that neutrinos have a Majorana nature. Therefore, we focus on tritium beta decay constraints which apply regardless of the Dirac vs Majorana nature of the neutrino.

the electron neutrino mass m_{ν_e}, which, in practice, when considering three active massive neutrinos, reads:

$$m_{\nu_e}^2 \equiv \sum_{i=1,3} |U_{ei}^2| m_i^2 \ , \tag{3.9}$$

being U_{ei} the first-row elements of the Pontecorvo-Maki-Nakagawa-Sakata leptonic mixing matrix. In the case of additional N_{ν_s} massive sterile neutrino species, m_{ν_e} would be given by

$$m_{\nu_e}^2 \equiv \sum_{i=1,3+N_{\nu_s}} |U_{ei}^2| m_i^2 \ , \tag{3.10}$$

Given the current best-fit values of the sterile-electron neutrino mixing terms $|U_{es}| < 10^{-1}$ [99] and the sub-eV sterile neutrino masses considered here, we neglect the contribution of the sterile neutrino species to m_{ν_e}. In the following, we apply the usual constraints on m_{ν_e} in our cosmological scenarios even if they contain massive sterile neutrino species. We therefore neglect the capability of beta decay experiments of measuring the individual neutrino masses and mixings. For a recent study of the KATRIN potential for sterile neutrino detection, see Ref. [128].

For sterile neutrino masses $m_{\nu_s} \sim 0.5$ eV and $N_{\nu_s} = 1, 2$, the shifts induced in H_0 are very large, for both BOSS and Euclid experiments combined with CMB Planck data. The reconstructed value of H_0 is within the range $\sim 20-50$ km/s/Mpc, values which are in strong disagreement with current measurements of the Hubble parameter from HST [106, 129]. The reconstructed value of the active neutrino mass is also in some cases $m_\nu \sim 2$ eV which is the current 95% CL limit from tritium β-decay experiments [130]. Consequently, after combining near future BOSS and Planck data one would conclude that the cosmological model assumed with $m_{\nu_s} \sim 0.5$ eV and $N_{\nu_s} = 1, 2$ is wrong. The same situation will arise when $m_{\nu_s} \sim 0.3$ eV and two sterile massive species, $N_{\nu_s} = 2$.

Parameter	Fiducial	Reconstructed	Shift (%)
H_0 [km/s/Mpc]	70.5	50.5	28%
m_ν [eV]	0.30	0.98	230%

Table 3.7: Shifted values and relative changes for the parameters H_0 and m_ν when the true cosmology has $N_{\nu_s} = 1$, $m_{\nu_s} = 0.3$ eV and $m_\nu = 0.1$ eV but BOSS plus Planck data are fitted to a cosmology with no sterile massive neutrino species.

For $m_{\nu_s} \sim 0.3$ eV and $N_{\nu_s} = 1$, the shifts using both BOSS and Euclid data are reported in Tabs. 3.7 and 3.8. While the shift induced in the Hubble constant is very large for the BOSS case, for Euclid that shift is still consistent with current estimates of H_0. A number of experiments (HST, Spitzer, GAIA and JWST [131]) are expected to measure H_0 with 2% uncertainty in the next decade and an inconsistency between the inferred H_0 values from

Parameter	Fiducial	Reconstructed	Shift (%)
H_0 [km/s/Mpc]	70.5	65.0	8%
m_ν [eV]	0.30	0.48	60%

Table 3.8: Shifted values and relative changes for the parameters H_0 and m_ν when the true cosmology has $N_{\nu_s} = 1$, $m_{\nu_s} = 0.3$ eV and $m_\nu = 0.1$ eV but Euclid plus Planck data are fitted to a cosmology with no sterile massive neutrino species.

these experiments and those from the cosmological probes considered here could point to the existence of additional sterile neutrino species. On the other hand, the aim of the tritium beta decay experiment KATRIN [132] is a sensitivity of $m_{\nu_e} < 0.2$ eV at 90% CL in case of a null result or a 5σ discovery potential for $m_{\nu_e} \geq 0.35$ eV. Therefore, the reconstructed values of $m_\nu = 0.48$ eV (Euclid plus Planck) and 0.98 eV (BOSS plus Planck) could be easily testable by the KATRIN experiment. Similar results are obtained for smaller sterile neutrino masses $m_{\nu_s} \sim 0.1$ eV with a higher number of sterile species $N_{\nu_s} = 2$.

For smaller sterile neutrino masses $m_{\nu_s} \sim 0.1$ eV and $N_{\nu_s} = 1$, the shift induced in H_0 is larger than 2% for both BOSS and Euclid data (combined with Planck). Therefore it would still be possible to check the fiducial cosmology with future measurements of H_0. The shift induced on the active neutrino mass using Euclid data is negligible and this means that it would be possible to recover the true value of the active neutrino mass even if the data is fitted to the wrong cosmology. Thus, the combination of Planck and Euclid data would not lead to an inconsistency between active neutrino mass estimates from Planck and Euclid on the one hand, and beta decay experiments on the other hand. Regarding BOSS plus Planck data however, the shift induced in the active neutrino mass m_ν is of the order of 100% and the comparison with an independent measurement of m_ν as that performed by KATRIN could test the validity of the cosmological model assumptions.

We have shown above that if the true $N_{\nu_s} = 1, 2$, wrongfully assuming $N_{\nu_s} = 0$ would lead to discrepancies between the cosmological probes considered here (large scale structure and CMB) and independent measurements of H_0 and m_ν. Of course, another clear indicator that the assumed model is incorrect is simply that the $N_{\nu_s} = 0$ would likely provide a bad fit to the large scale structure and CMB data themselves. However, the induced bias discussed above would provide a useful extra check when independent measurements of H_0 and/or m_ν are available. In addition, the bias calculation shows that even if one is not interested in the sterile neutrinos per se, not taking them into account could lead to very wrong conclusions about the other cosmological parameters.

3.4 Summary

Neutrino oscillation experiments have brought to light the first departure from the Standard Model of particle physics, indicating that neutrinos have non zero masses and opening the possibility for a number of extra sterile neutrinos. LSND and MiniBooNE antineutrino

data require these extra sterile species to be massive. Much effort has been devoted in the literature to constrain the so called (3+1) (three active plus one sterile) and (3+2) (three active plus two sterile) models.

Cosmology can set bounds on both the active and sterile neutrino masses as well as on the number of sterile neutrino species. We have explored here the current constraints on these parameters in the most natural scenario which corresponds to the case in which both the active and sterile neutrinos are massive particles. We find that models with two massive sub-eV sterile neutrinos plus three sub-eV active states are perfectly allowed at the 95% CL by current Cosmic Microwave Background, galaxy clustering and Supernovae Ia data. The bounds derived here were obtained in the context of a ΛCDM cosmology and other scenarios with a dark energy component could allow for larger neutrino masses and/or abundances. We have also shown that Big Bang Nucleosynthesis Helium-4 and deuterium abundances exclude (3+2) models at the 95% CL. However, the extra sterile states do not necessarily need to feature thermal abundances at decoupling. Their precise abundances are related to their mixings with the active neutrinos in the early universe.

We have also forecasted the errors on the active and sterile neutrino parameters from Planck and galaxy survey data. Future cosmological data are expected to measure sub-eV active and sterile neutrino masses and sterile abundances with $10-30\%$ precision, for sub-eV (0.5 eV$> m_{\nu_s} >$ 0.1 eV) sterile neutrino masses. We have also shown that the presence of massive sterile neutrinos in the universe could be inferred from inconsistencies among the values of H_0 obtained from cosmic microwave and galaxy clustering probes and those arising from independent measurements of the Hubble constant over the next decade. The validity of the cosmological assumptions could also be tested by comparing cosmological measurements of the active neutrino mass with those obtained from tritium beta decay experiments.

Chapter 4

New Neutrino Mass Bounds from Sloan Digital Sky Survey III Data Release 8 Photometric Luminous Galaxies

In this Chapter we derive neutrino mass bounds from the angular power spectra from the Sloan Digital Sky Survey III Data Release Eight (SDSS DR8) sample of photometric galaxies with CMASS selection criteria. This Chapter is a copy of the paper:

New Neutrino Mass Bounds from Sloan Digital Sky Survey III Data Release 8 Photometric Luminous Galaxies, Roland de Putter, Olga Mena, Elena Giusarma, Shirley Ho, Antonio Cuesta, Hee-Jong Seo, Ashley J. Ross & Martin White *et al.*, Astrophys. J. **761**, 12 (2012).

4.1 Introduction

During the last several years, experiments involving solar, atmospheric, reactor and accelerator neutrinos have adduced robust evidence for flavor change, implying non-zero neutrino mass, see Ref. [89] and references therein. The most economical description of the neutrino oscillation phenomena requires at least two massive neutrino mass eigenstates to explain the two mass differences[1], $\Delta m^2_{12} = 7.59 \cdot 10^{-5}$ eV^2 and $\Delta m^2_{23} = 2.5 \cdot 10^{-3}$ eV^2 [56, 133], which drive the solar and atmospheric transitions. Despite the remarkable success of past and present oscillation experiments, and the promising prospects for future searches, the individual neutrino masses and the Dirac versus Majorana neutrino character are key questions that continue to be unanswered by oscillation experiments.

Direct information on the absolute scale of neutrino masses can be extracted from kinematical studies of weak decays producing neutrinos. The present upper bound on the electron-neutrino mass from tritium beta-decay experiments is 2 eV (95% confidence level (CL)) [58, 134], and in the future the KATRIN experiment is expected to be sensitive to electron-neutrino masses approaching 0.2 eV (90% CL) [130]. Searches for the Majorana

[1]Neutrino oscillations are described by mass squared differences and not by the absolute values of the mass eigenstates

neutrino nature involve neutrinoless double beta decay $\beta\beta(0\nu)$, a rare and as yet unobserved transition between two nuclei. Observational upper limits on $\beta\beta(0\nu)$ rates provide an upper bound on the so-called effective Majorana mass of the electron neutrino, $\langle m_{\rm eff}\rangle < 0.3{-}1.0$ eV, bound which would only apply if neutrinos are Majorana particles [61]. Forthcoming $\beta\beta(0\nu)$ experiments aim for sensitivity approaching $\langle m_{\rm eff}\rangle < 0.05$ eV [61].

Cosmology provides one of the means to tackle the absolute scale of neutrino masses. Some of the earliest cosmological bounds on neutrino masses followed from the requirement that massive relic neutrinos, present today in the expected numbers, do not saturate the critical density of the Universe, i.e., that the neutrino mass energy density given by

$$\Omega_\nu = \frac{\sum m_\nu}{93.1 h^2 \mathrm{eV}} \tag{4.1}$$

satisfies $\Omega_\nu \leq 1$. The Universe therefore offers a new laboratory for testing neutrino masses and neutrino physics. Accurate measurements of the Cosmic Microwave Background (CMB) temperature and polarization anisotropy from satellite, balloon-borne and ground-based experiments have fully confirmed the predictions of the standard cosmological model and allow us to weigh neutrinos [84]. Indeed, neutrinos can play a relevant role in large-scale structure formation and leave key signatures in several cosmological data sets. More specifically, the amount of primordial relativistic neutrinos changes the epoch of matter-radiation equality, leaving an imprint on CMB anisotropies. After becoming non-relativistic, their free-streaming nature damps power on small scales, suppressing the growth of matter density fluctuations and thus affecting both the CMB and galaxy clustering observables in the low-redshift universe [84]. Measurements of all of these observations have been used to place new bounds on neutrino physics from cosmology [135, 136, 137, 138, 139, 140, 141, 142, 143, 144, 124, 145, 146, 147, 148, 149, 105, 91, 150, 90, 151, 152, 153], with a current limit on the sum of neutrino masses $\Sigma m_\nu \lesssim 0.6$ eV at 95% CL (e.g. [105]), depending on the precise combination of data sets and on the underlying cosmological model.

We present here neutrino mass bounds from the final imaging data set of the Sloan Digital Sky Survey (SDSS-III) [32], using the photometric redshift catalog of *Ross et al.* [36]. We consider the CMASS sample [37] of luminous galaxies of SDSS DR8 [40], the eighth data release of SDSS and the first data release of the Baryon Oscillation Spectroscopic Survey (BOSS) [35], with photometric redshifts $z = 0.45 - 0.65$. This sample covers an area of approximately 10,000 square degrees and consists of 900,000 galaxies. It is thus the largest sample of luminous galaxies so far and promises strong constraints on the neutrino properties (see [150] for an analysis of a slightly smaller SDSS photometric sample).

We derive neutrino constraints from the angular power spectra of the galaxy density at different redshifts, in combination with priors from the CMB and from measurements of the Hubble parameter, supernovae distances and the BAO scale. The spectra and the analysis of a minimal ΛCDM cosmology are described in detail in [154] and the measurement of the BAO scale from the spectra is presented in [155]. We will often refer to these works for details and focus here on the neutrino bound.

The structure of the paper is as follows. In section 6.3, we describe the data set and the derived angular spectra. We then discuss our theoretical model for the spectra and their

cosmology dependence in section 4.3. In section 4.4 we explain the specific signature of neutrino mass on galaxy clustering data. We test our model for the angular power spectra against mock data in section 4.5 and present the constraints on the sum of the neutrino masses and other parameters for several data combinations in section 6.4. Finally, we discuss these results and conclude in section 4.7.

4.2 Data

The data and the method for obtaining angular spectra have been described in detail in Ref. [36] and in [154]. Here we provide a brief description of the main properties and refer the reader to those papers for details. Our galaxy sample is obtained from imaging data from DR8 [40] of SDSS-III [32]. This survey mapped about $15,000$ square degrees of the sky in five pass bands (u, g, r, i and z) [156] using a wide field CCD camera [157] on the 2.5 meter Sloan telescope at Apache Point Observatory [158] (the subsequent astrometric calibration of these imaging data is described in [159]). A sample of $112,778$ galaxy spectra from BOSS [35] were used as a training sample for the photometric redshift catalog, as described in [36].

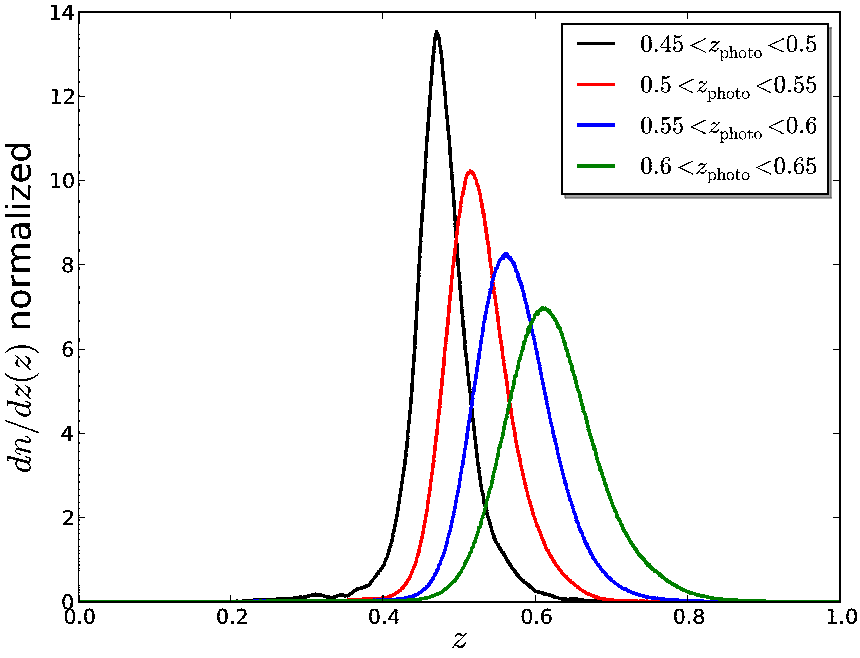

Figure 4.1: Normalized true redshift distribution of CMASS galaxies in four photometric redshift bins. The number of galaxies in each bin is 214971, 258736, 248895 and 150319 (from low to high redshift).

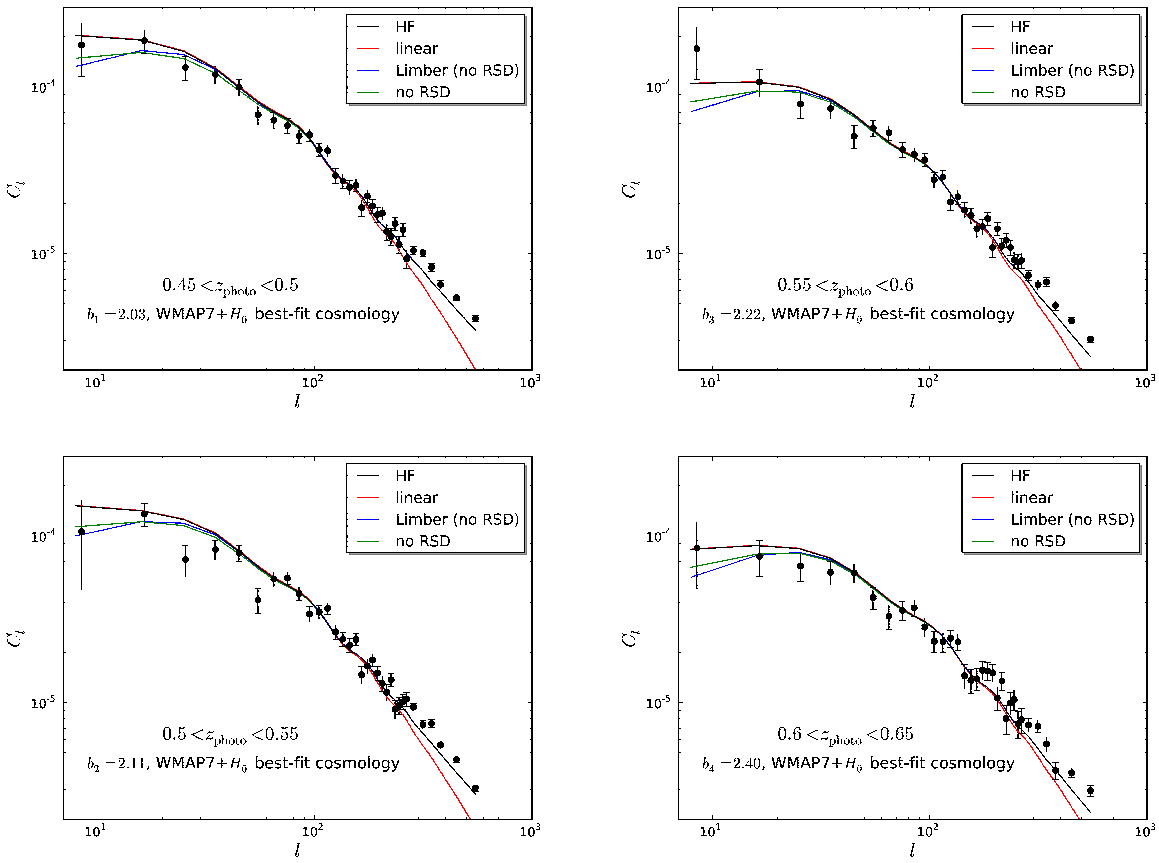

Figure 4.2: Observed power spectra (black points) with error bars and theoretical power spectra (solid curves). We show the theoretical power spectra for different models: the default, HaloFit (HF) based model used in our analysis (black; see text for details), the same model, but using the linear matter power spectrum as input (red), the default model, but using the Limber approximation (blue) and the default model without redshift space distortions (green). We restrict ourselves to the range $\ell = 30 - 200$ in our analysis. For the theoretical spectra, we assume the WMAP7+HST best-fit cosmology and use the bias b_i that best fits the data. We do not here include the shot noise parameters a_i.

We focus on the approximately stellar mass-limited CMASS sample of luminous galaxies, detailed in [37], which are divided into four photometric redshift bins, $z_{\rm photo} = 0.45 - 0.5 - 0.55 - 0.6 - 0.65$. The photometric redshift error lies in the range $\sigma_z(z) = 0.04 - 0.06$, increasing from low to high redshift. Figure 4.1 shows the estimated true redshift distribution of each bin, determined using the methods described in section 5.3 of [36].

The calculation of the angular power spectrum for each bin is described in detail in [154] and uses the optimal quadratic estimator (OQE) method outlined in [160, 161, 162, 163]. The four power spectra are binned in ℓ space with a typical wave band width of $\Delta\ell = 10$. The expectation value of the power spectrum in a wave band is a convolution of the true power spectrum with a window function of width roughly equal to the typical wave band width. Examples of these window functions are shown in Fig. 3 of [155]. When fitting the data to the underlying theoretical model, we always apply these window functions to the theoretical power spectra before calculating the likelihood relative to the data.

The four power spectra are plotted with their error bars in Fig. 4.2. The solid curves represent theoretical power spectra based on several assumptions. These power spectra will be discussed in detail in section 4.3. Since the low ℓ wave bands are more prone to systematics [36], we are conservative and do not consider bands with $\ell < 30$ in our analysis. We shall apply cuts at $\ell_{\rm max} = 150$ and 200 in order to suppress uncertainties from non-linear corrections to the modeled power spectra, as discussed in the following sections. The median redshift ($z \approx 0.55$) contributions to these maximum angular modes arise from three-dimensional modes with wave vectors $k \approx 0.10h{\rm Mpc}^{-1}$ and $k \approx 0.14h{\rm Mpc}^{-1}$, respectively. We thus use 17 (12) data points per redshift slice for $\ell_{\rm max} = 200\,(150)$.

4.3 Modeling the angular power spectra

The galaxy overdensity in the i-th redshift bin can be expanded in terms of spherical harmonics,

$$\delta_g^{(i)}(\hat{n}) = \sum_{\ell m} a_{\ell m}^{(i)}\, Y_{\ell m}(\hat{n})\ , \tag{4.2}$$

so that the angular power (and cross) spectra are defined as

$$\langle a^{(i)}_{\ell m} a^{(j)*}_{\ell' m'}\rangle \equiv C_\ell^{(ij)}\, \delta^{\rm K}_{\ell\ell'}\, \delta^{\rm K}_{mm'}, \tag{4.3}$$

where $\delta^{\rm K}_{ij}$ is the Kronecker delta function. As mentioned in the previous section, we do not estimate our spectra by directly transforming the observed density field to harmonics space, but use instead the optimal quadratic estimator technique. To constrain the sum of the neutrino masses and other cosmological parameters, the observed spectra are compared to a cosmology dependent model, which we now describe.

The galaxy overdensity on the sky is a line-of-sight projection of the three-dimensional redshift space galaxy overdensity $\delta_g(d(z)\,\hat{\mathbf{n}}, z)$,

$$\delta_g^{(i)}(\hat{\mathbf{n}}) = \int dz\, g_i(z)\ \left(\delta_g(d(z)\,\hat{\mathbf{n}}, z) - (H(z))^{-1}\,\hat{\mathbf{n}}\cdot\nabla(\hat{\mathbf{n}}\cdot\mathbf{v}(d(z)\,\hat{\mathbf{n}}, z))\right), \tag{4.4}$$

where

$$g_i(z) = \frac{dn_i/dz(z)}{\int dz'\, dn_i/dz(z')} \tag{4.5}$$

is the normalized redshift distribution of galaxies in bin i (with $dn_i/dz(z)$ the number of galaxies per steradian per unit redshift), $d(z)$ is the comoving distance to redshift z (assuming a flat universe) and $\mathbf{v}$ is the galaxy velocity field. The velocity term arises because gradients of the peculiar velocity contribution to the distance in redshift space change the volume, and consequently, the number density[2].

We assume a linear, scale-independent bias for the galaxy density,

$$\delta_g(\mathbf{x}, z) = b_g(z)\, \delta_m(\mathbf{x}, z)\ , \tag{4.6}$$

with δ_m the matter overdensity. For the peculiar velocity field, we use the continuity equation in the linear regime, which gives for a Fourier mode with wave vector $\mathbf{k}$,

$$\mathbf{v} = -i\beta(z)\delta_g(\mathbf{k})\frac{\mathbf{k}}{k^2}\ , \tag{4.7}$$

where $\beta(z) = f(z)/b_g(z)$ is the redshift distortion parameter and

$$f(z) \equiv \frac{d\ln D(z)}{d\ln a} \tag{4.8}$$

is the growth factor (with $D(z)$ the linear growth function). In the presence of neutrinos, the growth function is no longer scale independent at late time as the neutrinos suppress growth on scales below the free streaming length [164, 165], but not on larger scales (with a broad transition regime in between). We shall ignore the scale dependent growth in $\beta(z)$ since it is a small ($\ll 10\%$) correction to the already small effect (on the scales of interest here) of redshift space distortions (RSD, see Fig. 4.2). However, this scale-dependent growth is included in the real space power spectrum, as this is the main signature of massive neutrinos.

We simplify our treatment of the galaxy bias adding four free parameters b_i to describe the bias in each bin. The results from our simulations barely change when considering a bias $b_g(z)$ that varies within redshift bins, showing that this is a safe approximation[3]. It then follows from the above (see [166, 167, 163]) that

$$C_\ell^{(ii)} = b_i^2\,\frac{2}{\pi}\int k^2 dk\, P_m(k, z=0)\,\left(\Delta_\ell^{(i)}(k) + \Delta_\ell^{\mathrm{RSD},(i)}(k)\right)^2\ , \tag{4.9}$$

where $P_m(k, z=0)$ is the matter power spectrum at redshift zero and

$$\Delta_\ell^{(i)}(k) = \int dz\, g_i(z)\, T(k, z)\, j_\ell(k\, d(z))\ . \tag{4.10}$$

[2]Instead of writing the projected galaxy overdensity as an integral over the observed redshift (including peculiar velocity contributions) as in Eq. (4.4), one could equivalently do the integral over "true" cosmic redshift, see Ref. [163], in which case only the true three-dimensional galaxy overdensity appears explicitly and the redshift space distortions come in through a modification of the distribution $g_i(z)$.

[3]A similar approach is considered to model $\beta(z)$, appearing in the redshift space distortion contribution. For each bin we calculate an effective growth rate $f_i = (\Omega_{\mathrm{DM}}(z_i))^{0.56}$ where z_i is the mean redshift of the i-th bin, ignoring the scale dependence of the RSD growth.

Here, j_ℓ is the spherical Bessel function and $T(k,z)$ the matter transfer function relative to redshift zero[4]. The contribution due to redshift space distortions is

$$\begin{aligned}\Delta_l^{\mathrm{RSD},(i)}(k) &= \beta_i \int dz\, g_i(z)\, T(k,z) \left[\frac{(2l^2+2l-1)}{(2l+3)(2l-1)} j_l(kd(z)) \right. \\ &\quad - \frac{l(l-1)}{(2l-1)(2l+1)} j_{l-2}(kd(z)) \\ &\quad \left. - \frac{(l+1)(l+2)}{(2l+1)(2l+3)} j_{l+2}(kd(z))\right] . \end{aligned} \tag{4.11}$$

To compute the matter power spectrum at a given redshift $P_m(k,z) = P_m(k,z=0)\,T^2(k,z)$, we first make use of the CAMB code [82], which provides the linear power spectrum by integrating the Boltzmann equations of all species including massive neutrinos. We then apply the HaloFit prescription[5] [168] to the linear power spectrum to account for non-linear effects on the matter power spectrum.

While in the linear regime the galaxy spectrum is easy to model, calculations on non-linear scales inevitably have large uncertainties. This effect is aggravated by the presence of massive neutrinos since for the massive neutrino case the non-linear regime has been explored less extensively in the literature than for a vanilla ΛCDM model. In the non-linear regime, the matter power spectrum receives corrections due to gravitational collapse, the galaxy bias becomes scale-dependent, and redshift space distortions receive important contributions from velocity dispersion in collapsed objects. We take into account non-linear corrections to the matter spectrum using HaloFit. The effect of non-linearities on redshift space distortions at the relevant scales here is small as it is largely washed out by line-of-sight projection. However, we do expect significant corrections to our model on small scales due to non-linear galaxy bias, which we address below.

For angular scales where non-linear effects cannot be ignored, the contribution to a given angular mode ℓ from a redshift z comes exclusively from three-dimensional modes with wave vector $k \approx \ell/d(z)$. Clearly, to avoid large non-linear corrections, the analysis must be restricted to low ℓ. On the other hand, the density of modes per unit ℓ increases with ℓ so we want to use as many modes as possible without biasing the results. Figure 4.3 (left panel) depicts (as a function of redshift z) the value of ℓ above which non-linear corrections to the three-dimensional power spectrum contributions to the angular spectrum become important (i.e. $\ell_{\mathrm{NL}} \equiv k_{\mathrm{NL}}(z)\, d(z)$), considering various assumptions for the non-linear scale $k_{\mathrm{NL}}(z)$. Given that most of our signal is produced in the range $z = 0.45-0.65$, and assuming that our model becomes inadequate at $k > 0.15h\mathrm{Mpc}^{-1}$, we conclude that a conservative choice would be ℓ_{max} somewhere between 150 and 200.

Alternatively, we can obtain an indication of the importance of non-linear galaxy bias by considering the effect of non-linear corrections to the *matter* power spectrum[6] (which we

[4]The transfer function is defined as $\delta_m(\mathbf{k},z) = T(k,z)\,\delta_m(\mathbf{k},z=0)$.

[5]Recently, [169] developed an extension to HaloFit that incorporates the effect of massive neutrinos. We do not use this prescription as the correction to standard HaloFit is negligible on the scales of our interest.

[6]However, one must keep in mind that this may underestimate the effect of non-linear galaxy bias, as galaxies are more strongly clustered than matter and are thus prone to larger non-linear corrections.

do include in our model). The right panel in Figure 4.3 therefore shows the signal to noise ratio squared in the difference between our default model and the same model, but using the linear matter power spectrum instead of the non-linear (HaloFit) one. The signal to noise reaches one somewhere between $\ell_{\rm max} = 150$ and 200, corresponding to contributions of modes $k_{\rm max} \approx 0.10h{\rm Mpc}^{-1}$ and $k_{\rm max} \approx 0.14h{\rm Mpc}^{-1}$ at the median redshift $z = 0.55$. Finally, a more concrete indication of the importance of non-linear galaxy bias to the range of scales of our choice is given by Fig. 13 (left panel) of [170], which shows the halo bias as a function of three-dimensional mode k. Since for our sample of galaxies the bias $b \sim 2$, the plot confirms that there is only a mild bias variation in the relevant range of three-dimensional scales relevant to the multipole range we have chosen.

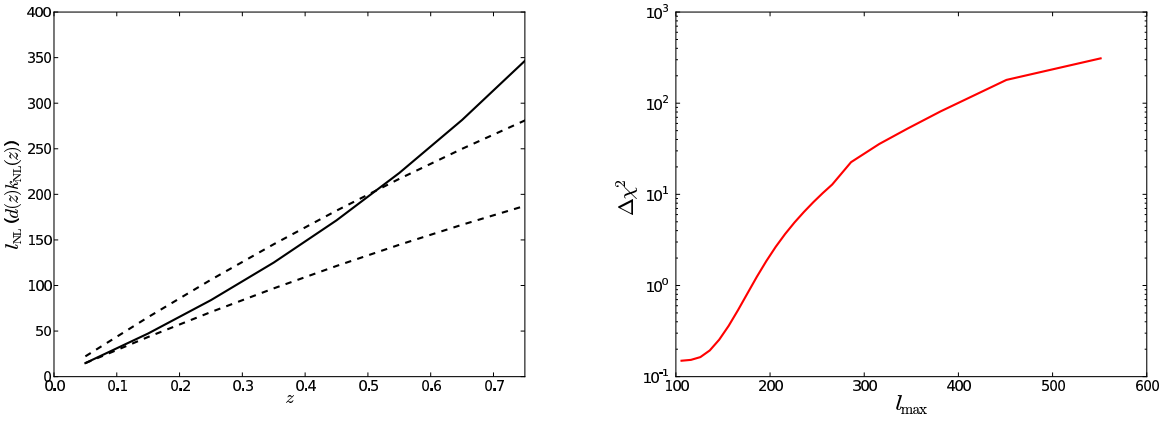

Figure 4.3: *Left panel*: Minimum multipole at which 3-D power spectrum contribution to the angular power spectrum receives important non-linear corrections, as a function of redshift, $\ell_{\rm NL} \equiv k_{\rm NL}\, d(z)$. We consider several choices of the non-linear scale $k_{\rm NL}$. The dashed curves are for $k = 0.15h{\rm Mpc}^{-1}$ (top) and $0.1h{\rm Mpc}^{-1}$ (bottom). The solid curve is for a simple model of a redshift dependent $k_{\rm NL}(z) = R_{\rm NL}(z = 0)/R_{\rm NL}(z) \times 0.1h{\rm Mpc}^{-1}$, where $R_{\rm NL}(z)$ is such that the matter overdensity variance averaged over spheres with this radius equals one (using the linear power spectrum). *Right panel*: The χ^2 difference as a function of $\ell_{\rm max}$ between our default template, which uses Halofit, and a template using the linear matter power spectrum, given the covariance matrix for the CMASS spectra. We assume the WMAP7 plus HST best fit cosmology and fix the bias parameters $b_i = 2$ ($a_i = 0$). Both plots suggest that non-linear effects start to become (mildly) relevant at $\ell_{\rm max}$ between 150 and 200.

Based on the above discussion, we choose a default value $\ell_{\rm max} = 200$, but we will also present results for the more conservative choice $\ell_{\rm max} = 150$. While it is possible to model the galaxy spectrum in a more sophisticated manner (see e.g. [171, 172, 151] for an approach based on perturbation theory and the local bias model [173], and [174] for a cross-comparison of a number of methods), we consider it appropriate, given the multipole range we include, to use the simple model described in Eq. (4.9), characterized by bias parameters b_i. In addition to this model, we also consider an alternative model with more freedom, by adding

shot noise-like parameters a_i,

$$C_\ell^{(ii)} = b_i^2 \frac{2}{\pi} \int k^2 dk \, P_m(k, z=0) \left(\Delta_\ell^{(i)}(k) + \Delta_\ell^{\mathrm{RSD},(i)}(k) \right)^2 + a_i \ . \tag{4.12}$$

The parameters a_i serve to mimic effects of scale-dependent galaxy bias and to model the effect of potential insufficient shot noise subtraction. This model is a version of what is sometimes referred to as the "P-model" (e.g. [175, 174]) and is independently motivated by the halo model [176, 177, 178, 179] and the local bias ansatz [180, 181, 172]. We further discuss the validity of the parameterizations with and without a_i in section 4.5.

Figure 4.2 shows the theoretical galaxy spectra as described in this section. The error bars follow from the optimal quadratic estimator method used to construct the power spectra (see [154] for details). Comparing the spectra with (black) and without (green) redshift space distortions shows that this effect is negligible for $\ell > 50$ and is probably not relevant for the range of scales we use in our data analysis, i.e. $\ell > 30$. Although we never employ it, we also show the effect of using the Limber approximation [182] and find that for $\ell > 30$ it works excellently.

4.4 Cosmological Signature of Neutrinos

In the analysis presented in this paper we assume that there are three species of massive neutrinos with equal masses m_ν. Massive neutrinos affect galaxy formation at scales below the Hubble horizon when they become non relativistic,

$$k_{nr} \simeq 0.0145 \left(\frac{m_\nu}{1 \text{ eV}} \right) \sqrt{\Omega_{\mathrm{DM}}} \, h\mathrm{Mpc}^{-1} \ , \tag{4.13}$$

with Ω_{DM} the present total dark matter energy density, i.e. cold dark matter plus massive neutrinos, relative to the critical density. The non-relativistic neutrino overdensities cluster at a given redshift z only at scales where the wavenumber of perturbations is below the neutrino free streaming scale

$$k_{fs}(z) = \frac{0.677}{(1+z)^{1/2}} \left(\frac{m_\nu}{1 \text{ eV}} \right) \sqrt{\Omega_{\mathrm{DM}}} \, h\mathrm{Mpc}^{-1} \ , \tag{4.14}$$

due to the pressure gradient, which prevents gravitational clustering. On spatial scales larger than the free streaming scale $k < k_{fs}$, neutrinos cluster and behave as cold dark matter (and baryons). Perturbations with comoving wavenumber larger than the free streaming scale can not grow due to the large neutrino velocity dispersion. As a consequence, the growth rate of density perturbations decreases and the matter power spectrum is suppressed at $k > k_{fs}$. Since the free streaming scale depends on the individual neutrino masses and not on their sum, a measurement of k_{fs} could, in principle, provide the ordering of the neutrino mass spectrum. In practice, such a task appears extremely challenging, see [183].

Figure 4.4 illustrates the effect of massive neutrinos on the angular power spectra. The solid curves depict the results for the four redshift bins exploited here in the case of a

ΛCDM model assuming no massive neutrino species and best fit parameters to WMAP7 year data [104, 90] and HST-H_0 data [2]. The dashed curves denote the angular power spectra results assuming three massive neutrinos with $\sum m_\nu = 0.3$ eV and keeping the cold dark matter mass energy density constant. In the presence of massive neutrinos the angular power spectra are suppressed at each redshift at an angular scale that is related to the free streaming scale by $\ell \sim d(z)\, k_{fs}(z)$. Therefore, the larger the neutrino mass (or the redshift), the larger the lowest angular wavenumber at which the power spectrum is maximally suppressed. In the redshift range of interest here and for $\sum m_\nu = 0.3$ eV, the suppression angular scale appears in the range $\ell = 20 - 50$ (however, there is some suppression even at lower ℓ). Note as well that there will exist a strong degeneracy between the neutrino masses and the amount of cold dark matter, since, in principle, one could partially compensate the growth suppression induced by massive neutrinos at scales $k > k_{fs}$ by increasing the cold dark matter mass-energy density. Combination with CMB and H_0 data will help to break this degeneracy.

Neutrino masses affect the angular power spectra C_ℓ, see Eq. (4.9), in two different ways: suppressing galaxy clustering and the growth of structure via $P_m(k)$ as well as modifying the background expansion rate via the comoving distance which appears in the argument of the Bessel function j_ℓ. Among these two effects (i.e. growth versus background) we find that the growth suppression effects in the matter power spectrum due to the presence of massive neutrinos will dominate over background effects. Therefore, the neutrino mass constraints presented in the following analysis arise mostly from the suppression of clustering rather than from purely geometrical effects.

4.5 Mocks

We first consider angular spectra based on mock galaxy catalogs to test that neither our method of estimating the spectra nor our modeling of the spectra introduces a bias in the reconstructed cosmological parameters. We use twenty independent CMASS mock catalogs based on N-body simulations and a Halo Occupation Distribution (HOD) model described in [37] (see also [154, 155] for details). The input cosmology for the simulations is $\Omega_{\rm DM} = 0.274, h = 0.7, \Omega_b = 0.046, n_s = 0.95, \sigma_8 = 0.8$ in a spatially flat universe, with n_s and σ_8 the scalar spectral index and the linear rms density fluctuations in spheres of radius $8\,h^{-1}$Mpc at $z = 0$, respectively. Neutrinos are massless in the input cosmology. The catalogs cover a cubic volume with side $1.5h^{-1}$ Gpc. To construct an "observed" catalog, we put the observer in one corner of the box and consider the subsample of galaxies in the shell octant between the observer's $z = 0.5 - 0.55$. For simplicity, we do not apply photometric redshift errors nor do we introduce redshift shifts due to peculiar velocities. This latter effect would only be significant on very large scales anyway (see Figure 4.2). Each mock covers $\pi/2$ rad^2 and consists of about 125,000 galaxies. Since both area and galaxy number are thus roughly half the values for the $z = 0.5 - 0.55$ redshift bin of the true data, the number density is comparable to that of the true photometric sample. We apply this procedure for eight different corners to get eight different lines of sight per simulation. Note, however, that

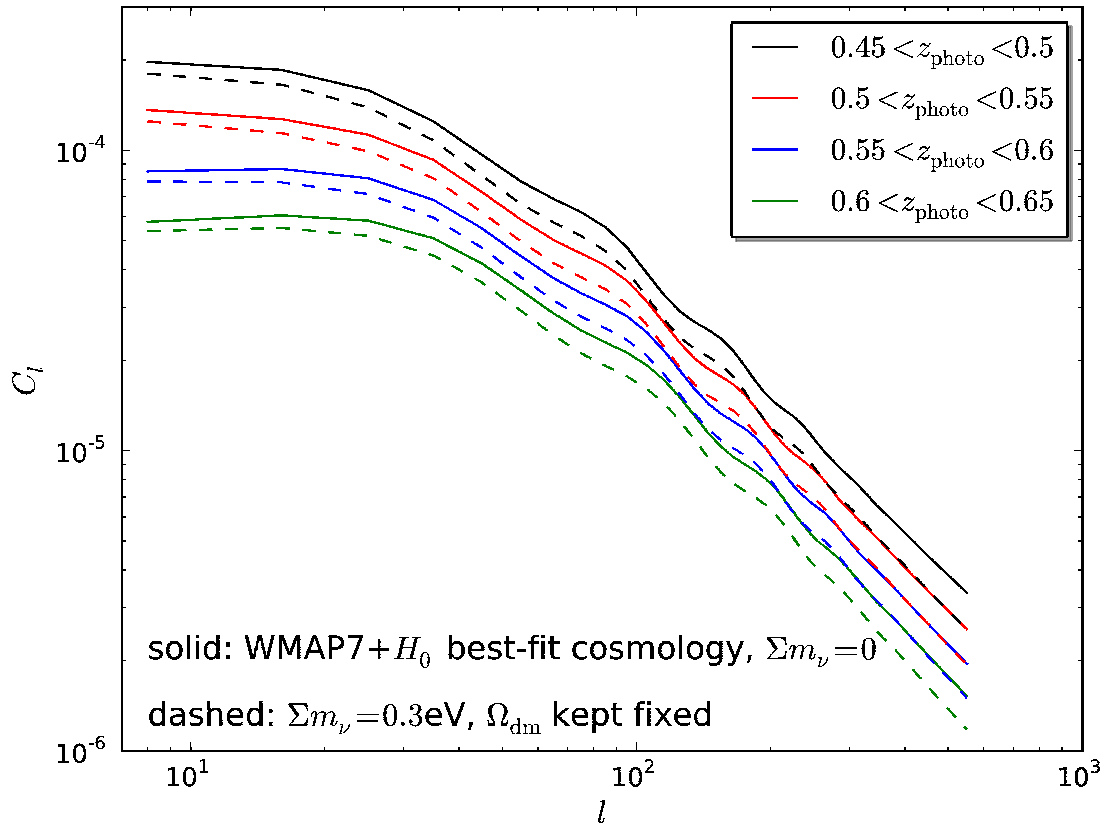

Figure 4.4: Effect of neutrinos on the angular power spectra. The solid and dashed curves depict the massless and $\Sigma m_\nu = 0.3$ eV cases, respectively.

these lines of sight are not completely independent as they are based on the same simulation volume. Finally, for each line of sight, we average the spectra over all twenty independent realizations in order to increase the signal to noise ratio. The covariance matrix for the mock angular power spectrum is rescaled accordingly to reflect the decrease in covariance due to taking the average.

As described in section 4.3, we consider a model characterized by the cosmological parameters and a galaxy bias b_0 (giving our mock bin the label 0), and a more conservative model with bias b_0 *and* nuisance parameter a_0, so that the spectrum is given by

$$C_\ell^{(00)} = b_0^2 \frac{2}{\pi} \int k^2 dk \, P_m(k, z=0) \left(\Delta_\ell^{(i)}(k)\right)^2 + a_0 \ . \tag{4.15}$$

In the galaxy bias-only version, a_0 is simply set to zero.

As a direct test of this model, we fit it to the averaged mock spectrum. In this first approach, we keep the cosmology fixed to the mock's input cosmology and restrict the fit to the range $\ell = 30 - 200$. The only free parameters are thus either b_0 or (b_0, a_0). We use a

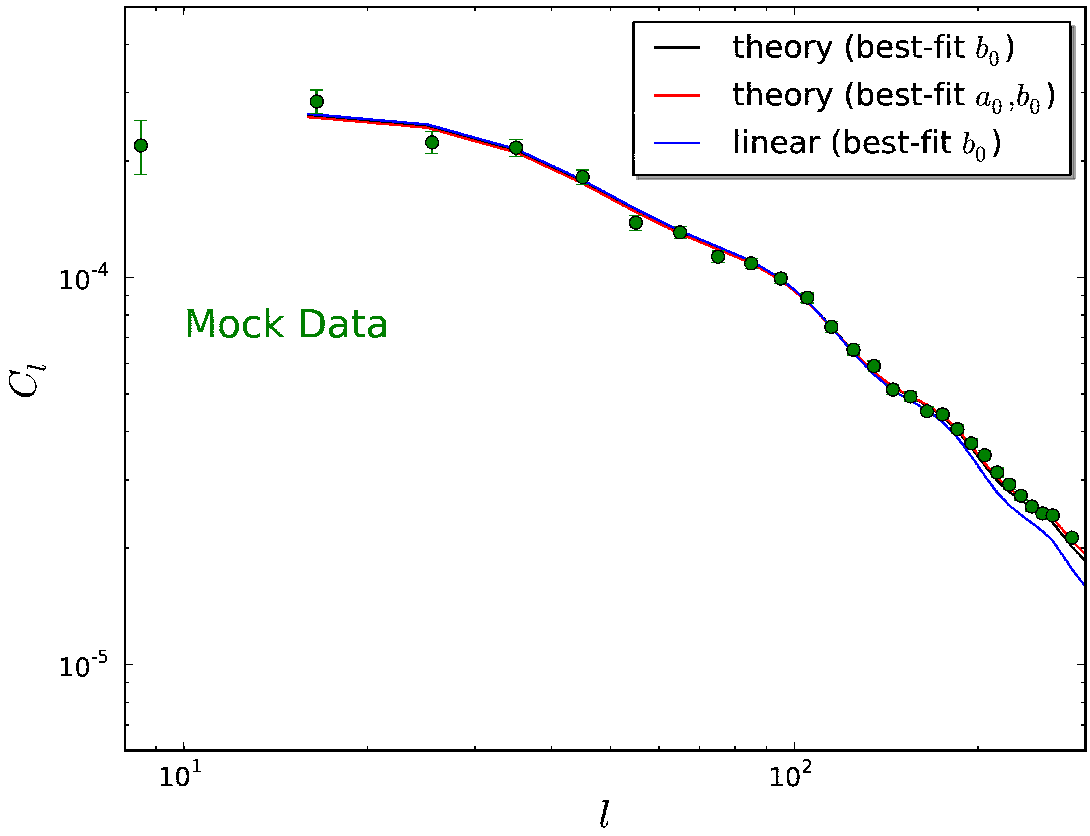

Figure 4.5: Example of an averaged mock spectrum (green points with error bars) and theoretical spectra (solid lines). Fixing the cosmology to the mock input cosmology (see text), we fit the averaged mock spectrum in the range $\ell = 30 - 200$ to our model described in the text. The black curve is the resulting best-fit spectrum if we only fit a (scale-independent) galaxy bias b_0 (best-fit value $b_0 = 2.02$), while the red curve is the best fit in a model that also includes the nuisance parameter a_0 (best fit values $b_0 = 2.00$, $a_0 = 1.05 \cdot 10^{-6}$). To provide a hint of the importance of non-linear effects in this multipole range, we plot the spectrum based on a linear three dimensional matter power spectrum in blue ($b_0 = 2.02, a_0 = 0$)

modification of the publicly available COSMOMC package [103] to sample this parameter space using Monte Carlo Markov Chains (MCMC). We show the resulting best-fit spectra together with the mock average in Fig. 4.5. Considering first the default, galaxy bias-only model (black curve), we find that the best fit to the mock result has a linear bias $b_0 = 2.02$ (with uncertainty $\sigma(b_0) < 0.01$) and has $\chi^2 = 11.3$. This should be compared to an expectation value of $\langle \chi^2 \rangle = 16$ based on 17 data bins and one free parameter. The galaxy bias model thus provides a good fit to the simulated spectrum (the probability of getting a χ^2 lower than 11.3 for an expectation value of 16 is approximately 20%).

Next, including the shot noise-like parameter a_0 to take into account potential resid-

ual shot noise and/or non-linear effects not captured by our simple Halofit plus scale-independent galaxy bias model, we find a best fit model with $a_0 = 1.1 \cdot 10^{-6}$ and $b_0 = 2.00$. However, the uncertainty in a_0 is $\sigma(a_0) = 1.0 \cdot 10^{-6}$ so the preference for a non-zero value cannot be considered significant. In this model, we find $\chi^2 = 10.1$, to be compared to the expected $\langle\chi^2\rangle = 15$. This is only a marginal ($\Delta\chi^2 \approx 1.2$) improvement.

Restricting the fitting range to $\ell = 30 - 150$, we find $\Delta\chi^2 = 1.1$ between the two best-fit models, and $a_0 = (1.8 \pm 1.9) \times 10^{-6}$.

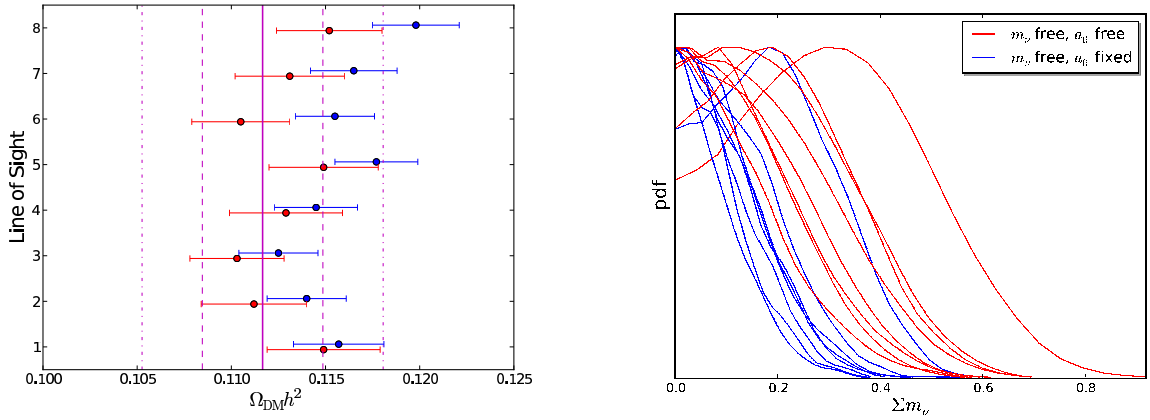

Figure 4.6: *Left panel:* Recovered values of $\Omega_{\rm DM}h^2$ from averaged mock spectrum together with CMB prior. We consider spectra from eight different lines of sight. The points with error bars show the posterior mean values and 1σ error bars after the Monte Carlo analysis for two scenarios: varying Σm_ν *with* (red) and *without* (blue) a_0 marginalized. The vertical magenta lines indicate the input value $\Omega_{\rm DM}h^2 = 0.11166$ (solid) and the input $\pm$ one and two σ, where $\sigma = 0.0032$ is the parameter uncertainty based on the data set WMAP7+HST+angular spectra ($a_i = 0$ fixed). There is a bias of about 1σ without the nuisance parameter, which disappears when a_i is marginalized over. *Right panel:* The posterior neutrino mass distributions for the two cases discussed above. The mock constraints are consistent with the input cosmology of $\Sigma m_\nu = 0$. Other parameters are all reconstructed to close to their input values and are not strongly affected by the angular spectra.

The comparison above suggests that for the range $\ell = 30 - 200$, the galaxy bias model without an extra nuisance parameter may be sufficient. We now undertake a more complete check of our model and the entire cosmology analysis by using MCMC to fit the full space of cosmological parameters as well as the galaxy bias (and shot noise parameter) to the averaged mock spectrum. The differences between the resulting best-fit parameter values and the "true", i.e. input, values give an indication of the parameter bias introduced by our method. To break parameter degeneracies, while not letting the prior bias us away from the input cosmology, we include a "mock" CMB prior[7], which will provide a likelihood similar

[7] The "mock" CMB prior is defined by $\chi^2_{\rm WMAP7} \equiv (p_i - p_{i,\rm input})\,{\rm COV}^{-1}_{ij}\,(p_j - p_{,\rm input})$, where p_i are the parameters at each point of the chain, $p_{i,\rm input}$ the input parameters, ${\rm COV}_{ij}$ is the WMAP7 covariance matrix and i, j are summed over.

to the true WMAP7 one, except shifted to be centered around the mock input parameters.

We want any deviation between the input cosmology and the recovered cosmology to be small compared to the uncertainty level of the actual data. We therefore take information from our final results and use the uncertainties for the WMAP+HST+CMASS ($\ell_{\rm max} = 200$) real data case for comparison. If the biases on parameter estimation are small compared to these numbers, it provides strong motivation for considering our approach sound, as most uncertainties in the next section will be larger than in the WMAP+HST+CMASS case. Therefore, parameter uncertainties σ referred to in the remainder of this section are these data-based uncertainties.

Starting with the parameter space[8] $\{\Omega_b h^2, \Omega_{\rm DM} h^2, \theta, A_s, n_s, \tau, b_0\}$, we find that all cosmological parameters are reproduced to within 1σ of the input values (although the parameter most affected by the mock CMASS data, $\Omega_{\rm DM} h^2$, is higher than the input by close to 1σ).

Unfortunately, we do not have mocks based on a cosmology with non-zero Σm_ν. One check we *can* do, however, is to fit a model with parameters $\{\Omega_b h^2, \Omega_{\rm DM} h^2, \theta, A_s, n_s, \tau, \Sigma m_\nu, b_0\}$ to our $\Sigma m_\nu = 0$ mock spectra. The parameters affected by far the most by the angular spectra are (again) $\Omega_{\rm DM} h^2$ and Σm_ν. We show the posteriors of this calculation in Fig. 4.6. In the left panel, the vertical lines indicate the $\Omega_{\rm DM} h^2$ input value, and the 1σ and 2σ bounds based on the uncertainty σ from the actual data. The blue points with error bars are the posterior mean values and 1σ recovered errors after fitting to the averaged mock spectrum. Note that the recovered error bars (from the averaged mock power spectrum) are typically similar to the data-based error bars. While the different lines of sight are not entirely independent, Fig. 4.6 points towards a bias of about $1 - 1.5\sigma$ in $\Omega_{\rm DM} h^2$. For the neutrino mass, the right panel shows the posterior probability distributions in blue. The posteriors are always consistent with the input value $\Sigma m_\nu = 0$ and can be interpreted as providing upper bounds. We have made the same plot as in the left panel for the other parameters and they were biased significantly less (as their reconstruction is dominated by the mock CMB prior).

Adding the nuisance parameter a_0, we obtain the red points and curves in Fig. 4.6. The effect of marginalizing over a_0 is to diminish the parameter bias so that $\Omega_{\rm DM} h^2$ is typically reconstructed to well within 1σ. We attribute this change to a_0 accounting for a possible scale-dependence in galaxy bias on quasilinear scales. The neutrino constraints are also still consistent with the input, although the mock upper limits do become significantly weaker. We have also studied mock cosmology constraints using $\ell_{\rm max} = 150$, and found that the main effect is to widen the posterior distributions slightly, while the change in parameter bias relative to $\ell_{\rm max} = 200$ is small.

We conclude that our galaxy bias-only model and the fitting method used here properly reproduce the input cosmology for our choices of $\ell_{\rm max}$, except that there is a bias of about $1 - 1.5\sigma$ in $\Omega_{\rm DM} h^2$. The model with nuisance parameter a_0 removes this parameter bias at the cost of larger error bars. While the bias in $\Omega_{\rm DM} h^2$ is not extreme, being only slightly above the 1σ level, it is sufficiently worrying that we will quote results for the galaxy bias-

[8]The parameters θ, A_s and τ represent the ratio between the sound horizon and the angular diameter distance at decoupling, the scalar amplitude of primordial fluctuations and the reionization optical depth, respectively.

only model *and* for the more conservative model with shot noise-like parameters. Changing $\ell_{\rm max}$ between 150 and 200 does not have a large effect on how well the models compare to mocks, suggesting that both are reasonable choices. We will quote results for both ranges.

4.6 Results

While the CMASS angular galaxy power spectra carry useful information about the sum of neutrino masses Σm_ν, the effect of Σm_ν is degenerate with certain other parameters which are not well constrained from the angular spectra alone. There are many combinations of external data sets that our angular spectra can be combined with to fix this problem. One approach would be to optimize the neutrino bound by combining as many data sets as possible. However, we choose instead to focus as much as possible on the effect of the CMASS photometric data and therefore consider mostly simple priors. Our two main prior choices are WMAP7 CMB data [104] and the combination of WMAP7 with the HST measurement of the Hubble parameter [2]. At the end of this section, we will briefly consider the effect of adding the Union 2 supernova compilation [15] and the measurement of the BAO scale based on SDSS Data Release 7 [184] spectroscopic data from Ref. [185].

We again use a modification of the publicly available COSMOMC package [103] to sample the parameter space using MCMC. Our parameter space consists of the six usual ΛCDM parameters, $(\Omega_b h^2, \Omega_{\rm DM} h^2, \theta, \ln(10^{10}\, A_s), n_s, \tau)$, the neutrino mass fraction f_ν, defined as $\Omega_\nu/\Omega_{\rm DM}$ (where $\Omega_{\rm DM}$ includes cold dark matter and massive neutrinos), in addition to $A_{\rm SZ}$, describing the amplitude relative to a template of the Sunyaev-Zel'dovich contribution to the CMB [186], the four galaxy bias parameters b_i and (optionally) the four nuisance parameters a_i, leaving us with a maximum total number of parameters of sixteen parameters. We put uniform priors on these parameters and derive Σm_ν using Eq. (4.1).

95% CL $\sum m_\nu$[eV]	prior only	prior+CMASS,$\ell_{\rm max} = 150$	prior+CMASS,$\ell_{\rm max} = 200$
WMAP7 prior	1.1	0.74 (0.92)	0.56 (0.90)
WMAP7 + HST prior	0.44	0.31 (0.40)	0.26 (0.36)

Table 4.1: The 95% confidence level upper limits on the sum of the neutrino masses Σm_ν. The top row investigates the effect of adding the CMASS galaxy power spectra to a WMAP prior while the bottom row uses WMAP and the H_0 constraint from HST as a prior. In parentheses we show results for the more conservative model marginalizing over the shot noise-like parameters a_i.

We first consider the WMAP7 prior and show how the neutrino bound improves as CMASS data are added. The resulting 95% CL upper limits are shown in the top row of Table 4.1, with the results with a_i marginalized in parentheses. The bound improves from 1.1 eV for CMB only to 0.56 eV for CMB with CMASS data ($\ell_{\rm max} = 200$). This constraint is comparable to the limit $\Sigma m_\nu < 0.62$ eV derived by [105] from the DR7 spectroscopic

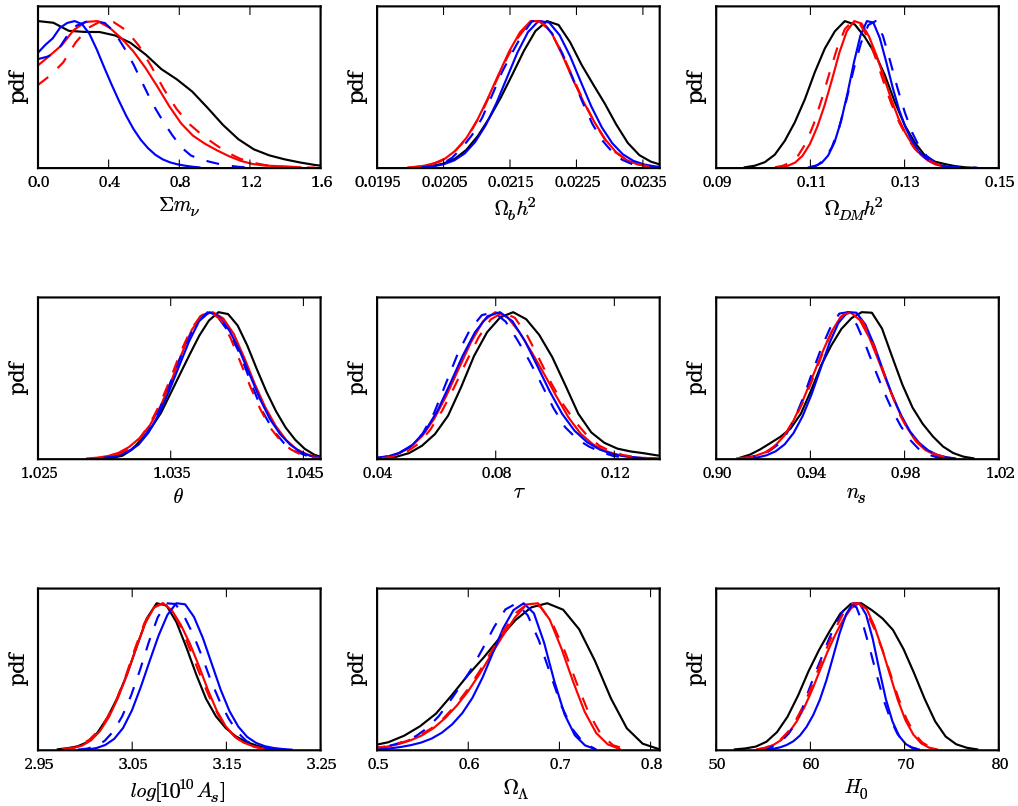

Figure 4.7: Cosmological constraints with a WMAP7 CMB prior. We show the probability distribution functions for CMB only (black), CMB with CMASS spectra in the range $\ell = 30 - 150$ (blue dashed) and CMB with CMASS spectra in the range $\ell = 30 - 200$ (blue solid). The red curves represent the constraints in the conservative model where we marginalize over a set of nuisance parameters a_i.

sample. It thus appears that the advantage of spectroscopic redshifts (providing information on clustering along the line of sight) in that sample is offset by the advantage of the current sample having a larger volume, although there are other differences between the samples and analyses as well. Note, however, that the constraint deteriorates significantly when marginalizing over the nuisance parameters a_i. In this case, the mass bound is not significantly better than with CMB alone. We show the posterior probability distributions for Σm_ν and the other cosmological parameters in Fig. 4.7.

We next consider the constraints using WMAP7 with HST H_0 prior. The CMB alone provides a strong measurement of one combination of late-universe parameters through its sensitivity to the distance to the last scattering surface. However, this distance measurement leaves a degeneracy between Ω_Λ and Σm_ν so that the CMB-only limit on the neutrino mass arises mainly from the effect of neutrinos on the primary anisotropies and not from this

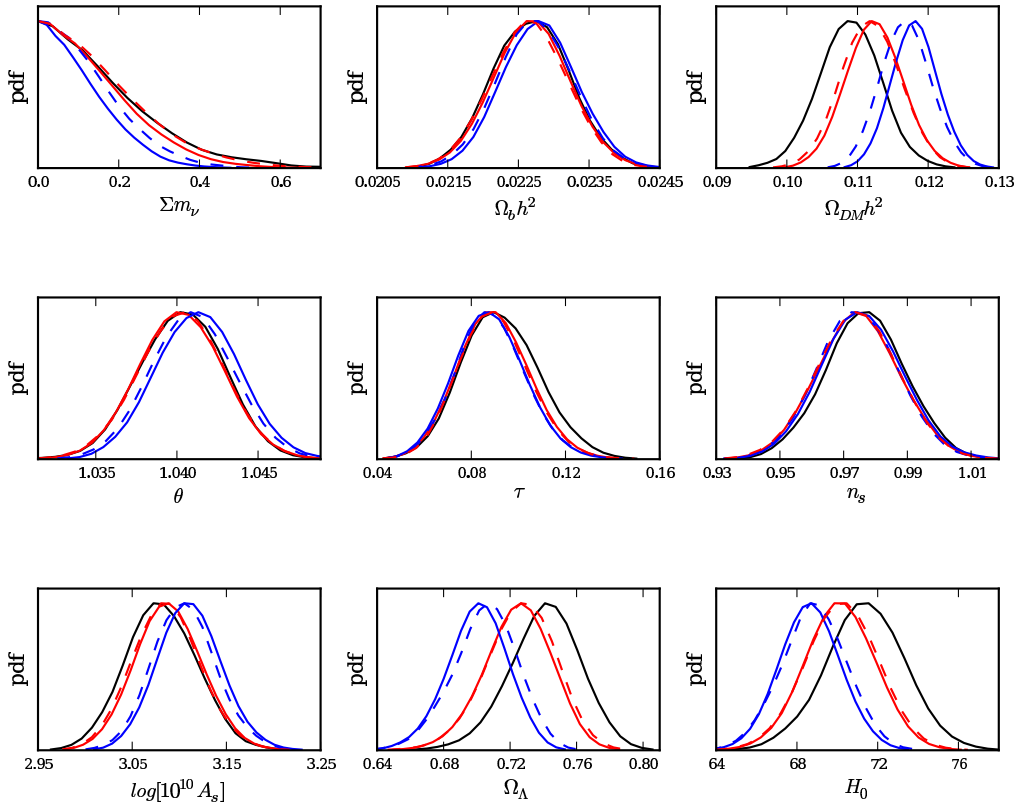

Figure 4.8: Cosmological constraints with a WMAP7 CMB *and* Hubble parameter prior. We show the probability distribution functions for CMB + H_0 only (black), CMB + H_0 with CMASS spectra in the range $\ell = 30 - 150$ (blue dashed) and CMB + H_0 with CMASS spectra in the range $\ell = 30 - 200$ (blue solid). The red curves represent the constraints in the conservative model where we marginalize over a set of nuisance parameters a_i. While this marginalization degrades the neutrino bound, simulations have shown it removes the bias in $\Omega_{\rm DM} h^2$ (see section 4.5).

distance measurement. Measuring H_0 constrains a different combination of late universe parameters and thus breaks the CMB degeneracy. This is why the WMAP7+HST bound is so much stronger than the WMAP7-only one, i.e. $\Sigma m_\nu < 0.44$ eV as opposed to $\Sigma m_\nu < 1.1$ eV. Adding the CMASS angular spectra tightens the bound significantly so that an impressive upper bound of $\Sigma m_\nu < 0.26$ eV is reached for $\ell_{\rm max} = 200$ (in the bias-only model), as is shown in the second row of Table 4.1. The effect of marginalization over a_i is again to bring the constraint back to closer to the CMB+HST bound.

The posteriors for all cosmological parameters are shown in Fig. 4.8. In addition to the full likelihoods for Σm_ν, summarized in Table 4.1, the $\Omega_{\rm DM} h^2$ posteriors are worth noting. The effect of the angular spectra is to strongly shift the average value of this parameter

(blue curve), while including the nuisance parameters (red curve) weakens the shift. The last two parameters in Fig. 4.8 (and 4.7), Ω_Λ and H_0, are not independent and can be expressed in terms of the preceding parameters. The shift thus is really only significant for one independent parameter, $\Omega_{\rm DM}h^2$, in our basis. The results in section 4.5 suggest that the shift in the bias-only case might partially be a bias due to our model and that the results with a_i marginalized are unbiased.

We do not explicitly show the correlations between parameters, but have verified that, in the CMB+CMASS case, the neutrino mass has its strongest degeneracies with $\Omega_{\rm DM}h^2$, the bias parameters b_i and σ_8. While, in agreement with our discussion in section 4.4, the inclusion of the Hubble prior removes the $\Sigma m_\nu - \Omega_{\rm DM}h^2$ degeneracy, the strong correlations with b_i and σ_8 remain.

We have also added supernova and BAO data to the CMB+HST+CMASS data set, and considered the neutrino mass bound in the bias-only model, but we found negligible improvement (from 0.26 eV to 0.25 eV) relative to the case without these additional data sets. These additional data sets do carry significant information, but this information is degenerate with the information already present in the three default data sets.

For the multipole range $\ell = 30 - 150$, we show the results using dashed lines in Figures 4.7 and 4.8. The 95% CL upper limit for CMB+HST+CMASS in this case is 0.31(0.40) eV and for CMB+CMASS it is 0.74 (0.92) eV fixing (varying) $a_i = 0$. A significant amount of information is thus contained in the large ℓ range of multipoles, which makes sense as the number of modes is large.

Finally, we consider the question of where most of the neutrino mass information comes from. In principle, massive neutrinos affect the angular power spectra both by their small-scale suppression of the three-dimensional power spectrum, and by changing the projection of physical scales onto angular scales through their effect on the background expansion. As discussed in section 4.4, we expect the former effect to carry more constraining power than the latter effect. We test this by running Monte Carlo chains where the effect of massive neutrinos on the three-dimensional power spectrum is artificially taken out, while the effect on the background expansion is left intact. Specifically, we replace the usual linear CAMB power spectrum by the spectrum given by the Eisenstein and Hu (EH) fitting formula [187], which does not include the effect of massive neutrinos. We find that in this setup, including the CMASS galaxy power spectra does *not* improve the neutrino mass bound relative to the case with CMB, or with CMB+HST, only. In other words, the projection effect alone carries little information on neutrino mass (at least after marginalizing over the effects of other parameters) and the bounds quoted in this manuscript can be attributed to the small-scale suppression of the three-dimensional power spectrum.

4.7 Conclusions

We have exploited angular power spectra from the SDSS-III DR8 sample of photometric galaxies with CMASS selection criteria to put interesting constraints on the sum of neutrino masses. We have used mock galaxy catalogs based on N-body simulations and HOD mod-

eling to test two models for the angular galaxy spectra. Based on these tests, we decided to compare the data to theoretical spectra based on the non-linear matter power spectrum augmented by a linear galaxy bias factor. However, since this model does result in a bias in $\Omega_{\rm DM}h^2$ of $\sim 1-1.5\sigma$, we have also fitted the data to a more conservative model, with an additional set of shot noise-like fitting parameters, in which this bias is virtually absent. The tests also motivated us to use the multipole range $\ell = 30-200$, but we quoted results for the more conservative choice $\ell = 30-150$ as well. The added advantage is that this analysis provides insight into the range of scales that yields the galaxy clustering information.

Combining the CMASS data with a CMB prior from the WMAP7 survey, we find an upper bound $\Sigma m_\nu < 0.56$ eV (0.90 eV) at 95% confidence level for $\ell_{\rm max} = 200$ in the model with free parameters b_i (b_i and a_i). Adding the HST measurement of the Hubble parameter, the probability distribution tightens and we find $\Sigma m_\nu < 0.26$ eV (0.36 eV). We have also considered the effect of adding supernova and a (lower redshift) BAO measurement, but when the HST prior is included already, these additions lower the upper limit to 0.25 eV (in the bias-only model). Considering the dependence on the multipole range, characterized by a maximum multipole $\ell_{\rm max}$, we find that a significant amount of information resides in the largest multipoles $\ell = 150-200$, but that even for $\ell_{\rm max} = 150$, the galaxy spectra place a strong bound on neutrino mass. Our main results are summarized in Table 4.1.

It is interesting to compare these results to the outcome of an analysis of a similar (but smaller) high redshift SDSS photometric catalog, the MegaZ sample [188]. In [150], the strongest bound quoted is a 95% CL upper limit of 0.28 eV, including SN and BAO data in addition to CMB, HST and MegaZ. However, this particular bound is based on a multipole range with $\ell_{\rm max} = 300$ and no nuisance parameters a_i. As we have discussed extensively, we believe $\ell_{\rm max} = 200$ (or even slightly lower) is a better choice if one wants to avoid significant, unknown non-linear corrections to the galaxy bias. For this choice, the MegaZ sample yields an upper bound of 0.34 eV. Assuming the aggressive, bias-only model (as in the MegaZ analysis). the value we find for the CMASS sample is 0.25 eV, which is thus a significant improvement. However, it must be kept in mind that this model causes a small parameter bias and that the more conservative model yields a weaker bound of 0.36 eV.

The bounds presented here rule out the quasi-degenerate neutrino mass hierarchy. For example, for $\Sigma m_\nu = 0.25$ eV, it follows from $|\Delta m^2_{23}| = 2.5\cdot 10^{-3}$ eV^2 that the mass difference $|m_3 - m_2| \approx 0.015$ eV, so that the largest mass difference is $|m_3 - m_2|/(\Sigma m_\nu/3) \approx 20\%$ of the average neutrino mass. We are thus entering the regime where the mass splittings are significant. Looking forward, the prospects are exciting. As the sensitivity of cosmological neutrino mass measurements improves, the sum of the masses will either be measured, i.e. a value that can be distinguished from zero will be found, or the upper limit will be sharpened. However, even in the latter case, interesting things can be learned. If the sum of the masses is found to be less than ~ 0.1eV, this rules out the inverted hierarchy, leaving the normal hierarchy as the only option. Moreover, even in the normal hierarchy, Σm_ν is not allowed to be lower than ~ 0.05eV so that sooner or later a measurement, rather than an upper bound, can be expected.

Finally, we note that BOSS is currently taking spectra for a sample of galaxies with the

same selection criteria as the galaxies considered in this paper and will reach a sample of approximately $1,500,000$ galaxies when finished in 2014. The results presented here are thus only the tip of the iceberg of what can be done with BOSS. The spectroscopic data will allow a measurement of the three-dimensional power spectrum for an even larger volume than considered here (if the low redshifts sample is included) so that also clustering in the line-of-sight direction can be resolved, thus promising significantly stronger cosmology constraints than from the photometric data.

Chapter 5

Neutrino and Dark Radiation properties in light of CMB observations

In this Chapter we set new bounds on the dark radiation and neutrino properties in different cosmological scenarios combining the ACT and SPT data with the nine-year data release of the Wilkinson Microwave Anisotropy Probe (WMAP-9), Baryon Acoustic Oscillation data, Hubble Telescope measurements of the Hubble constant and Supernovae Ia luminosity distance data. This Chapter is a copy of the paper:

Neutrino and Dark Radiation properties in light of latest CMB observations, Maria Archidiacono, Elena Giusarma, Alessandro Melchiorri & Olga Mena, 2013, published in Physical Review D 87, 103519 (2013),

5.1 Introduction

Solar, atmospheric, reactor, and accelerator neutrinos have provided compelling evidence for the existence of neutrino oscillations. Barring exotic explanations, oscillation data imply non-zero neutrino masses. However, oscillation experiments only provide bounds on the neutrino mass squared differences, and therefore the measurement of the absolute scale of the neutrino mass must come from different observations. In the Standard Model of elementary particles, there are three active neutrinos. However, additional sterile neutrino species, or extra relativistic degrees of freedom could also arise in a number of extensions to the standard model of particle physics, as for instance, in axion models [70, 71], in decaying of non-relativistic matter models [72], in scenarios with gravity waves [73], extra dimensions [74, 75, 76], early dark energy [77] or in asymmetric dark matter models [78]. Cosmological data provide a tool to test the neutrino properties, since the neutrino masses and abundances affect both the Cosmic Microwave Background (CMB) physics as well as the galaxy clustering properties, see Refs [93, 94, 100, 99, 91, 92, 101, 189, 87, 94, 190, 191, 192, 193, 194, 195, 196, 197] for constraints on the neutrino masses and/or abundances with a variety of cosmological data sets and different assumptions regarding the fiducial cosmology.

On the other hand, cosmological measurements also allow to test the clustering properties of the extra relativistic degrees of freedom, parameterized via $N_{\rm eff}$, being $N_{\rm eff} = 3.04$ in the standard model scenario. The clustering pattern of the dark radiation component is represented by its rest frame speed of sound $c^2_{\rm eff}$ and its viscosity parameter $c^2_{\rm vis}$. The former parameter controls the relationship between velocity and anisotropic stress, being these parameters $c^2_{\rm eff} = c^2_{\rm vis} = 1/3$ if the dark radiation background is composed by neutrinos. Several analyses have set bounds on these parameters [198, 199, 200] under different assumptions regarding the underlying cosmological model.

Recently new CMB data have become available. The Wilkinson Microwave Anisotropy Probe (WMAP) collaboration has presented the cosmological implications of their final nine–year data release [18], finding $\sum m_\nu < 0.44$ eV at the 95% CL and $N_{\rm eff} = 3.84 \pm 0.40$ (being $N_{\rm eff}$ the number of thermalised massless neutrino species) when they combine their data with CMB small scale measurements (as those from previous data releases from both the Atacama Cosmology Telescope ACT [201] and the South Pole Telescope SPT [19]), Baryon Acoustic Oscillations (BAO) and Hubble Space Telescope (HST) measurements.

The SPT collaboration has also recently presented their observations of 2540 deg^2 of sky, providing the CMB temperature anisotropy power over the multipole range $650 < \ell < 3000$ [20, 21], corresponding to the region from the third to the ninth acoustic peak. The SPT measurements have found evidence for a decreasing power at high multipoles relative to the predictions within a ΛCDM scenario, which suggest, potentially, that extensions to the minimal ΛCDM scenario might be needed. In the case in which massive neutrinos are added in the cosmological data analyses, the SPT collaboration finds that the combination of SPT data with WMAP (7 year data), together with Baryon Acoustic Oscillation (BAO) and Hubble Space Telescope (HST) measurements shows a 2σ preference for these models (when compared to the ΛCDM scenario). In the case of three active massive neutrinos, they find $\sum m_\nu = 0.32 \pm 0.11$ after considering CMB, BAO, HST and SPT cluster measurements. However, if the BAO measurements are removed and only CMB and HST data are considered, the evidence for neutrino masses disappears at the 95% CL. The authors of Ref. [20] also find that when a curvature component or a running in the spectral index of the primordial perturbation spectrum are added as free parameters together with $\sum m_\nu$, the preference for nonzero neutrino masses is significantly reduced. When $N_{\rm eff}$ massless neutrinos are considered, the bounds are $N_{\rm eff} = 3.71 \pm 0.35$ for the combination of CMB, BAO and HST data sets. Finally, when allowing for $N_{\rm eff}$ massive neutrino species the bounds are $\sum m_\nu = 0.51 \pm 0.15$ eV and $N_{\rm eff} = 3.86 \pm 0.37$, implying a $\sim 3\sigma$ preference for $\sum m_\nu > 0$ and a 2.2σ preference for $N_{\rm eff} > 3.046$.

These findings, if confirmed by future CMB observations, as those by the ongoing Planck mission [9], have an enormous impact for Majorana neutrino searches. The mean value for $\sum m_\nu$ found by the SPT collaboration implies a quasi-degenerate neutrino spectrum and therefore the discovery of the neutrino character becomes at reach at near future neutrinoless double beta decay experiments [202].

However, and also recently, the ACT collaboration has released new measurements of the CMB damping tail [22], finding a much lower value for $N_{\rm eff} = 2.79 \pm 0.56$ when combining with WMAP 7 year data. When considering also BAO and HST measurements, the value

is higher, $N_{\rm eff} = 3.50 \pm 0.42$.

The two data sets, SPT and ACT, seem also to disagree in the value of the lensing amplitude parameter A_L at more than 95% CL [203]. On the other hand, ACT data do not seem to see evidence for neutrino masses, placing an upper limit of $\sum m_\nu < 0.39$ eV at 95% CL when ACT data are combined with WMAP 7 year data together with BAO and HST measurements.

We explore here the cosmological constraints in several neutrino and dark radiation scenarios including the new WMAP 9 year data as well as the new SPT and ACT measurements at high multipoles ℓ. We also consider the impact of other cosmological data sets, as BAO, HST and Supernova Ia luminosity distance measurements. We start with the massive neutrino case within a ΛCDM scenario, setting bounds first on $\sum m_\nu$ assuming three massive neutrinos and then moving to the case in which there are $N_{\rm eff}$ massive species with a total mass given by $\sum m_\nu$. We then enlarge the minimal ΛCDM scenario allowing for more general models with a constant dark energy equation of state or with a running of the scalar spectral index. We continue by studying the dark radiation properties, focusing first on the thermal abundances $N_{\rm eff}$ and adding after the dark radiation clustering properties $c^2_{\rm vis}$ and $c^2_{\rm eff}$ as free parameters in the analysis.

The structure of the paper is as follows. In Sec. 6.3 we describe the data sets used in the numerical analyses as well as the cosmological parameters used in each of the neutrino and dark radiation models examined in Sec. 5.3. We draw our conclusions in Sec. 5.4.

5.2 Data and Cosmological parameters

The standard, three massive neutrino scenario we explore here is described by the following set of parameters:

$$\{\omega_b, \omega_c, \Theta_s, \tau, n_s, \log[10^{10} A_s], \sum m_\nu\} \ , \tag{5.1}$$

being $\omega_b \equiv \Omega_b h^2$ and $\omega_c \equiv \Omega_c h^2$ the physical baryon and cold dark matter energy densities, Θ_s the ratio between the sound horizon and the angular diameter distance at decoupling, τ is the reionization optical depth, n_s the scalar spectral index, A_s the amplitude of the primordial spectrum and $\sum m_\nu$ the sum of the masses of the three active neutrinos in eV. We assume a degenerate neutrino mass spectrum in the following. The former scenario is enlarged with $N_{\rm eff}$ massive neutrinos in the case of extended models

$$\{\omega_b, \omega_c, \Theta_s, \tau, n_s, \log[10^{10} A_s], N_{\rm eff}, \sum m_\nu\} \ , \tag{5.2}$$

or with a constant dark energy equation of state w (or with a running of the scalar spectral index $n_{\rm run}$) when considering more general cosmological models:

$$\{\omega_b, \omega_c, \Theta_s, \tau, n_s, \log[10^{10} A_s], w(n_{\rm run}), \sum m_\nu\} \ . \tag{5.3}$$

We also study dark radiation models, described by $\Delta N_{\rm eff}$ relativistic (i.e..massless) degrees of freedom together with three massive neutrinos with $\sum m_\nu = 0.3$ eV. This first dark

radiation scheme is described by

$$\{\omega_b, \omega_c, \Theta_s, \tau, n_s, \log[10^{10} A_s], \Delta N_{\rm eff}\} \ . \tag{5.4}$$

Then we also consider extended parameter scenarios, with $c^2_{\rm eff}$ and $c^2_{\rm vis}$ also as free parameters:

$$\{\omega_b, \omega_c, \Theta_s, \tau, n_s, \log[10^{10} A_s], \Delta N_{\rm eff}, c^2_{\rm vis}, c^2_{\rm eff}\} \ , \tag{5.5}$$

as well as the more general case in which the sum of the three neutrino masses is also fitted to the data:

$$\{\omega_b, \omega_c, \Theta_s, \tau, n_s, \log[10^{10} A_s], \Delta N_{\rm eff}, c^2_{\rm vis}, c^2_{\rm eff}, \sum m_\nu\} \ . \tag{5.6}$$

For our numerical analyses, we have used the Boltzmann CAMB code [82] and extracted cosmological parameters from current data using a Monte Carlo Markov Chain (MCMC) analysis based on the publicly available MCMC package `cosmomc` [103]. Table 5.1 specifies the priors considered on the different cosmological parameters. Our neutrino mass prior is cast in the form of a (uniform) prior on the neutrino density fraction $f_\nu = \Omega_\nu/\Omega_{\rm DM}$, where Ω_ν is the ratio of the neutrino energy density over the critical density at redshift zero, and $\Omega_{\rm DM}$ is the same ratio, but for the total dark matter density, which includes cold dark matter and neutrinos.

Parameter	Prior
$\Omega_b h^2$	$0.005 \to 0.1$
$\Omega_c h^2$	$0.01 \to 0.99$
Θ_s	$0.5 \to 10$
τ	$0.01 \to 0.8$
n_s	$0.5 \to 1.5$
$\ln(10^{10} A_s)$	$2.7 \to 4$
f_ν	$0 \to 0.2$
$N_{\rm eff}$	$1.047 \to 10$
	$(0 \to 10)$
w	$-2 \to 0$
$n_{\rm run}$	$-0.07 \to 0.02$

Table 5.1: Uniform priors for the cosmological parameters considered here.

Our baseline data set is the nine–year WMAP data [18] (temperature and polarization) with the routine for computing the likelihood supplied by the WMAP team. We then also add CMB data from the SPT experiment [20, 21]. In order to address for foreground contributions, the SZ amplitude A_{SZ}, the amplitude of the clustered point source contribution, A_C, and the amplitude of the Poisson distributed point source contribution, A_P, are added as nuisance parameters in the CMB data analyses. Separately, we also consider data from the ACT CMB experiment [22], in order to check the constraints on neutrino and dark radiation properties with the combination of both WMAP plus SPT data sets and WMAP

plus ACT data sets. To the CMB basic data sets we add the latest constraint on the Hubble constant H_0 from the Hubble Space Telescope (HST) [2], or supernova data from the 3 year Supernova Legacy Survey (SNLS3), see Ref. [12]. We do not consider the combination of HST and SNLS3 measurements because these two data sets are not totally independent. In the case of SNLS3 data, we add in the MCMC analysis two extra nuisance parameters related to the light curve fitting procedure used to analyse the supernova (SN) data. These parameters characterise the dependence of the intrinsic supernova magnitude on stretch (which measures the shape of the SN light curve) and color [12]. Galaxy clustering measurements are considered in our analyses via BAO signals. We use here the BAO signal from DR9 [46] of the Baryon Acoustic Spectroscopic Survey (BOSS) [204, 205], with a median redshift of $z = 0.57$. Together with the CMASS DR9 data, we also include the recent measurement of the BAO scale based on a re-analysis (using reconstruction [206]) of the LRG sample from Data Release 7 with a median redshift of $z = 0.35$ [43], the measurement of the BAO signal at a lower redshift $z = 0.106$ from the 6dF Galaxy Survey 6dFGS [45] and the BAO measurements from the WiggleZ Survey at $z = 0.44$, $z = 0.6$ and $z = 0.73$ [44]. The data combinations for which we will show results in the next section are the following: WMAP and SPT/ACT; WMAP, SPT/ACT and HST; WMAP, SPT/ACT and SNLS3; WMAP, SPT/ACT and BAO; WMAP, SPT/ACT, HST and BAO; and finally WMAP, SPT/ACT, SNLS3 and BAO.

5.3 Results

Here we present the constraints from current cosmological data sets on the neutrino thermal abundance $N_{\rm eff}$ and on the sum of their masses $\sum m_\nu$ in different scenarios, considering separately SPT and ACT CMB data sets.

5.3.1 Standard Cosmology plus massive neutrinos

Through this section we shall assume a ΛCDM cosmology with either three or $N_{\rm eff}$ light massive neutrinos. The left panels of Figs. 5.1 and 5.2, depict our results for the three and $N_{\rm eff}$ massive neutrino assumptions, respectively, in the case of considering SPT CMB data, combined with the other data sets exploited here. Tables 5.2 and 5.3 present the mean values and errors (or 95% CL bounds) in the three and $N_{\rm eff}$ massive neutrino scenarios in the case of considering SPT for the different data combinations detailed in the previous section. Our results agree with those presented in Ref. [20] by the SPT collaboration. Notice that BAO data are crucial for the preference for massive neutrinos in the three massive neutrino case, in which $\sum m_\nu = 0.33 \pm 0.17$ ($\sum m_\nu = 0.40 \pm 0.18$ eV) for CMB plus BAO plus HST (SNLS3) data. In the $N_{\rm eff}$ massive neutrino scenario, the bounds are $\sum m_\nu = 0.56 \pm 0.23$ eV and $N_{\rm eff} = 4.21 \pm 0.46$ ($\sum m_\nu = 0.50 \pm 0.21$ eV and $N_{\rm eff} = 3.87 \pm 0.68$) for CMB plus BAO plus HST (SNLS3) data.

If BAO data are removed, the preference for massive neutrinos disappears in the three massive neutrino case, with a 95% CL upper limit on the sum of the three active neutrinos

	W9+SPT	W9+SPT + HST	W9+SPT +BAO	W9+SPT +SNLS3	W9+SPT +BAO+HST	W9+SPT +BAO+SNLS3
$\sum m_\nu$ (eV)	1.14 ± 0.41	< 0.50	0.46 ± 0.18	< 0.80	0.33 ± 0.17	0.40 ± 0.18

Table 5.2: Mean values and errors (or 95% CL upper bounds) on $\sum m_\nu$ (in eV) in a standard cosmology with three massive neutrinos for the different combinations of data sets in the case of considering SPT high multipole data.

of $\sum m_\nu < 0.50$ eV in the case of considering WMAP, SPT and HST measurements. For the same combination of data sets, in the $N_{\rm eff}$ massive neutrino case explored here, $\sum m_\nu = 0.48 \pm 0.33$ eV and $N_{\rm eff} = 4.08 \pm 0.54$.

We then consider separately new ACT data and perform identical analyses to the ones done with SPT data, see Tabs. 5.4, 5.5. Figures 5.1 and 5.2 (right panels) depict our results for the three and $N_{\rm eff}$ massive neutrino assumptions, respectively, in the case of considering ACT CMB data combined with the other data sets described in the previous section. Notice that there is no evidence for neutrino masses in any of the data combinations explored here. A 95% CL upper limit on the sum of the neutrino masses of $\sum m_\nu < 0.44$ eV (< 0.54 eV) is found when considering CMB, BAO and HST (SNLS3) data, which agrees with the results presented in Ref. [22]. In the $N_{\rm eff}$ massive neutrino case, we find $\sum m_\nu < 0.50$ eV ($\sum m_\nu < 0.53$ eV) at 95% CL and $N_{\rm eff} = 3.44 \pm 0.37$ ($N_{\rm eff} = 2.77 \pm 0.46$) when considering CMB, BAO and HST (SNLS3) data. Only when adding HST measurements the allowed values of $N_{\rm eff}$ are larger than 3, see Tab. 5.5, bringing the mean value of $N_{\rm eff}$ closer to the one found in the SPT data analyses. When removing BAO data, we get $\sum m_\nu < 0.34$ eV (95% CL) for the combination of CMB and HST measurements in the three massive neutrino case and $\sum m_\nu < 0.39$ eV (95% CL), $N_{\rm eff} < 3.20 \pm 0.38$ in the $N_{\rm eff}$ massive neutrino case.

Therefore, we conclude that, within a standard cosmology with three massive neutrinos, ACT and SPT CMB measurements are compatible if BAO data are not considered in the analyses and if a prior on H_0 from the HST experiment is also considered. However, the predictions in the $N_{\rm eff}$ massive neutrino case arising from ACT and SPT data are not consistent even if BAO data are removed and a prior on H_0 from the HST experiment is also added.

5.3.2 Massive neutrinos and extended cosmologies

In this section we compute the bounds on the sum of the three active neutrino masses considering extended cosmologies with a dark energy equation of state or with a running of the scalar spectral index.

Concerning the dark energy equation of state w, there is a strong and very well known degeneracy among the sum of neutrino masses and the dark energy equation of state w, see Ref. [124]. The bounds from cosmology on the sum of the neutrino masses will be much weaker if the dark energy fluid is not interpreted as a cosmological contant, in which

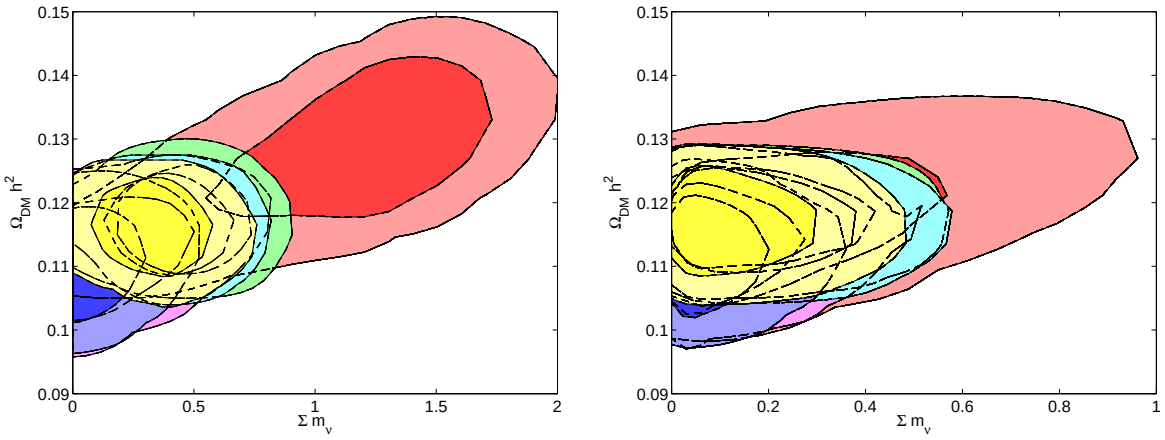

Figure 5.1: Left panel (Three massive neutrino case): the red contours show the 68% and 95% CL allowed regions from the combination of WMAP and SPT measurements in the ($\sum m_\nu$ (eV), $\Omega_{\rm dm}h^2$) plane, while the magenta (blue) ones show the impact of the addition of SNLS3 (HST) data sets. The green contours depict the results from the combination of CMB and BAO data, while the cyan and yellow ones show the impact of the SNLS3 (HST) data combined with CMB and BAO measurements. Right panel: as in the left panel but considering ACT data instead of SPT.

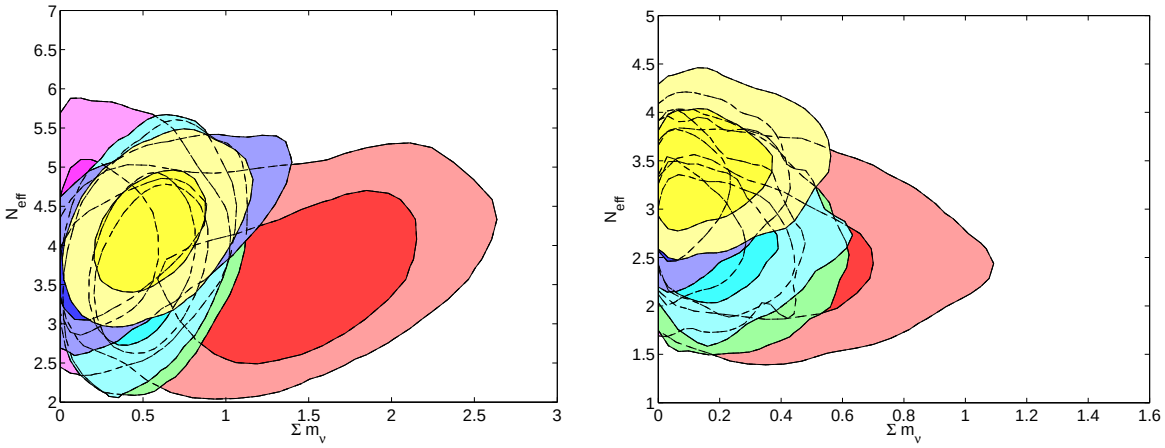

Figure 5.2: Left panel ($N_{\rm eff}$ massive neutrino case): the red contours show the 68% and 95% CL allowed regions from the combination of WMAP and ACT measurements in the ($\sum m_\nu$ (eV), $N_{\rm eff}$) plane, while the magenta (blue) ones show the impact of the addition of SNLS3 (HST) data sets. The green contours depict the results from the combination of CMB and BAO data, while the cyan and yellow ones show the impact of the SNLS3 (HST) data combined with CMB and BAO measurements. Right panel: as in the left panel but considering ACT data instead of SPT.

	W9+SPT	W9+SPT + HST	W9+SPT +BAO	W9+SPT +SNLS3	W9+SPT +BAO+HST	W9+SPT +BAO+SNLS3
$N_{\rm eff}$	3.66 ± 0.61	4.08 ± 0.54	3.76 ± 0.67	4.04 ± 0.68	4.21 ± 0.46	3.87 ± 0.68
$\sum m_\nu$ (eV)	1.35 ± 0.55	0.48 ± 0.33	0.56 ± 0.22	< 0.91	0.56 ± 0.23	0.50 ± 0.21

Table 5.3: Mean values and errors(or 95% CL bounds) on $N_{\rm eff}$ and $\sum m_\nu$ (in eV) in a standard cosmology with $N_{\rm eff}$ massive neutrinos for the different combinations of data sets in the case of considering SPT high multipole data.

	W9+ACT	W9+ACT + HST	W9+ACT +BAO	W9+ACT +SNLS3	W9+ACT +BAO+HST	W9+ACT +BAO+SNLS3
$\sum m_\nu$ (eV)	< 0.89	< 0.34	< 0.53	< 0.49	< 0.44	< 0.54

Table 5.4: 95% CL upper bounds on $\sum m_\nu$ (in eV) in a standard cosmology with three massive neutrinos for the different combinations of data sets in the case of considering ACT high multipole data.

	W9+ACT	W9+ACT + HST	W9+ACT +BAO	W9+ACT +SNLS3	W9+ACT +BAO+HST	W9+ACT +BAO+SNLS3
$N_{\rm eff}$	2.64 ± 0.51	3.20 ± 0.38	2.63 ± 0.48	2.75 ± 0.44	3.44 ± 037	2.78 ± 0.46
$\sum m_\nu$ (eV)	< 0.95	< 0.39	< 0.55	< 0.44	< 0.50	< 0.53

Table 5.5: Mean values and errors on $N_{\rm eff}$ and 95% CL upper bounds on $\sum m_\nu$ (in eV) in a standard cosmology with $N_{\rm eff}$ massive neutrinos for the different combinations of data sets in the case of considering ACT high multipole data.

case, the dark energy equation of state will be an extra free parameter. If w is allowed to vary, $\Omega_{\rm dm}$ can be much higher and consequently the neutrino mass also increases to leave unchanged the matter power spectrum and the growth of matter perturbations. The SPT collaboration [20] has also considered the impact of a constant dark energy equation of state w, and they find $\sum m_\nu = 0.27 \pm 0.11$ eV for the combination of their CMB and clusters data with WMAP 7 year, HST and BAO data sets. Figure 5.3, left panel, shows our results for SPT data within the different combinations of data sets addressed here. Notice that, in general, the evidence for neutrino masses in much milder than in the cosmological constant case, and the bounds on $\sum m_\nu$ are much larger than those shown in Tab. 5.2 due to the degeneracy between $\sum m_\nu$ and w. Supernovae measurements are, for this particular case, more useful than the H_0 prior from the HST experiment. Figure 5.3, right panel, shows the constraints in the ($\sum m_\nu$ (eV), w) plane in the case of considering ACT data. Notice that the bounds on $\sum m_\nu$ are tighter than those found for the case of analysing SPT data. Indeed, the bounds on the sum of the three massive neutrino masses computed for the case of a dark energy equation of state $w \neq -1$ are not very different from those obtained for a ΛCDM universe, see Tab. 5.4. SNLS3 measurements have a much larger constraining power than the HST prior also in the ACT data analyses performed in this section, especially for measuring the dark energy equation of state w.

We also explore the case in which a running in the spectral index of primordial perturbations is added to the minimal ΛCDM cosmology. In general, the spectrum of the scalar perturbations is not exactly a power law but it varies with scale. Therefore one must consider the scale dependent running of the spectral index $n_{\rm run} = dn_s/d\ln k$. Following [207], the power spectrum for the scalar perturbations reads

$$P(k) \equiv A_s k^{n(k)} \propto \left(\frac{k}{k_0}\right)^{n_s + \ln(k/k_0)(dn/d\ln k) + \cdots} ,$$

being $k_0 = 0.002$ Mpc^{-1} the pivot scale. Figure 5.4, left panel, shows our results for SPT data within the different combinations of data sets addressed here. The evidence for neutrino masses found for the SPT data in the cosmological constant case disappears in all the data combinations explored here. We find, for the case of the SPT data analyses, a 2σ preference for a negative running, in agreement with the results presented in Ref. [20].

Figure 5.4, right panel, shows our results for ACT data in the case of considering a running in the scalar spectral index. The bounds on the sum of the three massive neutrinos are now very similar to those found for the SPT experiment and also very similar to those found for ACT in the case of the minimal ΛCDM scenario. However, the preferred region for $n_{\rm run}$ is perfectly consistent with no running of the scalar spectral index, in agreement with the results presented by the ACT team [22].

5.3.3 Standard cosmology plus dark radiation

In this section we explore the bounds on the $N_{\rm eff}$ parameter, neglecting light neutrino masses and therefore assuming that there exist in nature $N_{\rm eff}$ massless neutrino species. The left (right) panel of Fig. 5.5 shows the constraints in the ($\Omega_{\rm dm}h^2$, $N_{\rm eff}$) plane arising from the

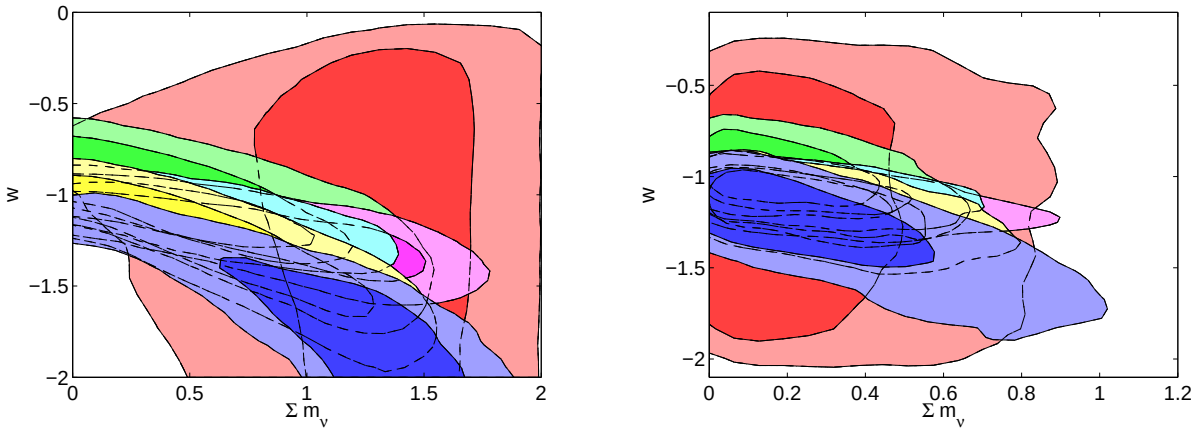

Figure 5.3: Left panel (Three massive neutrino case plus dark energy): the red contours show the 68% and 95% CL allowed regions from the combination of WMAP and SPT measurements in the ($\sum m_\nu$ (eV), w) plane, while the magenta (blue) ones show the impact of the addition of SNLS3 (HST) data sets. The green contours depict the results from the combination of CMB and BAO data, while the cyan and yellow ones show the impact of the SNLS3 (HST) data combined with CMB and BAO measurements. Right panel: as in the left panel but for the case of ACT data.

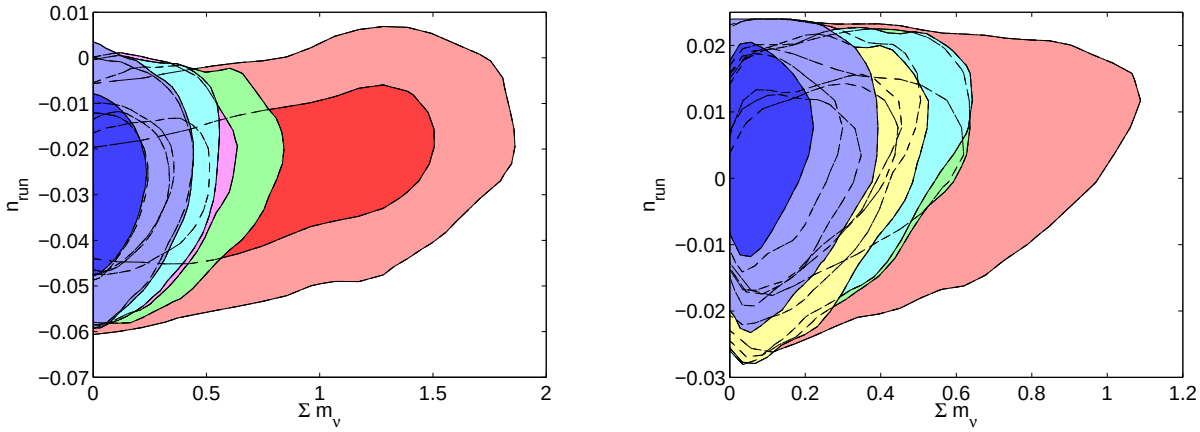

Figure 5.4: Left panel (Three massive neutrino case plus $n_{\rm run}$): the red contours show the 68% and 95% CL allowed regions from the combination of WMAP and SPT measurements in the ($\sum m_\nu$ (eV), $n_{\rm run}$) plane, while the magenta (blue) ones show the impact of the addition of SNLS3 (HST) data sets. The green contours depict the results from the combination of CMB and BAO data, while the cyan and yellow ones show the impact of the SNLS3 (HST) data combined with CMB and BAO measurements. Right panel: as in the left panel but for the case of ACT data.

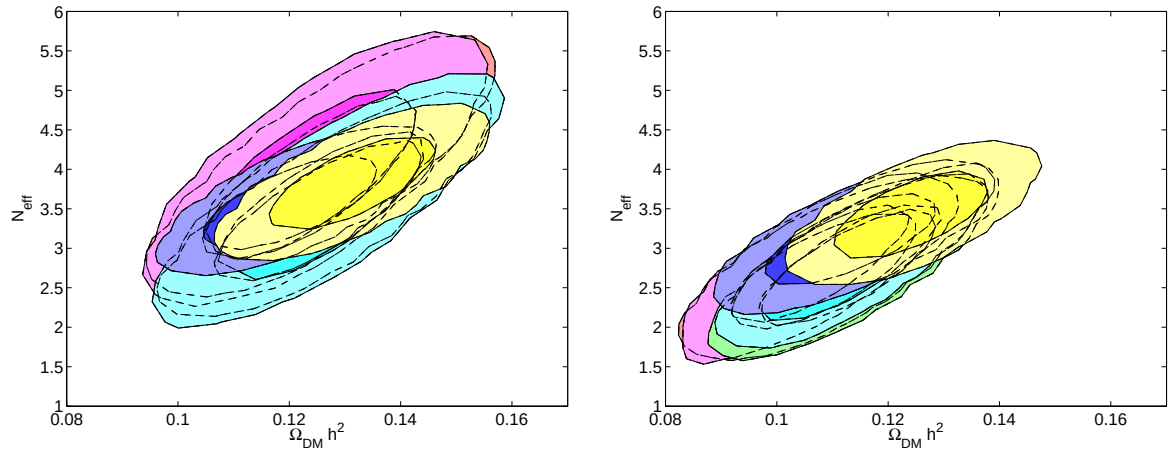

Figure 5.5: Left panel (Massless neutrino case): the red contours show the 68% and 95% CL allowed regions from the combination of WMAP and SPT measurements in the ($\Omega_{\rm dm}h^2$, $N_{\rm eff}$) plane, while the magenta (blue) ones show the impact of the addition of SNLS3 (HST) data sets. The green contours depict the results from the combination of CMB and BAO data, while the cyan and yellow ones show the impact of the SNLS3 (HST) data combined with CMB and BAO measurements. Right panel: as in the left panel but considering ACT data instead of SPT CMB data.

combination of WMAP plus SPT (ACT) as well as the other data combinations shown in the previous sections. Notice that the mean value of $N_{\rm eff}$ is, in general, much higher in the case of the SPT data analyses. When considering CMB data only, $N_{\rm eff} = 3.93 \pm 0.68$ for the case of WMAP plus SPT data, while $N_{\rm eff} = 2.74 \pm 0.47$ if analysing WMAP and ACT data. The tension among these two $N_{\rm eff}$ mean values gets diluted if BAO data and a prior on H_0 from the HST experiment are added in the analyses. In that case, $N_{\rm eff} = 3.83 \pm 0.41$ ($N_{\rm eff} = 3.43 \pm 0.36$) for WMAP plus SPT (ACT), being these two measurements perfectly consistent and indicating both $N_{\rm eff} > 3$ at 1-2 standard deviations. The addition of SNLS3 data will not help much in improving the agreement between these two data sets, see Tabs. 5.6 and 5.7, where we summarise the mean values and errors found for $N_{\rm eff}$ for the different data combinations considered here. Therefore, as in the three massive neutrino case, the consistency between ACT and SPT CMB results is greatly improved if BAO and HST data are considered as well.

5.3.4 Massive neutrinos and dark radiation

In this section we consider extended dark radiation cosmologies, parameterised via the dark radiation abundance $N_{\rm eff}$ and its clustering properties, represented by $c^2_{\rm eff}$ and $c^2_{\rm vis}$, see also Refs. [198, 199, 200] for bounds on these parameters within different cosmological models. Here three possible scenarios are examined. In the first scenario there are three massive neutrinos with $\sum m_\nu = 0.3$ eV, which roughly corresponds to the mean value obtained in Ref. [20], and $\Delta N_{\rm eff}$ massless neutrino species with $c^2_{\rm vis} = c^2_{\rm eff} = 1/3$. In the second scenario

	W9+SPT	W9+SPT + HST	W9+SPT +BAO	W9+SPT +SNLS3	W9+SPT +BAO+HST	W9+SPT +BAO+SNLS3
$N_{\rm eff}$	3.93 ± 0.68	3.59 ± 0.39	3.50 ± 0.59	3.96 ± 0.69	3.83 ± 0.41	3.55 ± 0.63

Table 5.6: Mean values and errors on $N_{\rm eff}$ in a standard cosmology with $N_{\rm eff}$ massless neutrinos for the different combinations of data sets in the case of considering high multipole data from SPT.

	W9+ACT	W9+ACT + HST	W9+ACT +BAO	W9+ACT +SNLS3	W9+ACT +BAO+HST	W9+ACT +BAO+SNLS3
$N_{\rm eff}$	2.74 ± 0.47	3.12 ± 0.38	2.77 ± 0.49	2.79 ± 0.47	3.43 ± 0.36	2.83 ± 0.47

Table 5.7: Mean values and errors on $N_{\rm eff}$ in a standard cosmology with $N_{\rm eff}$ massless neutrinos for the different combinations of data sets in the case of considering high multipole data from ACT.

the clustering parameters of the dark radiation component are allowed to vary, as well as in the third scenario, in which also the sum pf the masses of the three massive neutrinos $\sum m_\nu$ varies. Our findings are summarised in Figs. 5.7 and 5.6, where we illustrate the constraints from SPT and ACT probes.

In the first scenario, in which both $c^2_{\rm eff}$ and $c^2_{\rm vis}$ are fixed to their standard values and assuming three massive neutrinos with $\sum m_\nu = 0.3$ eV, we find that $\Delta N_{\rm eff} = 0.89 \pm 0.56$ ($\Delta N_{\rm eff} = 0.42 \pm 0.34$) when considering WMAP plus SPT (ACT) measurements. When HST data are added in the analyses, the mean values of $\Delta N_{\rm eff}$ for these two probes are similar: $\Delta N_{\rm eff} = 0.95 \pm 0.42$ ($\Delta N_{\rm eff} = 0.71 \pm 0.40$) for WMAP, SPT and HST (WMAP, ACT and HST) measurements. The addition of BAO data does not improve the agreement between SPT and ACT.

In the second scenario, only $\sum m_\nu = 0.3$ eV remains as a fixed parameter. In this case, the discrepancy between SPT and ACT data sets is larger, being the mean values for $\Delta N_{\rm eff} = 1.31 \pm 0.60$ and $\Delta N_{\rm eff} = 0.38 \pm 0.32$ respectively. The addition of HST brings these two mean values closer, being $\Delta N_{\rm eff} = 0.92 \pm 0.39$ ($\Delta N_{\rm eff} = 0.62 \pm 0.41$) for the combinations of WMAP, SPT and HST (WMAP, ACT and HST) data sets. Concerning the values of the dark radiation clustering parameters $c^2_{\rm eff}$ and $c^2_{\rm vis}$, we find that SPT data exclude the standard value of $c^2_{\rm vis} = 1/3$ at the 2σ CL. The mean value is $c^2_{\rm vis} = 0.15 \pm 0.07$ ($c^2_{\rm vis} < 0.28$ at 95% CL) when combining SPT, WMAP, BAO and HST data sets. The results for the effective speed of sound seem to be consistent with standard expectations, finding, for the same combination of data sets, that $c^2_{\rm eff} = 0.32 \pm 0.012$. Similar results are obtained when

SPT data is combined with the other data sets considered here. However, the results of the analyses of ACT data provide values for the clustering parameters which perfectly agree with standard expectations, being $c^2_{\rm eff} = 0.35 \pm 0.02$ and $c^2_{\rm vis} = 0.25 \pm 0.13$ ($c^2_{\rm vis} < 0.61$ at 95% CL) for the analysis of ACT, WMAP, BAO and HST data sets.

In the third scenario, all four parameters $\Delta N_{\rm eff}$, $c^2_{\rm vis}$, $c^2_{\rm eff}$ and $\sum m_\nu$ are allowed to freely vary, and we depict the constraints arising from our analyses in Figs. 5.6. The evidence for neutrino masses when analysing SPT data gets diluted for all the data combinations except when BAO data is also added in the analyses. We find $\Delta N_{\rm eff} = 1.34 \pm 0.67$, ($\Delta N_{\rm eff} = 1.15 \pm 0.64$) and $\sum m_\nu < 1.3$ eV ($\sum m_\nu < 1.75$ eV) at 95% CL when considering CMB (CMB plus HST) measurements. For the combination of WMAP, SPT and BAO (WMAP, SPT, BAO and HST) data sets, the cosmological evidence for neutrino masses still remains, finding that $\Delta N_{\rm eff} = 1.30 \pm 0.77$ ($\Delta N_{\rm eff} = 1.35 \pm 0.50$) and $\sum m_\nu = 0.68 \pm 0.31$ eV ($\sum m_\nu = 0.67 \pm 0.29$ eV). When analysing ACT data (see right panel of Fig. 5.6) the bounds on both $\Delta N_{\rm eff}$ and $\sum m_\nu$ are tighter than those found for SPT data. For the combination of WMAP, ACT, HST and BAO data sets, $\Delta N_{\rm eff} = 0.74 \pm 0.40$ and $\sum m_\nu < 0.46$ eV at 95% CL. Regarding the values of $c^2_{\rm eff}$ and $c^2_{\rm vis}$, we find very similar results to those shown previously. In this third scenario in which the sum of the three massive neutrinos is also a free parameter, we find that SPT data again exclude the standard value of $c^2_{\rm vis} = 1/3$ at the 2σ CL, while the value of $c^2_{\rm eff}$ agrees with its standard prediction. The analysis of SPT, WMAP, BAO and HST gives $c^2_{\rm vis} = 0.13 \pm 0.07$ ($c^2_{\rm vis} < 0.26$ at 95% CL) and $c^2_{\rm eff} = 0.32 \pm 0.01$. In the case of ACT data, the values for both clustering parameters perfectly agree with standard expectations, being $c^2_{\rm eff} = 0.35 \pm 0.02$ and $c^2_{\rm vis} = 0.25 \pm 0.11$ ($c^2_{\rm vis} < 0.47$ at 95% CL) for the analysis of ACT, WMAP, BAO and HST data sets.

Figure 5.7, left (right) panel, shows the constraints on the dark radiation abundance versus the effective speed of sound (viscosity parameter) for the combination of SPT or ACT with WMAP, BAO and HST measurements. Note that SPT and ACT data seem to be again in disagreement, this time concerning the dark radiation clustering parameter $c^2_{\rm vis}$.

5.4 Conclusions

New Cosmic Microwave Background measurements have become recently available, motivating us to explore the improvements in the measurements of the properties of the cosmic neutrino and dark radiation backgrounds. Interestingly, the new measurements of the CMB damping tail from the South Pole Telescope, SPT, and from the Atacama Cosmology Telescope, ACT, seem to give different results concerning neutrino masses and abundances. While the SPT collaboration finds $\sim 3\sigma$ evidence for neutrino masses and $N_{\rm eff} > 3$ at $\sim 2\sigma$, the ACT collaboration does not find evidence for neutrino masses and their value for $N_{\rm eff}$ is much lower, agreeing perfectly with the standard model prediction of $N_{\rm eff} = 3$. The success of future Majorana neutrino searches relies on the absolute scale of neutrino masses; therefore a detailed analysis of both data sets separately combined with other cosmological measurements is mandatory. We have considered the most recent Baryon Acoustic Oscillation data, measurements of the Hubble constant from the Hubble Space Telescope, as well

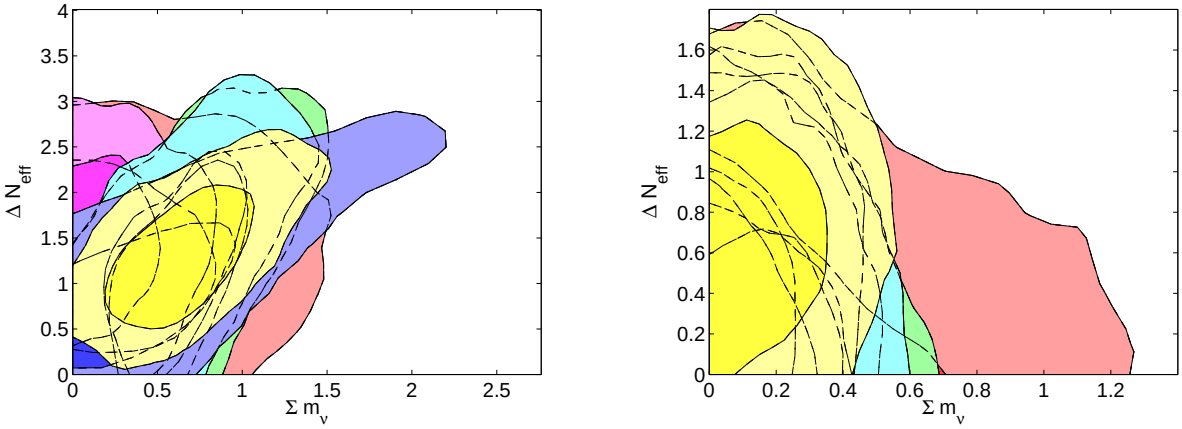

Figure 5.6: Left panel ($\Delta N_{\rm eff}$ dark radiation species plus three massive neutrinos): the red contours show the 68% and 95% CL allowed regions from the combination of WMAP and SPT measurements in the ($\sum m_\nu$ (eV), $\Delta N_{\rm eff}$) plane, while the magenta (blue) ones show the impact of the addition of SNLS3 (HST) data sets. The green contours depict the results from the combination of CMB and BAO data, while the cyan and yellow ones show the impact of the SNLS3 (HST) data combined with CMB and BAO measurements. Right panel: as in the left panel but considering ACT measurements instead of SPT data.

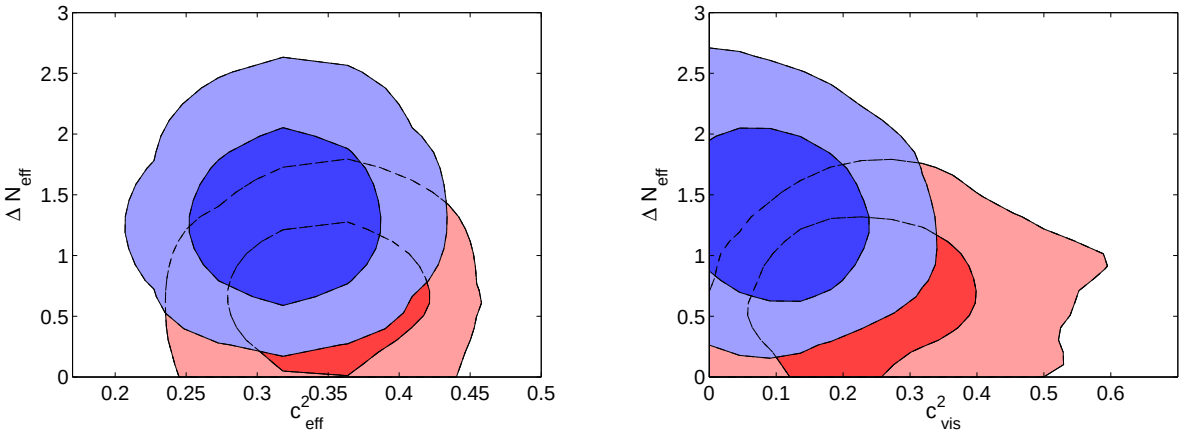

Figure 5.7: Left panel ($\Delta N_{\rm eff}$ massless neutrinos and three massive with $\sum m_\nu = 0.3$ eV): the red (blue) contours show the 68% and 95% CL allowed regions from the combination of WMAP, SPT (ACT), BAO and HST measurements in the ($c^2_{\rm eff}$, $\Delta N_{\rm eff}$) plane. Right panel: as in the left panel but in the ($c^2_{\rm vis}$, $\Delta N_{\rm eff}$) plane.

as Supernovae Ia luminosity distance measurements. In the standard ΛCDM scenario with either three massive neutrino species or $N_{\rm eff}$ massless species, the results from the two high CMB multiple probes are consistent if Baryon Acoustic Oscillation data is removed from the analyses and a prior on H_0 from HST is also considered. In the case of $N_{\rm eff}$ massive neutrino species, SPT and ACT data analyses give very different results for $\sum m_\nu$: while the evidence for $\sum m_\nu \sim 0.5$ eV found for SPT data persists independently of the data sets combined, the ACT data provide a 95% CL upper bound of ~ 0.4 eV on $\sum m_\nu$. We then explore extended cosmologies models, finding that, in general, the SPT data evidence for neutrino masses found in the minimal ΛCDM scenario gets diluted except for the case of a dark radiation background of unknown clustering properties with BAO data included. In the former case, SPT data exclude the standard value for the viscosity parameter of the dark radiation fluid $c^2_{\rm vis} = 1/3$ at the 2σ CL, regardless of the data sets considered in the analysis. Upcoming, high precision CMB data from the Planck satellite will help in disentangling the high tail CMB neutrino–dark radiation puzzle.

Chapter 6

Dark Radiation and interacting scenarios

In this Chapter we derive the cosmological constraints on the dark radiation abundance, on its effective velocity and on its viscosity parameter from current data in dark radiation-dark matter coupled models. This Chapter is a copy of the paper:

Dark Radiation and interacting scenarios, Roberta Diamanti, Elena Giusarma, Olga Mena, Maria Archidiacono & Alessandro Melchiorri, 2013, Physical Review D 87, 063509.

6.1 Introduction

From observations of the Cosmic Microwave Background (CMB) and large scale structure (LSS) we can probe the fundamental properties of the constituents of the cosmic dark radiation background. The energy density of the total radiation component reads

$$\rho_{rad} = \left[1 + \frac{7}{8}\left(\frac{4}{11}\right)^{4/3} N_{\rm eff}\right]\rho_\gamma \,, \tag{6.1}$$

where ρ_γ is the current energy density of the CMB and $N_{\rm eff}$ is a free parameter, defined as the effective number of relativistic degrees of freedom in the cosmic dark radiation background. In the standard scenario, the expected value is $N_{\rm eff} = 3.046$, corresponding to the three active neutrino contribution and considering effects related to non-instantaneous neutrino decoupling and QED finite temperature corrections to the plasma. The most recent CMB data analyses gives $N_{\rm eff} = 3.89 \pm 0.67$ (68% CL) [18], see also Refs. [196, 93, 94, 91, 90, 208, 92, 87, 19, 209, 210, 200, 190, 191, 211, 199, 212]. The simplest scenario to explain the extra dark radiation $\Delta N_{\rm eff} \equiv N_{\rm eff} - 3.046$ arising from cosmological data analyses assumes the existence of extra sterile neutrino species. However, there are other possibilities which are as well closely related to minimal extensions to the standard model of elementary particles, as axions, extra dimensions or asymmetric dark matter models.

Dark radiation, apart from being parametrized by its effective number of relativistic degrees of freedom, $N_{\rm eff}$, is also characterized by its clustering properties, i.e, its rest-frame speed of sound, $c^2_{\rm eff}$, and its viscosity parameter, $c^2_{\rm vis}$, which controls the relationship between velocity/metric shear and anisotropic stress in the dark radiation background [79]. A value

of $c^2_{\rm vis}$ different from zero, as expected in the standard scenario, sustains the existence of dark radiation anisotropies [213]. The standard value of $c^2_{\rm vis} = 1/3$ implies that the anisotropies in the dark radiation background are present and they are identical to the neutrino viscosity. On the other hand, the case $c^2_{\rm vis} = 0$ cuts the Boltzmann hierarchy of the dark radiation perturbations at the quadrupole, representing a perfect fluid with density and velocity (pressure) perturbations exclusively. A value of $c^2_{\rm eff}$ different from the canonical $c^2_{\rm eff} = 1/3$ leads to a non-adiabatic dark radiation pressure perturbation, i.e. $(\delta p - \delta\rho/3)/\bar{\rho} = (c^2_{\rm eff} - 1/3)\delta^{rest}_{dr}$, where δ^{rest}_{dr} is the density perturbation in the rest frame, where the dark radiation velocity perturbation is zero.

Interacting dark radiation arises naturally in the so-called asymmetric dark matter models (see e.g. [80] and references therein), in which the dark matter production mechanism is similar and related to the one in the baryonic sector. In these models, there exists a particle-antiparticle asymmetry at high temperatures in the dark matter sector. The thermally symmetric dark matter component will annihilate and decay into dark radiation degrees of freedom. Since the dark radiation and the dark matter fluids are interacting, there was an epoch in the early Universe in which these two dark fluids were strongly coupled. This results in a tightly coupled fluid with a pressure producing oscillations in the matter power spectrum analogous to the acoustic oscillations in the baryon-photon fluid before the recombination era. Due to the presence of a dark radiation-dark matter interaction, the clustering properties of the dark radiation component can be modified [209]. In other words, if dark radiation is made of interacting particles, the values of the clustering parameters $c^2_{\rm eff}$ and $c^2_{\rm vis}$ may differ from the canonical $c^2_{\rm eff} = c^2_{\rm vis} = 1/3$.

The cosmological implications of interacting dark radiation with canonical clustering properties have been carefully explored in Refs. [81, 214, 78], see also the recent work of Ref. [212]. Here we generalize the analysis and leave the three dark radiation parameters $\Delta N_{\rm eff}$, $c^2_{\rm eff}$ and $c^2_{\rm vis}$ to vary freely within a ΛCDM scenario with a dark radiation-dark matter interaction. We will see that the bounds from current cosmological data on the dark radiation properties derived in non interacting schemes in Refs. [200, 209, 199] will be, in general, relaxed, when an interaction between the dark radiation and the dark matter fluids is switched on. While the bounds on the number of extra dark radiation species will not be largely modified in coupled schemes, the errors on the dark radiation effective velocity and viscosity parameters will be drastically increased in interacting scenarios. We also show here how future CMB measurements, as those from the Planck [215] and COrE [216] experiments, can lead to large biases on the dark radiation clustering parameters if the dark radiation and dark matter fluids interact in nature but the data is analyzed in the absence of such a coupling.

The paper is organized as follows. Section 6.2 presents the parametrization used for dark radiation, describing the dark radiation-dark matter interactions explored here and their impact on the cosmological observables used in the analysis, as the CMB temperature anisotropies and the matter power spectrum. In Sec. 6.3 we describe the data sets used in the Monte Carlo analyses presented in Sec. 6.4, which summarizes the constraints on interacting dark radiation properties from current cosmological data. Future CMB dark radiation measurements are presented in Sec. 6.5. We draw our conclusions in Sec. 6.6.

6.2 Dark radiation-dark matter interaction model

The evolution of the dark radiation linear perturbations reads [79]

$$\dot{\delta}_{dr} - \frac{\dot{a}}{a}(1-3c_{\rm eff}^2)\left(\delta_{dr} + 4\frac{\dot{a}}{a}\frac{\theta_{dr}}{k^2}\right) + \frac{4}{3}\theta_{dr} + \frac{2}{3}\dot{h} = 0 \ ; \tag{6.2}$$

$$\dot{\theta}_{dr} - 3k^2 c_{\rm eff}^2\left(\frac{1}{4}\delta_{dr} + \frac{\dot{a}}{a}\frac{\theta_{dr}}{k^2}\right) + \frac{\dot{a}}{a}\theta_{dr} + \frac{1}{2}k^2\pi_{dr} = 0 \ ; \tag{6.3}$$

$$\dot{\pi}_{dr} + \frac{3}{5}kF_{dr,3} - \frac{8}{5}c_{\rm vis}^2\left(\frac{\theta_{dr}}{k} + \sigma\right) = 0 \ ; \tag{6.4}$$

$$\frac{2l+1}{k}\dot{F}_{dr,3} - lF_{dr,l-1} + (l+1)F_{dr,l+1} = 0 \quad l \geq 3 \ , \tag{6.5}$$

where the dots refer to derivatives with respect to conformal time, a is the scale factor, k is the wavenumber, $c_{\rm eff}^2$ is the effective sound speed, $c_{\rm vis}^2$ is the viscosity parameter, δ_{dr} and θ_{dr} are the dark radiation energy density perturbation and velocity divergence, respectively, and $F_{dr,l}$ are the higher order moments of the dark radiation distribution function. In the set of equations above, π_{dr} is the anisotropic stress perturbation, and σ is the metric shear, defined as $\sigma = (\dot{h} + 6\dot{\eta})/(2k)$, with h and η the scalar metric perturbations in the synchronous gauge. The anisotropic stress would affect the density perturbations, as in the case of a real fluid, in which the stress represents the viscosity, damping the density perturbations. The relationship between the metric shear and the anisotropic stress can be parametrized through a "viscosity parameter", $c_{\rm vis}^2$ [79]:

$$\dot{\pi} = -3\frac{\dot{a}}{a}\pi + 4c_{\rm vis}^2\left(\theta + \sigma\right) \ , \tag{6.6}$$

where θ is the divergence of the fluid velocity. Although the perturbed Einstein and energy-momentum conservation equations are enough to describe the evolution of the cosmological perturbations of non-relativistic particles, it is convenient to introduce the full distribution function in phase space to follow the perturbation evolution of relativistic particles, that is, to consider their Boltzmann equation. In order to determine the evolution equation of dark radiation, the Boltzmann equation is transformed into an infinite hierarchy of moment equations, that must be truncated at some maximum multipole order ℓ_{max}. Then, the higher order moments of the distribution function are truncated with appropriate boundary conditions, following Ref. [82].

In the presence of a dark radiation-dark matter interaction, the Euler equations for these two dark fluids read

$$\dot{\theta}_{dm} = -\frac{\dot{a}}{a}\theta_{dm} + \frac{4\rho_{dr}}{3\rho_{dm}}an_{dm}\sigma_{dm-dr}(\theta_{dr} - \theta_{dm}) \ , \tag{6.7}$$

$$\dot{\theta}_{dr} = \frac{1}{4}k^2\left(\delta_{dr} - 2\pi_{dr}\right) + an_{dm}\sigma_{dm-dr}(\theta_{dm} - \theta_{dr}) \tag{6.8}$$

where the momentum transfer to the dark radiation component is given by $an_{dm}\sigma_{dm-dr}(\theta_{dm}-\theta_{dr})$. Indeed, the former quantity is the differential opacity, which gives the scattering rate of dark radiation by dark matter [81, 214]. The complete Euler equation for dark radiation, including the interaction term with the dark matter fluid, reads

$$\begin{aligned}\dot{\theta}_{dr} &= 3k^2c^2_{\rm eff}\left(\frac{1}{4}\delta_{dr}+\frac{\dot{a}}{a}\frac{\theta_{dr}}{k^2}\right)-\frac{\dot{a}}{a}\theta_{dr}-\frac{1}{2}k^2\pi_{dr}\\ &+ an_{dm}\sigma_{dm-dr}(\theta_{dm}-\theta_{dr})\ .\end{aligned} \tag{6.9}$$

Following Refs. [81, 214] we parameterize the coupling between massless neutrinos and dark matter through a cross section given by

$$\langle\sigma_{dm-dr}|v|\rangle \sim Q_0\, m_{dm}\ , \tag{6.10}$$

if it is constant, or

$$\langle\sigma_{dm-dr}|v|\rangle \sim \frac{Q_2}{a^2}\, m_{dm}\ , \tag{6.11}$$

if it is proportional to T^2, where the parameters Q_0 and Q_2 are constants in cm^2 MeV^{-1} units. It has been shown in Ref. [78] that the cosmological implications of both constant and T-dependent interacting cross sections are very similar. Therefore, in the following, we focus on the constant cross section case, parameterized via Q_0.

Figure 6.1, upper panel, shows the CMB temperature anisotropies for $Q_0 = 10^{-32}$ cm^2 MeV^{-1} and one dark radiation interacting species, i.e. $\Delta N_{\rm eff} = 1$, as well as for the non interacting case for the best fit parameter values from WMAP seven year data analysis [90, 104] together with WMAP and South Pole Telescope (SPT) data [19]. We illustrate the behavior of the temperature anisotropies for different assumptions of the dark radiation clustering parameters. Notice that the presence of a dark radiation-dark matter interaction enhances the height of the CMB peaks due to both the presence of an extra radiation component ($\Delta N_{\rm eff}$) and the fact that dark matter is no longer pressureless (due to a non zero Q_0). Therefore $\Delta N_{\rm eff}$ and Q_0 will be negatively correlated. The location of the peaks also changes, mostly due to the presence of extra radiation $\Delta N_{\rm eff}$. The peaks will be shifted to higher multipoles ℓ due to changes in the acoustic scale, given by

$$\theta_A = \frac{r_s(z_{rec})}{r_\theta(z_{rec})}\ , \tag{6.12}$$

where $r_\theta(z_{rec})$ and $r_s(z_{rec})$ are the comoving angular diameter distance to the last scattering surface and the sound horizon at the recombination epoch z_{rec}, respectively. Although $r_\theta(z_{rec})$ almost remains the same for different values of $\Delta N_{\rm eff}$, $r_s(z_{rec})$ becomes smaller when $\Delta N_{\rm eff}$ is increased. Therefore, the positions of the acoustic peaks are shifted to higher multipoles (smaller angular scales) if the value of $\Delta N_{\rm eff}$ is increased. Notice, however, that this effect can be compensated by changing the cold dark matter density, in such a way that z_{rec} remains fixed, see Ref. [87]. Changing $c^2_{\rm vis}$ modifies the ability of the dark radiation to free-stream out of the potential wells [217, 218, 219]. Notice from Fig. 6.1

(upper panel), that lowering $c^2_{\rm vis}$ to the value $c^2_{\rm vis} = 0$, the TT power spectrum is enhanced with respect to the standard case without the dark radiation and the dark matter species interacting. This situation can be explained, roughly, as the dark radiation component becoming a perfect fluid. That is, we are dealing with a single fluid characterized by an effective viscosity. Disregarding the fluid nature and the physical origin of the viscosity, the general consideration holds: for a given perturbation induced in the fluid, the amplitude of the oscillations that the viscosity produces (see, e.g. [209]) increases as the viscosity is reduced. Therefore, lowering $c^2_{\rm vis}$ diminishes the amount of damping induced by the dark radiation viscosity, and, consequently, in this case, the amplitude of the CMB oscillations will increase, increasing in turn the amplitude of the angular power spectrum. Therefore, we expect the interaction strength size Q_0 and the $c^2_{\rm vis}$ parameter to be positively correlated.

On the other hand, a change of $c^2_{\rm eff}$ implies a decrease of pressure perturbations for the dark radiation component in its rest frame. As shown in Fig. 6.1 (upper panel), a decrease in $c^2_{\rm eff}$ from its canonical 1/3 to the value $c^2_{\rm eff} = 0$ leads to a damping of the CMB peaks, since dark radiation is behaving as a pressureless fluid from the perturbation perspective. In the case of $c^2_{\rm eff}$, we expect this parameter to be negatively correlated with Q_0.

Figure 6.1 (lower panel) depicts the matter power spectrum in the presence of a dark radiation-dark matter interaction for different values of the dark radiation clustering parameters (including the standard case with $c^2_{\rm eff} = c^2_{\rm vis} = 1/3$) for one dark radiation interacting species, i.e. $\Delta N_{\rm eff} = 1$. We illustrate as well the case of a pure ΛCDM universe. Notice that, since the dark matter fluid is interacting with the dark radiation component, the dark matter component is no longer presureless, showing damped oscillations. The smaller wave mode at which the interaction between the dark fluids will leave a signature on the matter power spectrum is roughly $k_f \sim a_f H(a_f)$, which corresponds to the size of the universe at the time that the dark radiation-dark matter interaction becomes ineffective [81, 214, 78], i.e. when $H(a_f) = \Gamma(a_f)$ (being H the Hubble parameter and Γ the effective dark radiation-dark matter scattering rate $\frac{\rho_{dr}}{\rho_{dm}} n_{dm} \langle \sigma_{dm-dr} |v| \rangle$). For the case of constant dark radiation-dark matter interacting cross section, the typical scale k_f reads, for $\Delta N_{\rm eff} = 1$:

$$k_f \sim 0.7 \left(\frac{10^{-32}\ {\rm cm}^2\ {\rm MeV}^{-1}}{Q_0} \right)^{1/2} h{\rm Mpc}^{-1}\ , \tag{6.13}$$

Notice however from Fig. 6.1 (lower panel) that, while varying $c^2_{\rm vis}$ the matter power spectrum barely changes, a change in $c^2_{\rm eff}$ changes dramatically the matter power spectrum, washing out any interacting signature. For instance, if $c^2_{\rm eff} = 0$, dark radiation is a presureless fluid which behaves as dark matter, inducing an enhancement of the matter fluctuations, and, consequently, the presence of a dark radiation-dark matter interaction will not modify the matter power spectrum, see the lower panel of Fig. 6.1. Therefore, one might expect a degeneracy between the dark radiation-dark matter coupling and the dark radiation $c^2_{\rm eff}$ parameter: the larger the interaction is, the smaller $c^2_{\rm eff}$ should be to compensate the suppression of power at scales $k \sim k_f$.

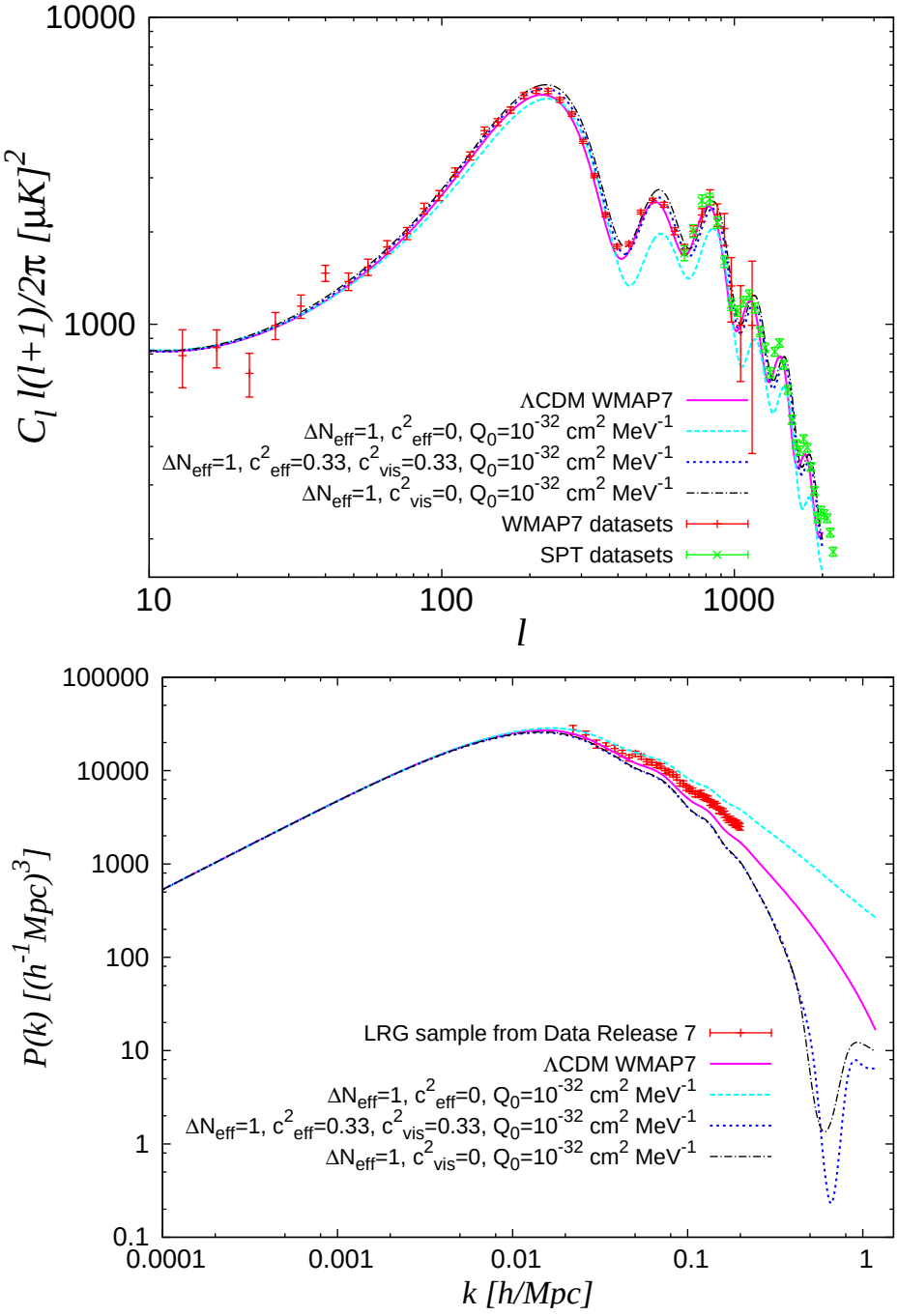

Figure 6.1: Upper panel: The magenta lines depict the CMB temperature power spectra C_ℓ^{TT} for the best fit parameters for a ΛCDM model from the WMAP seven year data set. The dotted curve shows the scenario with a constant interacting cross section with $Q_0 = 10^{-32}\text{cm}^2$ MeV^{-1} for $\Delta N_{\text{eff}} = 1$ and assuming canonical values for $c^2_{\text{eff}} = c^2_{\text{vis}} = 1/3$. The dashed (dot dashed) curve illustrates the same interacting scenario but with $c^2_{\text{eff}} = 0$ and $c^2_{\text{vis}} = 1/3$ ($c^2_{\text{eff}} = 1/3$ and $c^2_{\text{vis}} = 0$). We depict as well the data from the WMAP and SPT experiments, see text for details. Lower panel: matter power spectrum for the different models described in the upper panel. The data correspond to the clustering measurements of luminous red galaxies from SDSS II DR7 [105].

6.3 Data

In order to constrain the dark radiation parameters $\Delta N_{\rm eff}$, $c^2_{\rm eff}$ and $c^2_{\rm vis}$, as well as the size of the dark radiation-dark matter interaction, we have modified the Boltzmann CAMB code [82] including the dark radiation-dark matter interaction scenario. Then, we perform a Monte Carlo Markov Chain (MCMC) analysis based on the publicly available MCMC package `cosmomc` [103]. We consider a ΛCDM cosmology with $\Delta N_{\rm eff}$ dark radiation species interacting with the dark matter and three massless active neutrinos. This scenario is described by the following set of parameters:

$$\{\omega_b,\, \omega_c,\, \Theta_s,\, \tau,\, n_s,\, \log[10^{10} A_s],\, \Delta N_{\rm eff},\, c^2_{\rm vis},\, c^2_{\rm eff},\, Q_0\},$$

where $\omega_b \equiv \Omega_b h^2$ and $\omega_c \equiv \Omega_c h^2$ are the physical baryon and cold dark matter energy densities, Θ_s is the ratio between the sound horizon and the angular diameter distance at decoupling, τ is the optical depth, n_s is the scalar spectral index, A_s is the amplitude of the primordial spectrum, $\Delta N_{\rm eff}$ is the extra dark radiation component, $c^2_{\rm vis}$ is the viscosity parameter, $c^2_{\rm eff}$ is the effective sound speed and Q_0, in units of cm^2 MeV^{-1}, encodes the dark radiation-dark matter interaction. The flat priors considered on the different cosmological parameters are specified in Tab. 6.1.

Parameter	Prior
$\Omega_b h^2$	$0.005 \to 0.1$
$\Omega_c h^2$	$0.01 \to 0.99$
Θ_s	$0.5 \to 10$
τ	$0.01 \to 0.8$
n_s	$0.5 \to 1.5$
$\ln(10^{10} A_s)$	$2.7 \to 4$
$\Delta N_{\rm eff}$	$0 \to 10$
$c^2_{\rm vis}$	$0 \to 1$
$c^2_{\rm eff}$	$0 \to 1$
$\log_{10}\left(Q_0/10^{-32}{\rm cm}^2{\rm MeV}^{-1}\right)$	$-4 \to 0$

Table 6.1: Uniform priors for the cosmological parameters considered here.

For CMB data, we use the seven year WMAP data [90, 104] (temperature and polarization) by means of the likelihood supplied by the WMAP collaboration. We consider as well CMB temperature anisotropies from the SPT experiment [19], which provides highly accurate measurements on scales $\lesssim 10$ arcmin. We account as well for foreground contributions, adding the SZ amplitude A_{SZ}, the amplitude of the clustered point source contribution, A_C, and the amplitude of the Poisson distributed point source contribution, A_P, as nuisance parameters in the CMB data analysis.

Furthermore, we include the latest constraint from the Hubble Space Telescope (HST) [2] on the Hubble parameter H_0. Separately, we also add Supernovae Ia luminosity distance

data from the 3 year Supernova Legacy Survey (SNLS3) [12], adding in the MCMC analysis two extra nuisance parameters, which are related to the intrinsic supernova magnitude dependence on stretch (which measures the shape of the SN light curve) and color, see Ref. [12] for details. We do not consider here the addition of HST and SNLS3 measurements simultaneously because these two data sets are not independent.

Galaxy clustering measurements are also added in our analysis via BAO data from the CMASS sample in Data Release 9 [34] of the Baryon Oscillation Spectroscopic Survey (BOSS) [204, 205], with a median redshift of $z = 0.57$ [46], as well as from the LRG sample from Data Release 7 with a median redshift of $z = 0.35$ [43], and from the 6dF Galaxy Survey 6dFGS at a lower redshift $z = 0.106$ [45].

Therefore, we illustrate two cases, namely, the results from the combination of WMAP, SPT, SNLS3 and BAO data as well as the results arising from the combination of WMAP, SPT, HST and BAO data.

6.4 Current constraints

Table 6.2 shows the 68% and 95% CL errors on the dark radiation parameters and on the size of the dark radiation-dark matter interaction strength arising from the two possible combinations of data sets considered here for both interacting and non interacting scenarios. Notice, first, that the $1-2\sigma$ preference found in the literature for extra dark radiation species is still present in both interacting and non interacting scenarios in which the dark radiation clustering properties are not standard. Overall, the bounds on $\Delta N_{\rm eff}$ are not largely modified when allowing for a dark radiation-dark matter coupling, see also the results presented in Ref. [212]. However, the bounds on the dark radiation clustering properties $c^2_{\rm eff}$ and $c^2_{\rm vis}$ in the ΛCDM scenario and in minimal extensions of this scheme presented in Refs. [200, 199] are drastically changed when considering the possibility of an interaction between the dark radiation and the dark matter fluids. For instance, in Ref. [200], in the context of a ΛCDM scenario, it is found that $c^2_{\rm eff} = 0.24^{+0.08}_{-0.13}$ at 95% CL. Similar results were found in Ref. [199], where the ΛCDM scenario was extended to consider other cosmological models with a dark energy equation of state or with a running spectral index. Indeed, within non interacting scenarios, we find $c^2_{\rm eff} = 0.32^{+0.04}_{-0.03}$ and $c^2_{\rm vis} = 0.27^{+0.34}_{-0.22}$ at 95% CL from the combination of WMAP, SPT, HST and BAO data sets. These bounds are much weaker when allowing for an interacting dark radiation component: the errors on $c^2_{\rm eff}$ are degraded by an order of magnitude, while the errors on $c^2_{\rm vis}$ increase by a factor of two. We find, for the same combination of data sets than the one quoted above, $c^2_{\rm eff} = 0.28^{+0.44}_{-0.28}$ and $0.45^{+0.52}_{-0.45}$, both at 95% CL.

Figure 6.2 (left panel) depicts the 68% and 95% CL allowed regions in the ($c^2_{\rm eff}$, $\Delta N_{\rm eff}$) plane arising from the MCMC analysis of the cosmological data sets described in the previous section. We illustrate here the four cases shown in Tab. 6.2. The green (yellow) contours refer to the case of WMAP, SPT, BAO and SNLS3 data sets with (without) interaction between the dark radiation and dark matter fluids. The magenta (red) contours refer to the case of WMAP, SPT, BAO and HST data sets with (without) interaction. Notice that

		WMAP+SPT+ BAO+HST int.	WMAP+SPT+ BAO+HST no int.	WMAP+SPT+ BAO+SNLS3 int.	WMAP+SPT+ BAO+SNLS3 no int.
$c^2_{\rm eff}$		$0.28^{+0.10+0.44}_{-0.12-0.28}$	$0.32^{+0.02+0.04}_{-0.02-0.03}$	$0.30^{+0.12+0.50}_{-0.15-0.30}$	$0.32^{+0.02+0.04}_{-0.02-0.04}$
$c^2_{\rm vis}$		$0.45^{+0.34+0.52}_{-0.31-0.45}$	$0.27^{+0.13+0.34}_{-0.13-0.22}$	$0.46^{+0.36+0.51}_{-0.32-0.46}$	$0.27^{+0.13+0.42}_{-0.14-0.23}$
$\Delta N_{\rm eff}$	68%CL	< 0.81	$0.62^{+0.36+0.80}_{-0.36-0.53}$	< 0.76	$0.77^{+0.50+1.29}_{-0.72-0.72}$
	95%CL	< 1.30		< 1.47	
Q_0	68%CL	< 0.8	—	< 0.8	—
$\left(10^{-33}\frac{\rm cm^2}{\rm MeV^{-1}}\right)$	95%CL	< 4.9	—	< 5.4	—

Table 6.2: 1D marginalized bounds on the dark radiation parameters and on the size of the dark radiation dark matter interaction Q_0 using WMAP, SPT, BAO data and HST/SNLS3 measurements, see text for details. We show the constraints for both interacting and non interacting models, presenting the mean as well as the 68% and 95% CL errors of the posterior distribution.

the errors on the $c^2_{\rm eff}$ parameter are largely increased when the interaction term is switched on, while the errors on $\Delta N_{\rm eff}$ are mildly affected by the presence of such an interaction. Notice that HST data is more powerful than SNLS3 data in constraining $\Delta N_{\rm eff}$, agreeing with previous results in the literature, see Ref. [196]. The reason is because $\Delta N_{\rm eff}$ is highly degenerate with H_0, and HST data provide a strong prior on the former parameter.

The right panel of Fig. 6.2 depicts the 68% and 95% CL allowed regions in the ($c^2_{\rm vis}$, $\Delta N_{\rm eff}$) plane, being the color code identical to the one used in the left panel. While the impact of the coupling is not as large as in the effective velocity case, the errors on the viscosity parameter $c^2_{\rm vis}$ are enlarged by a factor of two in interacting dark radiation models.

6.5 Forecasts from future cosmological data

We evaluate here the constraints on the dark radiation parameters, $\Delta N_{\rm eff}$, $c^2_{\rm eff}$, $c^2_{\rm vis}$, by means of an analysis of future mock CMB data for the ongoing Planck experiment and the future COrE mission. These CMB mock data sets are then fitted using a MCMC analysis to a non interacting cosmological scenario but allowing the dark radiation parameters to have non standard values. The CMB mock data sets are generated accordingly to noise properties consistent with the Planck and COrE CMB missions. The fiducial C_ℓ model we use is a ΛCDM scenario (i.e. a flat universe with a cosmological constant and three massless active neutrino species) adding an interaction between the dark radiation and dark matter sectors with $Q_0 = 10^{-32}{\rm cm}^2$ MeV^{-1}, assuming one dark radiation interacting species $\Delta N_{\rm eff}$=1 and standard clustering and viscosity parameters for the dark radiation, i.e. $c^2_{\rm vis} =$

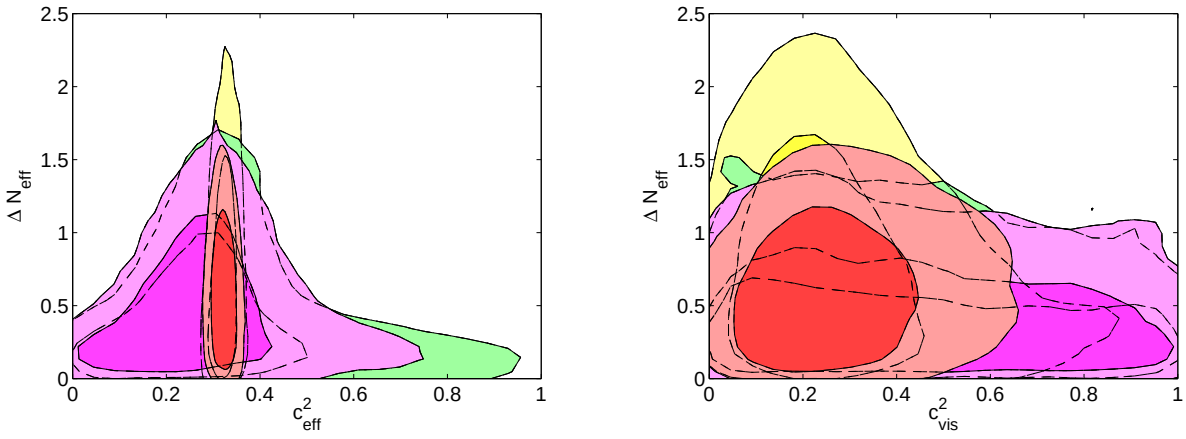

Figure 6.2: Left panel: 68% and 95% CL contours in the ($c^2_{\rm eff}$, $\Delta N_{\rm eff}$) plane arising from the MCMC analysis of WMAP, SPT, BAO and HST/SNLS3 data. The green (yellow) contours refer to the case of WMAP, SPT, BAO and SNLS3 data sets with (without) interaction between the dark radiation and dark matter fluids. The magenta (red) contours refer to the case of WMAP, SPT, BAO and HST data sets with (without) interaction between the dark radiation and dark matter sectors. Right panel: as in the left panel but in the ($c^2_{\rm vis}$, $\Delta N_{\rm eff}$) plane.

$c^2_{\rm eff} = 1/3$. For each frequency channel we consider a detector noise given by $\omega^{-1} = (\theta\sigma)^2$, being θ the FWHM of the gaussian beam and $\sigma = \Delta T/T$ the temperature sensitivity (the polarization sensitivity is $\Delta E/E = \sqrt{2}\Delta T/T$). Consequently the C_ℓ fiducial spectra get a noise contribution which reads $N_\ell = \omega^{-1} \exp\left(\ell(\ell+1)/\ell_b^2\right)$, where $\ell_b \equiv \sqrt{8ln2}/\theta$.

Figure 6.3 (left panel) depicts the 68% and 95% CL contours in the ($c^2_{\rm eff}$,$\Delta N_{\rm eff}$) plane arising from the MCMC analysis of Planck and COrE mock data. Notice that the reconstructed value for $c^2_{\rm eff}$ is larger than the simulated value $c^2_{\rm eff} = 1/3$. The reason for that is due to the degeneracy between the dark radiation-dark matter interaction Q_0 and $c^2_{\rm eff}$, see Fig. 6.1, from which one would expect a negative correlation between the interaction cross section and the effective velocity. If such an interaction occurs in nature but future CMB data is analysed assuming a non interacting model, the reconstructed value of $c^2_{\rm eff}$ will be higher than the standard expectation of 1/3, see Tab. 6.3. From what regards to $c^2_{\rm vis}$, see Fig. 6.3 (right panel), the effect is the opposite since these two parameters are positively correlated and therefore the reconstructed value of $c^2_{\rm vis}$ is lower than the canonical 1/3, see Tab. 6.3. Therefore, if the dark radiation and dark matter sectors interact, a large bias on the dark radiation clustering parameters could be induced if future CMB data are analysed neglecting such coupling. On the other hand, the bias induced in $\Delta N_{\rm eff}$ is not very significant, being the reconstructed value consistent with the $\Delta N_{\rm eff} = 1$ simulated one within 1σ.

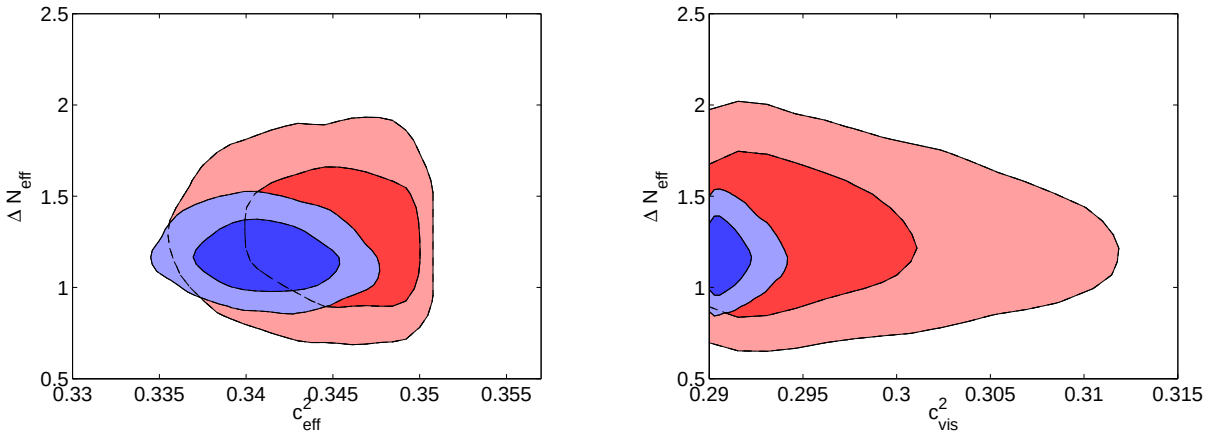

Figure 6.3: Left panel: 68% and 95% CL contours in the ($c^2_{\rm eff}$, $\Delta N_{\rm eff}$) arising from the MCMC analysis of Planck (red contours) and COrE (blue contours) CMB mock data. The mock data are generated adding an interaction between the dark radiation and dark matter sectors with $Q_0 = 10^{-32}{\rm cm}^2$ MeV^{-1}, assuming one dark radiation interacting species $\Delta N_{\rm eff}$=1 and standard clustering and viscosity parameters for the dark radiation. The CMB mock data is then fitted to a non interacting cosmology but allowing the dark radiation parameters $c^2_{\rm eff}$ and $c^2_{\rm vis}$ to have non standard values. Right panel: as in the left panel but in the ($c^2_{\rm vis}$, $\Delta N_{\rm eff}$) plane.

	Planck	COrE
$c^2_{\rm eff}$	$0.35^{+0.003+0.005}_{-0.003-0.007}$	$0.34^{+0.004+0.006}_{-0.001-0.003}$
$c^2_{\rm vis}$	$0.30^{+0.005+0.017}_{-0.006-0.006}$	$0.29^{+0.001+0.002}_{-0.001-0.001}$
$\Delta N_{\rm eff}$	$1.26^{+0.27+0.54}_{-0.25-0.51}$	$1.17^{+0.13+0.27}_{-0.12-0.23}$

Table 6.3: Constraints on the dark radiation clustering parameters from the Plank and COrE mock data sets described in the text. We present the mean as well as the 68% and 95% CL errors of the posterior distribution. We have set $Q_0 = 10^{-32}{\rm cm}^2$ MeV^{-1}, $c^2_{\rm eff} = c^2_{\rm vis} = 1/3$ in the mock data sets. Then, we have fitted these data to non interacting models in which both $c^2_{\rm eff}$ and $c^2_{\rm vis}$ are free parameters.

6.6 Conclusions

Standard dark radiation is made of three light active neutrinos. However, many extensions of the standard model of elementary particles predict an extra dark radiation component in the form of sterile neutrinos, axions or other very light degrees of freedom which may interact with the dark matter sector. In fact, once that one assumes the existence of extra dark radiation species as well as the existence of a dark matter sector there is a priori no fundamental symmetry which forbids couplings between these two dark fluids. If one allows

for such a possibility, the clustering properties of these extra dark radiation particles might not be identical to those of the standard model neutrinos, since the extra dark radiation particles are coupled to the dark matter. In this paper we have analyzed the constraints from recent cosmological data on the dark radiation abundances, effective velocities and viscosity parameters. While the bounds on $\Delta N_{\rm eff}$ are very close to those of uncoupled models, the errors on the clustering dark radiation properties are largely increased, mostly due to the existing degeneracies among the dark radiation-dark matter coupling and $c^2_{\rm eff}$, $c^2_{\rm vis}$. The cosmological bounds on the dark radiation effective velocity $c^2_{\rm eff}$ found in non-interacting schemes are degraded by an order of magnitude when a dark radiation-dark matter interaction is switched on. In the case of the viscosity parameter $c^2_{\rm vis}$, the errors on this parameter are a factor of two larger when considering interacting scenarios. We have also explored the perspectives from future Cosmic Microwave Background data. If dark radiation and dark matter interact in nature, but the data are analysed assuming the standard, non interacting picture, the reconstructed values for the effective velocity and for the viscosity parameter will be shifted from their standard 1/3 expectation, namely $c^2_{\rm eff} = 0.34^{+0.006}_{-0.003}$ and $c^2_{\rm vis} = 0.29^{+0.002}_{-0.001}$ at 95% CL for the future COrE CMB mission.

Part III

Summary and Conclusions

Chapter 7

Summary and Conclusions

Neutrinos are one of the most mysterious particles in nature. Nowadays we know from experimental results on neutrino oscillations that neutrinos are massive. Unfortunately, oscillation experiments are not sensitive to the overall neutrino mass scale.

Cosmology provides one of the means to test the absolute scale of neutrino masses and plays an important role to constrain neutrino properties. Neutrinos affect both the Cosmic Microwave Background (CMB) physics as well as the galaxy clustering, leaving a significant imprint either in the full shape clustering signal (exploited by matter power spectrum measurements) or in the geometrical signal (exploited via Baryon Acoustic Oscillation (BAO) measurements).

In this thesis we have derived bounds on the neutrino masses and on the neutrino abundances from the recent cosmological data, considering a ΛCDM scenario as well as other extended cosmological scenarios.

Chapter I contains a brief description of the current cosmological model and the measurements which support it. A detailed description of the different signatures in cosmology arising from the neutrino properties, as its mass and its abundance, can be found in Chapter II.

In Chapter III [189] we have studied a flat ΛCDM scenario with $N_{\rm eff}$ active plus sterile massive neutrino species, in order to test the so-called (3+2) models with cosmological data. We have found that this model is allowed at the 95 % CL by current cosmological data (which include CMB, galaxy clustering and Supernovae Ia). We have also considered the Big Bang Nucleosynthesis Helium-4 and Deuterium abundances and we have found that these measurements compromise the viability of (3+2) models. Moreover, we have presented a forecast to compute the errors on the active and sterile neutrino parameters from the ongoing Planck CMB mission data and from the BOSS and Euclid galaxy survey data. Future cosmological data could determine sub-eV active and sterile neutrino masses and sterile neutrino abundances with 10−30% precision, for sub-eV (0.5 eV$> m_{\nu_s} >$ 0.1 eV) sterile neutrino masses. We have also shown that the presence of massive sterile neutrinos in the universe could be inferred from inconsistencies among the values of the Hubble con-

stant H_0 obtained from CMB and galaxy clustering data and those arising from independent measurements of the Hubble constant over the next decade.

In Chapter IV [193] we have derived the neutrino mass bounds from the angular power spectra from the BOSS experiment, part of the Sloan Digital Sky Survey III, Data Release Eight (BOSS DR8) photometric sample of CMASS galaxies, dividing this sample into four photometric redshift bins, from $z = 0.45$ to $z = 0.65$, and considering a free constant bias parameter for each of these bins. To mimic the effects of a scale dependent galaxy bias, we have also fitted the data with an additional set of shot noise-like parameters. We have calculated the power spectra in two multipole ranges, $30 < \ell < 150$ and $30 < \ell < 200$, in order to minimize non-linear effects and we have considered a flat ΛCDM model plus three active massive neutrino species. Combining the BOSS DR8 data with CMB WMAP 7 year data, we have found an upper bound on the sum of the three active neutrino masses of $\sum m_\nu < 0.56$ eV at 95% CL for $\ell_{max} = 200$ (in the model with free bias parameters) and an upper bound $\sum m_\nu < 0.26$ eV at 95% CL if a prior on the Hubble constant from the Hubble Space Telescope (HST) data is also included. Considering a conservative galaxy bias model containing shot noise-like parameters, we have found $\sum m_\nu < 0.90$ eV at 95% CL using CMB and BOSS DR8 data and $\sum m_\nu < 0.36$ eV at 95% CL using CMB, HST and BOSS DR8 data sets. We have also shown that the addition of Supernova and/or BAO data does not significantly improve the neutrino mass bound once the HST prior is included.

New measurements of the CMB damping tail released in late 2012 and early 2013 from the South Pole Telescope, SPT, and from the Atacama Cosmology Telescope, ACT, seem to give different results concerning neutrino masses and abundances. Motivated by the discrepancies between SPT and ACT findings, we have explored in Chapter V [221] the cosmological constraints in several neutrino and dark radiation scenarios using CMB WMAP 9 year data, the new SPT and ACT measurements at high multipoles ℓ, BAO data, HST measurements of the Hubble constant and Supernovae Ia luminosity distance data. In the standard ΛCDM scenario with either three massive neutrino species or $N_{\rm eff}$ massless species, the two high ℓ CMB probes give similar results if BAO data are removed from the analyses and a prior on H_0 from HST is also considered. In the case of $N_{\rm eff}$ massive neutrino species, SPT and ACT data analyses give very different results for $\sum m_\nu$: while the evidence for $\sum m_\nu \sim 0.5$ eV found for SPT data persists independently of the data sets combined in the analysis, the ACT data provide a 95% CL upper bound of ~ 0.4 eV on $\sum m_\nu$. We then have explored extended cosmological scenarios with a dark energy equation of state and with a running of the scalar spectral index and we have proved that the evidence for neutrino masses found by the South Pole Telescope in the three neutrino scenario disappears for all the data combinations. Again, the agreement between the two high multipole CMB measurements considered is highly improved when adding HST data. Finally, we have considered the case of a dark radiation background of unknown clustering properties, finding that SPT data exclude the standard value for the viscosity parameter of the dark radiation fluid $c^2_{\rm vis} = 1/3$ at the 2σ CL.

In Chapter VI [198] we have studied a dark radiation-dark matter interacting model

deriving the constraints from recent cosmological data on the dark radiation abundances, effective velocities and viscosity parameters. If one assumes the existence of extra dark radiation species interacting with the dark matter sector, the clustering properties of these extra dark radiation particles might not be identical to those of the Standard Model neutrinos (for which $c^2_{\rm eff} = c^2_{\rm vis} = 1/3$), since the extra dark radiation particles are coupled to the dark matter fluid. We have found that the cosmological bounds on the number of extra dark radiation species do not change significantly when considering interacting schemes, while the errors on the clustering dark radiation properties are largely increased, mostly due to the existing degeneracies among the dark radiation-dark matter coupling and $c^2_{\rm eff}$, $c^2_{\rm vis}$. The cosmological bounds on the dark radiation effective velocity $c^2_{\rm eff}$ found in non-interacting schemes are degraded by an order of magnitude when a dark radiation-dark matter interaction is switched on. In the case of the viscosity parameter $c^2_{\rm vis}$, the errors on this parameter are a factor of two larger when considering interacting scenarios. We have also explored the perspectives from future CMB measurements. If dark radiation and dark matter interact in nature, but the data are analysed assuming the standard, non interacting picture, the reconstructed values for the effective velocity and for the viscosity parameter will be shifted from their standard 1/3 expectation, namely $c^2_{\rm eff} = 0.34^{+0.006}_{-0.003}$ and $c^2_{\rm vis} = 0.29^{+0.002}_{-0.001}$ at 95% CL for the future COrE CMB mission.

Latest measurements of the CMB temperature anisotropies released by the Planck satellite provide the tightest constraints on cosmological parameters [9] but they do not provide a strong bound on the sum of neutrino masses if they are not combined with external data sets. The upper limit from Planck, considering lensing, combined with low-ℓ polarization measurements from WMAP-9 year data is $\sum m_\nu < 1.1$ eV at 95% CL. The addition of the HST prior on the Hubble constant improves the constraints to $\sum m_\nu < 0.21$ eV at 95% CL. Planck mesurements alone find no evidence for additional relativistic particles beyond the three families of neutrinos in the Standard Model, while the constraint obtained combining CMB Planck data with the HST Hubble constant measurement is $N_{\rm eff} = 3.62 \pm 0.25$, due to the strong degeneracy between H_0 and $N_{\rm eff}$.

The future planned Euclid galaxy survey could provide the ideal tool to test neutrino properties with cosmology. Combining Euclid measurements of the custering of galaxies, of weak lensing shear and of clusters with CMB data, the sum of neutrino masses could be measured with a 1 σ precision of 0.01 eV assuming a fiducial model with $\sum m_\nu = 0.056$ eV, even in the case that the dark energy equation of state varies with time [220]. The same data combination could reach a 1σ sensitivity to $N_{\rm eff}$ of 0.02, implying that the small departure of 0.046 from the standard expectation of 3 (arising from non instantaneous neutrino decoupling, neutrino mixing and finite temperature corrections) could be tested with 2σ precision [220].

Part IV

Bibliography

Bibliography

[1] S. Dodelson, "Modern cosmology," Amsterdam, Netherlands: Academic Pr. (2003) 440 p.

[2] A. G. Riess, L. Macri, S. Casertano, H. Lampeitl, H. C. Ferguson, A. V. Filippenko, S. W. Jha and W. Li *et al.*, Astrophys. J. **730**, 119 (2011) [Erratum-ibid. **732**, 129 (2011)] [arXiv:1103.2976 [astro-ph.CO]].

[3] P. Coles and F. Lucchin, "Cosmology: The Origin and evolution of cosmic structure," Chichester, UK: Wiley (2002) 492 p.

[4] Einstein A., Sitzungsber. Preuss. Akad. Wiss. phys.-math. Klasse VI, 142 (1917).

[5] A. S. Eddington, Mon. Not. Roy. Astron. Soc. **90**, 668 (1930).

[6] Friedmann A., 1922, ZPhy, 10, 377.

[7] Friedmann A., 1924, ZPhy, 21, 326 .

[8] C. -P. Ma and E. Bertschinger, Astrophys. J. **455**, 7 (1995) [astro-ph/9506072].

[9] P. A. R. Ade *et al.* [Planck Collaboration], arXiv:1303.5076 [astro-ph.CO].

[10] S. Perlmutter *et al.* [Supernova Cosmology Project Collaboration], Astrophys. J. **517**, 565 (1999) [astro-ph/9812133].

[11] A. G. Riess *et al.* [Supernova Search Team Collaboration], Astron. J. **116**, 1009 (1998) [astro-ph/9805201].

[12] A. Conley, J. Guy, M. Sullivan, N. Regnault, P. Astier, C. Balland, S. Basa and R. G. Carlberg *et al.*, Astrophys. J. Suppl. **192** (2011) 1 [arXiv:1104.1443 [astro-ph.CO]].

[13] E. S. Walker, I. M. Hook, M. Sullivan, D. A. Howell, P. Astier, C. Balland, S. Basa and T. J. Bronder *et al.*, arXiv:1008.2308 [astro-ph.CO].

[14] M. Sullivan, J. Guy, A. Conley, N. Regnault, P. Astier, C. Balland, S. Basa and R. G. Carlberg *et al.*, Astrophys. J. **737**, 102 (2011) [arXiv:1104.1444 [astro-ph.CO]].

[15] R. Amanullah, C. Lidman, D. Rubin, G. Aldering, P. Astier, K. Barbary, M. S. Burns and A. Conley *et al.*, Astrophys. J. **716**, 712 (2010) [arXiv:1004.1711 [astro-ph.CO]].

[16] E. L. Wright, S. S. Meyer, C. L. Bennett, N. W. Boggess, E. S. Cheng, M. G. Hauser, A. Kogut and C. Lineweaver *et al.*, Astrophys. J. **396**, L13 (1992).

[17] J. Lesgourgues, G. Mangano, G. Miele and S. Pastor "Neutrino Cosmology," Cambridge, UK: Cambridge University Press (2013) 378 p.

[18] G. Hinshaw, D. Larson, E. Komatsu, D. N. Spergel, C. L. Bennett, J. Dunkley, M. R. Nolta and M. Halpern *et al.*, arXiv:1212.5226 [astro-ph.CO].

[19] R. Keisler, C. L. Reichardt, K. A. Aird, B. A. Benson, L. E. Bleem, J. E. Carlstrom, C. L. Chang and H. M. Cho *et al.*, Astrophys. J. **743**, 28 (2011) [arXiv:1105.3182 [astro-ph.CO]].

[20] Z. Hou, C. L. Reichardt, K. T. Story, B. Follin, R. Keisler, K. A. Aird, B. A. Benson and L. E. Bleem *et al.*, arXiv:1212.6267 [astro-ph.CO].

[21] K. T. Story, C. L. Reichardt, Z. Hou, R. Keisler, K. A. Aird, B. A. Benson, L. E. Bleem and J. E. Carlstrom *et al.*, arXiv:1210.7231 [astro-ph.CO].

[22] J. L. Sievers, R. A. Hlozek, M. R. Nolta, V. Acquaviva, G. E. Addison, P. A. R. Ade, P. Aguirre and M. Amiri *et al.*, arXiv:1301.0824 [astro-ph.CO].

[23] S. Das, T. Louis, M. R. Nolta, G. E. Addison, E. S. Battistelli, J R. Bond, E. Calabrese and D. C. M. J. Devlin *et al.*, arXiv:1301.1037 [astro-ph.CO].

[24] J. Silk, Astrophys. J. **151**, 459 (1968).

[25] P. A. R. Ade *et al.* [Planck Collaboration], arXiv:1303.5062 [astro-ph.CO].

[26] M. Tegmark, astro-ph/9511148.

[27] W. Hu and S. Dodelson, Ann. Rev. Astron. Astrophys. **40**, 171 (2002) [astro-ph/0110414].

[28] A. J. S. Hamilton, Lect. Notes Phys. **665**, 415 (2008) [astro-ph/0503603].

[29] A. J. S. Hamilton, Lect. Notes Phys. **665**, 433 (2008) [astro-ph/0503604]. Hamilton A. J. S., 2005, astro, arXiv:astro-ph/0503604

[30] Martínez V. J., 2009, LNP, 665, 269

[31] D. H. Weinberg, M. J. Mortonson, D. J. Eisenstein, C. Hirata, A. G. Riess and E. Rozo, arXiv:1201.2434 [astro-ph.CO].

[32] D. G. York *et al.* [SDSS Collaboration], Astron. J. **120**, 1579 (2000) [astro-ph/0006396].

[33] J. A. Frieman, B. Bassett, A. Becker, C. Choi, D. Cinabro, D. F. DeJongh, D. L. Depoy and M. Doi *et al.*, Astron. J. **135**, 338 (2008) [arXiv:0708.2749 [astro-ph]].

[34] C. P. Ahn *et al.* [SDSS Collaboration], Astrophys. J. Suppl. **203**, 21 (2012) [arXiv:1207.7137 [astro-ph.IM]].

[35] D. J. Eisenstein *et al.* [SDSS Collaboration], Astron. J. **142**, 72 (2011) [arXiv:1101.1529 [astro-ph.IM]].

[36] A. Ross, S. Ho, A. J. Cuesta, R. Tojeiro, W. J. Percival, D. Wake, K. L. Masters and R. C. Nichol *et al.*, Mon. Not. Roy. Astron. Soc. **417**, 1350 (2011) [arXiv:1105.2320 [astro-ph.CO]].

[37] M. White, M. Blanton, A. Bolton, D. Schlegel, J. Tinker, A. Berlind, L. da Costa and E. Kazin *et al.*, Astrophys. J. **728**, 126 (2011) [arXiv:1010.4915 [astro-ph.CO]].

[38] M. Tegmark *et al.* [SDSS Collaboration], Astrophys. J. **571**, 191 (2002) [astro-ph/0107418].

[39] D. Huterer, L. Knox, R. C. Nichol and , Astrophys. J. **555**, 547 (2001) [astro-ph/0011069].

[40] H. Aihara *et al.* [SDSS Collaboration], Astrophys. J. Suppl. **193**, 29 (2011) [Erratum-ibid. **195**, 26 (2011)] [arXiv:1101.1559 [astro-ph.IM]].

[41] A. J. S. Hamilton, astro-ph/9708102.

[42] N. Benitez, E. Gaztanaga, R. Miquel, F. Castander, M. Moles, M. Crocce, A. Fernandez-Soto and P. Fosalba *et al.*, Astrophys. J. **691**, 241 (2009) [arXiv:0807.0535 [astro-ph]].

[43] N. Padmanabhan, X. Xu, D. J. Eisenstein, R. Scalzo, A. J. Cuesta, K. T. Mehta and E. Kazin, arXiv:1202.0090 [astro-ph.CO].

[44] C. Blake, E. Kazin, F. Beutler, T. Davis, D. Parkinson, S. Brough, M. Colless and C. Contreras *et al.*, Mon. Not. Roy. Astron. Soc. **418**, 1707 (2011) [arXiv:1108.2635 [astro-ph.CO]].

[45] F. Beutler, C. Blake, M. Colless, D. H. Jones, L. Staveley-Smith, L. Campbell, Q. Parker and W. Saunders *et al.*, Mon. Not. Roy. Astron. Soc. **416**, 3017 (2011) [arXiv:1106.3366 [astro-ph.CO]].

[46] L. Anderson, E. Aubourg, S. Bailey, D. Bizyaev, M. Blanton, A. S. Bolton, J. Brinkmann and J. R. Brownstein *et al.*, Mon. Not. Roy. Astron. Soc. **428**, 1036 (2013) [arXiv:1203.6594 [astro-ph.CO]].

[47] L. Anderson, E. Aubourg, S. Bailey, F. Beutler, A. S. Bolton, J. Brinkmann, J. R. Brownstein and C. -H. Chuang *et al.*, arXiv:1303.4666 [astro-ph.CO].

[48] S. Hannestad and J. Madsen, Phys. Rev. D **52**, 1764 (1995) [astro-ph/9506015].

[49] A. D. Dolgov, S. H. Hansen and D. V. Semikoz, Nucl. Phys. B **543**, 269 (1999) [hep-ph/9805467].

[50] G. Mangano, G. Miele, S. Pastor and M. Peloso, Phys. Lett. B **534**, 8 (2002) [astro-ph/0111408].

[51] G. Mangano, G. Miele, S. Pastor, T. Pinto, O. Pisanti and P. D. Serpico, Nucl. Phys. B **729**, 221 (2005) [hep-ph/0506164].

[52] Cowan C. L., Jr., Reines F., Harrison F. B., Kruse H. W., McGuire A. D., 1956, Sci, 124, 103

[53] B. Pontecorvo, Sov. Phys. JETP **7**, 172 (1958) [Zh. Eksp. Teor. Fiz. **34**, 247 (1957)].

[54] Z. Maki, M. Nakagawa and S. Sakata, Prog. Theor. Phys. **28**, 870 (1962).

[55] M. C. Gonzalez-Garcia, M. Maltoni, J. Salvado and T. Schwetz, JHEP **1212**, 123 (2012) [arXiv:1209.3023 [hep-ph]].

[56] D. V. Forero, M. Tortola and J. W. F. Valle, Phys. Rev. D **86**, 073012 (2012) [arXiv:1205.4018 [hep-ph]].

[57] G. L. Fogli, E. Lisi, A. Marrone, D. Montanino, A. Palazzo and A. M. Rotunno, Phys. Rev. D **86**, 013012 (2012) [arXiv:1205.5254 [hep-ph]].

[58] V. M. Lobashev, Nucl. Phys. A **719**, 153 (2003).

[59] C. .Kraus, B. Bornschein, L. Bornschein, J. Bonn, B. Flatt, A. Kovalik, B. Ostrick and E. W. Otten *et al.*, Eur. Phys. J. C **40** (2005) 447 [hep-ex/0412056].

[60] A. Osipowicz *et al.* [KATRIN Collaboration], hep-ex/0109033.

[61] J. J. Gomez-Cadenas, J. Martin-Albo, M. Mezzetto, F. Monrabal and M. Sorel, Riv. Nuovo Cim. **35**, 29 (2012) [arXiv:1109.5515 [hep-ex]].

[62] O. Mena and S. J. Parke, Phys. Rev. D **69**, 117301 (2004) [hep-ph/0312131].

[63] K. N. Abazajian, M. A. Acero, S. K. Agarwalla, A. A. Aguilar-Arevalo, C. H. Albright, S. Antusch, C. A. Arguelles and A. B. Balantekin *et al.*, arXiv:1204.5379 [hep-ph].

[64] A. Aguilar-Arevalo *et al.* [LSND Collaboration], Phys. Rev. D **64**, 112007 (2001) [hep-ex/0104049].

[65] A. A. Aguilar-Arevalo *et al.* [MiniBooNE Collaboration], Phys. Rev. Lett. **98**, 231801 (2007) [arXiv:0704.1500 [hep-ex]].

[66] A. A. Aguilar-Arevalo *et al.* [MiniBooNE Collaboration], arXiv:1303.2588 [hep-ex].

[67] M. Sorel, J. M. Conrad and M. Shaevitz, Phys. Rev. D **70**, 073004 (2004) [hep-ph/0305255].

[68] G. Karagiorgi, A. Aguilar-Arevalo, J. M. Conrad, M. H. Shaevitz, K. Whisnant, M. Sorel and V. Barger, Phys. Rev. D **75**, 013011 (2007) [Erratum-ibid. D **80**, 099902 (2009)] [hep-ph/0609177].

[69] J. M. Conrad, C. M. Ignarra, G. Karagiorgi, M. H. Shaevitz and J. Spitz, Adv. High Energy Phys. **2013**, 163897 (2013) [arXiv:1207.4765 [hep-ex]].

[70] S. Hannestad, A. Mirizzi, G. G. Raffelt and Y. Y. Y. Wong, JCAP **1008**, 001 (2010) [arXiv:1004.0695 [astro-ph.CO]].

[71] A. Melchiorri, O. Mena and A. Slosar, Phys. Rev. D **76**, 041303 (2007) [arXiv:0705.2695 [astro-ph]].

[72] W. Fischler and J. Meyers, Phys. Rev. D **83**, 063520 (2011) [arXiv:1011.3501 [astro-ph.CO]].

[73] T. L. Smith, E. Pierpaoli and M. Kamionkowski, Phys. Rev. Lett. **97**, 021301 (2006) [astro-ph/0603144].

[74] P. Binetruy, C. Deffayet, U. Ellwanger and D. Langlois, Phys. Lett. B **477**, 285 (2000) [hep-th/9910219].

[75] T. Shiromizu, K. -i. Maeda and M. Sasaki, Phys. Rev. D **62**, 024012 (2000) [gr-qc/9910076].

[76] V. V. Flambaum and E. V. Shuryak, Europhys. Lett. **74**, 813 (2006) [hep-th/0512038].

[77] E. Calabrese, D. Huterer, E. V. Linder, A. Melchiorri and L. Pagano, Phys. Rev. D **83**, 123504 (2011) [arXiv:1103.4132 [astro-ph.CO]].

[78] M. Blennow, E. Fernandez-Martinez, O. Mena, J. Redondo and P. Serra, JCAP **1207**, 022 (2012) [arXiv:1203.5803 [hep-ph]].

[79] W. Hu, Astrophys. J. **506**, 485 (1998) [astro-ph/9801234].

[80] M. Blennow, B. Dasgupta, E. Fernandez-Martinez and N. Rius, JHEP **1103**, 014 (2011) [arXiv:1009.3159 [hep-ph]].

[81] G. Mangano, A. Melchiorri, P. Serra, A. Cooray and M. Kamionkowski, Phys. Rev. D **74**, 043517 (2006) [astro-ph/0606190].

[82] A. Lewis, A. Challinor and A. Lasenby, Astrophys. J. **538**, 473 (2000) [arXiv:astro-ph/9911177].

[83] M. Takada, E. Komatsu and T. Futamase, Phys. Rev. D **73**, 083520 (2006) [astro-ph/0512374].

[84] J. Lesgourgues and S. Pastor, Phys. Rept. **429**, 307 (2006) [astro-ph/0603494].

[85] W. Hu, D. J. Eisenstein and M. Tegmark, Phys. Rev. Lett. **80**, 5255 (1998) [astro-ph/9712057].

[86] K. Ichikawa, T. Sekiguchi and T. Takahashi, Phys. Rev. D **78**, 083526 (2008) [arXiv:0803.0889 [astro-ph]].

[87] Z. Hou, R. Keisler, L. Knox, M. Millea and C. Reichardt, arXiv:1104.2333 [astro-ph.CO].

[88] M. Gerbino, E. Di Valentino and N. Said, arXiv:1304.7400 [astro-ph.CO].

[89] M. C. Gonzalez-Garcia and M. Maltoni, Phys. Rept. **460**, 1 (2008) [arXiv:0704.1800 [hep-ph]].

[90] E. Komatsu *et al.* [WMAP Collaboration], Astrophys. J. Suppl. **192**, 18 (2011) [arXiv:1001.4538 [astro-ph.CO]].

[91] B. A. Reid, L. Verde, R. Jimenez and O. Mena, JCAP **1001**, 003 (2010) [arXiv:0910.0008 [astro-ph.CO]].

[92] J. Hamann, S. Hannestad, J. Lesgourgues, C. Rampf and Y. Y. Y. Wong, JCAP **1007**, 022 (2010) [arXiv:1003.3999 [astro-ph.CO]].

[93] G. Mangano, A. Melchiorri, O. Mena, G. Miele and A. Slosar, JCAP **0703**, 006 (2007) [arXiv:astro-ph/0612150].

[94] J. Hamann, S. Hannestad, G. G. Raffelt and Y. Y. Y. Wong, JCAP **0708**, 021 (2007) [arXiv:0705.0440 [astro-ph]].

[95] G. Mangano, G. Miele, S. Pastor, O. Pisanti and S. Sarikas, JCAP **1103** (2011) 035 [arXiv:1011.0916 [astro-ph.CO]].

[96] A. A. Aguilar-Arevalo *et al.* [MiniBooNE Collaboration], Phys. Rev. Lett. **103**, 111801 (2009) [arXiv:0904.1958 [hep-ex]].

[97] G. Karagiorgi, Z. Djurcic, J. M. Conrad, M. H. Shaevitz and M. Sorel, Phys. Rev. D **80**, 073001 (2009) [Erratum-ibid. D **81**, 039902 (2010)] [arXiv:0906.1997 [hep-ph]].

[98] E. Akhmedov and T. Schwetz, JHEP **1010** (2010) 115 [arXiv:1007.4171 [hep-ph]].

[99] A. Melchiorri, O. Mena, S. Palomares-Ruiz, S. Pascoli, A. Slosar and M. Sorel, JCAP **0901**, 036 (2009) [arXiv:0810.5133 [hep-ph]].

[100] M. A. Acero and J. Lesgourgues, Phys. Rev. D **79** (2009) 045026 [arXiv:0812.2249 [astro-ph]].

[101] J. Hamann, S. Hannestad, G. G. Raffelt, I. Tamborra and Y. Y. Y. Wong, Phys. Rev. Lett. **105**, 181301 (2010) [arXiv:1006.5276 [hep-ph]].

[102] S. Dodelson, A. Melchiorri and A. Slosar, Phys. Rev. Lett. **97**, 04301 (2006) [arXiv:astro-ph/0511500].

[103] A. Lewis and S. Bridle, Phys. Rev. D **66**, 103511 (2002) [arXiv:astro-ph/0205436].

[104] D. Larson *et al.*, Astrophys. J. Suppl. **192**, 16 (2011) [arXiv:1001.4635 [astro-ph.CO]].

[105] B. A. Reid, W. J. Percival, D. J. Eisenstein, L. Verde, D. N. Spergel, R. A. Skibba, N. A. Bahcall and T. Budavari *et al.*, Mon. Not. Roy. Astron. Soc. **404**, 60 (2010) [arXiv:0907.1659 [astro-ph.CO]].

[106] A. G. Riess *et al.*, Astrophys. J. **699**, 539 (2009) [arXiv:0905.0695 [astro-ph.CO]].

[107] E. Aver, K. A. Olive and E. D. Skillman, JCAP **1005**, 003 (2010) [arXiv:1001.5218 [astro-ph.CO]].

[108] Y. I. Izotov and T. X. Thuan, Astrophys. J. **710**, L67 (2010) [arXiv:1001.4440 [astro-ph.CO]].

[109] M. Pettini, B. J. Zych, M. T. Murphy, A. Lewis and C. C. Steidel, arXiv:0805.0594 [astro-ph].

[110] O. Pisanti, A. Cirillo, S. Esposito, F. Iocco, G. Mangano, G. Miele and P. D. Serpico, Comput. Phys. Commun. **178**, 956 (2008) [arXiv:0705.0290 [astro-ph]].

[111] J. Hamann, J. Lesgourgues, G. Mangano, JCAP **0803** (2008) 004. [arXiv:0712.2826 [astro-ph]].

[112] M. Blennow *et al.*, in preparation.

[113] G. Mention, M. Fechner, T. Lasserre, T. A. Mueller, D. Lhuillier, M. Cribier and A. Letourneau, arXiv:1101.2755 [hep-ex].

[114] C. Carbone, L. Verde, Y. Wang and A. Cimatti, JCAP **1103**, 030 (2011) [arXiv:1012.2868 [astro-ph.CO]].

[115] M. Tegmark, A. Taylor and A. Heavens, Astrophys. J. **480**, 22 (1997) [arXiv:astro-ph/9603021].

[116] G. Jungman, M. Kamionkowski, A. Kosowsky and D. N. Spergel, Phys. Rev. D **54**, 1332 (1996) [arXiv:astro-ph/9512139].

[117] R. A. Fisher, Annals Eugen. **6** (1935) 391.

[118] L. Perotto, J. Lesgourgues, S. Hannestad, H. Tu and Y. Y. Y. Wong, JCAP **0610** (2006) 013 [arXiv:astro-ph/0606227].

[119] [Planck Collaboration], [arXiv:astro-ph/0604069]

[120] L. Verde, H. Peiris and R. Jimenez, JCAP **0601**, 019 (2006) [arXiv:astro-ph/0506036].

[121] H. J. Seo and D. J. Eisenstein, Astrophys. J. **598**, 720 (2003) [arXiv:astro-ph/0307460].

[122] A. Refregier *et al.*, arXiv:astro-ph/0610062.

[123] A. Refregier, A. Amara, T. D. Kitching, A. Rassat, R. Scaramella, J. Weller and f. t. E. Consortium, arXiv:1001.0061 [astro-ph.IM].

[124] S. Hannestad, Phys. Rev. Lett. **95** (2005) 221301 [arXiv:astro-ph/0505551].

[125] G. La Vacca, S. A. Bonometto and L. P. L. Colombo, New Astron. **14**, 435 (2009) [arXiv:0810.0127 [astro-ph]].

[126] M. B. Gavela, D. Hernandez, L. L. Honorez, O. Mena and S. Rigolin, JCAP **0907**, 034 (2009) [Erratum-ibid. **1005**, E01 (2010)] [arXiv:0901.1611 [astro-ph]].

[127] A. F. Heavens, T. D. Kitching and L. Verde, Mon. Not. Roy. Astron. Soc. **380**, 1029 (2007) [arXiv:astro-ph/0703191].

[128] A. S. Riis and S. Hannestad, arXiv:1008.1495 [astro-ph.CO].

[129] W. L. Freedman *et al.* [HST Collaboration], Astrophys. J. **553**, 47 (2001) [arXiv:astro-ph/0012376].

[130] E. W. Otten and C. Weinheimer, Rept. Prog. Phys. **71**, 086201 (2008) [arXiv:0909.2104 [hep-ex]].

[131] W. L. Freedman and B. F. Madore, arXiv:1004.1856 [astro-ph.CO].

[132] G. Drexlin [KATRIN Collaboration], Nucl. Phys. Proc. Suppl. **145** (2005) 263.

[133] G. L. Fogli, E. Lisi, A. Marrone, A. Palazzo and A. M. Rotunno, Phys. Rev. D **84**, 053007 (2011) [arXiv:1106.6028 [hep-ph]].

[134] K. Eitel, Nucl. Phys. Proc. Suppl. **143** (2005) 197.

[135] O. Elgaroy, O. Lahav, W. J. Percival, J. A. Peacock, D. S. Madgwick, S. L. Bridle, C. M. Baugh and I. K. Baldry *et al.*, Phys. Rev. Lett. **89**, 061301 (2002) [astro-ph/0204152].

[136] D. N. Spergel *et al.* [WMAP Collaboration], Astrophys. J. Suppl. **148**, 175 (2003) [astro-ph/0302209].

[137] S. Hannestad, JCAP **0305**, 004 (2003) [astro-ph/0303076].

[138] S. W. Allen, R. W. Schmidt and S. L. Bridle, Mon. Not. Roy. Astron. Soc. **346**, 593 (2003) [astro-ph/0306386].

[139] M. Tegmark *et al.* [SDSS Collaboration], Phys. Rev. D **69** (2004) 103501 [astro-ph/0310723].

[140] V. Barger, D. Marfatia and A. Tregre, Phys. Lett. B **595**, 55 (2004) [hep-ph/0312065].

[141] S. Hannestad and G. Raffelt, JCAP **0404**, 008 (2004) [hep-ph/0312154].

[142] P. Crotty, J. Lesgourgues and S. Pastor, Phys. Rev. D **69**, 123007 (2004) [hep-ph/0402049].

[143] U. Seljak *et al.* [SDSS Collaboration], Phys. Rev. D **71**, 103515 (2005) [astro-ph/0407372].

[144] O. Elgaroy and O. Lahav, New J. Phys. **7**, 61 (2005) [hep-ph/0412075].

[145] A. Goobar, S. Hannestad, E. Mortsell and H. Tu, JCAP **0606**, 019 (2006) [astro-ph/0602155].

[146] D. N. Spergel *et al.* [WMAP Collaboration], Astrophys. J. Suppl. **170**, 377 (2007) [astro-ph/0603449].

[147] U. Seljak, A. Slosar and P. McDonald, JCAP **0610**, 014 (2006) [astro-ph/0604335].

[148] G. L. Fogli, E. Lisi, A. Marrone, A. Melchiorri, A. Palazzo, A. M. Rotunno, P. Serra and J. Silk *et al.*, Phys. Rev. D **78**, 033010 (2008) [arXiv:0805.2517 [hep-ph]].

[149] E. Komatsu *et al.* [WMAP Collaboration], Astrophys. J. Suppl. **180**, 330 (2009) [arXiv:0803.0547 [astro-ph]].

[150] S. A. Thomas, F. B. Abdalla and O. Lahav, Phys. Rev. Lett. **105**, 031301 (2010) [arXiv:0911.5291 [astro-ph.CO]].

[151] S. Saito, M. Takada and A. Taruya, Phys. Rev. D **83**, 043529 (2011) [arXiv:1006.4845 [astro-ph.CO]].

[152] S. Riemer-Sorensen, C. Blake, D. Parkinson, T. M. Davis, S. Brough, M. Colless, C. Contreras and W. Couch *et al.*, Phys. Rev. D **85**, 081101 (2012) [arXiv:1112.4940 [astro-ph.CO]].

[153] B. A. Benson, T. de Haan, J. P. Dudley, C. L. Reichardt, K. A. Aird, K. Andersson, R. Armstrong and M. Bautz *et al.*, Apj, 763, **147** (2013) [arXiv:1112.5435 [astro-ph.CO]].

[154] Ho, S., Cuesta, A., & Seo, H.-J. *et al.* 2012, submitted to ApJ

[155] H. -J. Seo, S. Ho, M. White, A. Cuesta, A. Ross, S. Saito, B. Reid and N. Padmanabhan *et al.*, Astrophys. J. **761**, 13 (2012) [arXiv:1201.2172 [astro-ph.CO]].

[156] M. Fukugita, T. Ichikawa, J. E. Gunn, M. Doi, K. Shimasaku and D. P. Schneider, Astron. J. **111**, 1748 (1996).

[157] J. E. Gunn *et al.* [SDSS Collaboration], Astron. J. **116**, 3040 (1998) [astro-ph/9809085].

[158] J. E. Gunn *et al.* [SDSS Collaboration], Astron. J. **131**, 2332 (2006) [astro-ph/0602326].

[159] J. R. Pier, J. A. Munn, R. B. Hindsley, G. S. Hennessy, S. M. Kent, R. H. Lupton and Z. Ivezic, Astron. J. **125**, 1559 (2003) [astro-ph/0211375].

[160] Seljak, U. 1998, ApJ, 506, 64

[161] M. Tegmark, A. J. S. Hamilton, M. A. Strauss, M. S. Vogeley and A. S. Szalay, Astrophys. J. **499**, 555 (1998) [astro-ph/9708020].

[162] N. Padmanabhan, U. Seljak and U. L. Pen, New Astron. **8**, 581 (2003) [astro-ph/0210478].

[163] N. Padmanabhan *et al.* [SDSS Collaboration], Mon. Not. Roy. Astron. Soc. **378**, 852 (2007) [astro-ph/0605302].

[164] W. Hu and D. J. Eisenstein, Astrophys. J. **498**, 497 (1998) [astro-ph/9710216].

[165] D. J. Eisenstein and W. Hu, Astrophys. J. **511**, 5 (1997) [astro-ph/9710252].

[166] K. B. Fisher, C. A. Scharf and O. Lahav, Mon. Not. Roy. Astron. Soc. **266**, 219 (1994) [astro-ph/9309027].

[167] A. F. Heavens and A. N. Taylor, Mon. Not. Roy. Astron. Soc. **275**, 483 (1995) [astro-ph/9409027].

[168] R. E. Smith *et al.* [Virgo Consortium Collaboration], Mon. Not. Roy. Astron. Soc. **341**, 1311 (2003) [astro-ph/0207664].

[169] S. Bird, M. Viel and M. G. Haehnelt, Mon. Not. Roy. Astron. Soc. **420**, 2551 (2012) [arXiv:1109.4416 [astro-ph.CO]].

[170] N. Hamaus, U. Seljak, V. Desjacques, R. E. Smith and T. Baldauf, Phys. Rev. D **82**, 043515 (2010) [arXiv:1004.5377 [astro-ph.CO]].

[171] S. Saito, M. Takada and A. Taruya, Phys. Rev. Lett. **100**, 191301 (2008) [arXiv:0801.0607 [astro-ph]].

[172] S. Saito, M. Takada and A. Taruya, Phys. Rev. D **80**, 083528 (2009) [arXiv:0907.2922 [astro-ph.CO]].

[173] P. McDonald, Phys. Rev. D **74**, 103512 (2006) [Erratum-ibid. D **74**, 129901 (2006)] [astro-ph/0609413].

[174] M. E. C. Swanson, W. J. Percival and O. Lahav, Mon. Not. Roy. Astron. Soc. **409**, 1100 (2010) [arXiv:1006.2825 [astro-ph.CO]].

[175] J. Hamann, S. Hannestad, A. Melchiorri and Y. Y. Y. Wong, JCAP **0807**, 017 (2008) [arXiv:0804.1789 [astro-ph]].

[176] U. Seljak, Mon. Not. Roy. Astron. Soc. **325**, 1359 (2001) [astro-ph/0009016].

[177] —. 2001, MNRAS, 325, 1359

[178] A. E. Schulz and M. J. White, 1, Astropart. Phys. **25**, 172 (2006) [astro-ph/0510100].

[179] J. Guzik and G. Bernstein, Mon. Not. Roy. Astron. Soc. **375**, 1329 (2007) [astro-ph/0605594].

[180] R. J. Scherrer and D. H. Weinberg, Astrophys. J. **504**, 607 (1998) [astro-ph/9712192].

[181] P. Coles, A. Melott and D. Munshi, astro-ph/9904253.

[182] D. N. Limber, Astrophys. J. **119**, 655 (1954).

[183] R. Jimenez, T. Kitching, C. Pena-Garay and L. Verde, JCAP **1005**, 035 (2010) [arXiv:1003.5918 [astro-ph.CO]].

[184] K. N. Abazajian *et al.* [SDSS Collaboration], Astrophys. J. Suppl. **182**, 543 (2009) [arXiv:0812.0649 [astro-ph]].

[185] W. J. Percival *et al.* [SDSS Collaboration], Mon. Not. Roy. Astron. Soc. **401**, 2148 (2010) [arXiv:0907.1660 [astro-ph.CO]].

[186] E. Komatsu and U. Seljak, Mon. Not. Roy. Astron. Soc. **336**, 1256 (2002) [astro-ph/0205468].

[187] D. J. Eisenstein and W. Hu, Astrophys. J. **496**, 605 (1998) [astro-ph/9709112].

[188] A. Collister, O. Lahav, C. Blake, R. Cannon, S. Croom, M. Drinkwater, A. Edge and D. Eisenstein *et al.*, Mon. Not. Roy. Astron. Soc. **375**, 68 (2007) [astro-ph/0607630].

[189] E. Giusarma, M. Corsi, M. Archidiacono, R. de Putter, A. Melchiorri, O. Mena, S. Pandolfi, Phys. Rev. **D83**, 115023 (2011). [arXiv:1102.4774 [astro-ph.CO]].

[190] J. Hamann, JCAP **1203**, 021 (2012) [arXiv:1110.4271 [astro-ph.CO]].

[191] K. M. Nollett and G. P. Holder, arXiv:1112.2683 [astro-ph.CO].

[192] E. Giusarma, M. Archidiacono, R. de Putter, A. Melchiorri and O. Mena, Phys. Rev. D **85**, 083522 (2012) [arXiv:1112.4661 [astro-ph.CO]].

[193] R. de Putter, O. Mena, E. Giusarma, S. Ho, A. Cuesta, H. -J. Seo, A. Ross and M. White *et al.*, arXiv:1201.1909 [astro-ph.CO].

[194] S. Joudaki, K. N. Abazajian and M. Kaplinghat, arXiv:1208.4354 [astro-ph.CO].

[195] S. Riemer-Sorensen, D. Parkinson, T. Davis and C. Blake, arXiv:1210.2131 [astro-ph.CO].

[196] E. Giusarma, R. de Putter and O. Mena, arXiv:1211.2154 [astro-ph.CO].

[197] M. Archidiacono, N. Fornengo, C. Giunti, S. Hannestad and A. Melchiorri, arXiv:1302.6720 [astro-ph.CO].

[198] R. Diamanti, E. Giusarma, O. Mena, M. Archidiacono and A. Melchiorri, arXiv:1212.6007 [astro-ph.CO].

[199] M. Archidiacono, E. Giusarma, A. Melchiorri and O. Mena, Phys. Rev. D **86** (2012) 043509 [arXiv:1206.0109 [astro-ph.CO]].

[200] M. Archidiacono, E. Calabrese and A. Melchiorri, Phys. Rev. D **84** (2011) 123008 [arXiv:1109.2767 [astro-ph.CO]].

[201] S. Das, B. D. Sherwin, P. Aguirre, J. W. Appel, J. R. Bond, C. S. Carvalho, M. J. Devlin and J. Dunkley *et al.*, Phys. Rev. Lett. **107**, 021301 (2011) [arXiv:1103.2124 [astro-ph.CO]].

[202] J. J. Gomez-Cadenas, J. Martin-Albo, J. M. Vidal and C. Pena-Garay, arXiv:1301.2901 [hep-ph].

[203] E. Di Valentino, S. Galli, M. Lattanzi, A. Melchiorri, P. Natoli, L. Pagano and N. Said, arXiv:1301.7343 [astro-ph.CO].

[204] D. Schlegel *et al.* [with input from the SDSS-III Collaboration], arXiv:0902.4680 [astro-ph.CO].

[205] K. S. Dawson *et al*, arXiv:1208.0022 [astro-ph.CO].

[206] D. J. Eisenstein *et al.*, Astrophys. J. **664**, 675 (2007) [arXiv:astro-ph/0604362.

[207] A. Kosowsky and M. S. Turner, Phys. Rev. D **52**, 1739 (1995) [astro-ph/9504071].

[208] Y. I. Izotov and T. X. Thuan, Astrophys. J. **710**, L67 (2010) [arXiv:1001.4440 [astro-ph.CO]].

[209] T. L. Smith, S. Das and O. Zahn, Phys. Rev. D **85**, 023001 (2012) [arXiv:1105.3246 [astro-ph.CO]].

[210] J. Dunkley, R. Hlozek, J. Sievers, V. Acquaviva, P. A. R. Ade, P. Aguirre, M. Amiri and J. W. Appel *et al.*, Astrophys. J. **739**, 52 (2011) [arXiv:1009.0866 [astro-ph.CO]].

[211] A. Smith, M. Archidiacono, A. Cooray, F. De Bernardis, A. Melchiorri and J. Smidt, Phys. Rev. D **85**, 123521 (2012) [arXiv:1112.3006 [astro-ph.CO]].

[212] M. C. Gonzalez-Garcia, V. Niro and J. Salvado, arXiv:1212.1472 [hep-ph].

[213] W. Hu, D. J. Eisenstein, M. Tegmark and M. J. White, Phys. Rev. D **59**, 023512 (1999) [astro-ph/9806362].

[214] P. Serra, F. Zalamea, A. Cooray, G. Mangano and A. Melchiorri, Phys. Rev. D **81**, 043507 (2010) [arXiv:0911.4411 [astro-ph.CO]].

[215] P. A. R. Ade *et al.* [Planck Collaboration], Astron. Astrophys. **536**, 16464 (2011) [arXiv:1101.2022 [astro-ph.IM]]; [Planck Collaboration], astro-ph/0604069.

[216] F. R. Bouchet *et al.* [COrE Collaboration], arXiv:1102.2181 [astro-ph.CO].

[217] W. Hu, D. Scott, N. Sugiyama and M. J. White, 1, Phys. Rev. D **52**, 5498 (1995) [astro-ph/9505043].

[218] W. Hu and N. Sugiyama, Astrophys. J. **471**, 542 (1996) [astro-ph/9510117].

[219] R. Bowen, S. H. Hansen, A. Melchiorri, J. Silk and R. Trotta, Mon. Not. Roy. Astron. Soc. **334**, 760 (2002) [astro-ph/0110636].

[220] T. Basse, O. E. Bjaelde, J. Hamann, S. Hannestad and Y. Y. Y. Wong, arXiv:1304.2321 [astro-ph.CO].

[221] M. Archidiacono, E. Giusarma, A. Melchiorri and O. Mena, arXiv:1303.0143 [astro-ph.CO].